Crack Coalescence in Rock-like Material under Cyclic Loading

by

Tae Young Ko

M. S., Geo-Environmental System Engineering
Hanyang University, 2001

B. S., Mineral and Petroleum Engineering
Hanyang University, 1999

Submitted to the Department of Civil and Environmental Engineering
in Partial Fulfillment of the Requirements for the Degree of
Master of Science in Civil and Environmental Engineering

at the

Massachusetts Institute of Technology

February 2005

Signature of Author ....
Department of Civil and Environmental Engineering
December 20, 2004

Certified by ....
Herbert H. Einstein
Professor of Civil and Environmental Engineering
Thesis Supervisor

Accepted by ....
Andrew J. Whittle
Chairman, Departmental Committee on Graduate Studies

Crack Coalescence in Rock-like Material under Cyclic Loading

by

Tae Young Ko

Submitted to the Department of Civil and Environmental Engineering
on December 20, 2004 in Partial Fulfillment of the
requirements for the Degree of Master of Science in
Civil and Environmental Engineering

ABSTRACT

A total of 170 tests (68 tests for monotonic loading, 102 tests for cyclic loading) have been performed to investigate crack initiation, propagation and coalescence. The specimens have two pre-existing flaws which are arranged at different distances and angles. Wing cracks and secondary cracks are observed in both monotonic and cyclic tests. Wing cracks, which are tension cracks, initiate at (or near) the tips of the flaws and propagate parallel to the compressive loading axis. Secondary cracks always appear after wing crack initiation and lead to final failure. Secondary cracks initiate at the tips of the flaws and propagate in the coplanar direction of the flaw or horizontal (quasi-coplanar) direction. Six types of coalescence are observed. For coplanar geometry specimens, coalescence occurs due to the internal shear cracks. For non-coplanar geometry specimens, coalescence occurs through combinations of internal shear cracks, internal wing cracks and tension cracks. Contrary to monotonic tests, cyclic tests produce fatigue cracks. Fatigue cracks usually occur when 1) after coalescence, the specimens behave as if they had only one larger crack 2) specimens have been subjected to a particular number of cycles. In these experiments, two different fatigue crack initiation directions are observed: horizontal and coplanar to the flaw.

Thesis Supervisor: Herbert H. Einstein
Title: Professor of Civil and Environmental Engineering

TABLE OF CONTENTS

LIST OF FIGURES

LIST OF TABLES

Chapter 1. Introduction

Rock is one of the most common materials, and it also has been used for a long time as construction material. From a constitutive point of view, most engineering materials are relatively homogeneous at least on a macroscopic scale. However, rock can be an extremely variable substance that consists of crystals, grains, voids, pores, cracks and the like. Under applied load, these microstructures interact with each other to give rise to a corresponding macroscopic mechanical response. The study of brittle fracture of rock is essential for an understanding of many processes encountered in rock mechanics and rock engineering.

Numerous experimental and theoretical efforts have been devoted to the understanding of the crack initiation, propagation, and coalescence of pre-existing cracks in brittle material. The first milestone was set by Griffith (1921, 1924). Griffith formulated the concept that a crack in a component will propagate if the total energy of the system is lowered with crack propagation. That is, if the change in elastic strain energy due to crack extension is larger than the energy required creating new crack surfaces, crack propagation will occur. Irwin (1957) introduced the concept of critical energy release rate and the crack tip stress intensity factor.

Under the monotonic compressive loading, both tensile and shear stress can develop at inclined pre-existing cracks in rock. As the compression increases, tensile cracks initiate from the tip of pre-existing cracks and grow progressively parallel to the compression direction. With increasing load, cracks coalesce later, which lead to specimen failure in most cases.

Although fracture behavior of rock under monotonic compression has been widely studied, the research performed on rock under cyclic compression has been limited (Burdine, 1963; Hardy and Chugh, 1970; Haimson and Kim, 1971; Li et al., 2001; Li et al., 2003). Rock and rock structures such as bridge abutments, dam and road foundations, and tunnel walls undergo cyclic loading caused by earthquakes, vehicle-induced vibrations, drilling, and blasting, etc. This type of loading often causes rock to fail at a lower stress than its monotonically determined compressive strength.

Under cyclic loading, brittle materials with flaws exhibit a completely different mode of crack initiation. When notched plates of brittle solids are subjected to uniaxial cyclic compression loading, fatigue crack initiation and growth occur perpendicularly to the compression axis in brittle materials (Figure 1.1) (Suresh, 1998). Whereas uniaxial monotonic compressive stresses promote a splitting mode of failure parallel to the stress axis.

Figure 1.2 shows the difference of the failure type between monotonic and cyclic loading. Under uniaxial monotonic loading, two typical cones develop in the proximity of the loaded base. Whereas under uniaxial cyclic loading, fracture occurs as a rule along an inclined plane that develops throughout the specimen's entire height (Royer-Carfagni and Salvatore, 2000).

It appears, therefore, that crack pattern and coalescence are different for monotonic and cyclic loading but the mechanisms of crack coalescence under cyclic loading have not been sufficiently investigated. The main goal in this study is to increase the understanding of the fracture process in rock material under cyclic loading.

This thesis consists of 6 chapters. Chapter 2 is a short review of previous research on brittle material under monotonic and cyclic loading. Chapter 3 contains the theoretical considerations. The most widely used fracture criteria and fracture propagation models are briefly introduced. Chapter 4 describes the specimen properties and the experimental procedure to prepare and test. Chapter 5 gives the experimental results from monotonic and cyclic tests and their interpretation. In chapter 6 conclusions of this study and recommendations for future study are provided.

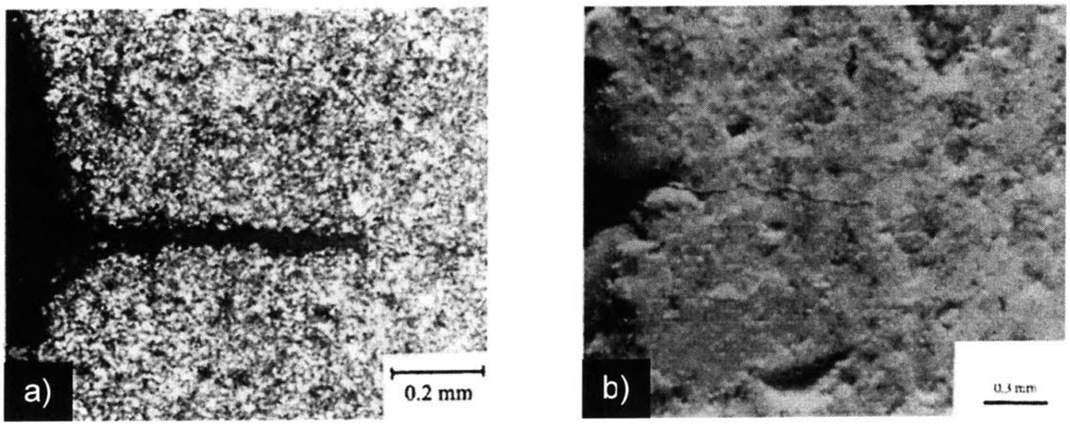

Figure 1.1 Examples of mode I fatigue cracks initiated at stress concentrations under far-field cyclic compression: (a) Polycrystalline Al_2O_3. (b) Cement mortar. The compression axis is vertical in both cases (Suresh, 1998).

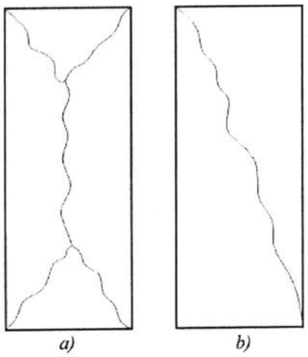

Figure 1.2 Typical fracture schemes in monotonic (a) and cyclic (b) test (Royer-Carfagni and Salvatore, 2000).

Chapter 2. Literature review

2.1 Intact specimens under monotonic loading

For monotonic uniaxial compressive tests on intact specimens of homogeneous rock, Hawkes and Mellor (1970) reported that the pattern of failure should be either axially symmetric or random under the ideal displacement boundary conditions. There are three broad modes of failure which are observed in monotonic compressive tests:

(1) Cataclasis, consists of a general internal crumbling by formation of multiple cracks in the direction of the applied load. When the specimens collapse, conical end fragments are left, together with long slivers of rock from around the periphery (Figure. 2.1(a), (b), (c))

(2) Axial cleavage of vertical splitting, in which one or more major cracks split the specimen along the loading direction (Figure. 2.1(d), (e)).

(3) Shearing of the specimen along a single oblique plane (Figure. 2.1(f)).

In some cases it is difficult to distinguish these different modes in a failed specimen, and occasionally all three may appear to be present.

2.2 Flaws induced specimens under monotonic loading

2.2.1 Single flaw specimens under monotonic loading

In monotonic compressive tests, wing cracks are always observed in brittle materials such as glass (Brace and Bombolakis, 1963; Hoek and Bieniawski, 1965), PMMA (McClinock and Walsh, 1962; Ashby and Hallam, 1986), Columbia resin CR39 (Horii and Nemat-Nasser, 1986), plaster of Paris (Lajtai, 1974), gypsum (Reyes, 1991; Shen et al, 1995; Bobet, 1997; Sagong, 2001) and rock (Ingraffa and Heuze, 1980; Petit and Barquins, 1988; Chen et al., 1995). Wing cracks initiate from the flaw tips, curve and propagate parallel to the applied compressive load. However, secondary (or shear) cracks were not observed in any of experiments on polymers.

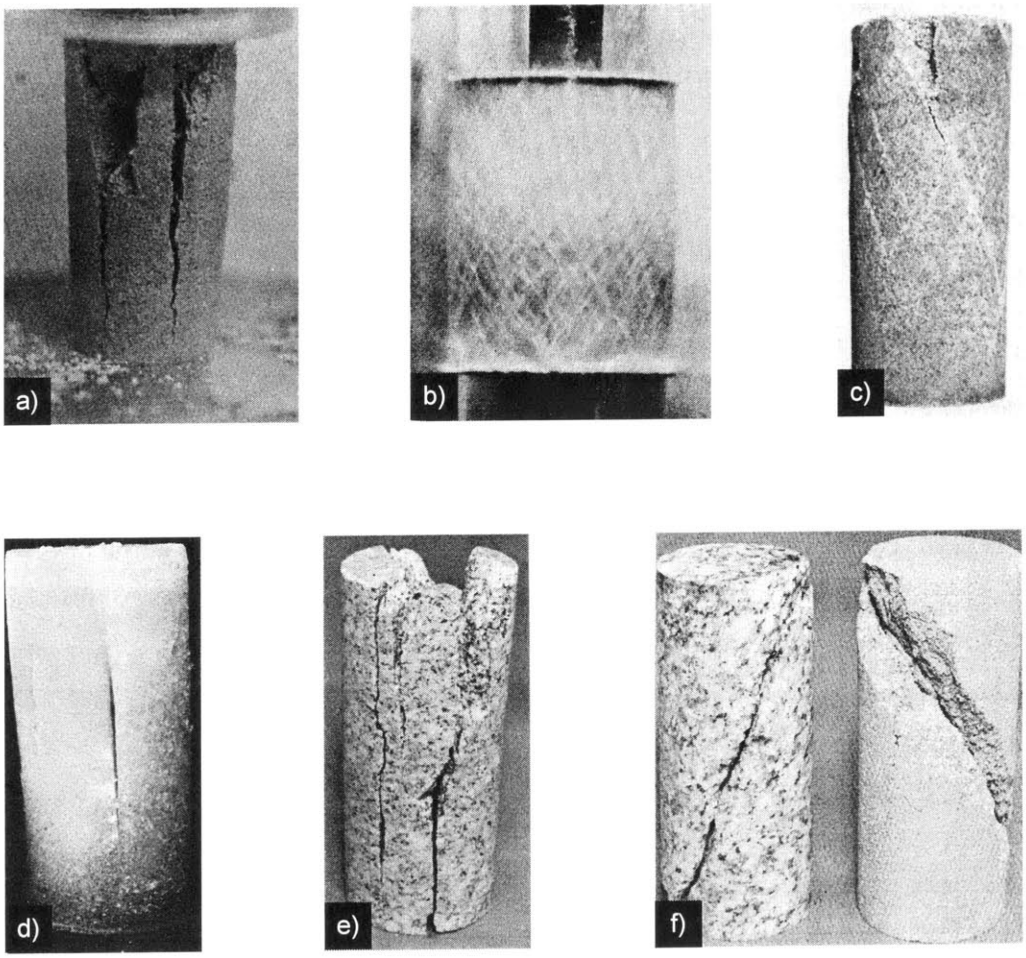

Figure 2.1 Modes of failure of cylindrical rock test specimens under uniaxial compression : a) Cataclasis, b) Cataclasis, Solenhofen Limestone, c) Cataclasis, Berea Sandstone, d) Axial cleavage, ice, e) Axial cleavage, granite, f) Shear failure (Hawkes and Mellor, 1970).

Lajtai(1974) performed tests on plaster of Paris specimens with a single flaw. He observed the following crack formation sequences:

1. Tensile fractures initiated form the tips of a flaw. They appeared suddenly with cracking noise.
2. Normal shear fractures initiated in the horizontal direction.
3. As the axial load increased, both tensile and shear fractures extended. Damage of material appeared near the normal shear fractures.
4. The shear zone developed noticeably in the axial direction.

Figure 2.2 shows the crack formation sequence that Lajtai(1974) observed.

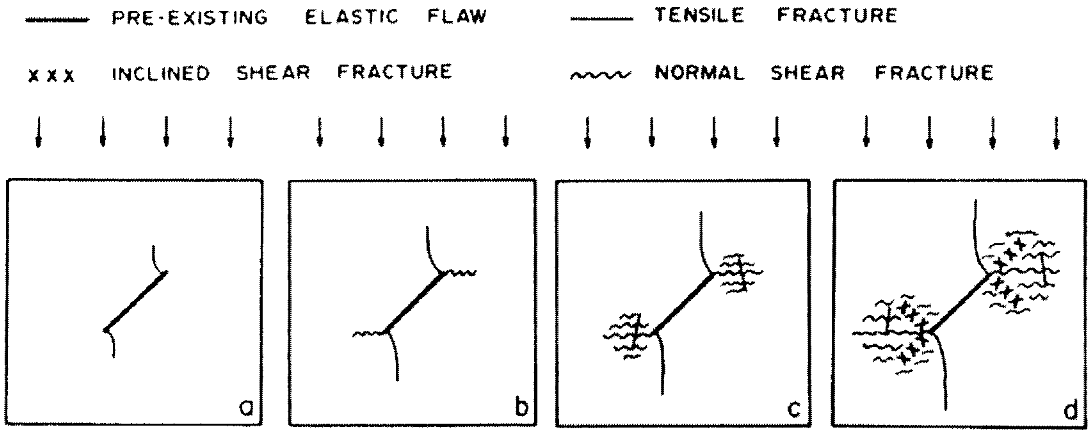

Figure 2.2 Crack formation sequence from a single flaw in a plaster of Paris specimen: (a) first tensile fracture, (b) first normal shear fracture, (c) expansion into a shear zone through subsequent normal shear and perhaps tensile fractures, (d) inclined shear fractures in the granulated cohesionless zone (Lajtai,1974).

Ingraffa and Heuze (1980) ran uniaxial compressive tests on limestone and grandioraite specimens with a single inclined flaw (Figure 2.3). The crack growth sequence was observed as follows:

(1) Cracks initiated from tensile stress concentration points near the flaw tips. These cracks were called "primary", which is equivalent to wing cracks in this study.

(2) These "primary" cracks propagated stably along a curvilinear path towards the direction of maximum compressive load.

(3) After considerable primary crack propagation, another set of cracks, called "secondary", apparently initiated at compressive stress concentration points near the flaw tips.

(4) These secondary cracks propagated in an unstable manner leading to the specimen failure at a stress 3 to 5 times greater than the primary crack initiation stress.

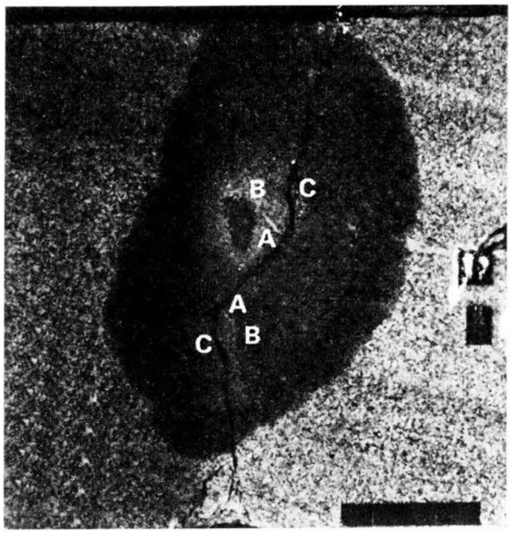

Figure 2.3 Failure of Indiana limestone with inclined single flaw. Primary cracks initiate at A and propagate to B. Secondary cracks nucleate in a region near C and propagate both toward the flaw tips and the specimen edge (Ingraffa and Heuze ,1980).

Petit and Barquins (1988) performed tests prismatic single flaw specimens of sandstone with low and high porosities. They reported that both a low porosity and a high porosity specimen showed axisymmetric "Branch Fractures", but it was less developed in the high porosity sandstone. In the high porosity sandstone, a shear zone is observed along the plane of the flaw. In the low porosity sandstone, microcracks form at the tip of the flaw and produce the initiation of branch fractures (Figure 2.4). With further increase of the load, this shear zone developed more and caused the specimens to fail.

Huang et al. (1990) conducted an experiment on Fangsan marble plate with an inclined flaw. The observed crack sequence was divided into five stages:

(1) Initiation and propagation of primary forward tensile cracks (PFTCs).
(2) Initiation and propagation of secondary forward tensile cracks (SFTCs).
(3) Initiation and intensification of shear belts (forward shear belts, FSBs and backward shear belts, BSBs).
(4) Initiation and propagation of backward tensile cracks (BTCs).
(5) The ultimate failure.

Three types of failure are observed: (i) axial splitting along tensile cracks, (ii) shear fracture along shear belts, (iii) combinations of splitting and shear fracture. Figure 2.5 gives a schematic diagram of the failure traces that Huang et al. observed.

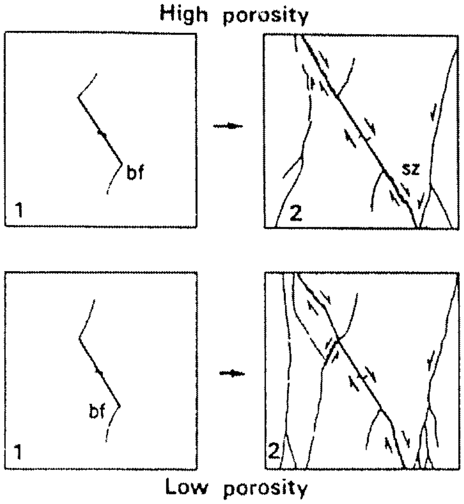

Figure 2.4 Crack growth from a single flaw in low and high porosity sandstone; bf, branch fracture; sz, shear zone. In the figure, 1 shows branch fracture formation before maximum stress and 2 shows shear zone formation and secondary fractures at or after maximum stress (Petit and Barquins, 1988).

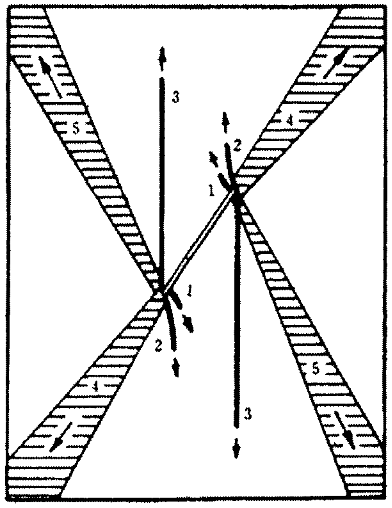

Figure 2.5 A schematic diagram showing the observed failure traces. 1-PFTCs; 2-SFTCs; 3-BTCs; 4-FSBs; 5-BSBs (Huang et al.,1990).

Chen et al. (1995) performed tests on marble plate with single flaw. They found that there exist three stages of fracturing: primary fracturing, secondary fracturing and final failure of the specimen. The crack growth sequence was:

(1) Primary cracks propagated perpendicular to the direction of the flaw (Figure 2.6b)

(2) Secondary cracks propagated in the direction of major principal stress. Secondary cracks developed faster and had longer lengths than the primary cracks. Both primary and secondary crack were stable and had finite lengths (Figure 2.6c).

(3) Final failure of the specimen occurred by the development of an "X" shaped microcrack band (Figure 2.6d).

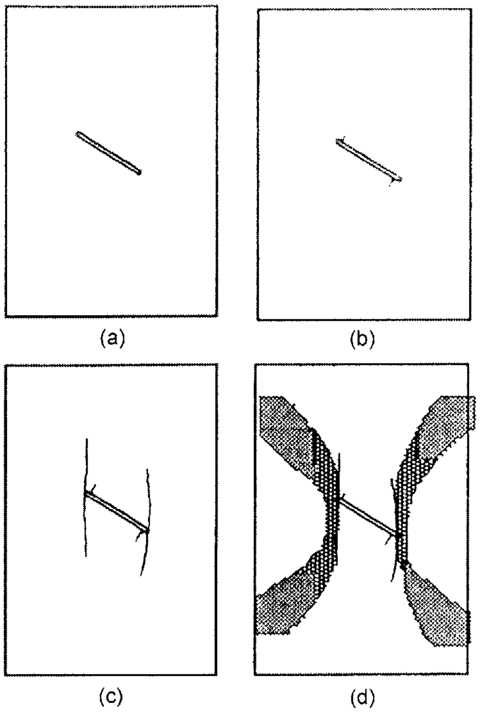

Figure 2.6 Crack growth around the flaw in the specimen under uniaxial compression (Chen et al.,1995).

2.2.2 Multiple flaw specimens under monotonic loading

Brace and Bombolakis (1963) performed uniaxial compression tests on glass with echelon cracks, as shown in Figure 2.7. Tension cracks initiated from the tips of the flaws and propagated along the loading direction. But, there were neither secondary crack nor coalescence crack.

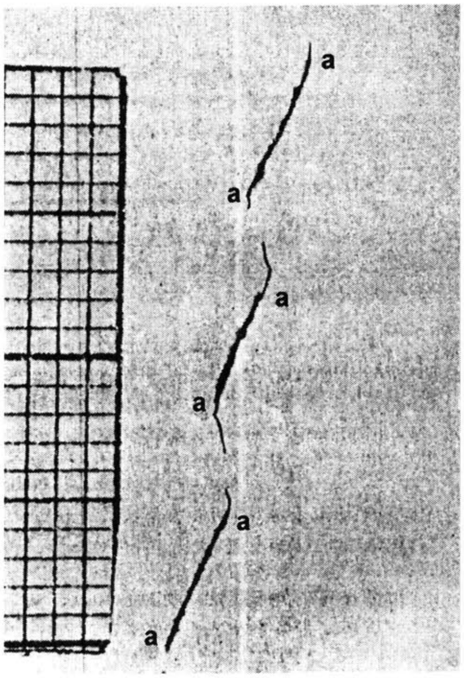

Figure 2.7 Growth of cracks array in glass under uniaxial compression (Brace and Bombolakis,1963).

Horri and Nemat-Nasser (1985) carried out tests on Columbia Resin CR 39. The tests showed that the process of splitting and shear failure of brittle material in uniaxial and biaxial compression. Two different types of flaw geometry specimens were prepared: (1) specimen containing a row of small flaws and several larger flaws and (2) specimen containing a band of small flaws and several larger flaws. Without confinement, splitting failure occurred by the growth of cracks at larger flaws in both specimens (Figure 2.8 (a), (c)). With confinement, shear failure occurred by coalescence cracks at smaller flaws in both specimens (figure 2.8 (b), (d))

Reyes and Einstein (1991) performed the tests on the prismatic gypsum specimens with two parallel flaws. They observed that if the two flaws overlapped, two flaws coalesced through interconnection of wing cracks; if the two flaws didn’t overlap, coalescence occurred through secondary cracks which occurred after the wing cracks.

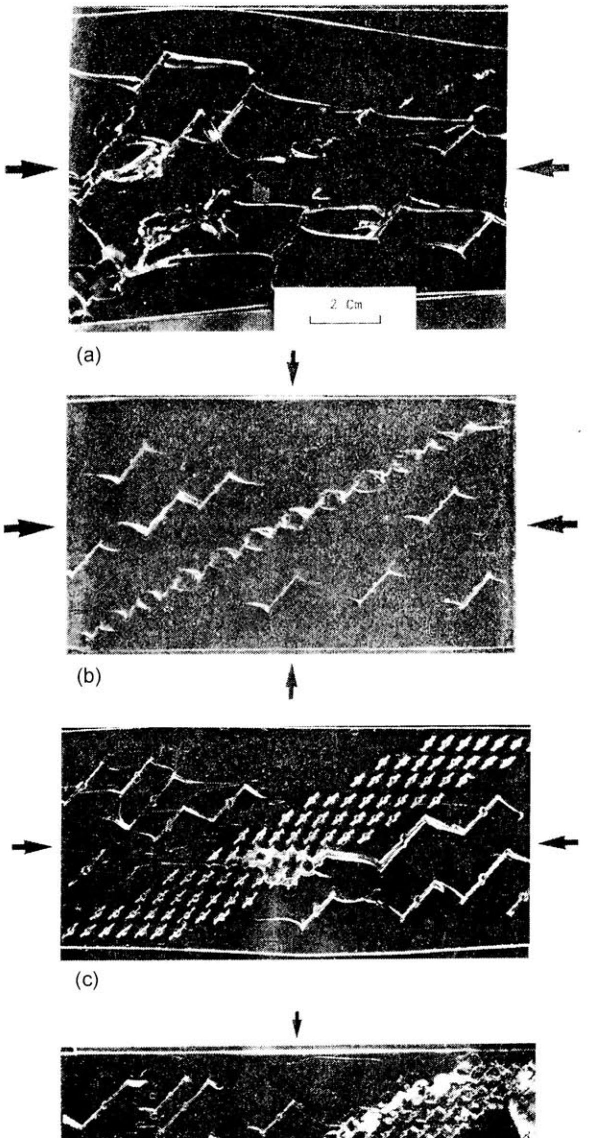

Figure 2.8 Axial splitting and shear failure in Columbia Resin CR 39 specimen. (a) axial splitting in specimen containing a row of small flaws and several larger flaws without confinement, (b) shear failure in specimen containing a row of small flaws and several larger flaws with confinement, (c) axial splitting in specimen containing a band of small flaws and several larger flaws without confinement, (d) shear failure in specimen containing a band of small flaws and several larger flaws with confinement (Horii and Nemat-Nasser, 1985).

Shen et al. (1995) tested prismatic molded gypsum specimens with two parallel flaws. They found that two inclined parallel flaws coalesced by shear failure and/or tensile fracture under the uniaxial compression. When the two flaws were coplanar, coalescence occurred by shear failure. When they overlapped, coalescence occurred by combination of shear and tensile fracture. In addition, two different flaw characteristics were used: (1) non-frictional flaws and (2) frictional flaws. It was found that coalescence of frictional flaws required higher load than non-frictional flaws.

Chen et al. (1995) conducted experiments on the marble plates with multiple flaws. The specimen had arrays of either three or five flaws. The experimental results are shown in Figure 2.9. The experiments showed that the coalescing of multiple flaws under compression had four stages:

(1) Relatively independent fracturing stage. The primary cracks appeared on each flaw and propagated in the direction perpendicular to the flaw.

(2) Coalescing stage. Primary cracks or secondary cracks propagated and connected the flaw.

(3) The fracturing of the whole flaw system.

(4) The failure of the specimen. An "X" shaped microcrack band occurred from the ends of the flaw system, and propagated to cause the failure of the specimen.

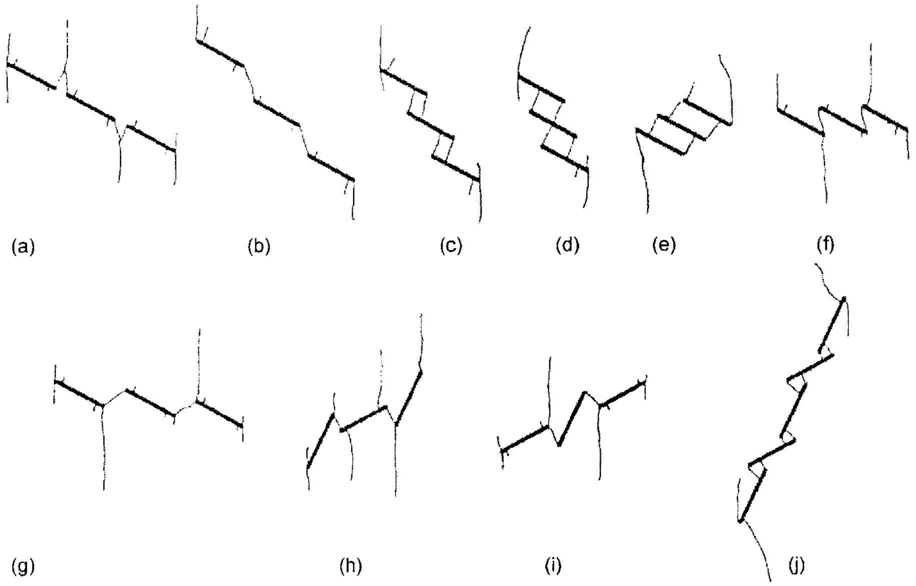

Figure 2.9 Coalescence patterns of flaws in the marble plate under compression (Chen et al.,1995).

Bobet and Einstein (1998) investigated crack coalescence in prismatic molded gypsum specimens in uniaxial and biaxial compression. The specimen had two parallel flaws, and that can be either open or closed. They observed that wing cracks appeared first and initiated at the tips of the flaws. Secondary cracks appeared later and in most case initiated in a direction coplanar to the flaw. They also studied secondary cracks in detail. Secondary cracks initiated and propagated as shear cracks. They gave three types of evidence that secondary cracks were shear cracks: (1) secondary cracks initiated with a protrusion of material or some material spalling from the surface; (2) The surface of secondary cracks showed crushed material and gypsum powder, which implies shear movement; (3) secondary cracks always initiated in a compressive stress field.

Tables 2.1 and 2.2 give the coalescence types that they observed in uniaxial and biaxial loading. Type I coalescence occurred through the connection of the internal secondary cracks when the two flaws were coplanar or close to coplanar. Type II coalescence was produced through the linkage of the two internal secondary cracks by another tensile crack when the spacing to continuity ratio was grater than 1/3. Type III coalescence occurred by the propagation of the internal secondary crack form on of the flaw until it reached the internal wing crack of the other flaw. It was observed when the specimen had a ligament angle of around 90°. Type I, II, and III occurred in uniaxial compression and Type I and II occurred in biaxial compression.

Wong and Chau (1998) ran tests on sandstone-like material to investigate the crack coalescence pattern. They observed three main modes of crack coalescence: (1) shear (S) mode – shear cracks occurred between the two flaws; (2) the mixed shear/tensile (M) mode – both wing and shear cracks propagated between the two flaws; (3) wing tensile (W) mode – wing cracks coalesced the two cracks. Figure 2.10 gives the detailed crack patterns in this experiment.

Sagong and Bobet (2002) carried out tests on the molded gypsum specimens with three and 16 flaws. They observed similar crack coalescence patterns with two flaws. They also found that there were two directions of secondary cracks: (1) coplanar or quasi-coplanar direction of secondary cracks, and (2) an angled or oblique direction of secondary cracks. Tables 2.3 and 2.4 show the types of crack coalescence in specimens with three flaws and 16 flaws.

Type	Coalescence Pattern	Characteristic of Coalescence	Mode of Coalescence
I	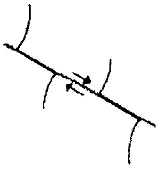	Type of cracks: secondary cracks. Initiation position: preexisting flaw tips. Crack surface characterization: rough, with many small kink steps; contains crushed gypsum.	Shear
II		Type of crack: secondary and wing cracks. Initiation position: preexisting flaw tips. Crack surface characterization: rough with crushed gypsum on secondary crack and clean and smooth on tensile crack	Shear + Tension
III		Type of crack: secondary and wing cracks. Initiation position: preexisting flaw tips. Crack surface characterization: rough with crushed gypsum on the secondary crack and clean and smooth on the tensile crack.	Shear + Tension
IV		Type of crack: wing crack. Initiation position: preexisting flaw tips. Crack surface characterization: smooth and clean	Tension
V	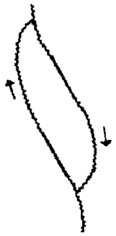	Type of crack: secondary cracks. Initiation position: preexisting flaw tips. Crack surface characterization: very rough, coated with a lot of crushed gypsum	Shearing?

Table 2.1 Coalescence types in uniaxial compression (Bobet and Einstein,1998).

Type	Coalescence Pattern	Description of Coalescence	Mode of Coalescence	Lateral Stress
I	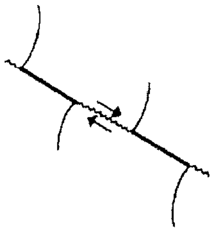	Type of coalescing fracture: secondary shear crack. Initiation position: pre-existing flaw tips. Crack surface characterization: rough, with many small kink steps; contains crushed gypsum. For s=0 only	Shearing	< 2.5 MPa
II		Type of coalescing fracture: secondary shear crack and tensile cracks. Initiation position: pre-existing flaw tips. Crack surface characterization: some parts are clean and smooth while other parts are rough with crushed gypsum. Wing cracks initiate from the tips of the flaws. s≠0	Shearing + tension	
	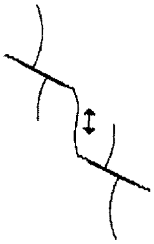	Type of coalescing fracture: secondary shear crack and tensile cracks. Initiation position: pre-existing flaw tips. Crack surface characterization: some parts are clean and smooth while other parts are rough with crushed gypsum. Wing cracks initiate near center of the flaws. s≠0	Shearing + tension	≤5.0 MPa
		Type of coalescing fracture: secondary shear crack and tensile cracks. Initiation position: pre-existing flaw tips. Crack surface characterization: rough with crushed gypsum. No wing cracks. s≠0	Shearing + Possible tension	> 5.0 MPa

Table 2.2 Coalescence types in biaxial compression (Bobet and Einstein,1998).

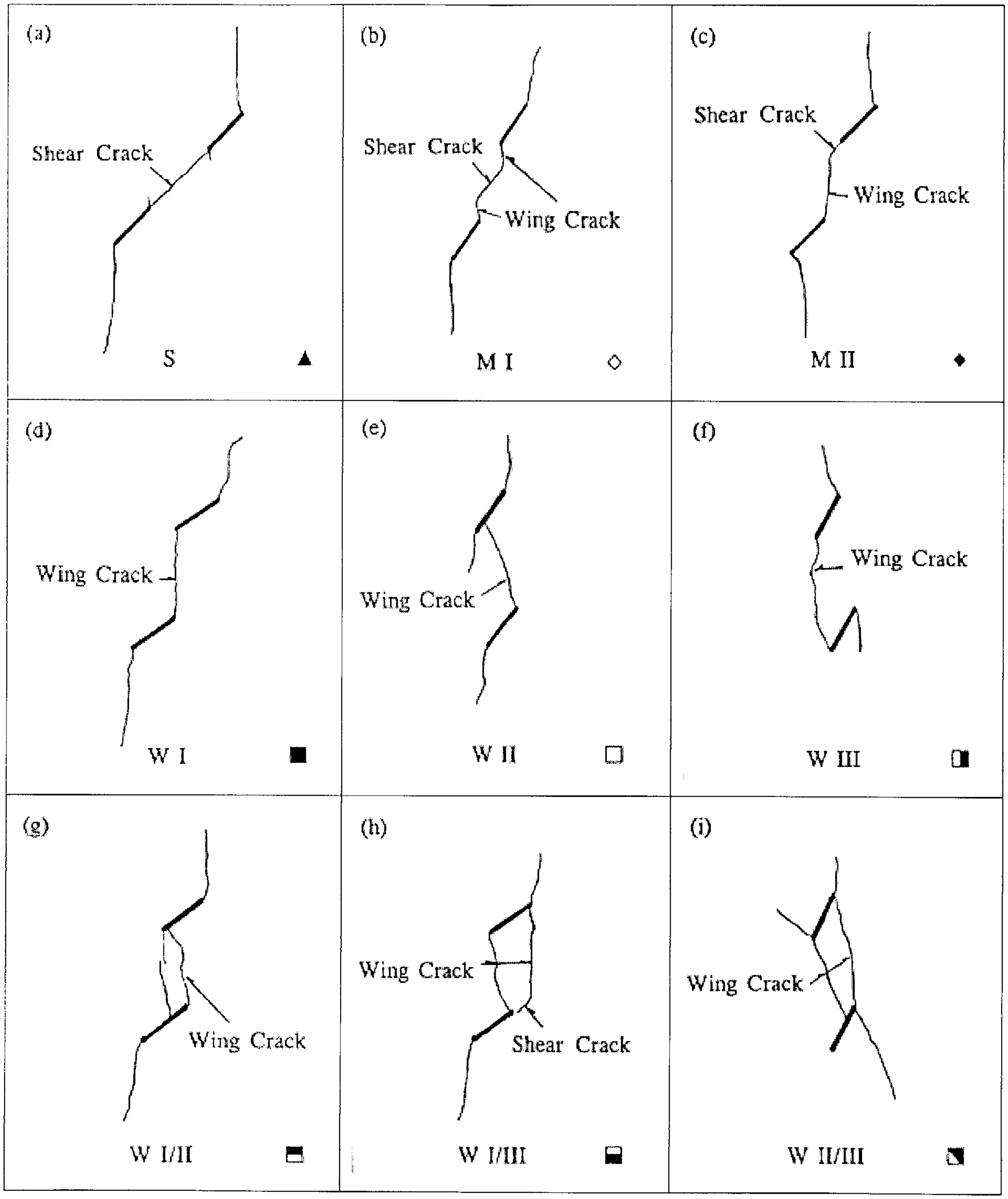

Figure 2.10 Crack coalescence patterns in sandstone-like material under uniaxial compression (Wong and Chau ,1998).

Type	Left Stepping	Type	Right Stepping	Coalescence cracks
I	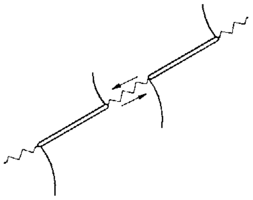	VI	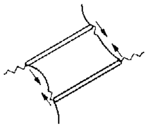	Type I: Quasi-coplanar secondary cracks. Type VI: Oblique secondary crack and wing crack.
II	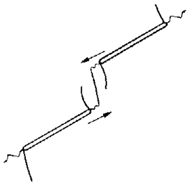	VII	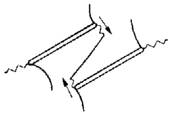	Type II: Quasi-coplanar secondary cracks and out of plane tensile secondary crack. Type VII: Oblique secondary cracks and out of plane tensile secondary crack.
III	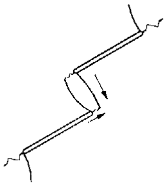	VIII	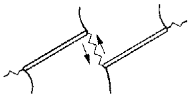	Type III: Quasi-coplanar secondary crack and wing crack. Type VIII: Oblique secondary cracks.
IV	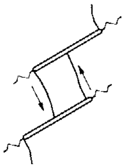	IX	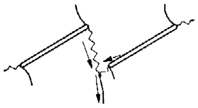	Type IV: Wing crack Type IX: Oblique secondary crack and quasi-coplanar secondary crack.
V	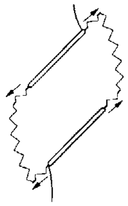			Type V: Quasi-coplanar secondary crack and out of plane secondary shear crack.

Table 2.3 types of crack coalescence in specimens with three flaws (Sagong and Bobet, 2002).

Type	Left Stepping	Type	Right Stepping	Coalescence cracks
I	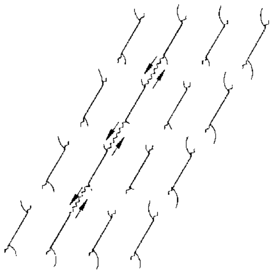	VI	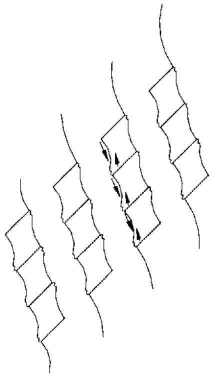	Type I: Quasi-coplanar secondary cracks. Cross-columnar coalescence Type VI: Oblique secondary crack and wing crack. Columnar coalescence
III	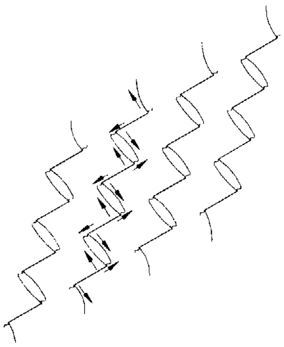	VII	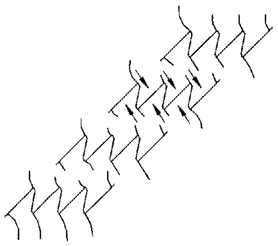	Type III: Quasi-coplanar secondary crack and wing crack. Columnar coalescence Type VII: Oblique secondary cracks and out of plane tensile crack. Columnar coalescence

Table 2.4 types of crack coalescence in specimens with 16 flaws (Sagong and Bobet, 2002).

2.3 Intact specimens under cyclic loading

The typical cyclic compression loading program is illustrated in Figure 2.11 with notations. This notation is used throughout the thesis and is defined below.

- Stress cycle – the smallest segment of the stress-time function which is repeated periodically.
- Maximum stress, σ_{max} – the highest value of the stress in the stress cycle. Compressive stress is considered positive.
- Minimum stress, σ_{min} – the lowest value of the stress in the stress cycle.
- Stress range, σ_r – the difference between the maximum and minimum stress in one cycle,

i.e., $\sigma_r = \sigma_{max} - \sigma_{min}$.

- Stress amplitude, σ_a – one-half the stress range, i.e., $\sigma_a = 1/2\ \sigma_r$.
- Mean stress, σ_m – the mean of the maximum and minimum stress in one cycle, i.e., $\sigma_m = (\sigma_{max} + \sigma_{min})\ /\ 2$.
- Loading frequency, f – the number of stress cycles per unit time, i.e., f = 1/ period = 1/T.
- Fatigue life, N – the number of stress cycles that a specimen sustains before failure.

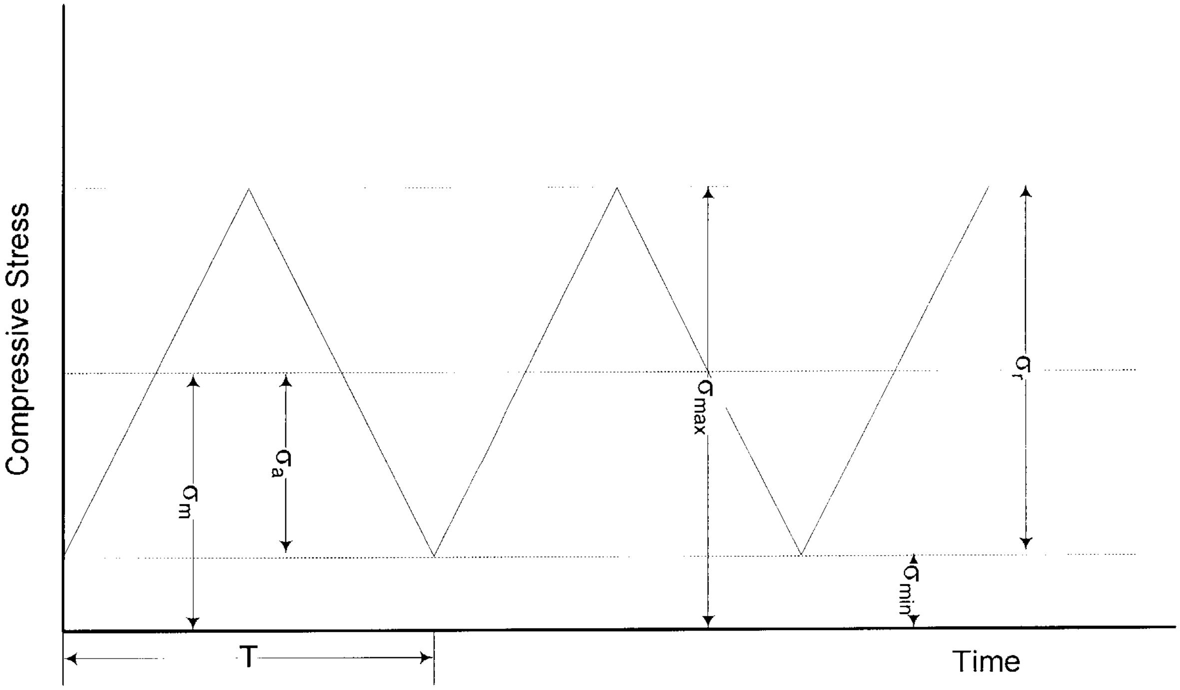

Figure 2.11 Typical cyclic loading program and notation.

During cyclic loading, rock material becomes fatigued because of creation of new microcracks and extension of existing microcracks (Haimson, 1974). This cracking causes an increased volume of the rock material.

Burdine (1963) carried out cyclic compression tests on Berea sandstone to investigate the cumulative damage to rock samples. He found that the stress-rate effect was negligible for the three frequencies tested. It was observed that the fatigue strength increased as the confining pressure increased.

Hardy and Chugh (1970) ran the cyclic compression tests on Barre granite, Tennessee sandstone and Indiana limestone. Figure 2.12 shows the typical S-N curve for three rock types. It was observed that all three rock types showed a reduction in strength when subjected to cyclic loading. They measured porosity in unreformed specimens and specimens fatigue loaded for 10000 cycles. There were no significant porosity changes for Tennessee sandstone and Indiana limestone; but, Barre granite showed a marked increase in porosity (28.8%) because of fatigue. They found that all rock types exhibited an increase in static strength after cyclic loading for 10000 cycles at sufficiently low values of maximum stress.

Haimson and Kim (1971) performed the cyclic tests on White Tennessee marble to study the mechanical behavior of rock under cyclic fatigue. Figure 2.13 gives the typical S-N curve for White Tennessee marble. They found that there was no apparent difference between the frequencies used as far as specimen fatigue life was concerned. Their results showed that cyclic loading had a definite weakening (fatigue) effect on the rock. As maximum compression stress decreased, the fatigue life of a specimen increased.

Stress-strain curves revealed that there were three stages during cyclic loading: (1) decreasing hysteresis, (2) no hysteresis, and (3) increasing hysteresis. Figure 2.14 shows the typical stress-stain curves for White Tennessee marble. Also failed rock or already weakened rock can sustain a certain amount of fatigue loading depending on the level of applied stresses.

Attewell and Farmer (1973) carried out a number of fatigue tests on dolomite specimens. Specimens of dolomite were subjected to cyclic loading at frequencies of 0.3, 2.5, 10 and 20 Hz. They found that at low frequencies some decreases in fatigue life occurred. These results were not substantiated by the work of Burdine (1963), who found no relationship between fatigue life and frequencies.

They argued that above a stress level at which cracks were initiated, deformation from successive sub-failure load cycles would be cumulative, and failure would occur when the strain energy stored in the specimens exceeds a critical energy level equivalent to failure under non-cyclic loading.

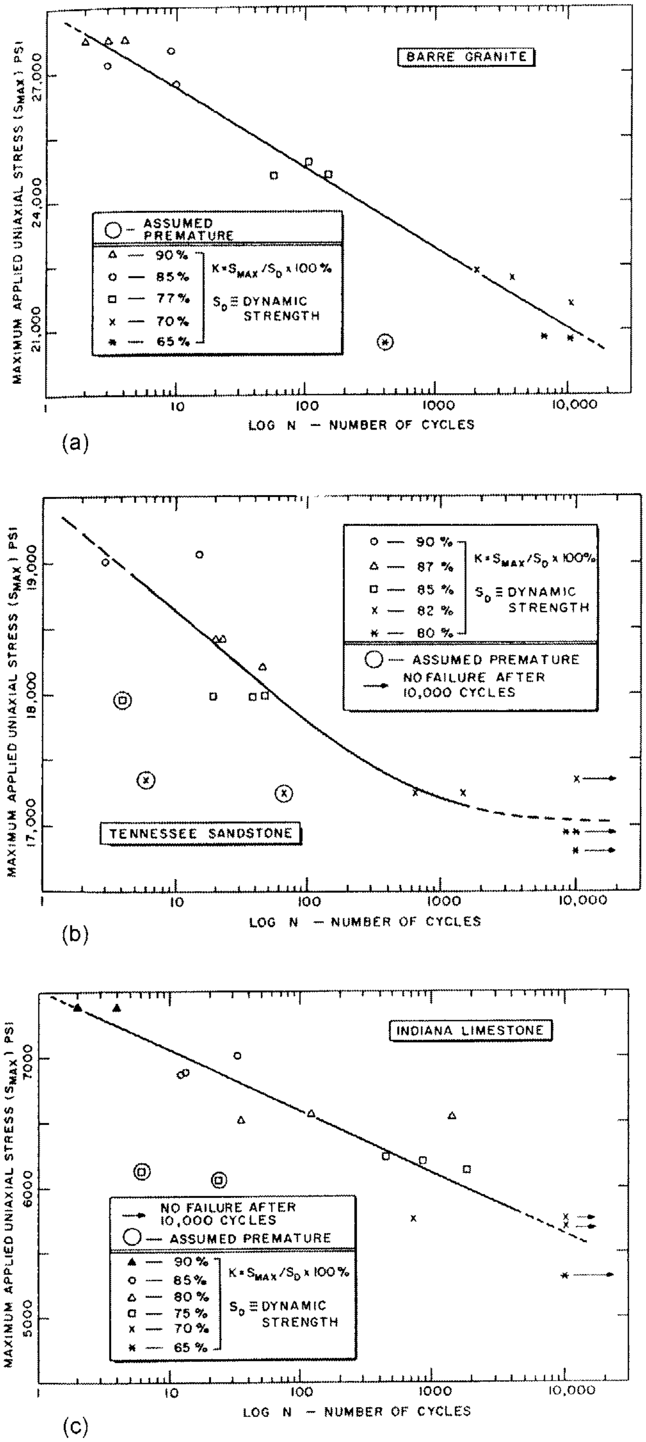

(a)

(b)

(c)

Figure 2.12 S-N curves for cyclic test. (a) Barre granite, (b) Tennessee sandstone and (c) Indiana limestone (Hardy and Chugh, 1970).

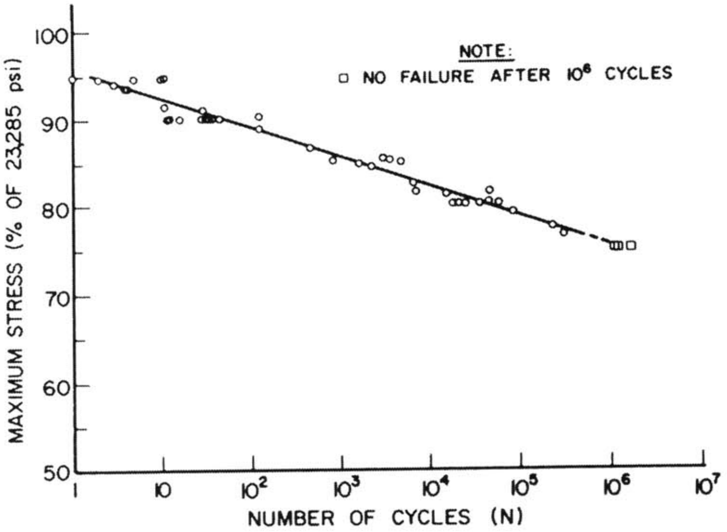

Figure 2.13 S-N curve for White Tennessee marble (Haimson and Kim, 1971).

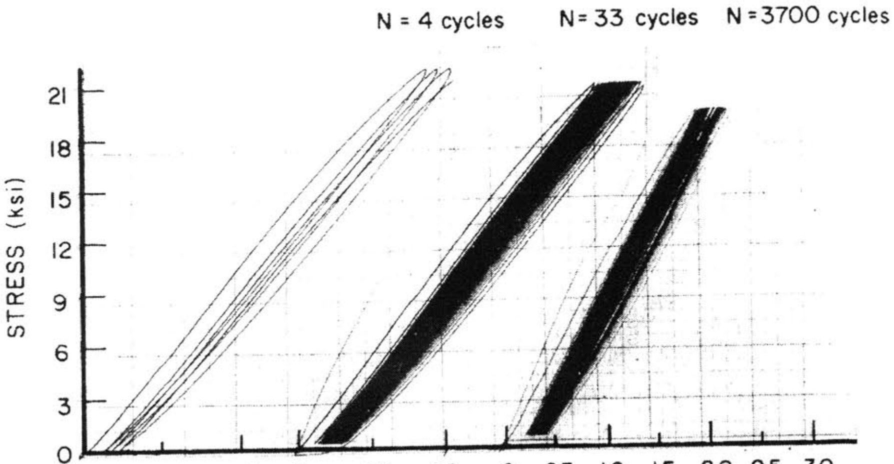

Figure 2.14 Stress-strain curves for White Tennessee marble cyclicly loaded to different maximum stress values (Haimson and Kim, 1971).

Costin and Holcomb (1981) developed a model which described the failure of brittle rock under cyclic loading. They assumed that the damage induced by cyclic loading was primarily in the form of extension of tensile microcracks. These microcracks grew by two principal mechanism, stress corrosion and cyclic fatigue. The prediction of the model was in good agreement with existing experimental data.

Zhenyu and Haihong (1990) studied the behaviour of rocks under cyclic loading. E-Cheng sandstone and Da-Ye marble were subjected to cyclic loading. They drew the following conclusions:

(1) During cycling, the total deformation of the specimen consisted of initial deformation induced by static loading, creep deformation and deformation and damage deformation produced by cycling itself. The damage deformation was the main factor, causing the specimen to fail;

(2) There was a critical strength that was related to amplitude, loading rate, and waveform. This critical strength, named cyclical strength, was lower than the static strength;

(3) The cycle amplitude and the loading waveform had important effects on deformation. In each cycle, the deformation caused by the sine waveform loading was larger than that by the triangle waveform loading. The larger the cycle amplitude, the shorter was the working life;

(4) During cyclic loading, the lateral deformation developed faster than the axial deformation;

(5) Because of the existence of damage deformation, the working life in cyclic loading was less than that in creep;

(6) For cycling in the pre-failure and post-failure regions, the specimen showed different deformation behaviour.

2.4 Flaws induced specimens under cyclic loading

Brown and Hudson (1974) studied the fatigue characteristics of idealized models of jointed rocks under cyclical uniaxial loading. Idealized models of block-jointed rock masses were prepared from a gypsum plaster. These test results showed that the jointed models were more susceptible to fatigue damage than the unjointed specimens.

Prost (1988) investigated the effect of a pre-existing joint on initiation and propagation of cracks across lithologic contacts in cyclic loading. Pikes Peak granite and Dakota sandstone were tested in uniaxial tension and compression, triaxial compression, and triaxial cyclic compression-tension. He reported that the largest axial loads and the largest cycle amplitudes generally caused failure in the least number of cycles in triaxial cyclic compression-tension tests.

Li et al. (2001) conducted tests on gypsum samples with man-made intermittent joints under cyclic loading with frequencies of 0.2, 2, and 21 Hz. The model sample is shown in Figure 2.15. They drew the following conclusions:

(1) The deformation modulus of jointed samples increased with the dynamic loading frequency while the irreversible deformation increased with the loading cycles and decreased with the dynamic loading frequency; the dynamic deformation increased with the joint density and decreased with the joint angle;

(2) The dynamic strength of the jointed samples decreased with the loading cycles and changed with the joint angles;

(3) The dynamic residual strength is not be zero like the static residual strength under the uniaxial loading condition, and

(4) From the energy relation between fracture theory and damage theory, a fracture-damage model for the intermittently jointed medium was proposed.

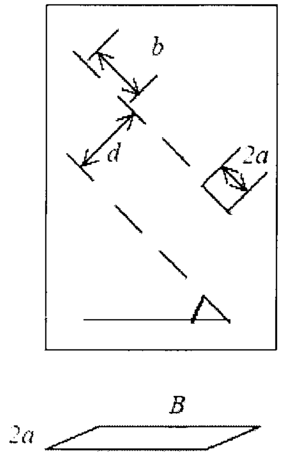

The plane pattern of the joint

Figure 2.15 Model of intermittently jointed rock mass: joint distance d-4.0cm, joint central distance b-2.5cm, joint half length a-0.5cm, joint depth B – 10.0cm (Li et al., 2001).

Jafari et al. (2003) investigated variation of the shear strength of rock joint due to cyclic loading. They prepared identical joint surface with molded mortar and performed shear tests on these specimens under cyclic loading. They found that shear strength of joint was related to rate of displacement, number of loading cycles and stress amplitude.

Li et al. (2003) performed the tests on dry, frozen, and saturated sandstone samples with intermittent cracks subjected to cyclic loading at frequencies of 2 and 20 Hz. They drew the following conclusions:

(1) The dry samples usually had a higher strength than the frozen samples, but the frozen samples usually had a higher strength than the saturated ones;
(2) The cracked samples experienced more obvious fatigue effects than the non-cracked samples under frozen conditions;
(3) Freezing reduced the fatigue effect much more for non-cracked samples than for cracked samples;
(4) Freezing also reduced the loading frequency effect for cracked samples, which meant that the strength increase with loading frequency for saturated samples was more marked than the frozen samples;

2.5 Summary

In this chapter a review of crack initiation and propagation in brittle material under monotonic and cyclic loading was presented. In the case of monotonic tests, wing cracks appear first and propagate parallel to the applied compressive load. Secondary crack appear later and are responsible for the specimen failure as a rule. In multiple flaw system, coalescence occurs through secondary cracks or a combination of wing cracks and secondary cracks.

In the case of cyclic test, most experiments are focused on fatigue properties of intact rock and influence of cyclic frequency and strain rates. Research related to the crack propagation under cyclic loading is very rare.

Chapter 3. Fracture mechanism in compression

3.1 Crack propagation theories

3.1.1 The maximum tangential stress criterion: σ-criterion

Erdogan and Sih (1963) proposed a crack propagation criterion known as the maximum tangential stress criterion or σ-criterion, which states that a crack will propagate radially from the crack tip in the direction of maximum tangential stress. Crack initiation occurs when the maximum tangential stress reaches a critical value. These hypotheses lead to two conditions: (1) the crack propagates in the direction θ_0 which satisfies the following equation,

$$K_I \sin\theta_0 + K_{II}(3\cos\theta_0 - 1) = 0 \tag{3.1}$$

where K_I is mode I stress intensity factor and K_{II} is mode II stress intensity factor.

(2) the condition of crack propagation is given by

$$\cos\frac{\theta_0}{2}(K_I \cos^2\frac{\theta_0}{2} - \frac{3}{2}K_{II}\sin\theta_0) = K_{IC} \tag{3.2}$$

where K_{IC} is the fracture toughness.

Figure 3.1 gives the compressive loading direction and the crack propagation angle θ_0.

3.1.2 The maximum energy release rate criterion: G-criterion

This criterion is based on Griffith failure criterion with modification, considering the angles of crack propagation in tension (Palinaswamy and Knauss, 1972; Hussain et al., 1974). It is based on the following premises:

(1) Crack extension occurs in the direction along which the strain energy release rate is

maximized

(2) Crack initiation occurs when the maximum strain energy release rate in this direction reaches a critical value.

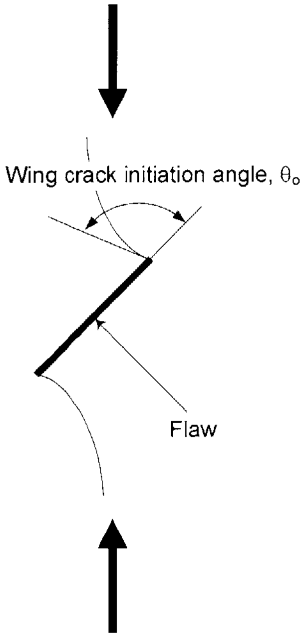

Figure 3.1 Compressive loading direction and the crack propagation angle θ_0

The strain energy release rate, G, can be expressed in terms of K_I and K_{II} as follows:

$$G(\theta)=\frac{1}{E'}\left(\frac{2}{4-\sin^2\theta}\right)^2\left(\frac{1-\theta/\pi}{1+\theta/\pi}\right)^{\theta/\pi} \times\left\{(4-3\sin^2\theta)K_I^2-4\sin 2\theta K_I K_{II}+(4+5\sin^2\theta)K_{II}^2\right\} \tag{3.3}$$

where,

E' = Effective Young's modulus: $E'=E$ for plane stress and $E'=E/(1-\nu^2)$ for plane strain

The crack propagation angle can be determined by $\frac{\partial G}{\partial\theta}=0$ and $\frac{\partial^2 G}{\partial\theta^2}<0$.

3.1.3 The minimum strain energy density criterion: S-criterion

The minimum strain energy density criterion, proposed by Sih (1973), is based on the field strength of the local strain energy density. It assumes that the crack extends in the direction of minimum strain density and crack extension occurs when this minimum strain energy density reaches a critical value. The strain energy density is defined as

$$S = a_{11}K_I^2 + 2a_{12}K_IK_{II} + a_{22}K_{II}^2 \tag{3.4}$$

The coefficients, a_{ij}, are

$$\begin{aligned} a_{11} &= \frac{1}{16\pi G}\{(1+\cos\theta)(\kappa-\cos\theta)\} \\ a_{12} &= \frac{\sin\theta}{16\pi G}\{2\cos\theta-(\kappa-1)\} \\ a_{22} &= \frac{1}{16\pi G}\{(\kappa+1)(1-\cos\theta)+(1+\cos\theta)(3\cos\theta-1)\} \end{aligned} \tag{3.5}$$

where,

G = shear modulus

$\kappa = (3-4\nu)$ in plane strain

$\kappa = (3-\nu)/(1+\nu)$ in plane stress

ν = Poisson's ratio

The crack propagation angle is determined by $\frac{\partial S}{\partial \theta} = 0$ and $\frac{\partial^2 S}{\partial \theta^2} > 0$.

3.2 Brittle fracture model in compression

3.2.1 Griffith's stress model

Griffith (1924) developed a failure criterion based on his theory of crack propagation. The basis of Griffith's stress model is that failure occurs when the most critically oriented crack begins to extend under the applied stress. Crack propagation occurs when the local tensile stress component around the crack reaches the interatomic cohesion of the material. For an elliptical crack subjected to principal stress σ_1 and σ_3 ($\sigma_1 > \sigma_3$), the criterion is

$$\begin{aligned} &(\sigma_1 - \sigma_3)^2 - 8T_0(\sigma_1 + \sigma_3) = 0, \ \text{if } (\sigma_1 + 3\sigma_3) > 0 \\ &\sigma_3 + T_0 = 0, \ \text{if } (\sigma_1 + 3\sigma_3) < 0 \end{aligned} \tag{3.6}$$

where, T_0 is uniaxial tensile strength.

Thus, Griffith's stress model predicts the value of the uniaxial compressive strength to be 8 times the value of the uniaxial tensile strength. This ratio is smaller than the ratio commonly measured for rocks.

3.2.2 Modified Griffith theory

McClintock and Walsh (1962) pointed out that, under compressive stress, crack would be expected to close at some normal stress and thereafter friction between the sliding crack surfaces would exist. They modified Griffith criterion to consider this assumption as follows:

$$\sigma_1 = \sigma_3 \frac{\sqrt{1+\mu^2} + \mu}{\sqrt{1+\mu^2} - \mu} + \sigma_C \tag{3.7}$$

where μ is the coefficient of friction and σ_c is the uniaxial compressive strength.

3.2.3 Sliding crack model

In this model the application of shear and normal stresses derived from the far-field compression causes the sliding of the two crack faces. This sliding produces the growth of tensile "wing cracks" in the direction of the maximum principal stress.

Ashby and Hallam (1986) analyzed mode I crack propagation subject to a compressive stress field and developed a sliding crack model (Figure 3.2). For wing crack initiation, the mode I stress intensity, K_I is given by

$$K_I = -\frac{\sigma_1\sqrt{\pi a}}{\sqrt{3}}\left\{(1-\lambda)\left(1+\mu^2\right)^{1/2}-(1+\lambda)\mu\right\} \tag{3.8}$$

in which μ is the coefficient of friction and λ is the ratio of principal stresses, i.e. σ_3/σ_1. For wing crack growth, the mode I stress intensity, K_I is given by

$$K_I = -\frac{\sigma_1\sqrt{\pi a}}{(1+L)^{3/2}}\left\{1-\lambda-\mu(1+\lambda)-4.3\lambda L\right\}\left\{0.23L+\frac{1}{\sqrt{3}\,(1+L)^{1/2}}\right\} \tag{3.9}$$

where L is the ratio of the wing crack length, l, to one-half the length of the initial crack, a.

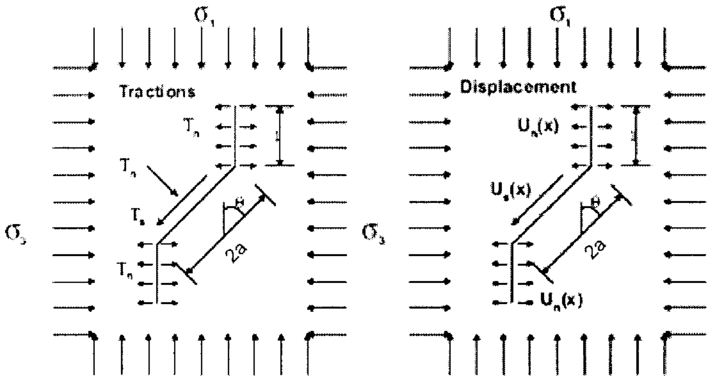

Figure 3.2 Sliding crack model proposed by Ashby and Hallam (1986).

Kemeny and Cook (1987) developed the sliding crack model to analyze the post failure behavior of rocks under triaxial compression (Figure 3.3). This model modified the Nemat-Nasser's model to allow for confinement as follow:

$$K_I = \frac{2a\tau^{*}\cos\theta}{\sqrt{\pi l}} - \sigma_3\sqrt{\pi l} \tag{3.10}$$

where $\tau^{*} = \tau_n - \mu\sigma_n$ and l is the wing crack length.

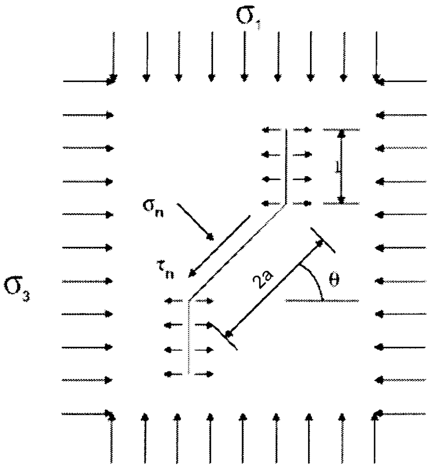

Figure 3.3 Sliding crack model proposed by Kemeny and Cook (1987).

Chapter 4. Experimental procedure

4.1 Specimen geometry and preparation

The material used for this study is gypsum, which is identical to the one used by Nelson (1968), Reyes (1991), Takeuchi (1991), Shen et al. (1995), and Bobet (1997). The reasons why we choose gypsum are:

(1) to generate specimens and flaws with ease;

(2) to reach their full strength so rapidly that a large number of specimens can be made in a reasonable period of time;

(3) to facilitate the comparison with the previous experience and results; and

(4) to have a stress-strain relationship similar to that of rock.

The material is a mixture of Hydrocal B-11 (a gypsum manufactured by U.S. Gypsum Company), Dicalite (diatomaceous earth manufactured by Grefco Inc.) and water. The same proportions of water, diatomaceous earth, and gypsum as in previous work are used. The proportions used are:

Water / gypsum = 0.4
Water / diatomaceous earth = 35.0
Gypsum : 560 g
Water : 224 cc
Diatomaceous earth : 6.4 g

Diatomaceous earth is used to make a mixture more viscous and prevent excessive ooze of the water to the top of the gypsum mixture during fabrication.

The specimens have the same geometry as in the previous experiments, which is 152.4mm(6 inches) high, 76.2mm (3 inches) wide , and around 30mm thick. Two pre-existing flaws of length 2a = 12.7mm are arranged in the center of specimen. 0.1mm steel shims are arranged in the mold to produce the desired flaw thickness 0.1mm (See Figure 4.1). In this study open flaws are used. Open flaws remain open during a compression test, so no stresses are transmitted across the open flaws.

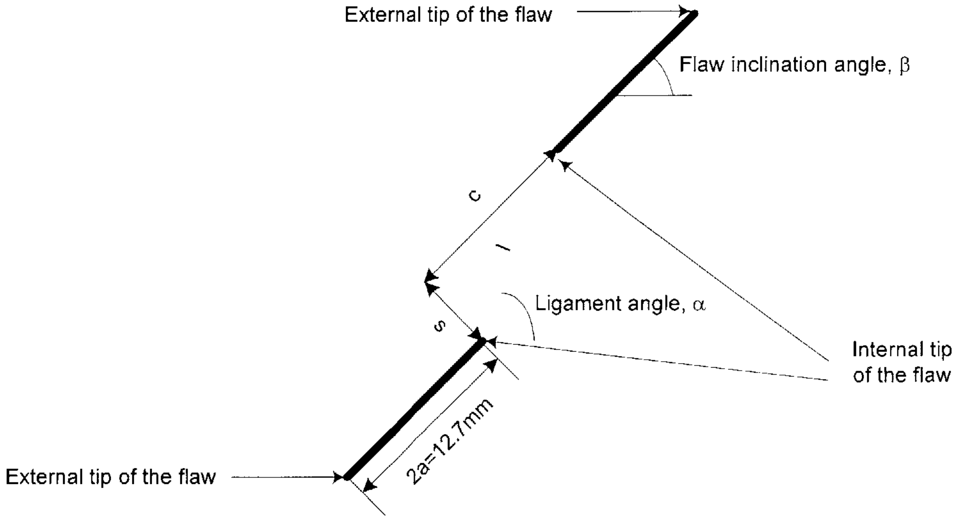

Figure 4.1 Specimen geometry.

Flaw inclination angle, β, is the angle of the flaw with the horizontal direction. Continuity, c, is the distance between flaws measured along the plane of the flaws. Spacing, s, is the distance between two flaws measured along a direction perpendicular to the plane of the flaws. The ligament length, *l*, is the shortest distance between the inner tips and the ligament angle, α, is the angle of the ligament with the horizontal direction. When the ligament angle is less than or equal to 90°, the flaws are non-overlapped. When α is greater than 90°, the flaws are overlapped (See Figure 4.2).

In order to express the degree of overlapping of two flaws the overlapping ratio is used. Overlapping ratio is defined as (Sagong, 2001) :

$$\text{Overlapping ratio(\%)}=\frac{\text{Horizontal projection of the overlapped zone}}{\text{Horizontal projection of the single flaw}}\times 100$$

For non-overlapping flaws,

$$\text{Overlapping ratio(\%)}=\frac{\text{Horizontal projection of the non-overlapped zone}}{\text{Horizontal projection of the single flaw}}\times 100$$

In this case, the ratio is represented as negative.

The flaw geometry is defined in the form of "flaw inclination angle (β)-spacing (s)-continuity (c)". Spacing and continuity are represented by multiples of 'a' (a= half flaw length) (Figure 4.1).

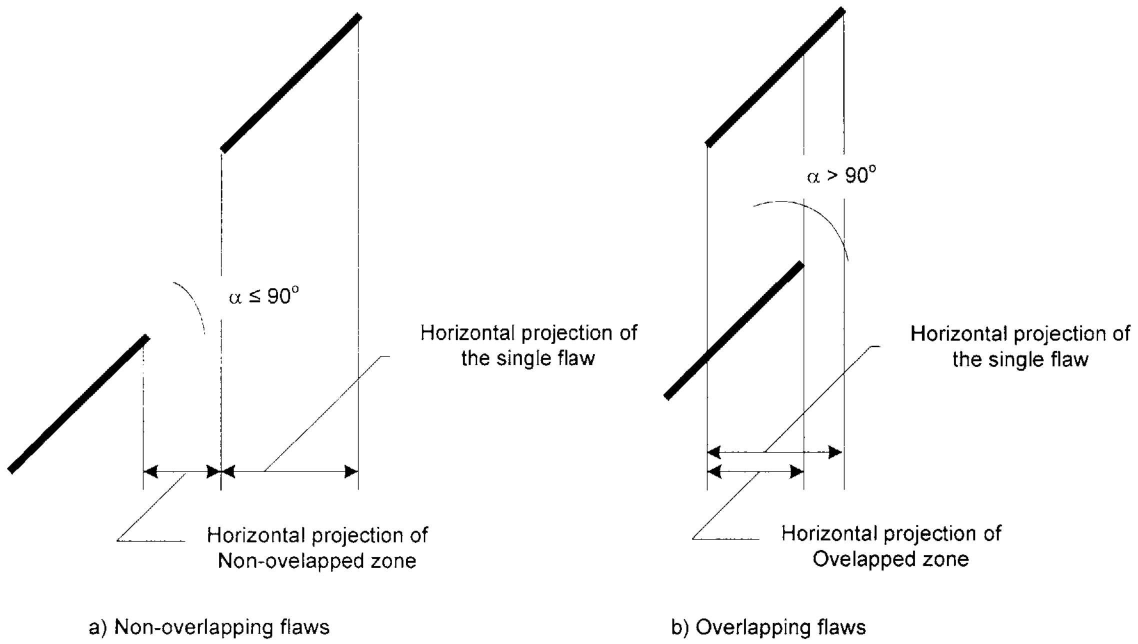

a) Non-overlapping flaws

b) Overlapping flaws

Figure 4.2 Non-overlapping and overlapping flaws.

Table 4.1 shows the geometries used in this study with corresponding ligament length, ligament angle and overlapping ratio.

The procedure for the preparation of specimen follows that of Bobet (1997) and Martinez (1999). This procedure is followed strictly to obtain uniform and homogeneous specimens.

(1) Assemble the two PMMA plates and the four metallic plates.
(2) Insert steel shims for open cracks.
(3) The water and diatomaceous earth are poured into a blender and mixed for 20 seconds.
(4) Add the gypsum to the water- diatomaceous earth mixture and mixed for 4 minutes.
(5) Pour mixture into mold. Then vibrate the mold for 2 minutes to remove entrapped air in the mixture.

(6) An hour after vibration, the steel shims are pulled out.

(7) Gypsum specimens solidify within an hour. Thus, after this time, unmold specimens.

(8) Dry for 24 hours at room temperature.

(9) Top and bottom faces of specimens are polished in a rotary grinding machine to obtain a smooth surface and a uniform thickness.

(10) The specimens are cured in an oven at 40□ for 4 days. After that, the specimens are taken from the oven and tested.

Geometry		Ligament length	Ligament angle	Overlapping ratio (%)
Coplanar	30-0-a	a	30°	-100
	45-0-a	a	45°	-100
	60-0-a	a	60°	-100
	30-0-2a	2a	30°	-200
	45-0-2a	2a	45°	-200
	60-0-2a	2a	60°	-200
	30-0-3a	3a	30°	-300
	45-0-3a	3a	45°	-300
	60-0-3a	3a	60°	-300
	30-0-4a	4a	30°	-400
	45-0-4a	4a	45°	-400
	60-0-4a	4a	60°	-400
Non Coplanar	30-a-0	a	120°	28.87
	45-a-0	a	135°	50
	60-a-0	a	150°	86.60
	30-a-a	1.41a	75°	-21.13
	45-a-a	1.41a	90°	0
	60-a-a	1.41a	105°	30.60
	30-a-2a	2.24a	56.57°	-71.13
	45-a-2a	2.24a	71.57°	-50
	60-a-2a	2.24a	86.57°	-13.40
	60-a-3a	3.16a	78.44°	-63.40
	30-2a-0	2a	120°	57.74
	45-2a-0	2a	135°	100

Table 4.1 Geometries tested in this study.

Geometry		Ligament length	Ligament angle	Overlapping ratio (%)
Non Coplanar	60-2a-0	2a	150°	29.74
	30-2a-a	2.24a	93.44°	7.73
	45-2a-a	2.24a	108.44°	50
	60-2a-a	2.24a	123.44°	88.20
	30-2a-2a	2.83a	75°	-42.27
	45-2a-2a	2.83a	90°	0
	60-2a-2a	2.83a	105°	73.21
	30-2a-3a	3.61a	63.69	-92.27
	45-2a-3a	3.61a	78.69°	-50
	60-2a-3a	3.61a	93.69°	23.21

Table 4.1 (continued)

4.2 Material properties

The average uniaxial compressive strength of intact specimen is 34.82 MPa and the average Young's modulus is 3355 MPa. Other properties, such as tensile strength, Poisson's ratio, mode I and II fracture toughness are obtained from the reference and summarized in Table 4.2.

W/G	W/D	σ_c	σ_t	ν	K_{IC}	K_{IIC}	E	Reference
0.40	∞	33.03	3.28	-	-	-	-	Nelson (1968)
0.45	32	22.96	2.30	-	-	-	-	Nelson (1968)
0.8	∞	8.72	1.54	-	-	-	-	Nelson (1968)
1.20	6	5.86	1.13	-	-	-	-	Nelson (1968)
0.45	32	24.61	2.74	0.24	-	-	-	Einstein and Hirschfeld (1973)
0.4	35	36.18	1.908	-	0.223	0.338	-	Takeuchi (1991)
0.4	35	34.5	3.2	0.15	-	-	5.96	Bobet (1997)

Table 4.2 Material properties of gypsum mixture (W/G = water/gypsum, W/D = water/ diatomaceous earth, σ_c = compressive strength [MPa], σ_t = tensile strength [MPa], ν = Poisson's ratio, K_{IC} = mode I fracture toughness, K_{IIC} = mode II fracture toughness, E = Young's modulus [GPa]).

4.3 Testing procedure

4.3.1 Monotonic compression

The specimens are loaded in the Baldwin 200Kip loading machine, until failure occurrs. Brush platens are used to reduce friction and shear stresses between specimen and loading platens. Loading is carried out using displacement control. Three steps of displacement rate are used. In the first step, until loading reaches 5MPa, a rate of 0.3mm/min is used. In the second step, the rate of 0.15mm/min is used until loading reaches 7.5MPa. In the third step, the displacement rate is 0.03mm/min. A rate of 0.03mm/min is low enough to observe crack initiation and coalescence.

Two kinds of scanning methods are possible. First, as the cracking process is usually very fast, the entire process of crack initiation and propagation is recorded by a digital camcorder. This method is suitable for the overall crack pattern study. Second, as the hairline microcracks can not be seen by eye, a low power microscope is used to scan the specimen surface. A camera or a digital camcorder is attached to the microscope and records the crack coalescence process. Since only a small area of the specimen can be seen through the microscope, loading has to pause until the entire surface is scanned for new cracks. Thus a stepwise testing process is necessary to accommodate scanning. The loading is first increased to a certain value, for example 15kN. At this point, the load is stopped, and, without unloading, the surface of the specimen is scanned. Afterward, the loading is resumed and increased by a step value, for example 5kN. After each step, the loading is stopped and the surface of the specimen is inspected for possible crack initiations. The loading is resumed again and increased stepwise until coalescence or failure occurs. Since there is no scanning of the specimen during loading, the interval between loadings can be considered as the observation error. In this study, the first method is used. The digital camcorder has a 10 x optical zoom lens, 720 x 480 resolutions and records the rate of 30 frames per second. Using FireWire interface (IEEE 1394 Interface) in the digital camcorder and Microsoft Movie Maker, videos are easily captured as AVI-files. These AVI-files are used to study the cracking process.

4.3.2 Cyclic compression

The cyclic loading used is termed ‘compression-compression’ since the applied stresses remain compressive during the complete loading-unloading cycle. It is necessary to maintain compressive loading to prevent loss of contact between the test specimen and platens during the unloading phase of the cycle, and to eliminate possible impact effects on the specimen during the subsequent phase. The cyclic rate is intended to simulate the frequencies of the major pulses in earthquakes (1-2Hz) and blasting (10Hz) (Haimson and Kim, 1971). However, 0.5 Hz loading frequency is used for the experiment. Higher frequencies are not used because of limitations in the compression machine. Several initial tests show that equivalent displacement rate for 0.5Hz loading frequency is 83.82 mm/min. This displacement rate is much higher than that of monotonic tests. In this study σ_{min} is held constant at 0.18 MPa,(Figure 4.3) for all tests and only the effect of different σ_{max} values is investigated. 90%, 85% and 80% of the dynamic compressive strength is used for σ_{max}.

The dynamic compressive strength is defined as the failure strength at the displacement rate of 83.82 mm/min. Table 4.3 shows the dynamic compressive strength with respect to different flaw geometries.

Similar to the monotonic compression test, two kinds of scanning methods are possible. First, the entire process of crack initiation and propagation is recorded by a digital camcorder. The cyclic loading continues until failure occurs or the number of cycles reaches 4,000 cycles. This method is also used for this study. Second, the specimen is scanned with a low power microscope. Every certain number of cycles, for example 100 cycles, the loading is stopped and unloading takes place. Then the surface of the specimen is scanned. The loading is resumed again and this process continues until failure occurs or the number of cycles reaches 4,000 cycles.

Geometry	Dynamic compressive strength (Unit : MPa)			
	1st test	2nd test	3rd test	**Average**
30-0-a	26.19	26.74	27.84	**26.92**
45-0-a	25.75	26.79	26.16	**26.23**
60-0-a	26.66	27.54	28.29	**27.50**
30-0-2a	27.51	25.44	26.78	**26.58**
45-0-2a	29.64	27.52	28.78	**28.65**
60-0-2a	31.07	31.56	33.26	**31.96**
30-0-3a	29.31	30.71	29.42	**29.81**
45-0-3a	27.52	27.93	28.43	**27.96**
60-0-3a	31.91	31.20	30.75	**31.29**
30-0-4a	31.22	31.75	31.24	**31.40**
45-0-4a	34.61	33.39	34.30	**34.10**
60-0-4a	35.83	35.76	36.12	**35.90**
30-a-0	25.45	23.88	24.08	**24.47**
45-a-0	30.08	29.94	28.09	**29.37**
60-a-0	32.23	32.56	32.41	**32.40**
30-a-a	25.16	24.20	23.09	**24.15**
45-a-a	28.91	29.13	29.71	**29.25**
60-a-a	35.06	34.77	34.36	**34.73**
30-a-2a	24.24	25.16	24.48	**24.63**
45-a-2a	26.68	27.36	28.33	**27.46**
60-a-2a	33.27	36.41	34.29	**34.66**
60-a-3a	33.28	35.75	32.18	**33.74**
30-2a-0	31.47	30.12	32.27	**31.29**
45-2a-0	36.18	38.66	37.37	**37.40**
60-2a-0	41.60	41.21	36.63	**39.81**
30-2a-a	34.52	35.83	36.39	**35.58**
45-2a-a	40.09	37.5	39.27	**38.95**
60-2a-a	40.85	41.14	44.24	**42.08**

Table 4.3 The dynamic compressive strength in this test.

Geometry	Dynamic compressive strength (Unit : MPa)			
	1st test	2nd test	3rd test	**Average**
30-2a-2a	25.18	24.38	25.47	**25.47**
45-2a-2a	29.47	28.89	29.68	**29.35**
60-2a-2a	30.47	32.33	33.09	**31.96**
30-2a-3a	28.66	28.78	28.30	**28.58**
45-2a-3a	31.53	32.70	32.30	**32.18**
60-2a-3a	41.81	42.27	36.30	**40.13**

Table 4.3 (continued)

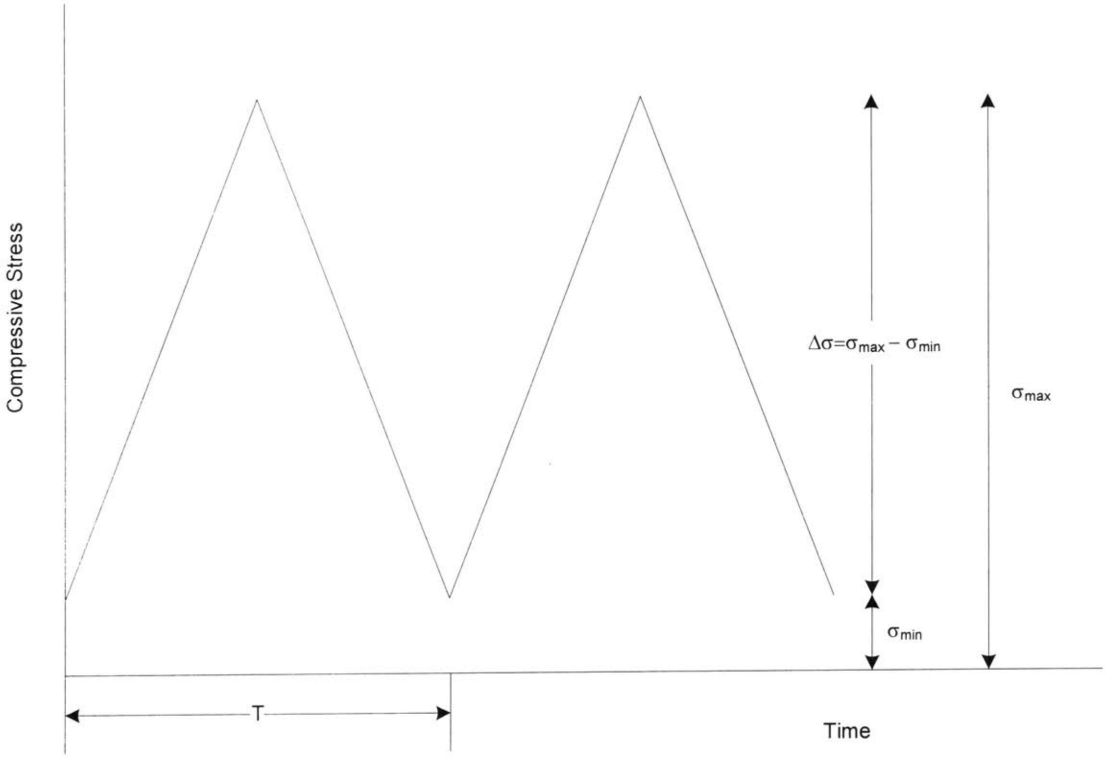

Figure 4.3. Fatigue loading.

Chapter 5. Experimental results

5.1 Wing cracks

As other researchers (Reyes, 1991; Shen et al., 1995; Bobet, 1997; Sagong, 2001) observed, wing cracks, which are tension cracks, initiate at (or near) the tips of the flaws and propagate parallel to the compressive loading axis both monotonic and cyclic tests. Even though wing cracks propagate to the top and bottom edges of the specimen, the specimen can sustain in some additional loads until final failure occurs.

According to the wing crack initiation position, wing cracks can be classified as upper external wing crack, lower external wing crack, upper internal wing crack, and lower internal wing crack (See Figure 5.1). External wing cracks are always observed for all the specimens and most of them propagate to the top and bottom edges of the specimens, while internal wing cracks are not observed for all the specimens and usually arrest and do not propagate further.

The wing crack initiation position differs for the different flaw inclination angles. Three different wing crack initiation positions are observed. Figure 5.2 shows these positions – at the tip, near the tip, and in the middle of the flaw. In table 5.1, the frequencies of wing crack initiation position for all the geometry in both monotonic and cyclic tests are presented. More than half of 30° flaw inclination specimens show that the wing crack initiation position is near the tip of the flaw. As the flaw inclination angle increases, a higher percentage of wing crack initiations occur at the tip. This has been observed in previous research (Barquins and Petit, 1992; Reyes and Einstein, 1991; Bobet, 1997; Sagong, 2001).

The frequencies of wing crack initiation position with respect to overlapping ratio and ligament length are presented in tables 5.2 and 5.3. The wing crack initiation position does not change much with increasing overlapping ratio. However, as the ligament length increases, wing cracks tend to initiate at the tips of the flaw. It seems that overlapping ratio has a less influence on the wing crack initiation position than flaw inclination angle and ligament length. Also loading types (monotonic and cyclic) do not affect the wing crack initiation position.

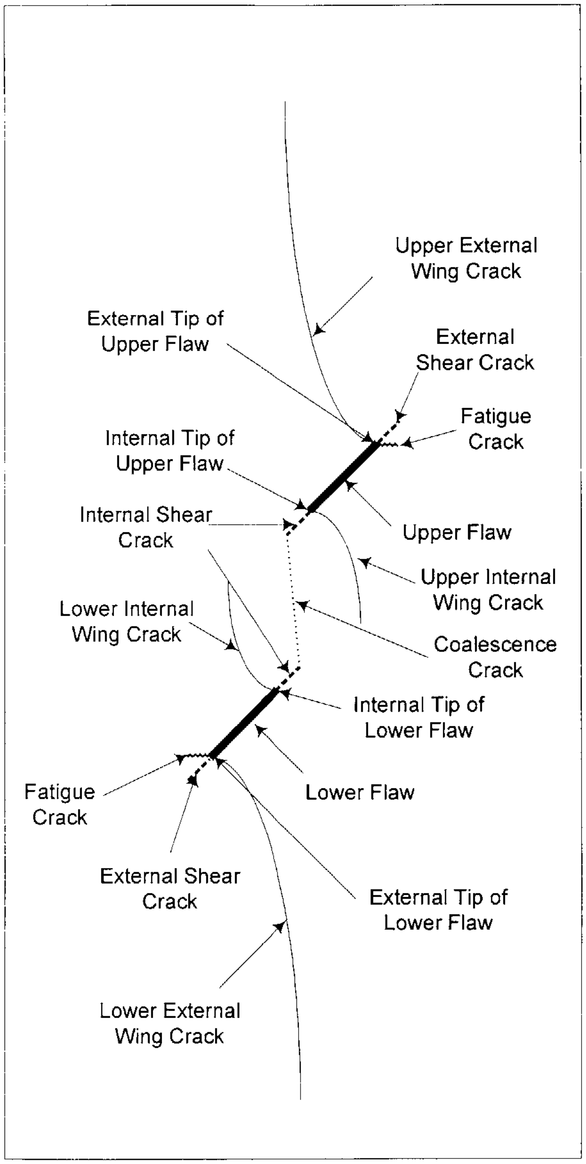

Figure 5.1 General crack patterns observed in this test.

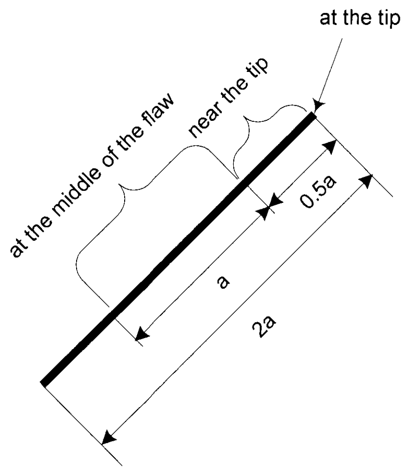

Figure 5.2 Wing crack initiation position.

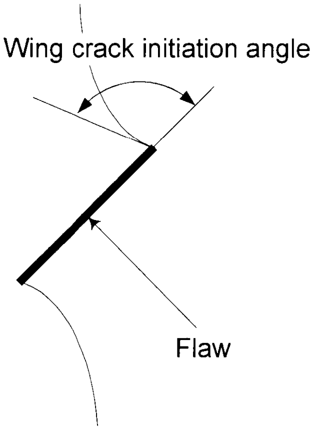

Figure 5.3 Wing crack initiation angle.

Geometry	Monotonic test			Cyclic test		
	At the tip	Near the tip	Middle of the flaw	At the tip	Near the tip	Middle of the flaw
30-0-a	1	3	0	3	3	0
30-0-2a	0	7	0	6	5	0
30-0-3a	3	5	0	7	5	0
30-0-4a	5	3	0	6	6	0
30-a-0	3	5	0	3	9	0
30-a-a	1	3	0	1	5	0
30-a-2a	2	2	0	6	4	0
30-2a-0	2	6	0	3	8	1
30-2a-a	6	2	0	6	5	1
30-2a-2a	4	4	0	8	2	0
30-2a-3a	4	3	0	6	4	0
30° Total	**31 (41.89%)**	**43 (58.11%)**	**0 (0%)**	**55 (48.67%)**	**56 (49.56%)**	**2 (1.77%)**
45-0-a	4	0	0	6	0	0
45-0-2a	3	1	0	6	0	0
45-0-3a	6	2	0	8	0	0
45-0-4a	6	2	0	12	0	0
45-a-0	3	5	0	7	5	0
45-a-a	6	2	0	9	3	0
45-a-2a	6	0	0	8	0	0
45-2a-0	6	1	0	2	10	0
45-2a-a	6	2	0	9	3	0
45-2a-2a	6	1	0	11	1	0
45-2a-3a	7	1	0	11	1	0
45° Total	**59 (77.63%)**	**17 (22.37%)**	**0 (0%)**	**89 (79.46%)**	**23 (20.54%)**	**0 (0%)**
60-0-a	4	0	0	6	0	0
60-0-2a	4	0	0	6	0	0
60-0-3a	4	0	0	6	0	0
60-0-4a	6	0	0	10	0	0
60-a-0	6	2	0	8	2	1
60-a-a	7	1	0	12	0	0
60-a-2a	5	3	0	9	3	0
60-a-3a	4	0	0	8	2	0
60-2a-0	5	1	0	12	0	0
60-2a-a	8	0	0	7	1	0
60-2a-2a	6	0	0	9	1	0
60-2a-3a	8	0	0	12	0	0
60° Total	**67 (90.54%)**	**7 (9.46%)**	**0 (0%)**	**105 (91.30%)**	**9 (7.83%)**	**1 (0.87%)**

Table 5.1 Frequency of wing crack initiation position for different flaw angles.

Geometry	Overlapping Ratio (%)	Monotonic test			Cyclic test		
		At the tip	Near the tip	Middle of the flaw	At the tip	Near the tip	Middle of the flaw
30-0-4a	-400	5	3	0	6	6	0
45-0-4a	-400	6	2	0	12	0	0
60-0-4a	-400	6	0	0	10	0	0
30-0-3a	-300	3	5	0	7	5	0
45-0-3a	-300	6	2	0	8	0	0
60-0-3a	-300	4	0	0	6	0	0
30-0-2a	-200	0	7	0	6	5	0
45-0-2a	-200	3	1	0	6	0	0
60-0-2a	-200	4	0	0	6	0	0
30-0-a	-100	1	3	0	3	3	0
45-0-a	-100	4	0	0	6	0	0
60-0-a	-100	4	0	0	6	0	0
30-2a-3a	-92.27	4	3	0	6	4	0
30-a-2a	-71.13	2	2	0	6	4	0
60-a-3a	-63.4	4	0	0	8	2	0
45-a-2a	-50	6	0	0	8	0	0
45-2a-3a	-50	7	1	0	11	1	0
30-2a-2a	-42.27	4	4	0	8	2	0
30-a-a	-21.13	1	3	0	1	5	0
60-a-2a	-13.4	5	3	0	9	3	0
Non-overlapping		**79 (66.95%)**	**39 (33.05%)**	**0 (0%)**	**139 (77.65%)**	**40 (22.35%)**	**0 (0%)**
45-a-a	0	6	2	0	9	3	0
45-2a-2a	0	6	1	0	11	1	0
30-2a-a	7.73	6	2	0	6	5	1
60-2a-3a	23.21	8	0	0	12	0	0
30-a-0	28.87	3	5	0	3	9	0
60-2a-0	29.74	5	1	0	12	0	0
60-a-a	30.6	7	1	0	12	0	0
45-a-0	50	3	5	0	7	5	0
45-2a-a	50	6	2	0	9	3	0
30-2a-0	57.75	2	6	0	3	8	1
60-2a-2a	73.21	6	0	0	9	1	0
60-a-0	86.6	6	2	0	8	2	1
60-2a-a	88.2	8	0	0	7	1	0
45-2a-0	100	6	1	0	2	10	0
Overlapping		**78 (73.58%)**	**28 (26.42%)**	**0 (0%)**	**110 (68.32%)**	**48 (29.81%)**	**3 (1.86%)**

Table 5.2 Frequency of wing crack initiation position with respect to overlapping ratio for different flaw angles.

Ligament Length	Monotonic			Cyclic		
	At the tip	Near the tip	Middle of the tip	At the tip	Near the tip	Middle of the tip
1a	21 (58.33%)	15 (41.67%)	0 (0%)	33 (62.26%)	19 (35.85%)	1 (1.89%)
1.41a	14 (70%)	6 (30%)	0 (0%)	22 (73.33%)	8 (26.67%)	0 (0%)
2a	20 (55.56%)	16 (44.44%)	0 (0%)	35 (59.32%)	23 (38.98%)	1 (1.7%)
2.24a	33 (78.57%)	9 (21.43%)	0 (0%)	45 (72.58%)	16 (25.81%)	1 (1.61%)
2.83a	16 (76.19%)	5 (23.81%)	0 (0%)	28 (87.5%)	4 (12.5%)	0 (0%)
3a	13 (65%)	7 (35%)	0 (0%)	21 (80.77%)	5 (19.23%)	0 (0%)
3.61a	23 (85.19%)	4 (14.81%)	0 (0%)	28 (80%)	7 (20%)	0 (0%)
4a	17 (77.27%)	5 (22.73%)	0 (0%)	28 (82.35%)	6 (17.65%)	0 (0%)

Table 5.3 Frequency of wing crack initiation position with respect to ligament length.

Wing crack initiation angles (Figure 5.3) are measured at each wing crack initiation position. Figures 5.4 to 5.7 are plots of the upper and lower external wing crack initiation angles, the upper and lower internal wing crack initiation angles, the upper external and internal wing crack initiation angles, and the lower external and internal wing crack initiation angles for all geometries and loading types. These indicate, roughly, that the upper and lower external wing crack initiation angle, the upper and lower internal wing crack initiation angles, external and internal wing crack initiation angle have a linear relation regardless of geometry and loading type. It is also observed that the wing crack initiation angles decrease as the flaw inclination angles increase. However, these plots show large scatter, more detailed observations are required. In Figures 5.8 and 5.9, the difference between the upper and lower external wing crack initiation angles, the upper and lower internal wing crack initiation angles, the upper external and internal wing crack initiation angles, and the lower external and internal wing crack initiation angles are plotted with respect to the ligament length. In these Figures, it is observed that differences between wing crack initiation angles are evenly distributed regardless of the ligament length. Thus wing crack initiation angles are probably not influenced by the ligament length.

In Figures 5.10 and 5.11, the differences between the upper and lower external wing crack initiation angles, the upper and lower internal wing crack initiation angles, the upper external and upper internal wing crack initiation angles, and the lower external and lower internal wing crack initiation angles are plotted with respect to the overlapping ratio.

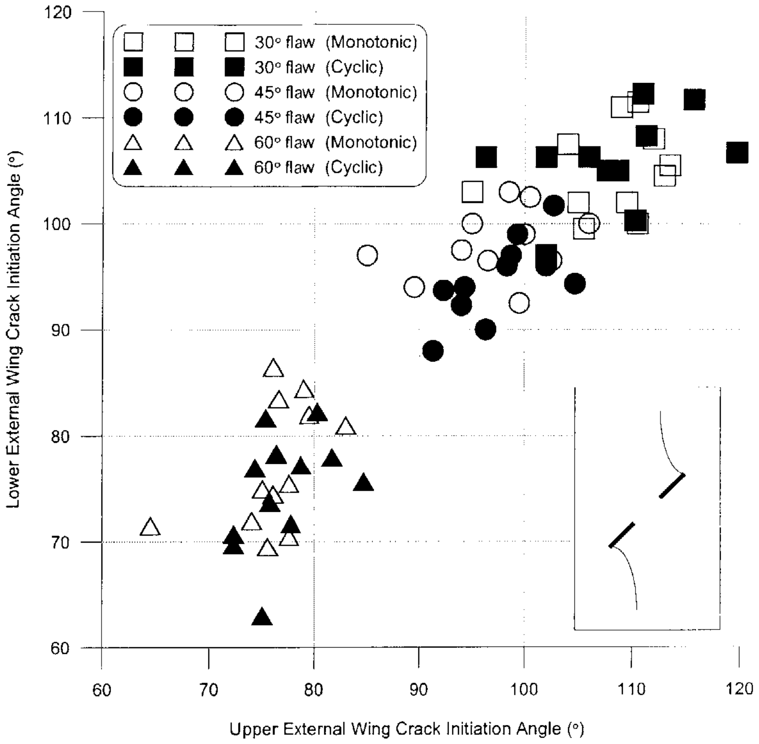

Figure 5.4 Upper and lower external wing crack initiation angle.

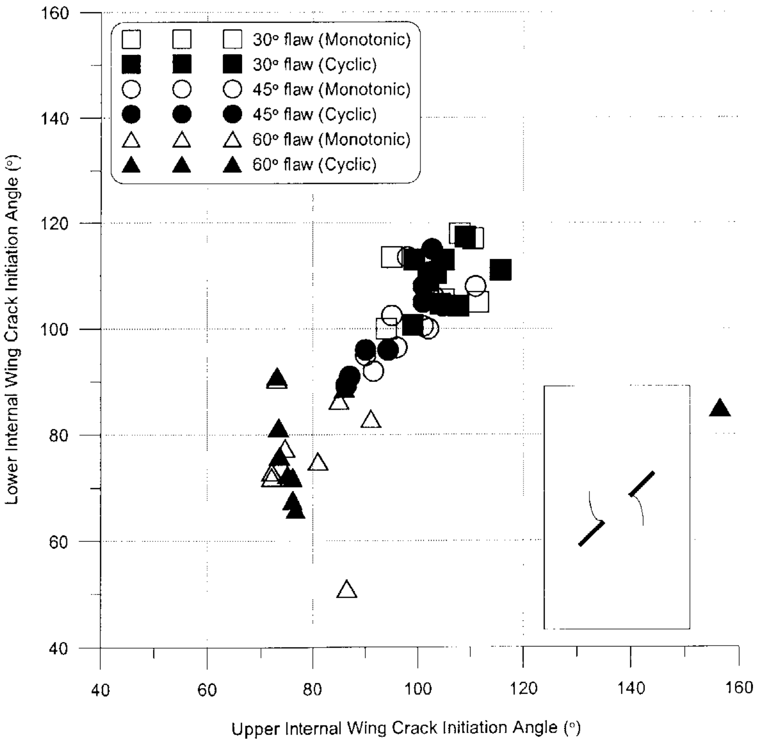

Figure 5.5 Upper and lower internal wing crack initiation angle.

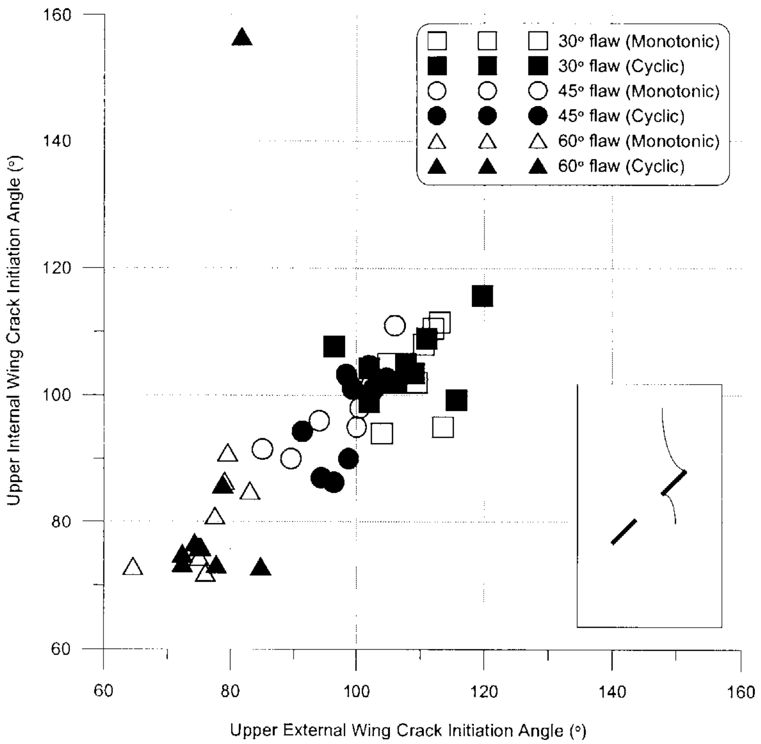

Figure 5.6 Upper external and internal wing crack initiation angle.

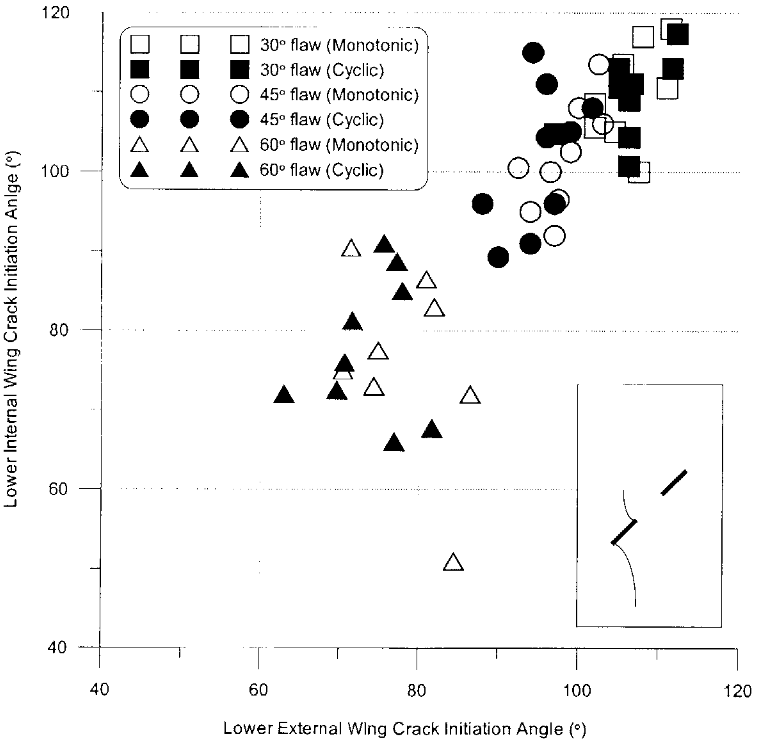

Figure 5.7 Lower external and internal wing crack initiation angle.

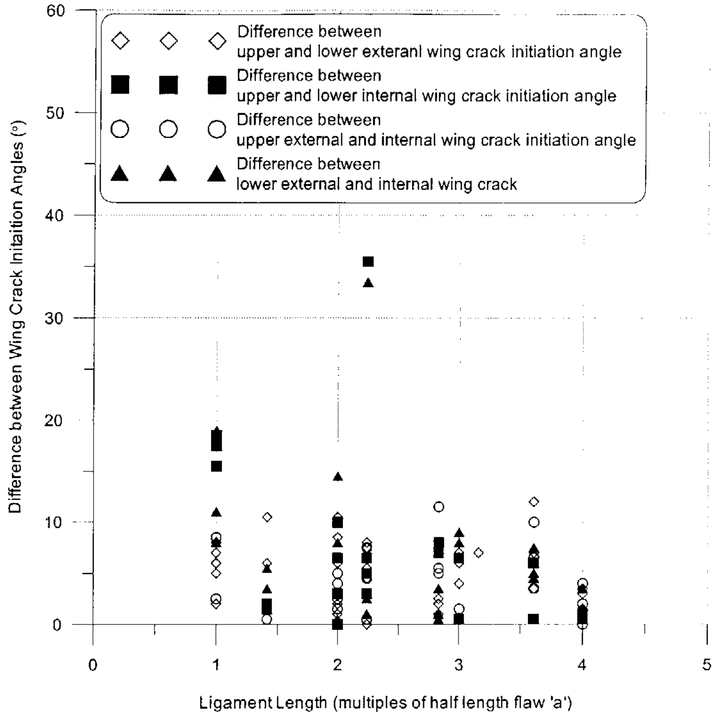

Figure 5.8 Differences between wing crack initiation angles with respect to the ligament length in monotonic tests.

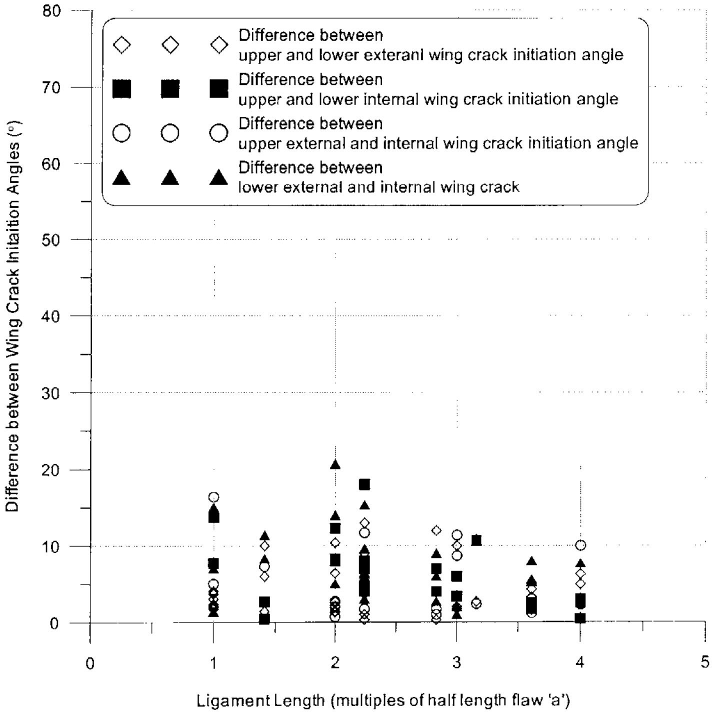

Figure 5.9 Differences between wing crack initiation angles with respect to the ligament length in cyclic tests.

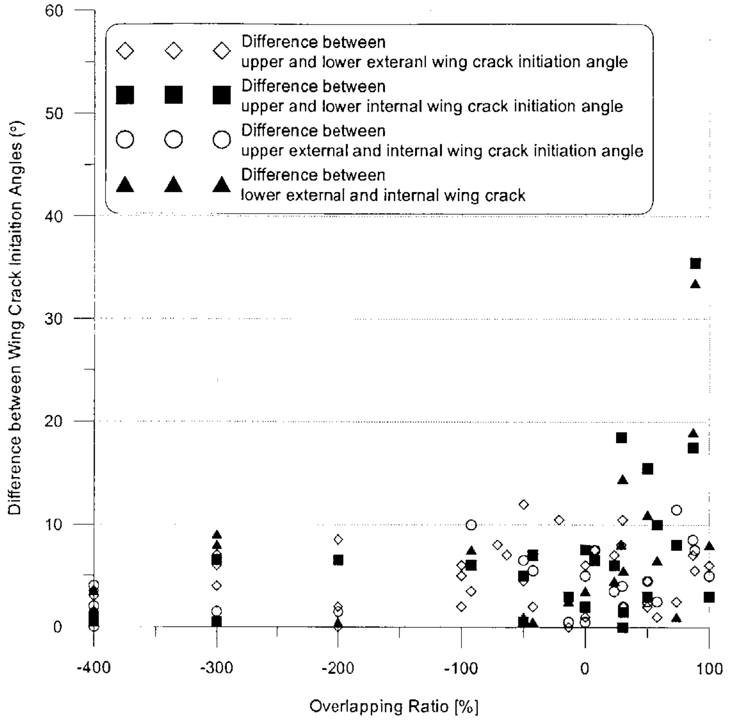

Figure 5.10 Differences between wing crack initiation angles with respect to the overlapping ratio in monotonic tests.

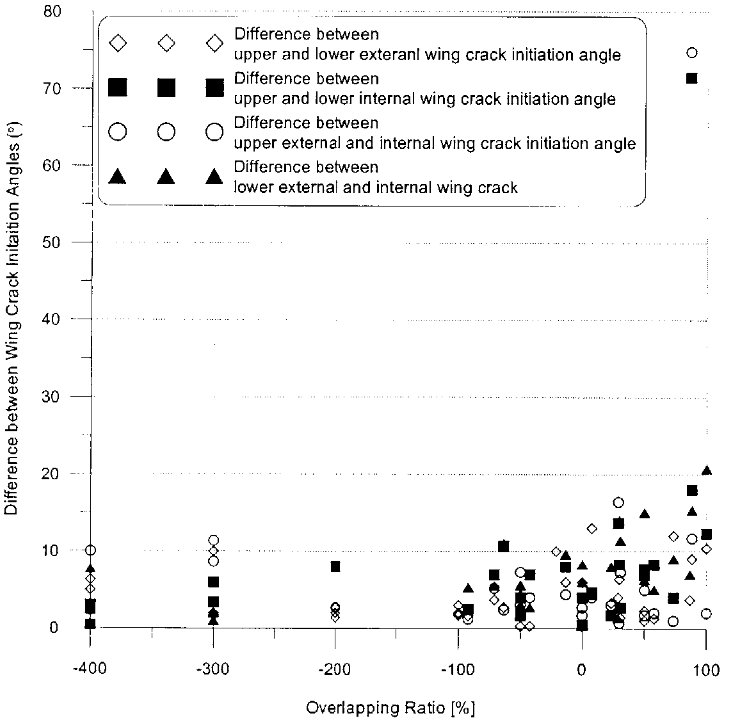

Figure 5.11 Differences between wing crack initiation angles with respect to the overlapping ratio in cyclic tests.

These Figure show that for the overlapping geometries, differences between wing crack initiation angles increase somewhat as the overlapping ratio increases. For the non-overlapping geometries, differences between wing crack initiation angles are relatively constant with the overlapping ratio.

Crack propagation directions from crack propagation theories such as the σ-criterion (Erdogan and Sih,1963), the G-criterion (Palinaswamy and Knauss, 1972; Hussain et al., 1974) and the S-criterion (Sih,1973) and external and internal wing crack initiation angles from monotonic and cyclic tests are presented in Figures 5.12 and 5.13. Wing crack initiation angles in monotonic tests are similar to those in cyclic tests. For the 30° and 45° flaw inclination specimens, both external and internal wing crack initiation angles occur between the S-criterion and G-criterion. For the 60° flaw inclination specimens, wing crack initiation angles are lower than the theoretical values.

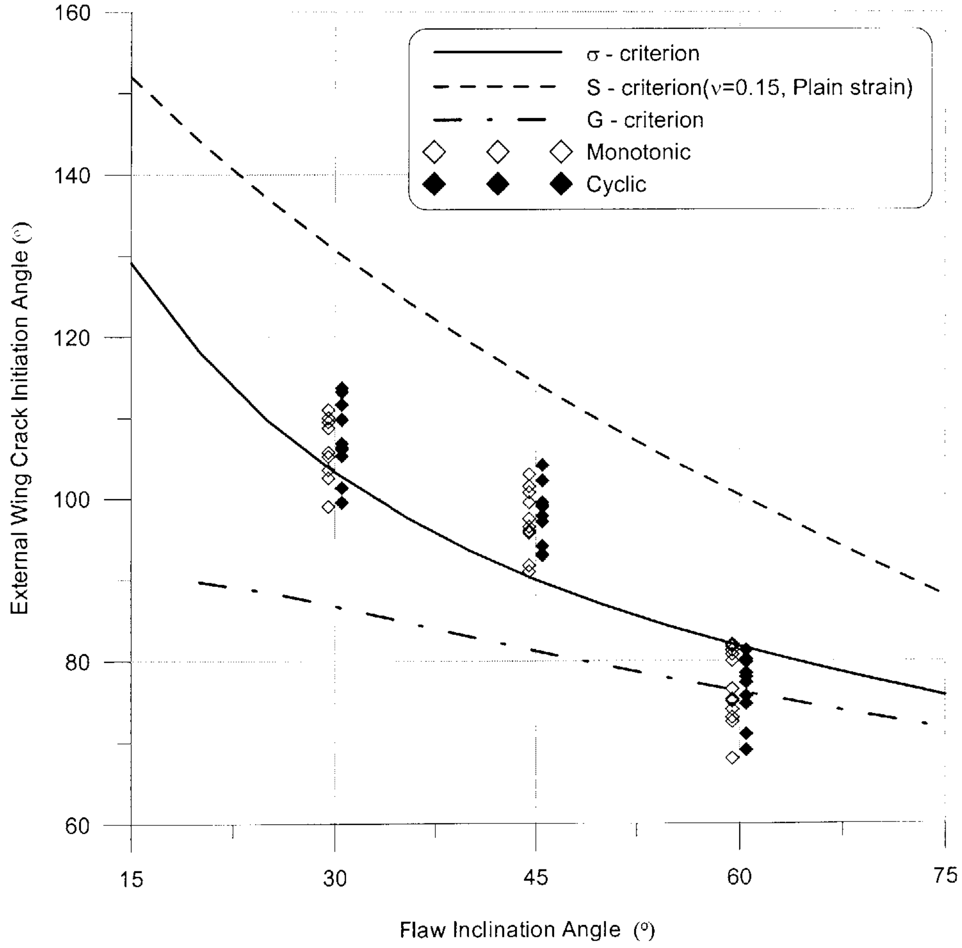

Figure 5.12 Comparison of external wing crack initiation angle.

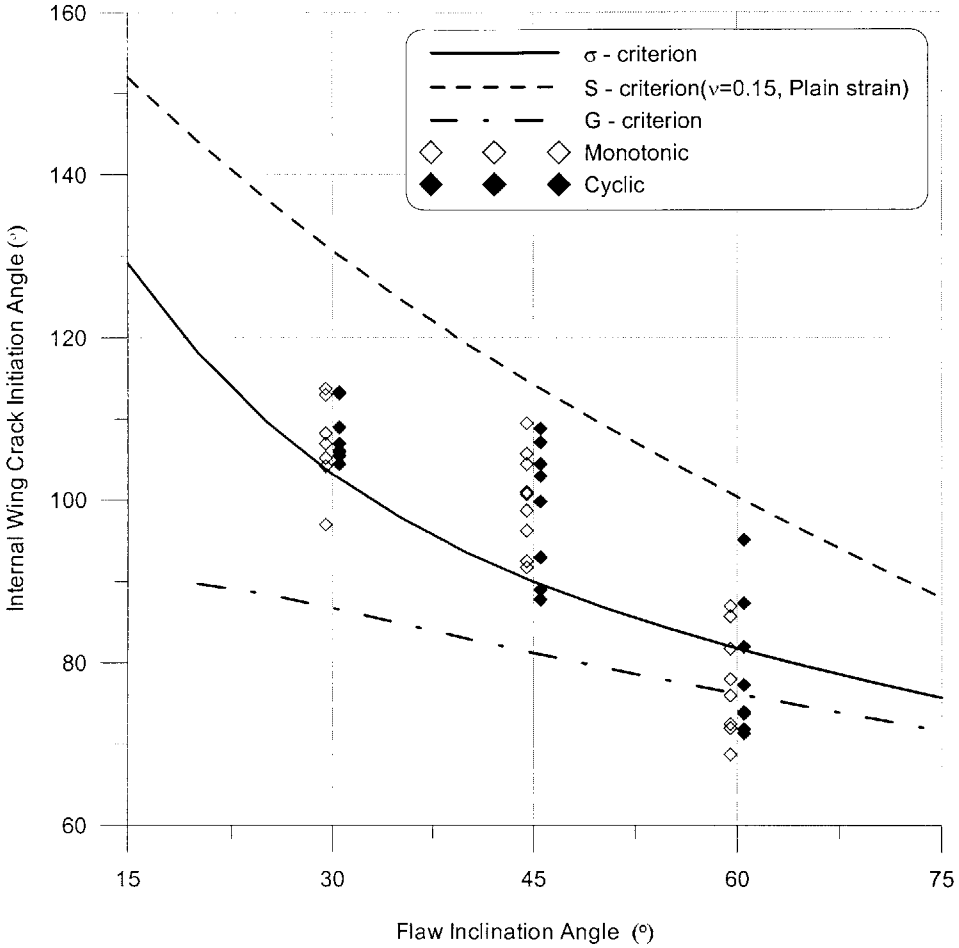

Figure 5.13 Comparison of internal wing crack initiation angle.

Table 5.4 lists the stress at initiation of external wing cracks, internal wing cracks, external shear cracks, and internal shear cracks, as well as the stress at coalescence, and failure in monotonic tests. Table 5.5 shows the number of cycles at initiation of external wing cracks, internal wing cracks, external shear cracks, internal shear cracks, and at coalescence and failure. Figure 5.14 is a plot of stresses at initiation of external and internal wing cracks for all geometries in monotonic tests. In Figure 5.15, the number of cycles at external and internal wing crack initiation in cyclic tests is presented. In both tests, external and internal wing cracks have the same crack initiation stress level or the same number of cycles at crack initiation regardless of geometries. These results are in good agreement with Bobet's result (Bobet, 1997). Wing cracks and coalescence initiation stresses and failure stresses increase as the flaw inclination angle increases.

Geometry	Ligament Length	External Wing crack Stress	Internal Wing crack Stress	External Shear crack Stress	Internal Shear crack Stress	Coalescence Stress	Failure Stress	Peak Stress
30-0-a	1.0a	20.13 19.84	- -	- 21.18	20.13 19.84	20.13 19.84	21.76 21.99	21.76 21.99
30-a-0	1.0a	14.07 13.07	14.07 13.07	23.78 22.89	- -	23.74 22.74	23.78 24.45	23.87 24.45
30-a-a	1.41a	12.81	-	22.2	22.46	22.46	22.34	21.07 22.46
30-0-2a	2.0a	22.26 25.43	27.33 27.94	24.12 28.02	24.12 26.84	28.75 28.11	28.76 28.11	28.76 28.11
30-2a-0	2.0a	12.89 11.03	12.89 11.03	27.47 29.27	- -	28.97 20.16	28.97 28.62	29.28 29.27
30-a-2a	2.24a	19.23 16.44	19.23 16.44	21.84 22.78	20.79 22.14	20.81 22.14	19.28 21.28	22.41 22.78
30-2a-a	2.24a	11.74 9.63	11.74 9.63	24.43 25.3	22.05 26.05	22.05 26.05	27.18 25.61	27.18 26.49
30-2a-2a	2.83a	19.2 17.2	19.2 17.2	25.7 23.23	25.08 23.29	25.08 23.29	26.21 25.63	27.1 25.63
30-0-3a	3.0a	25.91 28.9	27.25 30.25	27.46 30.69	27.38 30.69	- -	27.81 30.69	27.81 30.69
30-2a-3a	3.61a	18.33 22.82	18.33 22.82	25.06 28.32	24.58 28.32	25.06 28.32	21.76 23.6	25.06 28.32
30-0-4a	4.0a	24.61 27.3	24.61 28.75	25.91 29.87	25.91 29.87	- -	26.28 29.87	26.28 29.87
30° Flaw average		18.71	19.54	25.48	24.68	23.98	25.43	25.94
45-0-a	1.0a	18.53 17.47	- -	20.32 22.12	18.53 17.47	18.53 17.47	22.95 22.46	22.95 22.46
45-a-0	1.0a	16.98 23.15	16.98 23.15	29.33 30.05	- -	29.42 28.8	30.2 31.19	30.2 31.19
45-a-a	1.41a	10.54 9.98	10.54 9.98	24.5 21.67	23.65 21.67	23.65 21.67	28.64 24.01	28.69 24.01
45-0-2a	2.0a	27.34 22.58	- -	29.39 25.68	27.34 22.58	27.62 25.11	29.51 26.03	29.51 26.03
45-2a-0	2.0a	30.45 26.95	30.45 26.95	36.88 33.18	34 33.18	30.45 26.95	34.7 33.43	36.97 33.43
45-a-2a	2.24a	24.29 11.34	24.29 21.19	29.69 24.46	26.71 21.67	26.71 21.67	29.76 28.95	29.76 28.95
45-2a-a	2.24a	15.02 22.65	15.02 22.65	32.69 35.8	- -	34.99 35.81	34.99 35.81	34.99 35.81
45-2a-2a	2.83a	15.78 16.48	15.78 16.48	28.43 29.03	29.41 28.53	29.41 28.53	27.69 29.03	29.41 29.03

Table 5.4 Stress at initiation of wing cracks, shear cracks as well as the stress at coalescence, and failure in monotonic tests (unit: MPa).

Geometry	Ligament Length	External Wing crack Stress	Internal Wing crack Stress	External Shear crack Stress	Internal Shear crack Stress	Coalescence Stress	Failure Stress	Peak Stress
45-0-3a	3.0a	26.29	27.68	29.62	28..71	-	29.62	29.62
		26.55	28.64	28.69	28.69	-	28.69	28.69
45-2a-3a	3.61a	19.68	19.68	29.2	31.43	31.43	26.77	31.43
		25.69	25.69	25	27.14	27.14	25	27.14
45-0-4a	4.0a	25.79	26.53	26.56	26.56	-	26.56	26.56
		28.7	30.72	33.69	33.69	-	33.69	33.69
45° Flaw average		21.01	21.80	28.45	26.60	26.96	29.08	29.57
60-0-a	1.0a	23.15	-	25.15	23.15	23.15	25.59	25.59
		25.94	-	27.79	25.94	25.94	28.04	28.04
60-a-0	1.0a	32.22	32.22	32.34	-	32.22	32.34	32.34
		24.36	24.36	27.04	-	27.04	27.04	
60-a-a	1.41a	20.34	20.34	32.85	31.66	31.66	31.66	32.85
		29.28	29.28	30.55	30.55	30.55	30.56	30.56
60-0-2a	2.0a	27.19	-	28.32	27.19	27.19	29.34	29.34
		26.62	-	26.66	26.62	26.62	27.62	27.62
60-2a-0	2.0a	36.25	36.25	39.62	38.3	40.99	40.99	40.99
		36.39	36.39	40.77	40.93	40.77	41.21	31.21
60-a-2a	2.24a	27.9	27.9	29.71	29.33	29.33	29.4	30.8
		28.66	28.66	29.91	29.88	29.88	29.88	29.91
60-2a-a	2.24a	33.33	33.33	-	-	35.83	37.98	37.98
		36.61	36.61	37.75	37.75	37.62	28.71	37.75
60-2a-2a	2.83a	31.17	-	35.45	-	31.17	35.45	35.77
		30.25	30.25	25.36	-	30.25	25.36	30..25
60-0-3a	3.0a	30.04	-	30.21	30.04	30.04	30.21	30.21
		31.99	-	32.1	32.1	32.1	32.63	32.63
60-a-3a	3.16a	30.94	30.94	32.38	32.24	32.24	32.5	32.5
		24.04	24.04	28.23	28.23	28.23	28.5	28.5
60-2a-3a	3.61a	36.44	36.44	36.76	36.76	36.76	33.15	36.76
		35.17	35.17	33.85	35.83	35.83	34.68	35.85
60-0-4a	4.0a	33.58	-	33.58	33.58	33.58	33.58	33.58
		37.34	-	37.34	37.34	37.34	37.52	37.52
60° Flaw average		30.38	30.81	31.90	31.97	31.93	31.83	32.65

Table 5.4 (continued)

Geometry	Ligament Length	σ_{max}/σ_c	σ_{max} [MPa]	External Wing Crack	Internal Wing Crack	External Shear Crack	Internal Shear Crack	Coalescence	Failure
30-0-a	1.0a	0.9	23.7	1	-	11	1	1	12
		0.85	22.6	2	-	11	2	2	31
		0.8	21.5	7	-	1383	15	15	1402
30-a-0	1.0a	0.9	21.21	1	1	8	-	1	12
		0.85	20.87	1	1	25	-	1	29
		0.8	20.12	1	1	-	-	1	N/A
30-a-a	1.41a	0.9	21.59	1	-	6	1	1	7
		0.85	19.85	1	-	7	1	1	10
		0.8	19.58	1	-	60	1	1	62
30-0-2a	2.0a	0.9	23.55	2	2	288	288	-	290
		0.85	22.23	12	12	348	347	-	352
		0.8	21.54	4	4	424	424	-	424
30-2a-0	2.0a	0.9	28.05	1	1	1	-	4	11
		0.85	26.18	1	1	640	-	19	728
		0.8	25.02	1	1	420	-	18	N/A
30-a-2a	2.24a	0.9	22.02	2	2	5	3	3	8
		0.85	20.84	1	1	130	27	27	742
		0.8	20.22	2	7	2123	151	1866	2479
30-2a-a	2.24a	0.9	31.02	1	1	4	2	2	6
		0.85	30.08	1	1	160	160	262	262
		0.8	28.63	1	1	10	242	-	N/A
30-2a-2a	2.83a	0.9	22.28	1	1	11	2	2	16
		0.85	21.76	1	1	1039	1	1	1043
		0.8	20.36	1	1	-	-	-	N/A
30-0-3a	3.0a	0.9	26.26	1	1	11	11	-	12
		0.85	24.57	1	3	19	19	-	20
		0.8	23.49	2	2	688	688	-	689
30-2a-3a	3.61a	0.9	25.39	1	1	44	39	39	46
		0.85	24.04	2	2	256	202	202	639
		0.8	23.06	1	1	-	-	-	N/A
30-0-4a	4.0a	0.9	28.92	1	1	3	3	-	4
		0.85	26.52	1	1	19	19	-	20
		0.8	25.13	1	1	312	564	-	567
45-0-a	1.0a	0.9	23.75	1	-	5	1	1	10
		0.85	22.28	1	-	1602	1	1	2735
		0.8	20.67	2	-	3718	2	2	N/A
45-a-0	1.0a	0.9	26.17	1	1	8	-	1	63
		0.85	24.97	1	1	591	-	1	592
		0.8	23.37	1	1	238	-	1	243

Table 5.5 Number of cycles at initiation of wing cracks, shear cracks, and at coalescence and failure in cyclic tests (σ_{max} = maximum applied stress, σ_c = dynamic compressive strength).

Geometry	Ligament Length	σ_{max}/σ_c	σ_{max} [MPa]	External Wing Crack	Internal Wing Crack	External Shear Crack	Internal Shear Crack	Coalescence	Failure
45-a-a	1.41a	0.9	26.19	1	1	13	22	22	23
		0.85	24.86	1	1	151	1	1	154
		0.8	22.97	1	1	1183	1183	1196	1202
45-0-2a	2.0a	0.9	24.91	1	-	1	1	1	2
		0.85	23.85	5	-	8	8	8	13
		0.8	22.7	2	-	207	19	19	216
45-2a-0	2.0a	0.9	33.73	1	1	271	59	1	288
		0.85	31.84	1	1	1670	-	1	1675
		0.8	30.08	2	2	-	-	2	N/A
45-a-2a	2.24a	0.9	24.36	2	-	10	2	2	12
		0.85	23.42	1	1	344	217	217	345
		0.8	22.06	1	1	4000	33	33	N/A
45-2a-a	2.24a	0.9	35	1	1	61	61	61	78
		0.85	33	1	1	30	30	30	88
		0.8	31.26	1	1	20	72	72	N/A
45-2a-2a	2.83a	0.9	26.4	1	1	6	5	6	7
		0.85	24.42	1	1	259	250	259	260
		0.8	22.86	1	1	1302	547	1300	1302
45-0-3a	3.0a	0.9	25.16	5	-	102	5	101	105
		0.85	23.39	32	72	119	118	118	120
		0.8	22.47	161	836	838	837	837	840
45-2a-3a	3.61a	0.9	28.61	1	1	12	10	11	13
		0.85	27.46	1	1	850	845	845	851
		0.8	25.7	1	1	409	405	409	N/A
45-0-4a	4.0a	0.9	30.54	1	1	7	7	-	8
		0.85	28.62	1	1	14	15	-	15
		0.8	27.81	1	1	39	39	-	40
60-0-a	1.0a	0.9	24.8	1	-	49	1	1	55
		0.85	23.66	1	-	83	1	1	578
		0.8	21.58	1	-	2087	1	1	N/A
60-a-0	1.0a	0.9	29.01	11	11	16	-	11	17
		0.85	27.23	12	12	21	-	12	22
		0.8	24.01	34	34	44	-	34	45
60-a-a	1.41a	0.9	30.52	1	1	6	6	6	7
		0.85	29.31	2	2	216	180	180	218
		0.8	28.08	2	2	612	612	615	615
60-0-2a	2.0a	0.9	28.38	1	-	2	1	1	5
		0.85	27.2	119	-	207	119	119	218
		0.8	25.25	80	-	240	80	80	257

Table 5.5 (continued)

Geometry	Ligament Length	σ_{max}/σ_c	σ_{max} [MPa]	External Wing Crack	Internal Wing Crack	External Shear Crack	Internal Shear Crack	Coalescence	Failure
60-2a-0	2.0a	0.9	35.58	1	1	15	-	25	29
		0.85	33.84	1	1	307	512	307	1659
		0.8	32.03	3	3	22	-	22	N/A
60-a-2a	2.24a	0.9	30.76	2	2	6	5	6	6
		0.85	28.96	5	5	36	29	29	37
		0.8	28.14	1	1	206	206	206	208
60-2a-a	2.24a	0.9	37.08	1	1	84	60	1	156
		0.85	35.82	1	1	1949	1949	1	1955
		0.8	33.82	4	4	-	104	4	N/A
60-2a-2a	2.83a	0.9	27.94	1	-	4	-	1	5
		0.85	26.85	2	-	5	4	2	5
		0.8	25.51	138	-	148	148	138	149
60-0-3a	3.0a	0.9	28.06	140	-	148	148	148	148
		0.85	26.96	714	-	716	715	715	717
		0.8	24.62	830	-	832	831	831	832
60-1a-3a	3.16a	0.9	29.85	1	1	64	63	63	67
		0.85	28.69	154	154	157	157	157	158
		0.8	27.14	89	89	350	346	346	351
60-2a-3a	3.61a	0.9	35.83	4	4	12	6	6	14
		0.85	33.95	3	3	63	30	54	64
		0.8	31.96	121	121	733	502	502	735
60-0-4a	4.0a	0.9	32.65	3	4	4	4	-	5
		0.85	30.41	14	-	14	14	14	15
		0.8	28.84	291	291	291	-	-	292

Table 5.5 (continued)

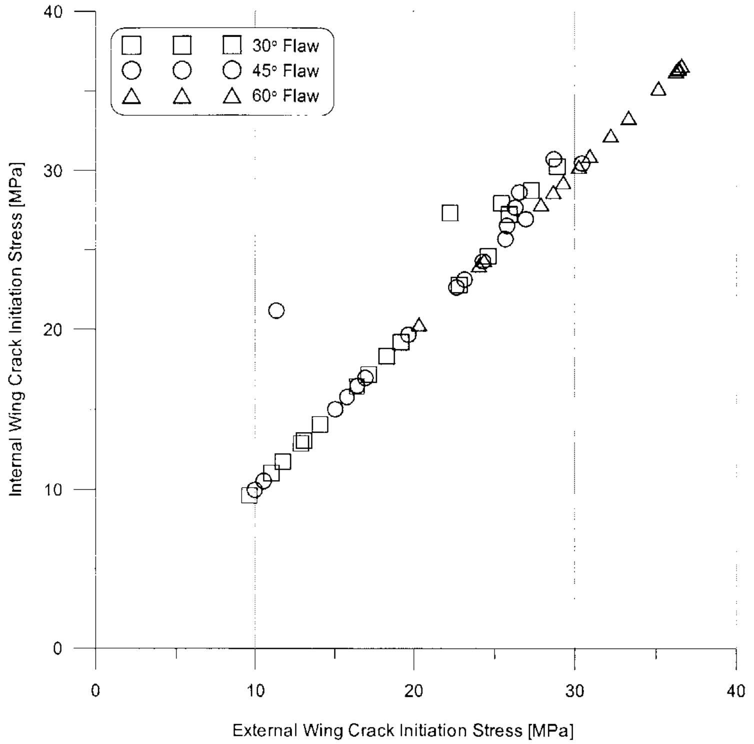

Figure 5.14 Comparison of external and internal wing crack initiation stress in monotonic tests.

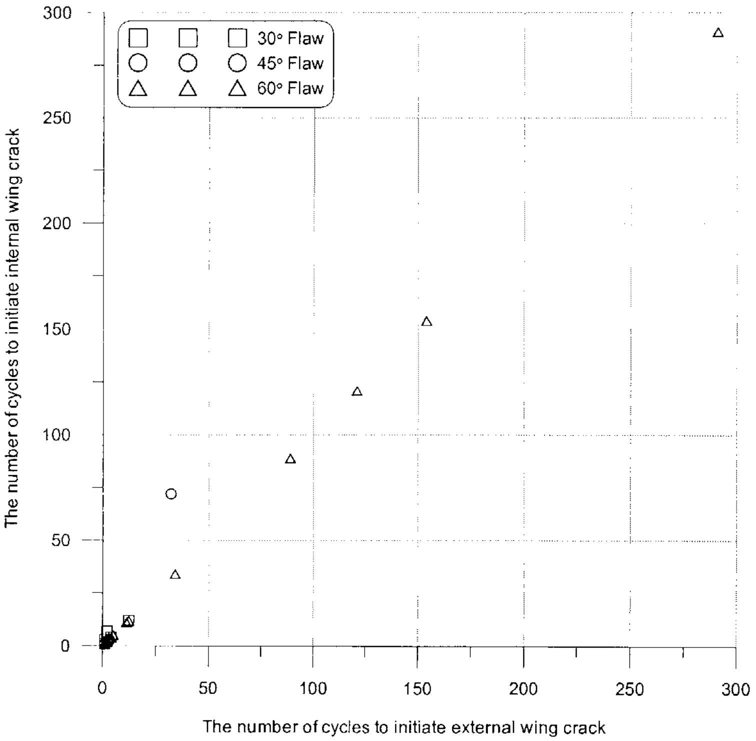

Figure 5.15 Comparison of external and internal wing crack initiation cycles in cyclic tests.

Figure 5.16 is a plot of wing crack initiation stress with respect to the ligament length in monotonic tests. Although there is some scatter, wing crack initiation stresses increase with the increasing ligament length.

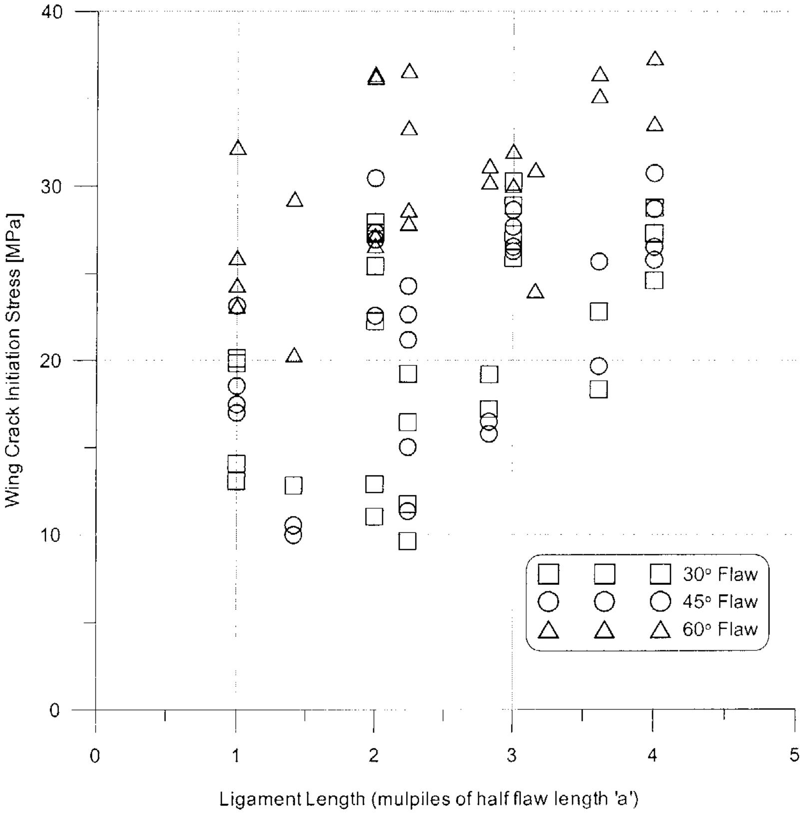

Figure 5.16 Wing crack initiation stress with respect to the ligament length.

5.2 Coalescence cracks

Coalescence types observed in this study are similar to the ones observed by previous researchers (Reyes, 1991; Shen et al., 1995; Bobet, 1997; Sagong, 2001). Both monotonic and cyclic tests show almost the same coalescence types. For coplanar geometry specimens, coalescence occurs due to the internal shear cracks. For non-coplanar geometry specimens, coalescence occurs through combinations of internal shear cracks, internal wing cracks and tension cracks. Table 5.6 summarizes all observed coalescence types.

Type I coalescence occurs by propagation of internal shear cracks in coplanar flaw geometry or almost coplanar flaw geometry. 30-0-a, 45-0-a, 60-0-a, 45-0-2a, 60-0-2a, 60-0-3a, 60-0-4a, 30-a-2a geometries show Type I coalescence. 30-0-2a geometry shows Type I coalescence just in monotonic tests and for the 45-0-3a geometry Type I coalescence occurs just in cyclic tests.

Type II coalescence is formed by the connection of two internal shear cracks by a vertical or quasi-vertical tension crack. This tension crack is not a wing crack but produced under tension. 30-a-a, 45-a-a, 45-a-2a, 60-a-2a, 60-a-3a, 30-2a-a, 30-2a-2a, 45-2a-2a, 30-2a-3a, 60-a-a, 30-2a-a, 45-2a-2a and 45-2a-3a geometries show Type II coalescence.

Type III coalescence can be divided into two classes; Type III-A and Type III-B coalescence. Type III-A coalescence takes place when an internal wing crack from one of the flaws reaches the other flaw. 60-2a-2a and 60-a-0 geometries show Type III-A coalescence. Type III-B coalescence takes place when an internal shear crack from one of the flaws reaches the internal wing crack of the other flaw. 60-2a-3a geometry shows Type III-B coalescence.

Type IV coalescence can be divided into three classes; Type IV-A, Type IV-B and Type IV-C coalescence. Type IV-A coalescence happens when two internal wing cracks from the flaw tips reach the other flaw tips. 30-a-0, 45-a-0, 60-a-a, 30-2a-0, 45-2a-a geometries show Type IV-A coalescence. Type IV-B coalescence appears when two internal wing cracks from the flaw tips reach the middle of other flaws and with a different wing crack curvature than for Type IV-A coalescence. 60-a-0 geometry is a good example of Type IV-B coalescence. Type IV-C coalescence occurs when two internal shear cracks from the flaws tips reach the internal wing cracks of the other flaws. 60-2a-0 geometry is a good example of Type IV-B coalescence.

Type V coalescence occurs by a combination of the connection of an internal wing crack which initiates from the internal tip of the upper flaw and an external wing crack which initiates from the external tip of the lower flaw and Type III-A or Type III-B coalescence. An internal wing crack and an external wing crack propagate until they unite. An external wing crack has a reverse propagation direction than the other external wing crack. 60-2a-a geometry is a good example of this type coalescence.

Type VI coalescence occurs by a combination of the connection of two internal wing cracks which propagate until they unite, tension cracks and internal shear cracks. First two internal wing cracks initiate from the internal tips of the flaws and propagate until they join. Then other tension cracks initiate from the external tips of the flaws and propagate to the other tips. Finally internal shear cracks develop at the external tips of the flaws and reach the other tension cracks. 45-2a-0 geometry is a good example of Type VI coalescence.

Type V and VI coalescence are new observations from this study.

Type	Coalescence Pattern	Characteristic of Coalescence	Mode of Coalescence
I	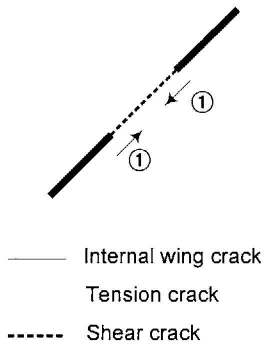	Type of crack: shear crack. Coalescence crack surface: rough with crushed gypsum	Shearing
II	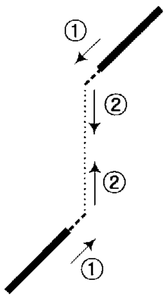	Type of crack: internal shear and tension crack. Coalescence crack surface: rough with crushed gypsum near the flaw tips and clean and smooth in other parts	Shearing and Tension
III-A	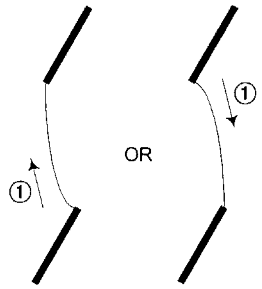	Type of crack: internal wing crack. Coalescence crack surface: clean and smooth	Tension

Table 5.6 Observed coalescence types.

Type	Coalescence Pattern	Characteristic of Coalescence	Mode of Coalescence
III-B	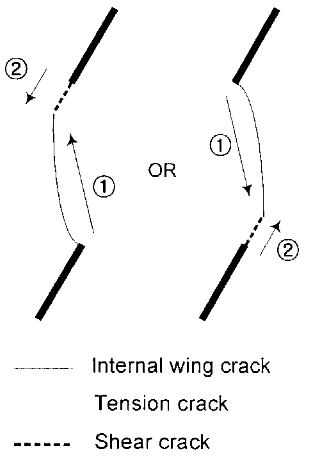	Type of crack: internal wing crack and internal shear crack. Coalescence crack surface: rough with crushed gypsum near the flaw tips and clean and smooth in other parts	Shearing and Tension
IV-A	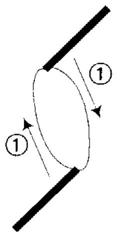	Type of crack: internal wing crack. Coalescence crack surface: clean and smooth	Tension
IV-B	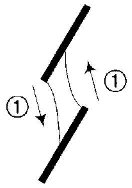	Type of crack: internal wing crack. Coalescence crack surface: clean and smooth	Tension
IV-C	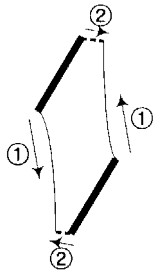	Type of crack: internal wing crack and internal shear crack. Coalescence crack surface: rough with crushed gypsum near the flaw tips and clean and smooth in other parts	Shearing and Tension

Table 5.6 (continued)

Type	Coalescence Pattern	Characteristic of Coalescence	Mode of Coalescence
V	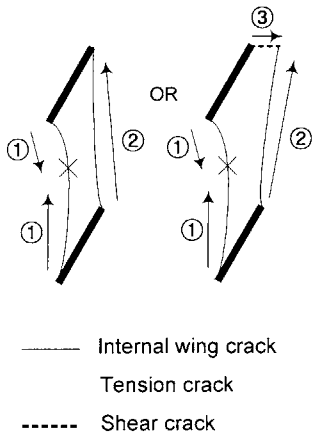	Type of crack: internal wing crack and internal shear crack. Coalescence crack surface: rough with crushed gypsum near the flaw tips and clean and smooth in other parts	Shearing and Tension
VI	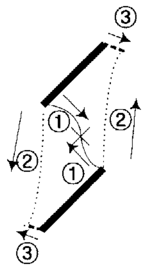	Type of crack: internal wing crack, internal shear crack and tension crack. Coalescence crack surface: rough with crushed gypsum near the flaw tips and clean and smooth in other parts	Shearing and Tension

Table 5.6 (continued)

Figure C.1 to C.11 in Appendix C are a comparison of the coalescence type in monotonic and cyclic tests. Except 30-0-2a and 45-0-3a, the coalescence types are identical in the monotonic and cyclic tests. For the 30-0-2a geometry, coalescence occurs in monotonic tests but does not occur in cyclic tests. On the other hand, for the 45-0-3a geometry, coalescence occurs in cyclic tests but does not occur in monotonic tests (Figure 5.17)

Table 5.7 lists the average coalescence stress and standard deviation with respect to the flaw inclination angles. Greater flaw inclination angles have a higher coalescence stress.

Figure 5.18 shows the variation of coalescence stress with respect to the ligament length. As a rule, greater ligament lengths result in a higher coalescence stress. Figure 5.19 is a plot of the coalescence stress with respect to overlapping ratio. For the non-overlapping geometry, as the non-overlapping ratio decreases (overlapping ratio increases), the coalescence stress decreases. On the other hand, for the overlapping geometry, increase of the overlapping ratio induces an increase of coalescence stress.

Flaw inclination Stress	30°	45°	60°
Average coalescence stress	23.98 MPa	26.96 MPa	31.93 MPa
Standard deviation	3.15 MPa	5.0 MPa	4.66 MPa

Table 5.7 Average coalescence stress and standard deviation with respect to the flaw inclination angles.

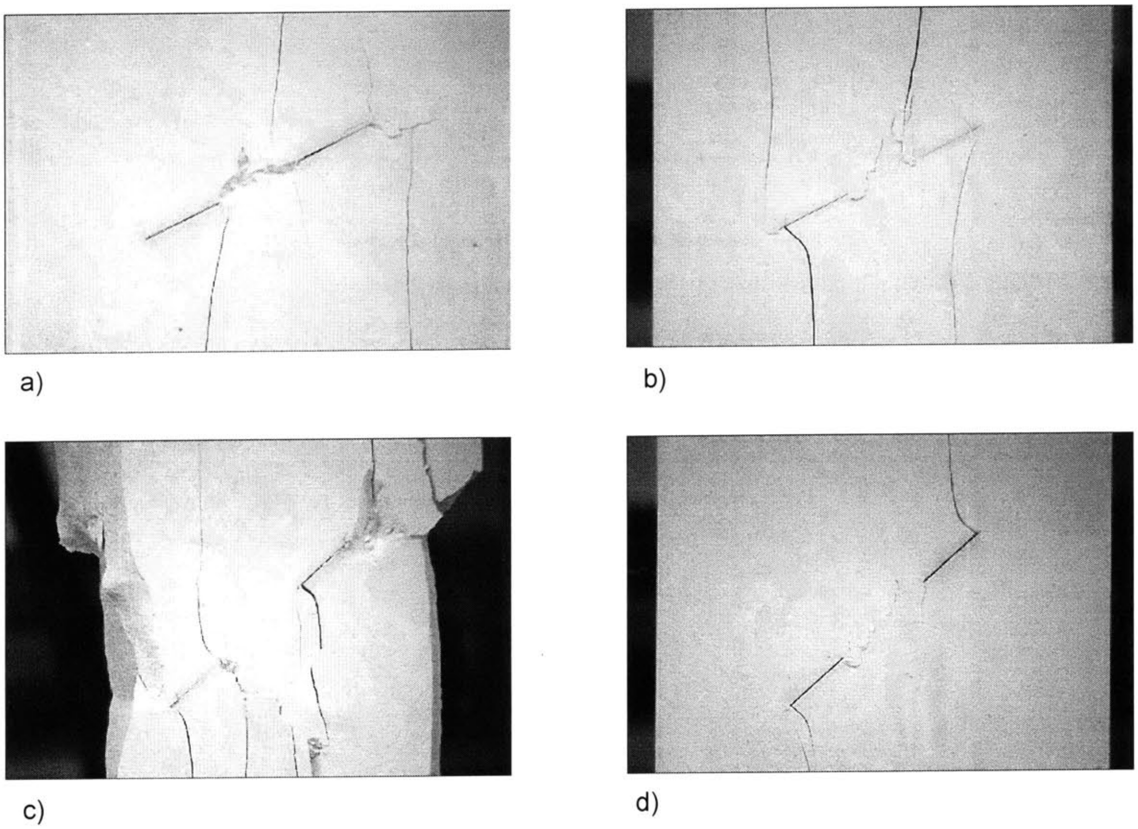

Figure 5.17 Comparison of the coalescence type in monotonic and cyclic tests; a) Type I coalescence occurs in monotonic tests for the 30-0-2a geometry.(at 28.11 MPa) b) Coalescence doesn't occur in cyclic tests for the 30-0-2a geometry. (at 349 cycles , $\sigma_{max}/\sigma_c = 0.85$, σ_{max} :22.23 MPa) c) Coalescence doesn't occur in monotonic tests for the 45-0-3a geometry. (at 28.69 MPa) d) Type I coalescence occurs in cyclic tests for the 45-0-3a geometry. (at 838 cycles, $\sigma_{max}/\sigma_c = 0.8$, σ_{max} : 22.47 MPa)

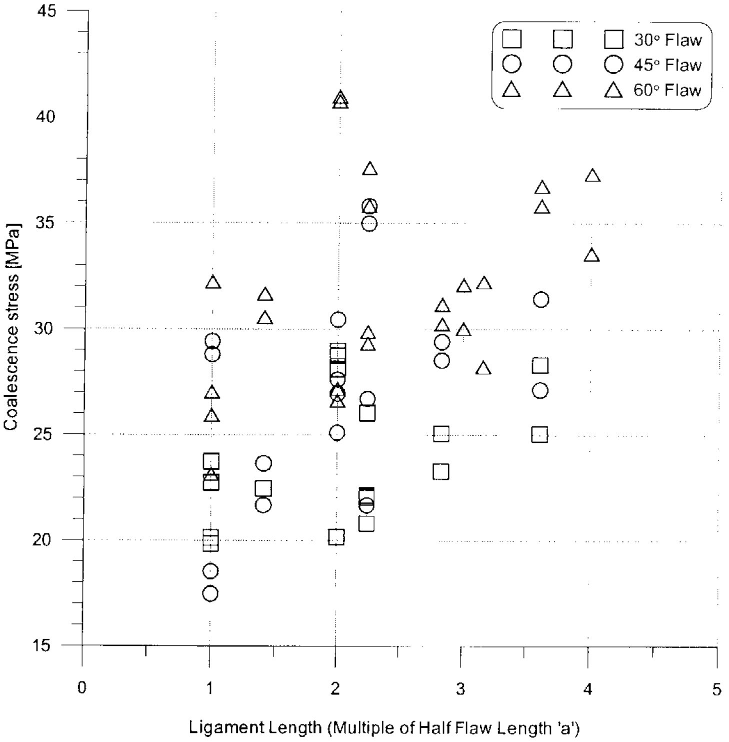

Figure 5.18 Variation of coalescence stress with respect to the ligament length.

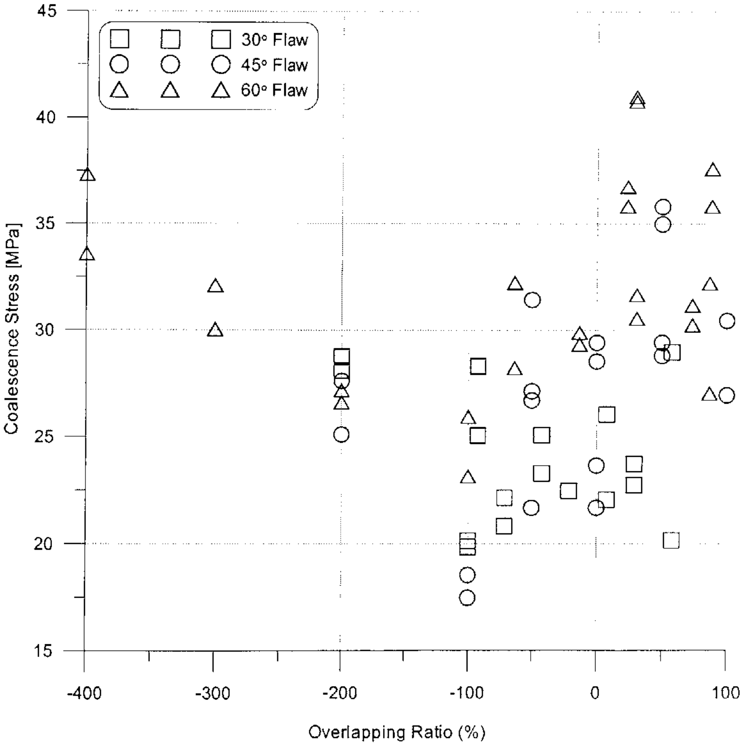

Figure 5.19 Variation of coalescence stress with respect to overlapping ratio.

5.3 Secondary cracks

Since secondary crack initiation and propagation is not as clear as wing crack initiation and propagation and secondary cracks usually occur near failure, secondary cracks are more difficult to observe than wing cracks. Secondary cracks are observed in both monotonic and cyclic tests. They always appear after wing crack initiation and lead to final failure. Secondary cracks initiate at the tips of the flaws and propagate in the coplanar direction of the flaw or horizontal (quasi-coplanar) direction. Figures 5.20 and 5.21 show two different types of secondary cracks. Figure 5.20 shows the initiation of coplanar second crack. Horizontal second cracks are shown in Figure 5.21.

Reyes (1991), Shen et al. (1995), and Bobet (1997) defined secondary cracks as shear cracks. Bobet and Einstein(1998) provided three reasons that secondary cracks were shear cracks: (1) secondary cracks initiated with a protrusion of material or some material spalling from the surface; (2) The surface of secondary cracks showed crushed material and gypsum powder, which implies shear movement; (3) secondary cracks always initiated in a compressive stress field.

In this research, secondary cracks are also shear cracks. First, the surface of secondary cracks is very rough, and composed of crushed gypsum and gypsum powder. Second, surface spalling or material falling from the specimen surface are observed. Figure 5.22 is a comparison of the crack surface. Figure 5.22 a) shows the surface of the coalescence crack due to the internal shear cracks. Figure 5.22 b) shows the surface of a wing crack, which is smooth and clean.

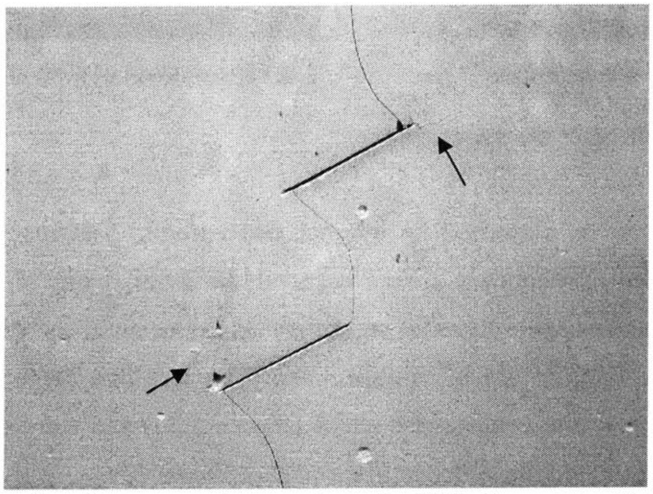

Figure 5.20 An example of coplanar secondary cracks in the 30-2a-0 geometry. External secondary cracks occur at the external tip of the upper flaw. Material spalling takes place at the external tip of the lower flaw.

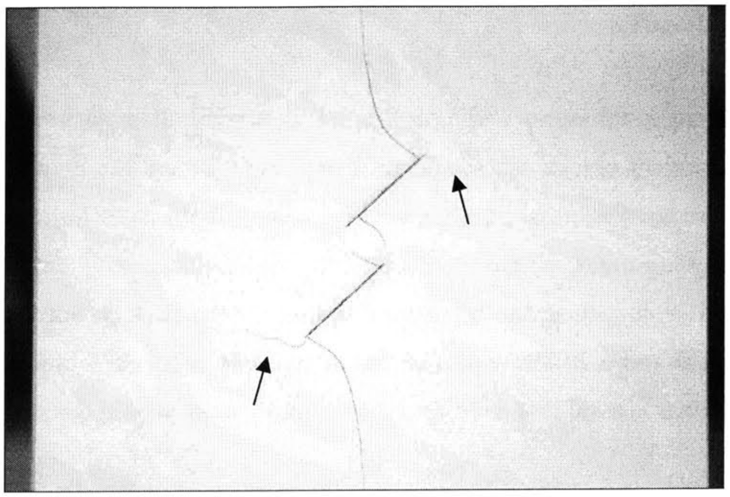

Figure 5.21 An example of horizontal secondary cracks in the 45-a-0 geometry.

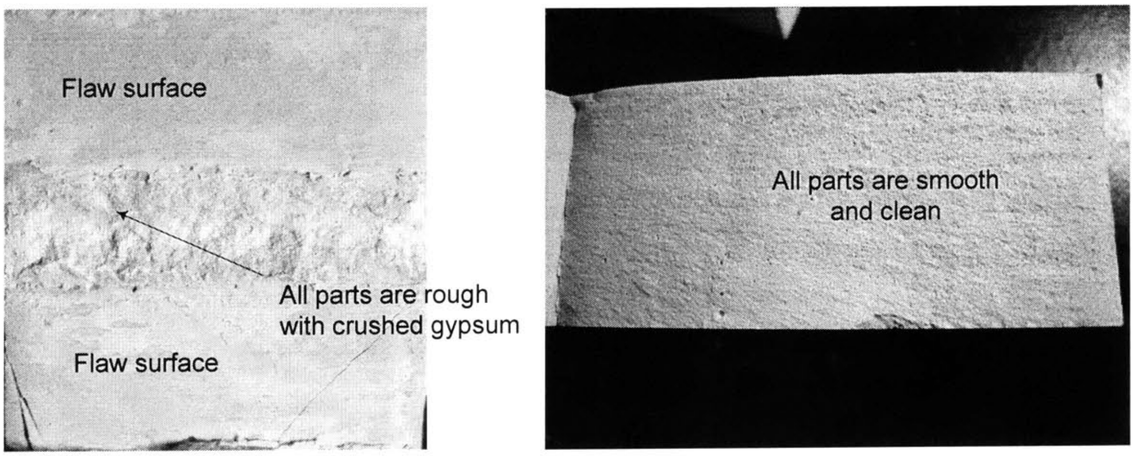

a) The surface of shear cracks

b) The surface of wing cracks

Figure 5.22 Comparison of the crack surface.

Secondary cracks can be classified as internal and external secondary cracks based on the initiation position. Internal secondary cracks occur at the internal tips of the flaws and play an important role in the coalescence. External secondary cracks occur at the external tips of the flaws and are related to the final failure of the specimen. The fact that the internal secondary crack initiation stress is close to the coalescence stress (Figure 5.23) and the external secondary crack initiation stress is close to the failure stress (Figure 5.24) proves this.

Figure 5.25 is a plot of external secondary crack initiation stress and internal secondary crack initiation stress. It seems that these stresses have a linear relation and that the external secondary crack initiation stress is slightly higher than internal secondary crack initiation stress. It is observed that a higher flaw inclination angle results in a higher secondary crack initiation stress.

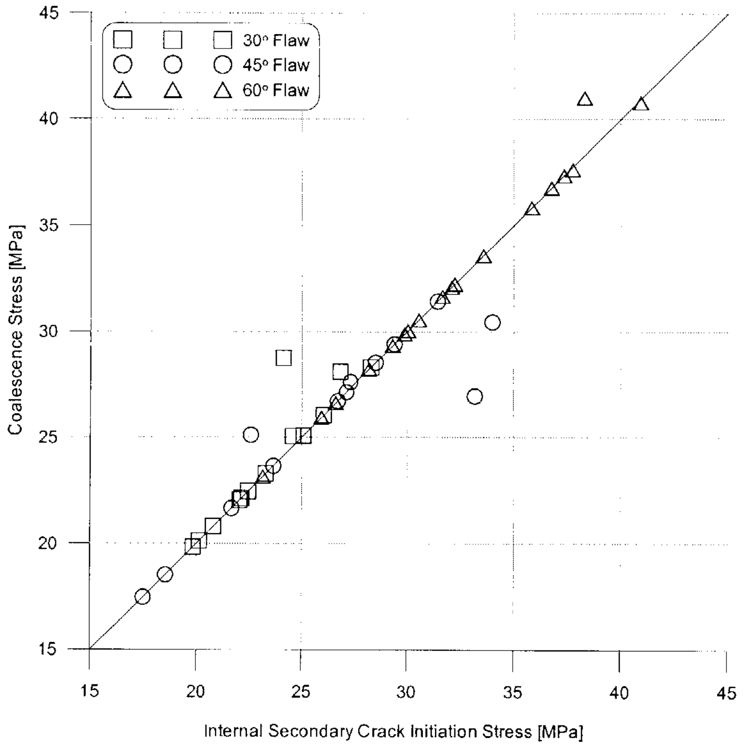

Figure 5.23 Comparison of coalescence- and internal secondary crack initiation stress.

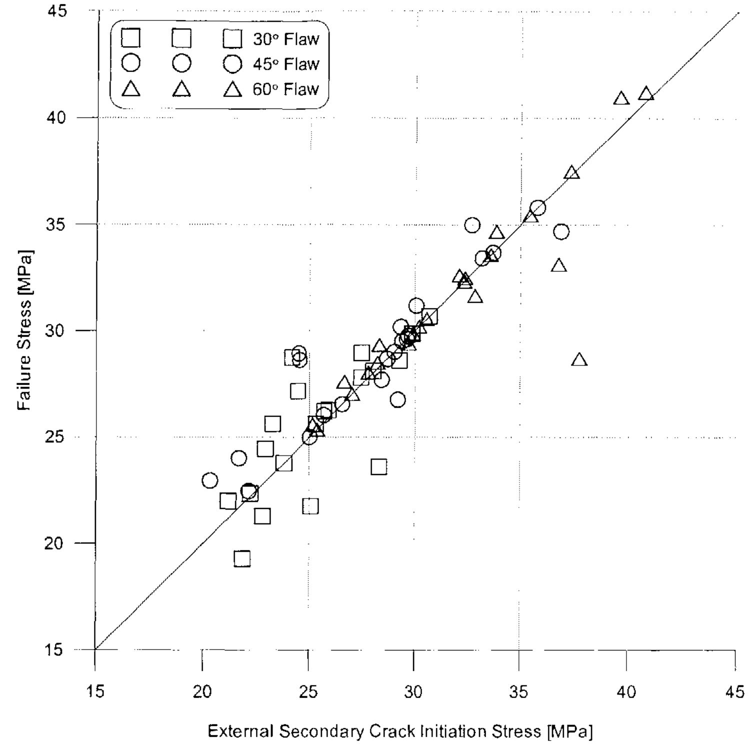

Figure 5.24 Comparison of failure- and external secondary crack initiation stress.

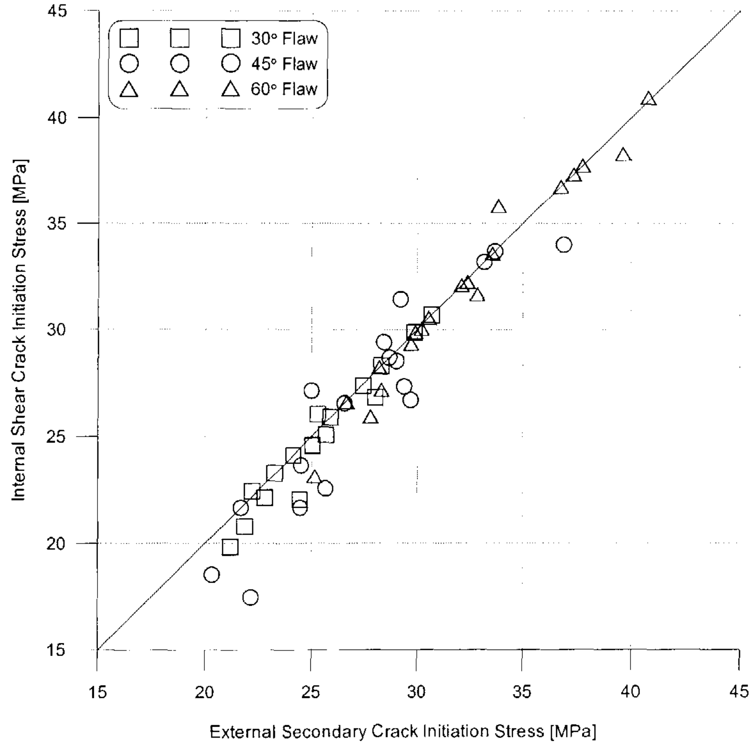

Figure 5.25 Comparison of internal and external secondary crack initiation stress.

5.4 Fatigue cracks

Contrary to monotonic tests, cyclic tests produce new types of cracks, fatigue cracks. Fatigue cracks usually occur when 1) after coalescence, the specimens behave as if they had only one larger crack 2) specimens have been subjected to a particular number of cycles. In these experiments, two different fatigue crack initiation directions are observed: horizontal and coplanar to the flaw. Figures 5.26 and 5.27 show two different types of fatigue cracks.

Horizontal fatigue cracks usually develop for coplanar or non-overlapping geometries. After coalescence occurs, the specimens behave as if they had only one larger crack. Then the specimens split into two parts. During loading, buckling occurs in the specimens and large lateral displacements take place in the middle of the specimens (Figure 5.28). External tips of the flaws act as stress concentrators. According to Pruitt and Suresh (1993) residual tensile stresses are induced ahead of the stress concentrations during unloading, and fatigue cracks develop horizontally to the compression load axis. Pruitt and Suresh (1993) found that residual stresses are induced ahead of the notch tip during unloading from the far-field compressive stress because there is no contact (closure) in the wake of the notch tip. In zero-tension fatigue, there develops a region of reversed flow ahead of a tensile crack within which residual stresses comparable in magnitude the flow stress in compression exist. If one considers the case of a sharp nonclosing notch which is subjected to a zero-compression-zero fatigue cycle, it is seen that the reverse flow induced within the monotonic plastic zone ahead of the notch tip upon unloading from the maximum compressive stress generates a zone of residual tensile stresses at the notch tip (Figure 5.29)(Suresh, 1998).

Coplanar fatigue cracks usually occur in overlapping geometries. During loading, buckling also occurs in the specimen but, relative small lateral displacement takes place. Shear stresses are more dominant ahead of the tips of the flaws than residual tensile stresses. Repeated compressive loading produces a shear stress zone ahead of the tips of the flaw and fatigue cracks develop in the coplanar direction.

Since the maximum number of cycles in this experiment is 4000, it is unknown if fatigue cracks can develop further or arrest.

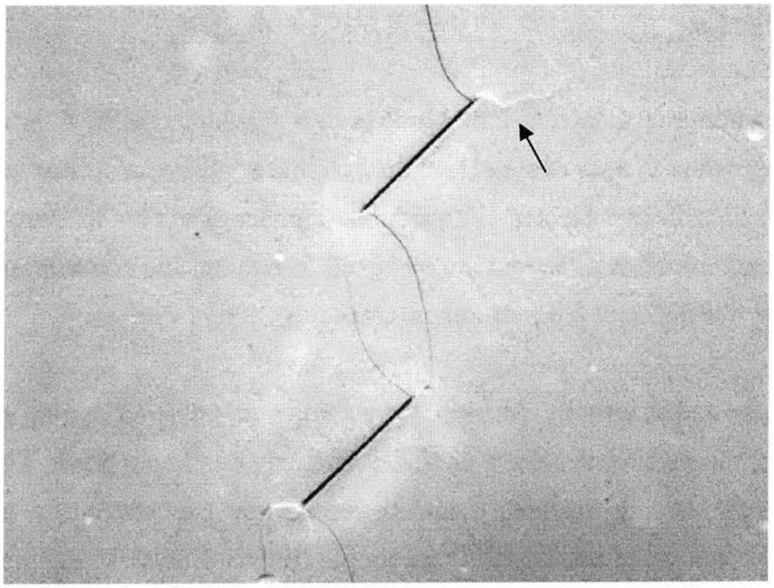

Figure 5.26 Horizontal fatigue cracks develop at the external tips of the flaws. (45-2a-a geometry, after 4000 cycles, $\sigma_{max}/\sigma_c = 0.8$, σ_{max} : 31.26 MPa)

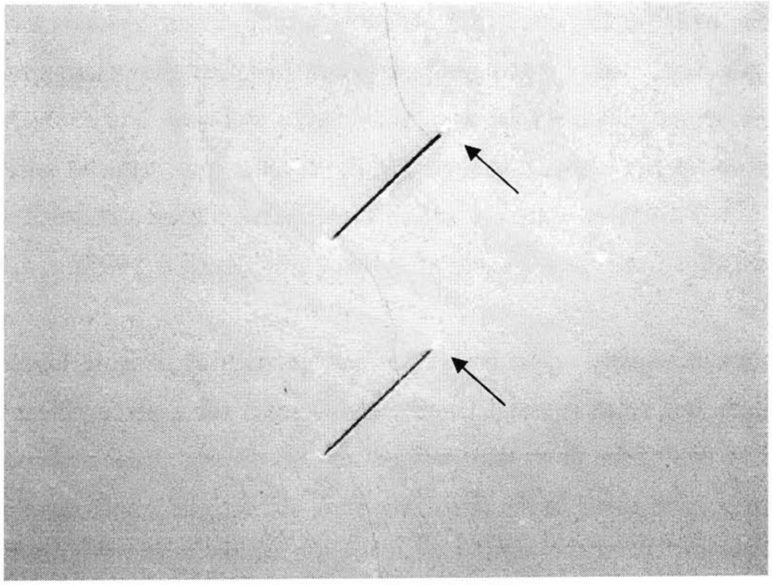

Figure 5.27 Coplanar fatigue cracks develop at the external tips of the flaws. (45-2a-0 geometry, after 4000 cycles, $\sigma_{max}/\sigma_c = 0.8$, σ_{max} : 30.08 MPa)

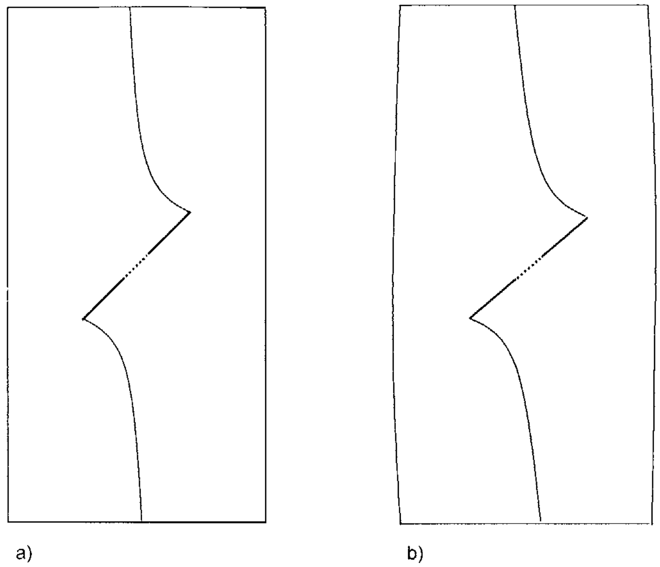

Figure 5.28 Buckling occurs in the specimens. a) before loading b) during loading. Large lateral displacements take place in the middle of the specimens.

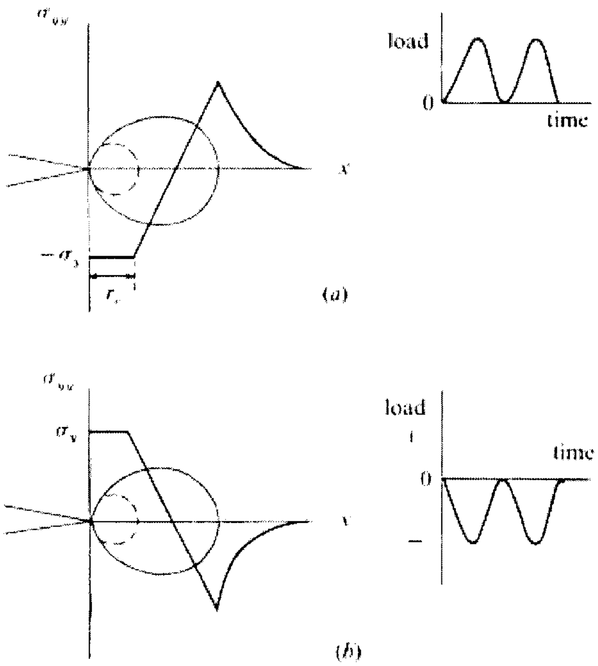

Figure 5.29 (a) A schematic of a zone of residual compression ahead of a sharp notch subjected to cyclic tension. r_c is the cyclic plastic zone. (b) A zone of residual tension for the nonclosing notch subjected to cyclic compression (Suresh, 1998).

5.5 Fatigue characteristics of the gypsum specimen

During cyclic tests, even though wing cracks propagate to the top and bottom edge of the specimen, the specimen can sustain a certain amount of fatigue loading. From table 5.5, it is observed that the number of coalescence cycles and failure cycles are sililar as the flaw inclination angles increase.

Table 5.8 gives average peak stress and standard deviation with respect to the flaw inclination angles in monotonic tests. Higher flaw inclination angle specimens have a higher peak stress. Similar results are observed in cyclic tests. For the same spacing and continuity specimens, higher flaw inclination angle specimens have a longer fatigue life. Figure 5.29 shows typical S-N curves for cyclic tests. As expected, the number of cycles increases as the maximum applied stress decreases.

Flaw inclination / Stress	30°	45°	60°
Average peak stress	25.94 MPa	29.57 MPa	32.65 MPa
Standard deviation	2.96 MPa	3.88 MPa	3.32 MPa

Table 5.8 Average peak stress and standard deviation with respect to the flaw inclination angles.

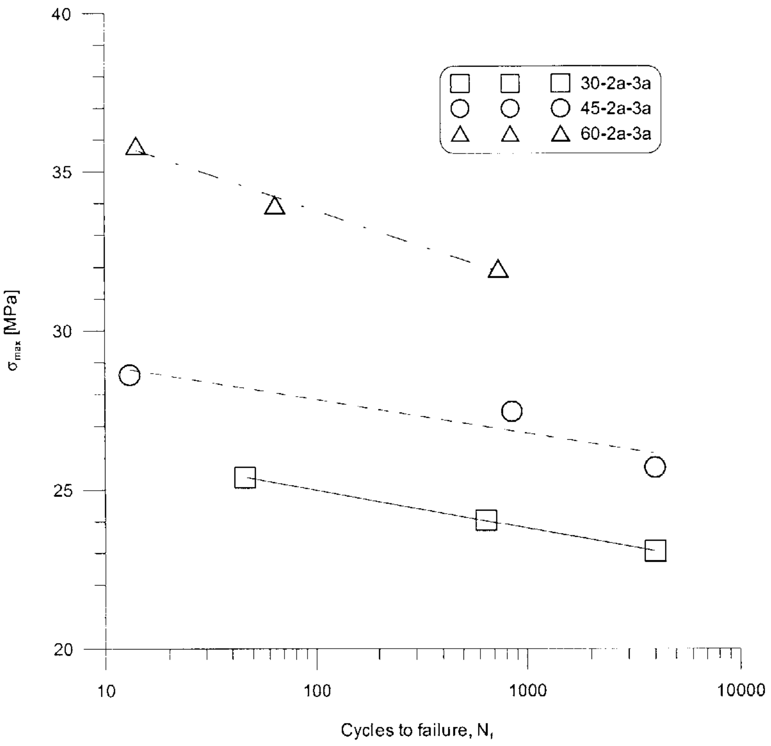

Figure 5.30 Typical S-N curves for the 2a-3a geometry.

Typical stress-strain curves are shown in Figure 5.30. Permanent strain appears in the specimen even when the applied stress is released. One of the common phenomena is a rather large hysteresis in the first few cycles. The hysteresis in the first cycles is probably due to loading at very fast displacement rates, which takes the specimen beyond its linear elastic limits and causes the irreversible deformation in the specimen.

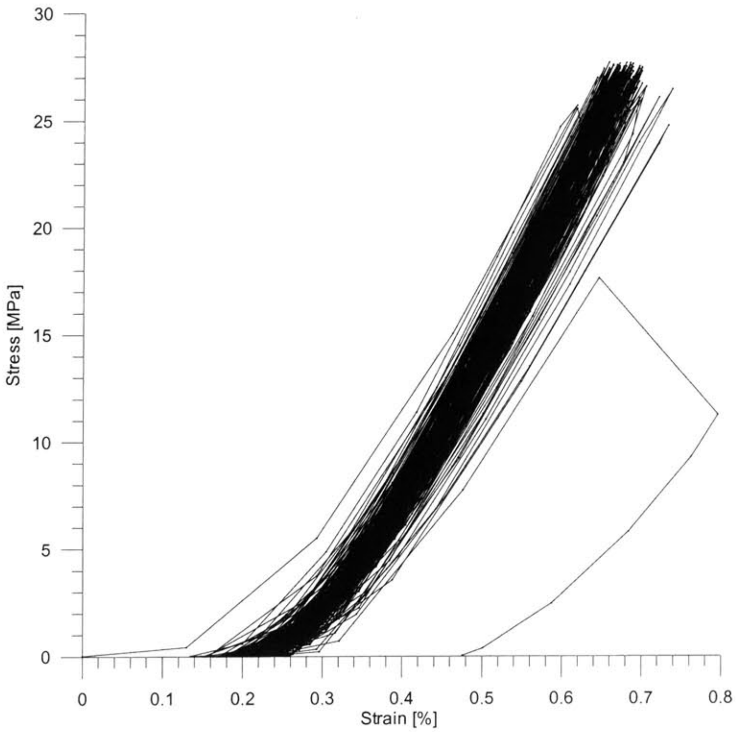

Figure 5.31 Typical stress-strain curves for the 45-2a-3a geometry (after 851 cycles, $\sigma_{max}/\sigma_c = 0.85$, $\sigma_{max} = 27.46$ MPa).

5.6 Crack growth sequence

As stated before, the crack growth sequence and the coalescence pattern are almost identical in both monotonic and cyclic tests. In Appendix D, more detailed pictures and descriptions of the crack growth sequence are presented. Tables 5.9 and 5.10 summarize the crack growth sequence in monotonic and cyclic tests.

Geometry	External Wing crack	Internal Wing crack	External Shear crack	Internal Shear crack	Coalescence	Failure
30-0-a	1	NO	NO	1	1	2
	1	NO	2	1	1	3
45-0-a	1	NO	2	1	1	3
	1	NO	2	1	1	3
60-0-a	1	NO	2	1	1	3
	1	NO	2	1	1	3
30-0-2a	1	3	2	2	4	5
	1	3	4	2	5	6
45-0-2a	1	NO	3	1	2	4
	1	NO	3	1	2	4
60-0-2a	1	NO	2	1	1	3
	1	NO	2	1	1	3
30-0-3a	1	2	4	3	NO	5
	1	2	3	3	NO	4
45-0-3a	1	2	4	3	NO	5
	1	2	3	3	NO	4
60-0-3a	1	NO	3	2	2	4
	1	NO	3	2	2	4
30-0-4a	1	1	2	2	NO	3
	1	2	3	3	NO	4
45-0-4a	1	2	3	3	NO	4
	1	2	3	3	NO	4
60-0-4a	1	NO	2	2	2	3
	1	NO	2	2	2	3
30-a-0	1	1	3	NO	2	4
	1	1	3	NO	2	4
45-a-0	1	1	2	NO	3	4
	1	1	3	NO	2	4
60-a-0	1	1	3	NO	2	4
	1	1	3	NO	2	4
30-a-a	1	NO	3	2	2	4
45-a-a	1	1	3	2	2	4
	1	1	2	2	2	3
60-a-a	1	1	3	2	2	4
	1	1	2	2	2	3
30-a-2a	1	1	4	2	3	5
	1	1	3	2	2	4
45-a-2a	1	1	3	2	2	4
	1	1	3	2	2	4

Table 5.9 The crack growth sequence in monotonic tests. The numbers in the table show the order of the cracking sequence.

Geometry	External Wing crack	Internal Wing crack	External Shear crack	Internal Shear crack	Coalescence	Failure
60-a-2a	1	1	3	2	2	4
	1	1	3	2	2	4
60-a-3a	1	1	3	2	2	4
	1	1	2	2	2	3
30-2a-0	1	1	2	NO	3	4
	1	1	2	NO	3	4
45-2a-0	1	1	3	2	1	4
	1	1	2	2	1	3
60-2a-0	1	1	3	2	4	5
	1	1	3	2	3	4
30-2a-a	1	1	3	2	2	4
	1	1	2	3	3	4
45-2a-a	1	1	2	NO	3	4
	1	1	2	NO	3	4
60-2a-a	1	1	NO	NO	2	3
	1	1	3	3	2	4
30-2a-2a	1	1	3	2	2	4
	1	1	3	2	2	4
45-2a-2a	1	1	3	2	2	4
	1	1	3	2	2	4
60-2a-2a	1	NO	2	NO	1	3
	1	1	2	NO	1	3
30-2a-3a	1	1	3	2	3	4
	1	1	2	2	2	3
45-2a-3a	1	1	2	3	3	4
	1	1	2	3	3	4
60-2a-3a	1	1	2	2	2	3
	1	1	2	2	2	3

Table 5.9 (continued)

Geometry	σ_{max}/σ_c	σ_{max} [Mpa]	External Wing Crack	Internal Wing Crack	External Shear Crack	Internal Shear Crack	Coalescence	Failure
30-0-a	0.9	23.7	1	NO	2	1	1	3
	0.85	22.6	1	NO	2	1	1	3
	0.8	21.5	1	NO	3	2	2	4
45-0-a	0.9	23.75	1	NO	2	1	1	3
	0.85	22.28	1	NO	2	1	1	3
	0.8	20.67	1	NO	2	1	1	NO
60-0-a	0.9	24.8	1	NO	2	1	1	3
	0.85	23.66	1	NO	2	1	1	3
	0.8	21.58	1	NO	2	1	1	NO
30-0-2a	0.9	23.55	1	1	2	2	NO	3
	0.85	22.23	1	1	3	2	NO	4
	0.8	21.54	1	1	2	2	NO	3
45-0-2a	0.9	24.91	1	NO	1	1	1	2
	0.85	23.85	1	NO	2	2	2	3
	0.8	22.7	1	NO	3	2	2	4
60-0-2a	0.9	28.38	1	NO	3	2	2	4
	0.85	27.2	1	NO	3	2	2	4
	0.8	25.25	1	NO	3	2	2	4
30-0-3a	0.9	26.26	1	1	2	2	NO	3
	0.85	24.57	1	2	3	3	NO	4
	0.8	23.49	1	1	2	2	NO	3
45-0-3a	0.9	25.16	1	NO	4	2	3	5
	0.85	23.39	1	2	4	3	3	5
	0.8	22.47	1	2	4	3	3	5
60-0-3a	0.9	28.06	1	NO	2	2	2	3
	0.85	26.96	1	NO	3	2	2	4
	0.8	24.62	1	NO	3	2	2	4
30-0-4a	0.9	28.92	1	1	2	2	NO	3
	0.85	26.52	1	1	2	2	NO	3
	0.8	25.13	1	1	2	3	NO	4
45-0-4a	0.9	30.54	1	1	2	2	NO	3
	0.85	28.62	1	1	2	3	NO	4
	0.8	27.81	1	1	2	2	NO	3
60-0-4a	0.9	32.65	1	2	2	2	NO	3
	0.85	30.41	1	NO	1	1	1	2
	0.8	28.84	1	1	1	NO	NO	2
30-a-0	0.9	21.21	1	1	2	NO	1	3
	0.85	20.87	1	1	2	NO	1	3
	0.8	20.12	1	1	NO	NO	1	NO

Table 5.10 The crack growth sequence in cyclic tests. The numbers in the table show the order of the cracking sequence.

Geometry	σ_{max}/σ_c	σ_{max} [Mpa]	External Wing Crack	Internal Wing Crack	External Shear Crack	Internal Shear Crack	Coalescence	Failure
45-a-0	0.9	26.17	1	1	2	NO	1	3
	0.85	24.97	1	1	2	NO	1	3
	0.8	23.37	1	1	2	NO	1	3
60-a-0	0.9	29.01	1	1	2	NO	1	3
	0.85	27.23	1	1	3	NO	2	4
	0.8	24.01	1	1	3	NO	2	4
30-a-a	0.9	21.59	1	NO	2	1	1	3
	0.85	19.85	1	NO	2	1	1	3
	0.8	19.58	1	NO	2	1	1	3
45-a-a	0.9	26.19	1	1	2	3	3	4
	0.85	24.86	1	1	2	1	1	3
	0.8	22.97	1	1	2	2	3	4
60-a-a	0.9	30.52	1	1	2	2	2	3
	0.85	29.31	1	1	3	2	2	4
	0.8	28.08	1	1	2	2	3	4
30-a-2a	0.9	22.02	1	1	3	2	2	4
	0.85	20.84	1	1	3	2	2	4
	0.8	20.22	1	2	5	3	4	6
45-a-2a	0.9	24.36	1	NO	3	2	2	4
	0.85	23.42	1	1	3	2	2	4
	0.8	22.06	1	1	3	2	2	NO
60-a-2a	0.9	30.76	1	1	3	2	3	4
	0.85	28.96	1	1	3	2	2	4
	0.8	28.14	1	1	2	2	2	3
60-a-3a	0.9	29.85	1	1	3	2	2	4
	0.85	28.69	1	1	2	2	2	3
	0.8	27.14	1	1	3	2	2	4
30-2a-0	0.9	28.05	1	1	1	NO	2	3
	0.85	26.18	1	1	3	NO	2	4
	0.8	25.02	1	1	3	NO	2	NO
45-2a-0	0.9	33.73	1	1	3	2	1	4
	0.85	31.84	1	1	2	NO	1	3
	0.8	30.08	1	1	NO	NO	2	NO
60-2a-0	0.9	35.58	1	1	2	NO	3	4
	0.85	33.84	1	1	2	3	2	4
	0.8	32.03	1	1	2	NO	2	NO
30-2a-a	0.9	31.02	1	1	3	2	2	4
	0.85	30.08	1	1	2	2	3	4
	0.8	28.63	1	1	2	2	NO	NO
45-2a-a	0.9	35	1	1	2	2	2	3
	0.85	33	1	1	2	2	2	3
	0.8	31.26	1	1	2	3	3	NO

Table 5.10 (continued)

Geometry	σ_{max}/σ_c	σ_{max} [Mpa]	External Wing Crack	Internal Wing Crack	External Shear Crack	Internal Shear Crack	Coalescence	Failure
60-2a-a	0.9	37.08	1	1	3	2	1	4
	0.85	35.82	1	1	2	2	1	3
	0.8	33.82	1	1	NO	3	2	NO
30-2a-2a	0.9	22.28	1	1	3	2	2	4
	0.85	21.76	1	1	2	1	1	3
	0.8	20.36	1	1	NO	NO	NO	NO
45-2a-2a	0.9	26.4	1	1	3	2	3	4
	0.85	24.42	1	1	3	2	3	4
	0.8	22.86	1	1	4	2	3	5
60-2a-2a	0.9	27.94	1	NO	2	NO	1	3
	0.85	26.85	1	NO	3	2	1	4
	0.8	25.51	1	NO	2	2	1	3
30-2a-3a	0.9	25.39	1	1	3	2	2	4
	0.85	24.04	1	1	3	2	2	4
	0.8	23.06	1	1	NO	NO	NO	NO
45-2a-3a	0.9	28.61	1	1	4	2	3	5
	0.85	27.46	1	1	3	2	2	4
	0.8	25.7	1	1	3	2	3	NO
60-2a-3a	0.9	35.83	1	1	3	2	2	4
	0.85	33.95	1	1	4	2	3	5
	0.8	31.96	1	1	3	2	2	4

Table 5.10 (continued)

Chapter 6. Summary and Conclusions

The present research focuses on the coalescence of pre-existing flaws in rock-like material under cyclic loading. Prismatic specimens of molded gypsum are prepared and tested in uniaxial monotonic compression and cyclic compression. Wing cracks and secondary cracks are produced by monotonic compression and fatigue cracks are produced by cyclic compression. A brief summary of the experimental results is presented in the following.

6.1 General results

1) Both monotonic and cyclic tests have a similar wing crack initiation position, wing crack initiation angle, cracking sequence and coalescence type.
2) The wing crack initiation position differs for the different flaw inclination angles. More than half of 30° flaw inclination specimens show that the wing crack initiation is near the tip of the flaw. At higher flaw inclination angle, the wing crack initiates at the tip of the flaw.
3) For the overlapping geometry, the wing crack initiation angles are influenced by the degree of overlapping as well as the flaw inclination angle. However, for the non-overlapping geometry the wing crack initiation angles mostly depend on the flaw inclination angle.
4) Observed coalescence types can be divided into 6 classes; Type I, II, III, IV, V, and VI where Type III coalescences is subdivided into 2 classes and Type IV coalescences into 3 classes. For coplanar geometry specimens, coalescence occurs due to the internal shear cracks. For non-coplanar geometry specimens, coalescence occurs through combinations of internal shear cracks, internal wing cracks and tension cracks. Type V and VI coalescence are new observations from this study.
5) Secondary cracks are observed in both monotonic and cyclic test. Secondary cracks initiate at the tips of the flaws and propagate in the coplanar direction of the flaw or in a horizontal direction.
6) Contrary to monotonic tests, fatigue cracks appear in cyclic tests. Depending on the flaw geometry, two types of fatigue crack initiation directions are observed. In coplanar and

1) non-overlapping geometry, horizontal fatigue cracks are observed. In overlapping geometry, coplanar fatigue cracks occur.
2) As the flaw inclination angle increases and maximum applied stresses (σ_{max}) decrease, the fatigue life increases.

6.2 Recommendations for further research

1) All the experiments which have been conducted so far have the same specimen size and flaw length. Thus scale effects on coalescence have not been fully investigated.
2) Most experiments have been carried out under uniaxial conditions. However, rock is usually subjected to a triaxial stress state in the ground. Thus confinement or constrainment effects on coalescence have not studied.
3) In the experiments, 0.5Hz frequency is used in the cyclic tests. Thus the influence of different frequencies was not investigated.
4) Usually the cracking process is very fast, so the 30 fps video camera may not be good enough to catch the cracking process. Thus a high-speed video camera is needed.
5) The cracking process and coalescence patterns in cyclic tests should be simulated by a numerical model such as FROCK.

Appendix A:

Cyclic test setup

1) Turn on the computer.
2) Click the “200Kips” icon on the Desktop. The MTESTWindows program will run.
3) The Live Indication Screen or Live Screen appears as the first screen after initialization.

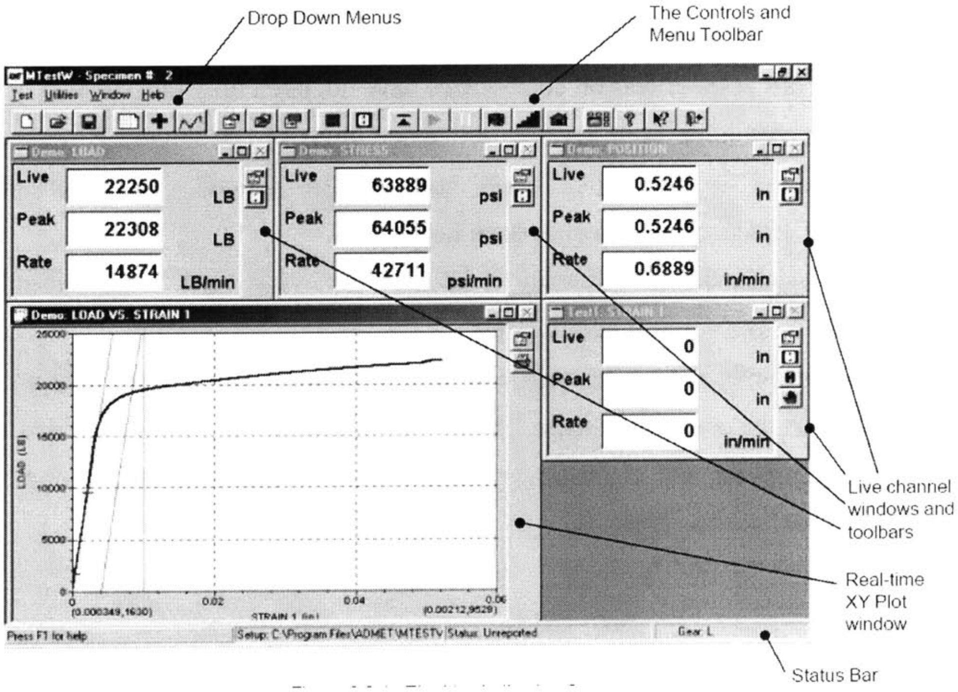

Live 22250 LB
Peak 22308 LB
Rate 14874 LB/min

Live 63889 psi
Peak 64055 psi
Rate 42711 psi/min

Live 0.5246 in
Peak 0.5246 in
Rate 0.6889 in/min

Live 0 in
Peak 0 in
Rate 0 in/min

Press F1 for help | Setup: C:\Program Files\ADMET\MTESTV | Status: Unreported | Gear: L

Figure A.1 The live indicating screen.

4) Click on test setup button.

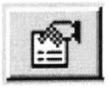

Figure A.2 Test setup button.

5) In the Test Setup dialog box, click the “Acquisition” tap. Input the value of “0” in “Sample Break:Peak Load” box. Input the value of “100” in “Threshold” box.

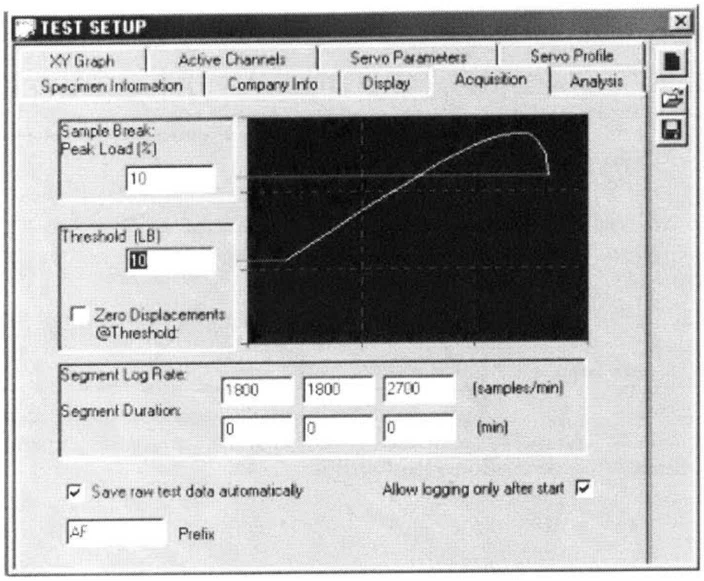

Sample Break:
Peak Load (%) 10

Threshold (LB) 10

☐ Zero Displacements @Threshold

Segment Log Rate: 1800 1800 2700 (samples/min)

Segment Duration: 0 0 0 (min)

☑ Save raw test data automatically

Allow logging only after start ☑

AF Prefix

Figure A.3 The acquisition menu.

1) In the Test Setup dialog box, click "Servo Profile" tap and "Cyclic" button. The cyclic control profile menu is given in figure A.4.

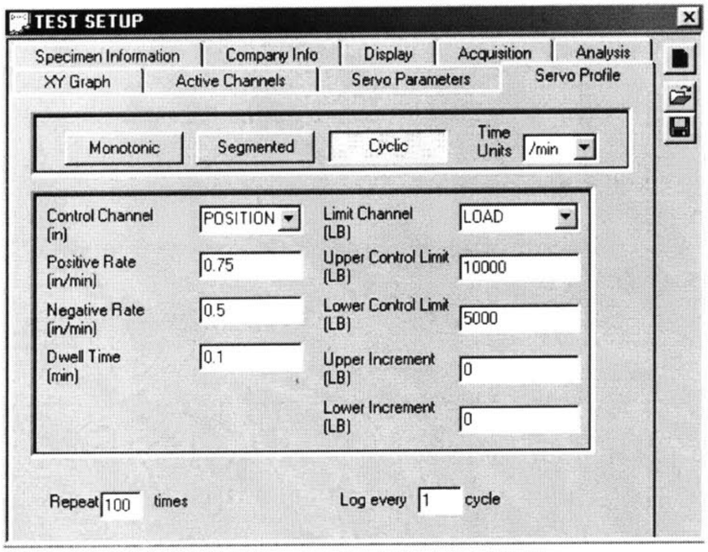

Time Units /min

Control Channel (in) POSITION

Positive Rate (in/min) 0.75

Negative Rate (in/min) 0.5

Dwell Time (min) 0.1

Limit Channel (LB) LOAD

Upper Control Limit (LB) 10000

Lower Control Limit (LB) 5000

Upper Increment (LB) 0

Lower Increment (LB) 0

Repeat 100 times

Log every 1 cycle

Figure A.4 The cyclic control profile menu.

Figure A.5 gives a graphical description of the cyclic control profile. Input the value of 3.3 in the Positive Rate and Negative Rate box for 0.5Hz frequency. Input the value of "0" in the Dwell Time, Upper Increment, and Lower Increment boxes. Upper Control Limit and

Lower Control Limit are maximum loading and minimum loading respectively.

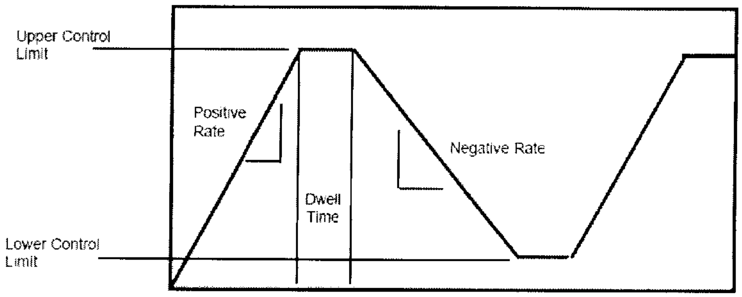

Figure A.5 Graphical description of cyclic control profile.

Appendix B:
Digital video capturing process

1) Plug the computer's FireWire cable into the DV-capable video camera, turn on the camera, and wait for the computer to detect that a Digital Video Device has been connected.

Digital Video Device

Windows can perform the same action each time you connect this device.

What do you want Windows to do?

☐ Always perform the selected action

Figure B.1 Digital video device dialog box.

Select Windows Movie Maker from the list beneath the caption "What do you want Windows to do?" in the Digital video device dialog box and then click the ok button (Figure B.1). The Movie Maker program will launch.

2) Specify a name for the video clip(s) and a location where they should be stored. (Figure B.2)

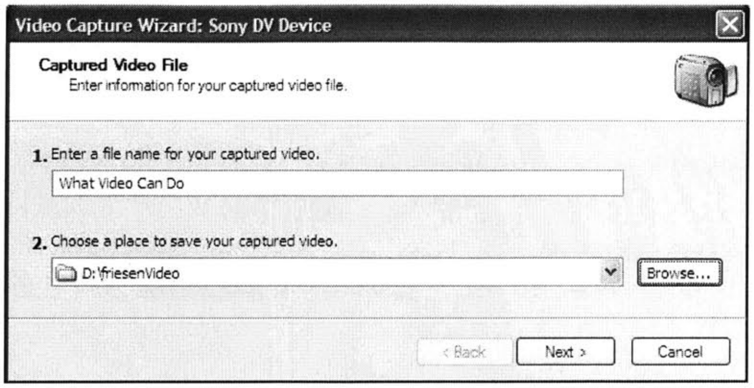

Video Capture Wizard: Sony DV Device

Captured Video File

Enter information for your captured video file.

1. Enter a file name for your captured video.

What Video Can Do

2. Choose a place to save your captured video.

D:\friesenVideo

Figure B.2 Captured video file dialog box.

3) Select the setting – Best quality for playback on my computer (Figure B.3).

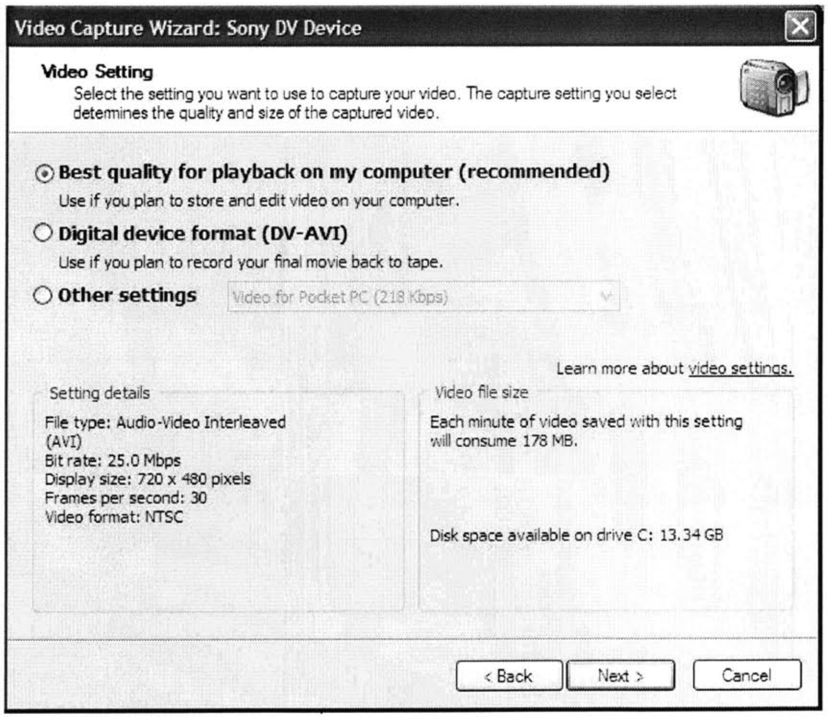

Video Capture Wizard: Sony DV Device

Video Setting

Select the setting you want to use to capture your video. The capture setting you select determines the quality and size of the captured video.

● **Best quality for playback on my computer (recommended)**
Use if you plan to store and edit video on your computer.

○ **Digital device format (DV-AVI)**
Use if you plan to record your final movie back to tape.

○ **Other settings** Video for Pocket PC (218 Kbps)

Learn more about video settings.

Setting details

File type: Audio-Video Interleaved (AVI)
Bit rate: 25.0 Mbps
Display size: 720 x 480 pixels
Frames per second: 30
Video format: NTSC

Video file size

Each minute of video saved with this setting will consume 178 MB.

Disk space available on drive C: 13.34 GB

Figure B.3 Video setting dialog box.

4) In capture method dialog box, select "Capture parts of the tape manually"

5) In order to begin the video capture, click the Start Capture button. Once you've captured a clip, click the Stop Capture button. If you have finished capturing video you can click the Finish button (Figure B.4).

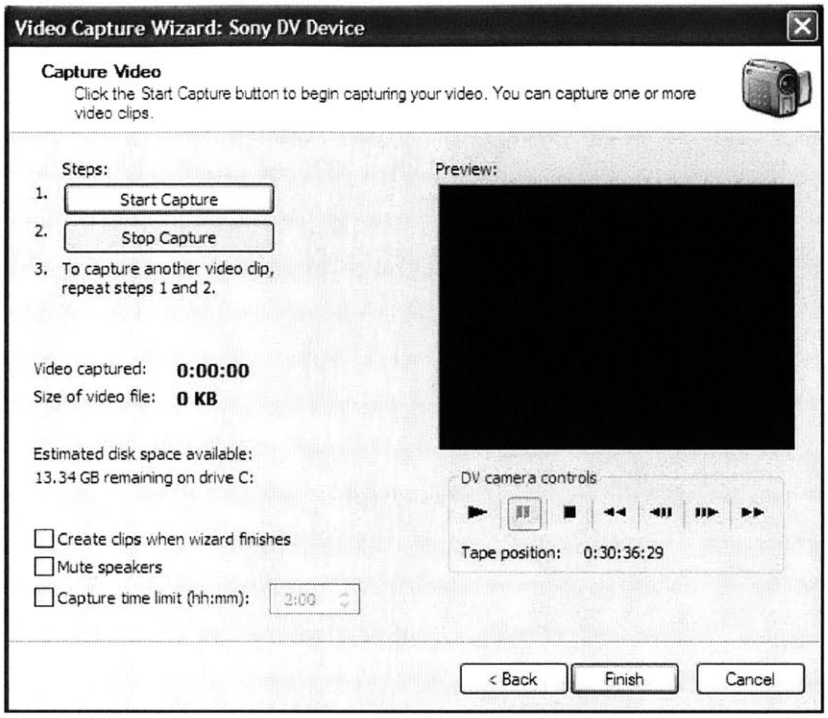

Capture Video

Click the Start Capture button to begin capturing your video. You can capture one or more video clips.

Steps:

1. Start Capture
2. Stop Capture
3. To capture another video clip, repeat steps 1 and 2.

Video captured: **0:00:00**

Size of video file: **0 KB**

Estimated disk space available:
13.34 GB remaining on drive C:

☐ Create clips when wizard finishes
☐ Mute speakers
☐ Capture time limit (hh:mm): 2:00

Tape position: 0:30:36:29

Figure B.4 Capture window dialog box.

6) DV or “digital video” is the video compression format that digital camcorder captures onto tape. The video is saved at a resolution of 720x480 pixels running at 30 frames per second. However, the digital video format has the major inconvenience of the huge file sizes. DV-AVI video takes up a lot of space. An hour tape will occupy about 13 gigabytes of hard-drive space. If one compresses the AVI files, the resolution is reduced and the quality if the picture is affected.

Appendix C:
Comparisons of the coalescence type in monotonic and cyclic tests

Geometry	Monotonic test	Cyclic test
30-0-a	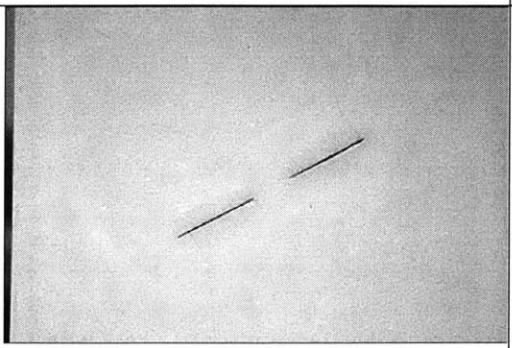 Type I coalescence occurs. (at 20.13 MPa)	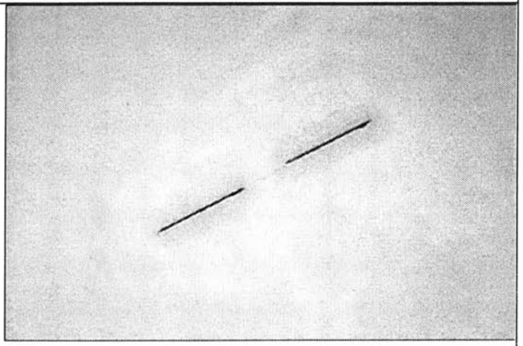 Type I coalescence occurs. (at 1 cycle, σ_{max} : 23.70 MPa)
45-0-a	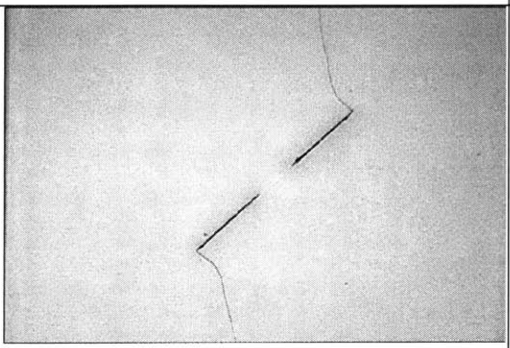 Type I coalescence occurs. (at 22.041 MPa)	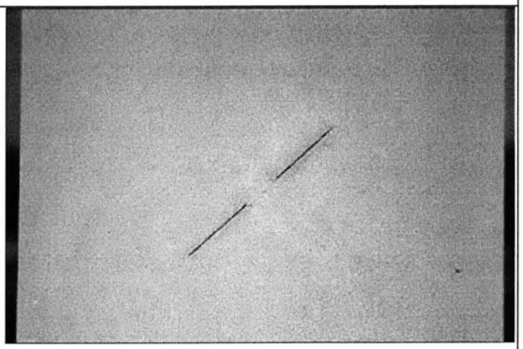 Type I coalescence occurs. (at 1 cycle, σ_{max} :22.28 MPa)
60-0-a	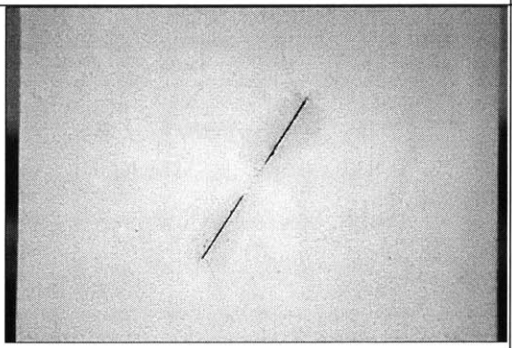 Type I coalescence occurs. (at 25.16 MPa)	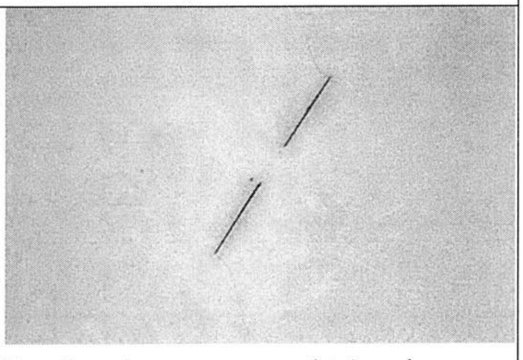 Type I coalescence occurs. (at 1 cycle, σ_{max} : 23.66 MPa)

Figure C.1 Comparisons of the coalescence type for 0-a geometry in monotonic and cyclic tests.

Geometry	Monotonic test	Cyclic test
30-0-2a	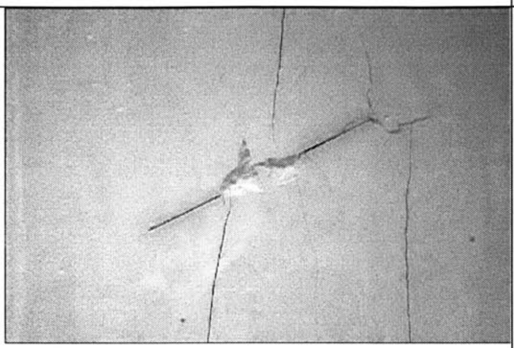 Type I coalescence occurs. (at 28.11 MPa)	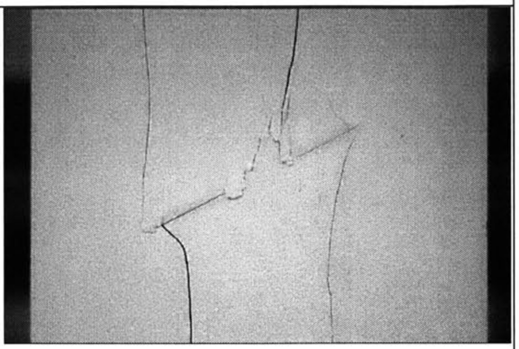 Coalescence doesn't occur. (at 349 cycles , σ_{max} :22.23 MPa)
45-0-2a	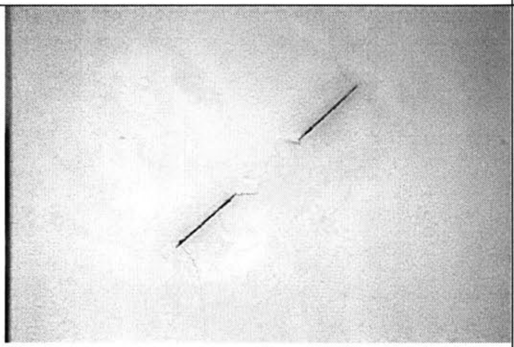 Type I coalescence occurs. (at 27.62 MPa)	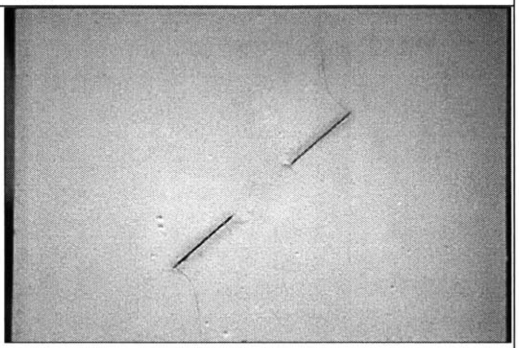 Type I coalescence occurs. (at 19 cycles, σ_{max} :22.70 MPa)
60-0-2a	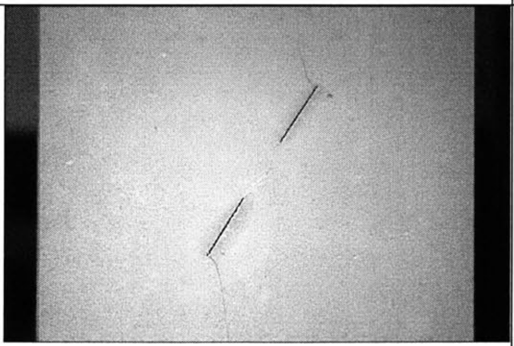 Type I coalescence occurs. (at 27.19 MPa)	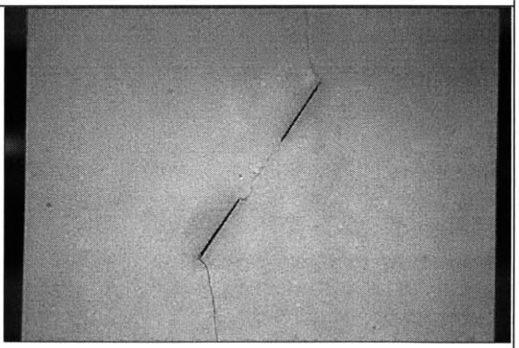 Type I coalescence occurs. (at 81 cycles, σ_{max} : 25.25 MPa)

Figure C.2 Comparisons of the coalescence type for 0-2a geometry in monotonic and cyclic tests.

Geometry	Monotonic test	Cyclic test
30-0-3a	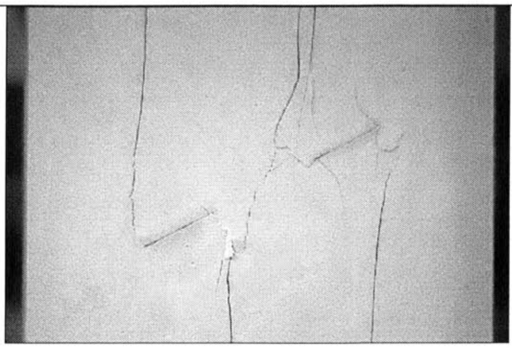 Coalescence doesn't occur. (at 27.41 MPa)	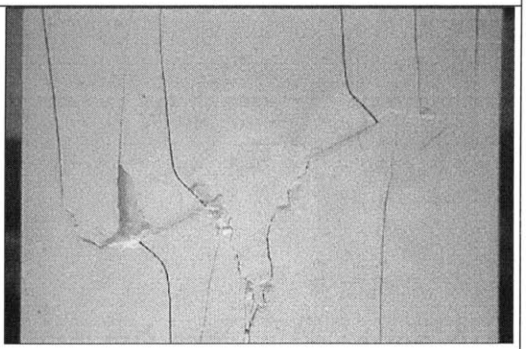 Coalescence doesn't occur. (at 688 cycles , σ_{max} :23.49 MPa)
45-0-3a	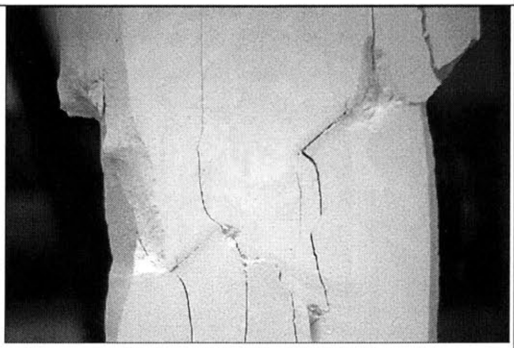 Type I coalescence doesn't occur. (at 28.69 MPa)	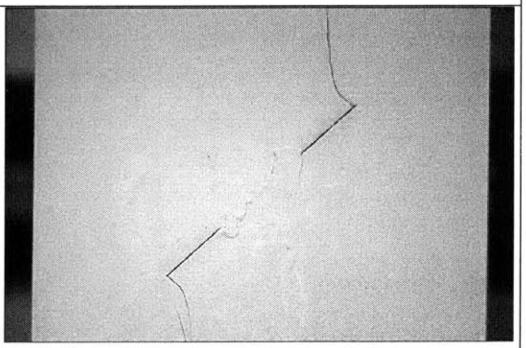 Type I coalescence occurs. (at 838 cycles, σ_{max} : 22.47 MPa)
60-0-3a	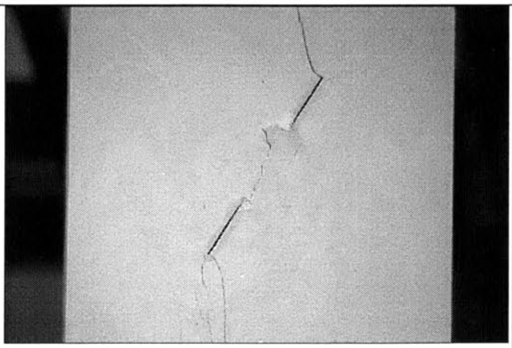 Type I coalescence occurs. (at 32.10 MPa)	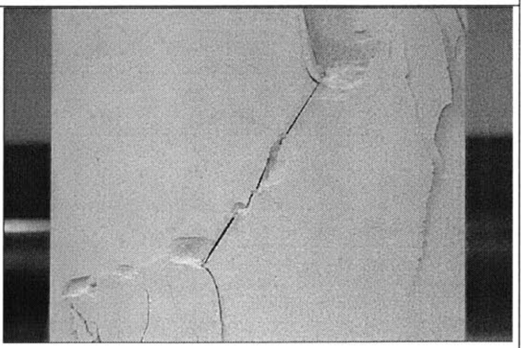 Type I coalescence occurs. (at 148 cycles, σ_{max} : 28.06 MPa)

Figure C.3 Comparisons of the coalescence type for 0-3a geometry in monotonic and cyclic tests.

Geometry	Monotonic test	Cyclic test
30-0-4a	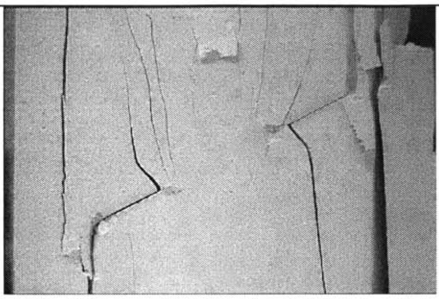 Coalescence doesn't occur. (at 29.87 MPa)	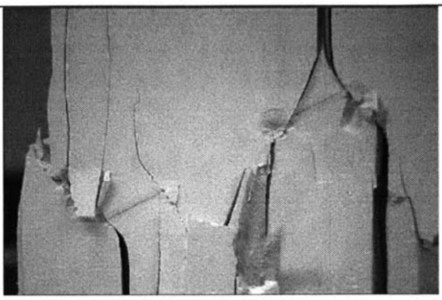 Coalescence doesn't occur. (at 29 cycles, σ_{max} :26.52 MPa)
45-0-4a	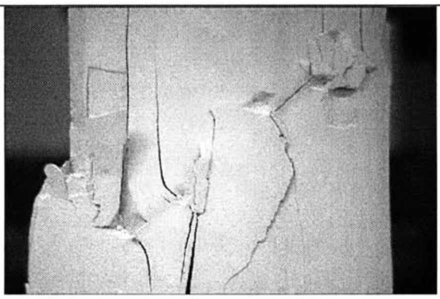 Coalescence doesn't occur. (at 33.69 MPa)	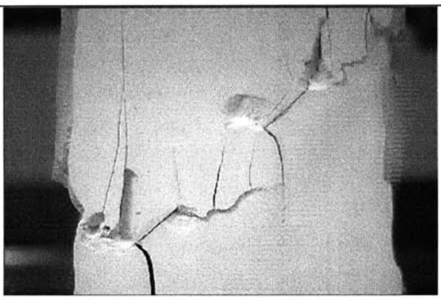 Coalescence doesn't occur. (at 40 cycles, σ_{max} :27.81 MPa)
60-0-4a	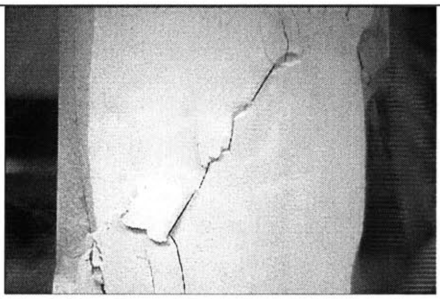 Type I coalescence occurs. (at 33.58 MPa)	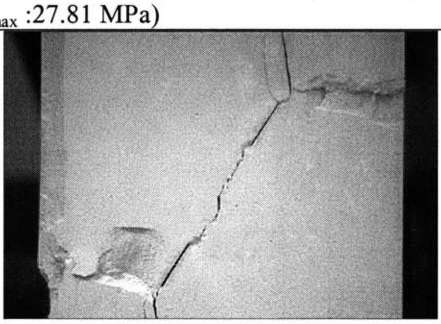 Type I coalescence occurs. (at 14 cycles ,σ_{max} : 30.41 MPa) 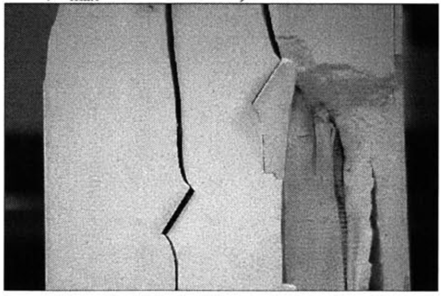 Coalescence doesn't occur. (at 292 cycles , σ_{max} :28.84 MPa)

Figure C.4 Comparisons of the coalescence type for 0-4a geometry in monotonic and cyclic tests.

Geometry	Monotonic test	Cyclic test
30-a-0	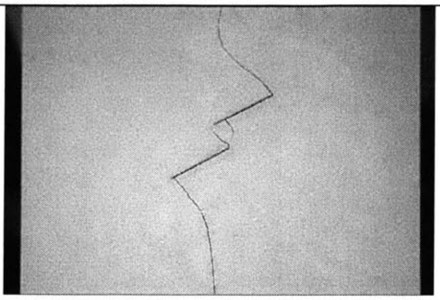 Type IV-A coalescence occurs. (at 23.74 MPa)	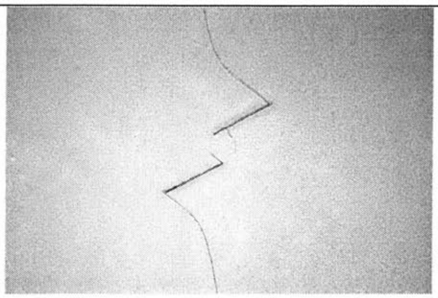 Type IV-A coalescence occurs. (at 1 cycle, σ_{max} : 21.21 MPa)
45-a-0	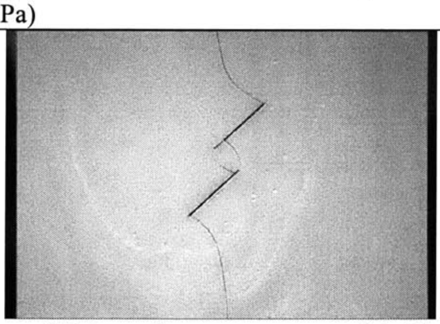 Type IV-A coalescence occurs. (at 29.42 MPa)	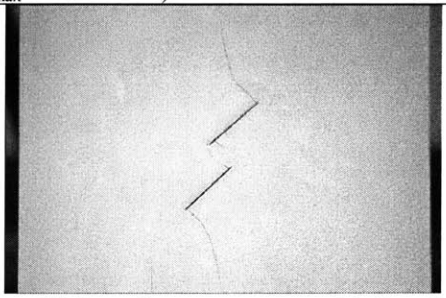 Type IV-A coalescence occurs. (at 4 cycles, σ_{max} : 26.17 MPa)
60-a-0	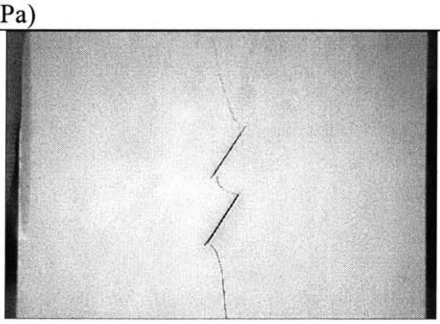 Type III-A coalescence occurs. (at 32.23 MPa) 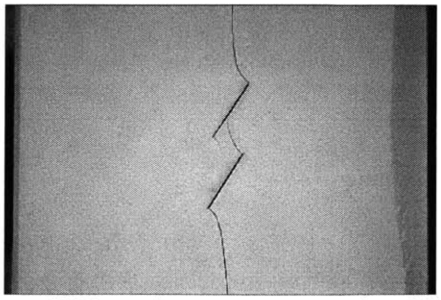 Type IV-B coalescence occurs. (at 27.04 MPa)	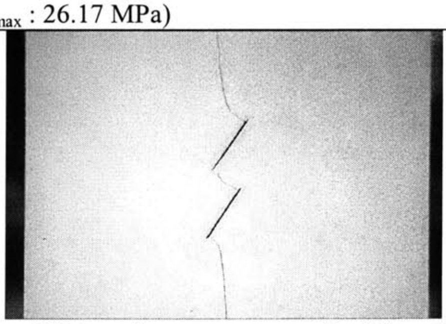 Type III-A coalescence occurs. (at 37 cycles, σ_{max} : 24.01 MPa)

Figure C.5 Comparisons of the coalescence type for a-0 geometry in monotonic and cyclic tests.

Geometry	Monotonic test	Cyclic test
30-a-a	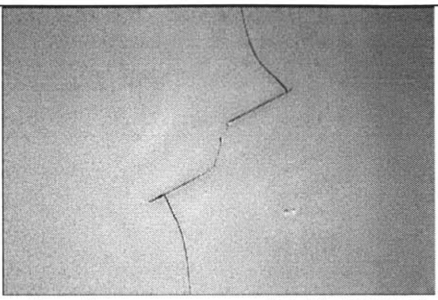 Type I coalescence occurs. (at 22.46 MPa)	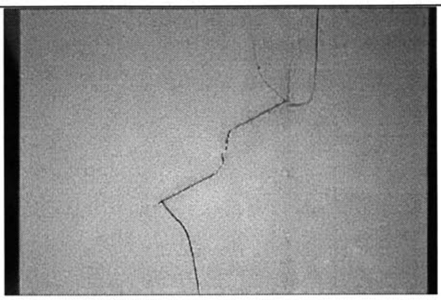 Type I coalescence occurs. (at 60 cycles, σ_{max} : 19.58 MPa)
45-a-a	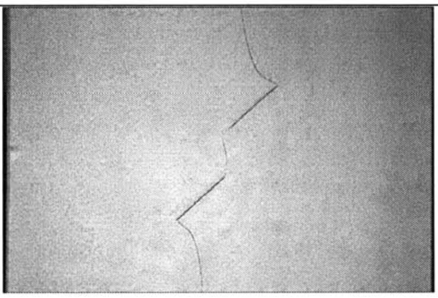 Type II coalescence occurs. (at 21.67 MPa)	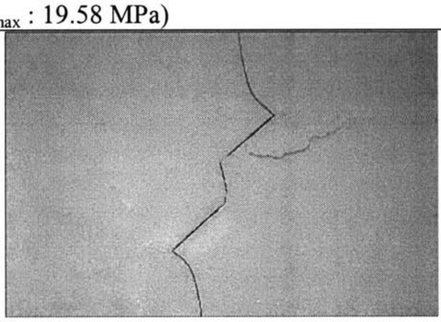 Type I coalescence occurs. (at 151 cycles, σ_{max} : 24.86 MPa)
60-a-a	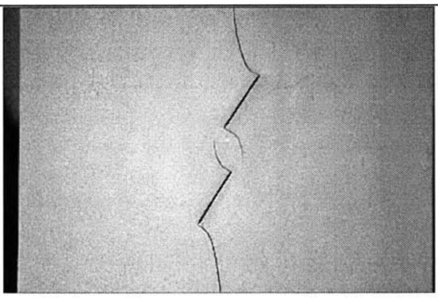 Type IV-A coalescence occurs.(at 32.85 MPa)	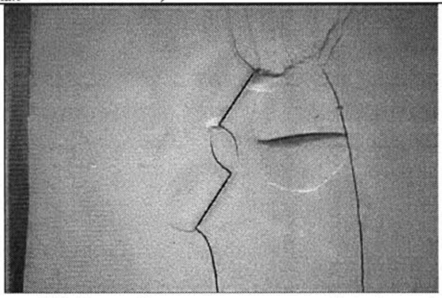 Type IV-A coalescence occurs. (at 6 cycles, σ_{max} : 30.52 MPa)
	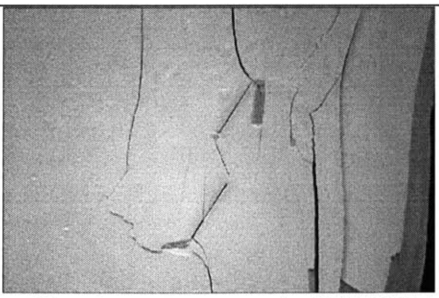 Type II coalescence occurs. (at 30.27 MPa)	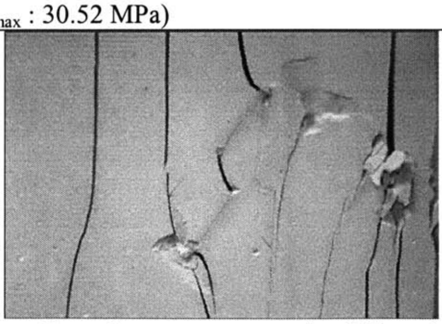 Type II coalescence occurs. (at 615 cycles, σ_{max} : 28.08 MPa)

Figure C.6 Comparisons of the coalescence type for a-a geometry in monotonic and cyclic tests.

Geometry	Monotonic test	Cyclic test
30-a-2a	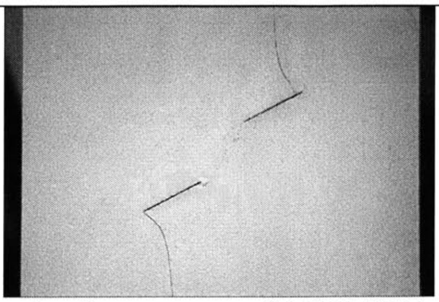 Type I coalescence occurs. (at 20.81 MPa)	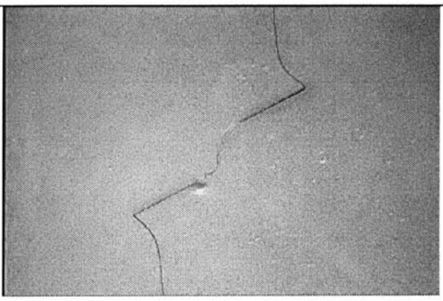 Type I coalescence occurs (at 3 cycles, σ_{max} : 22.02 MPa)
45-a-2a	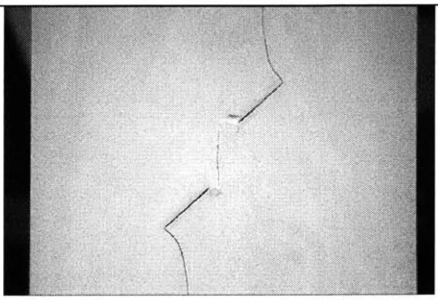 Type II coalescence occurs. (at 26.71 MPa)	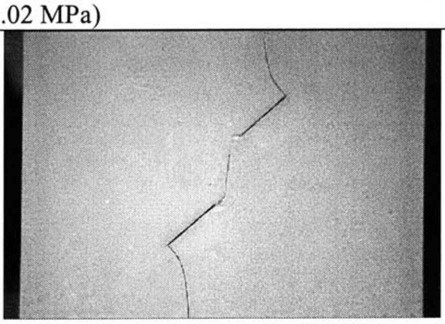 Type II coalescence occurs. (at 217 cycles, σ_{max} : 23.42 MPa)
60-a-2a	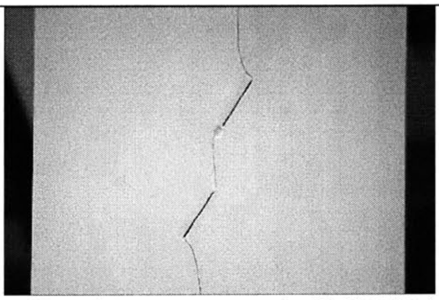 Type II coalescence occurs. (at 29.88 MPa)	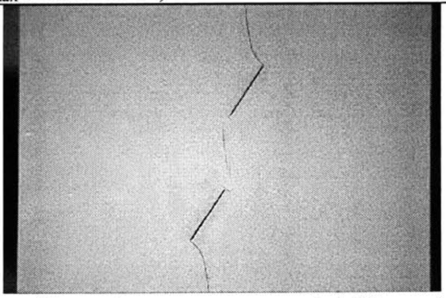 Type II coalescence occurs. (at 29 cycles, σ_{max} : 28.96 MPa)
60-a-3a	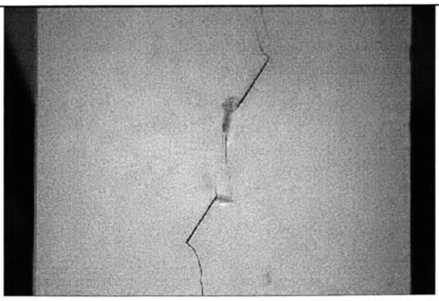 Type II coalescence occurs. (at 32.24 MPa)	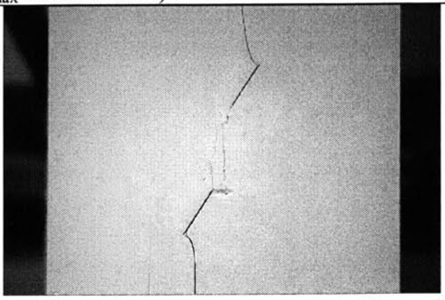 Type II coalescence occurs. (at 61 cycles, σ_{max} : 29.36 MPa)

Figure C.7 Comparisons of the coalescence type for a-2a and 60-a-3a geometries in monotonic and cyclic tests.

Geometry	Monotonic test	Cyclic test
30-2a-0	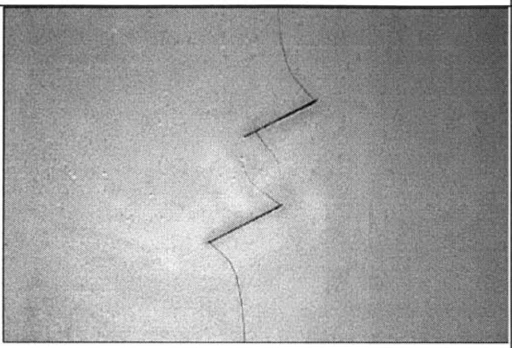 Type IV-A coalescence occurs. (at 20.16 MPa)	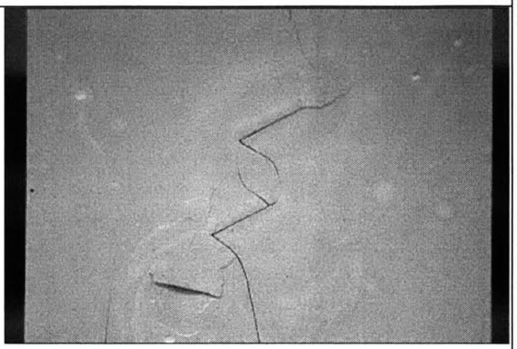 Type IV-A coalescence occurs. (at 4 cycles, σ_{max} : 28.05 MPa)
45-2a-0	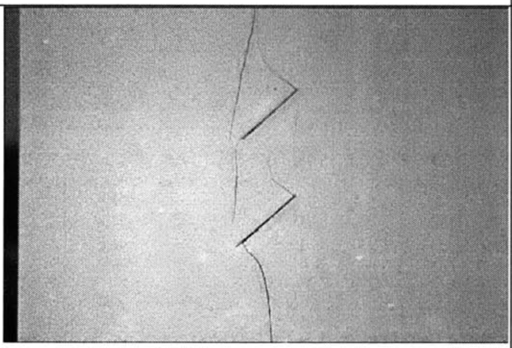 Type VII coalescence occurs. (at 33.18 MPa)	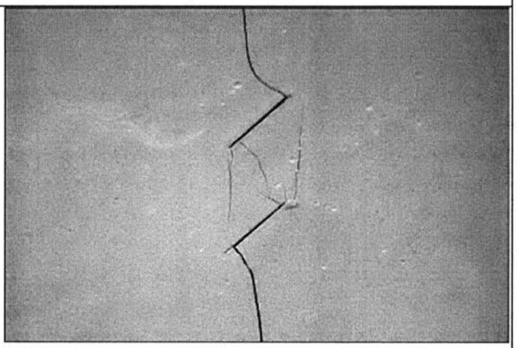 Type IV-A coalescence occurs. (at 271 cycles, σ_{max} : 33.73 MPa)
60-2a-0	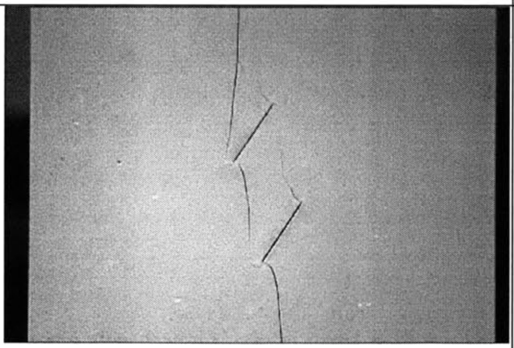 Type IV-C coalescence occurs. (at 40.77 MPa)	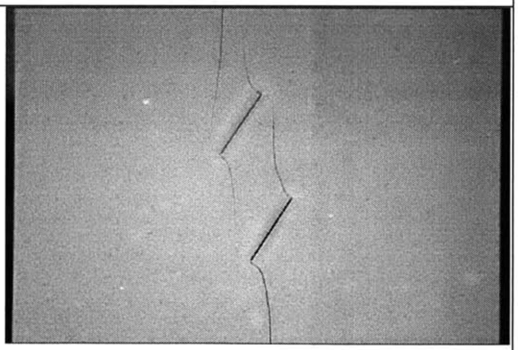 Type IV-C coalescence occurs. (at 25 cycles, σ_{max} : 35.58 MPa)

Figure C.8 Comparisons of the coalescence type for 2a-0 geometry in monotonic and cyclic tests.

Geometry	Monotonic test	Cyclic test
30-2a-a	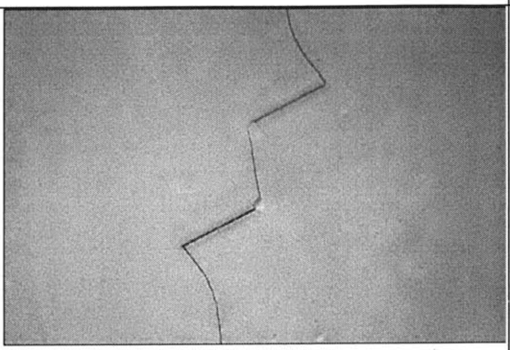 Type II coalescence occurs. (at 22.05 MPa)	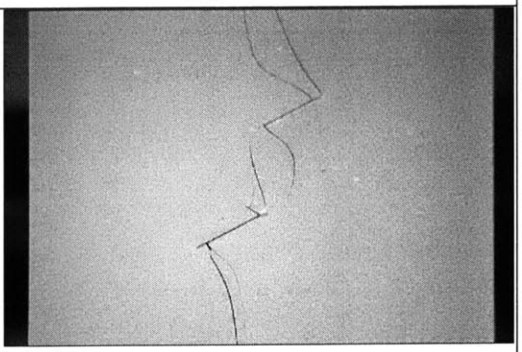 Type II coalescence occurs. (at 2 cycles, σ_{max} : 31.02 MPa)
45-2a-a	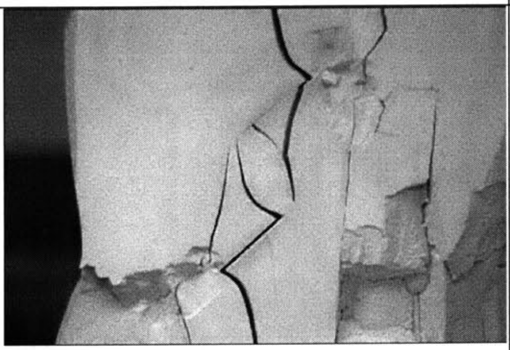 Type IV-A coalescence occurs. (at 35.81 MPa)	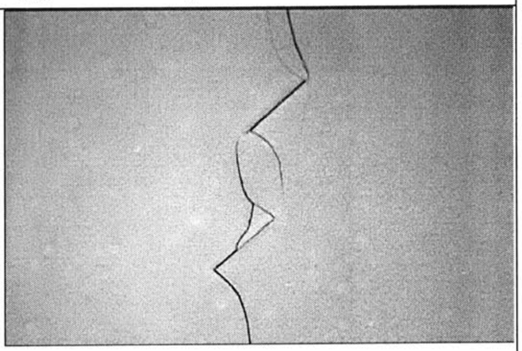 Type IV-A coalescence occurs. (at 61 cycles, σ_{max} :3 5.00 MPa)
60-2a-a	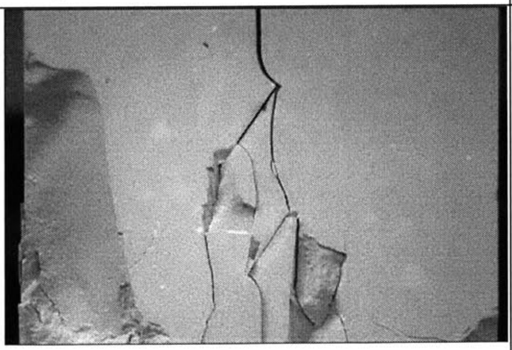 Type VI coalescence occurs. (at 37.98 MPa)	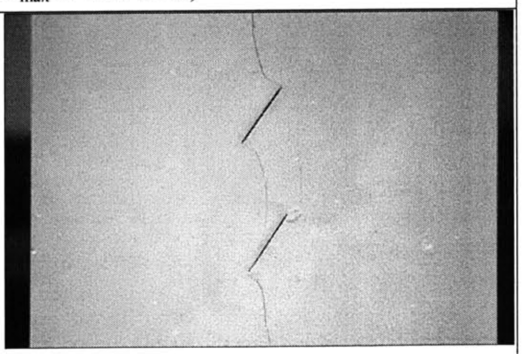 Type VI coalescence occurs. (at 104 cycles, σ_{max} : 33.82 MPa)

Figure C.9 Comparisons of the coalescence type for 2a-a geometry in monotonic and cyclic tests.

Geometry	Monotonic test	Cyclic test
30-2a-2a	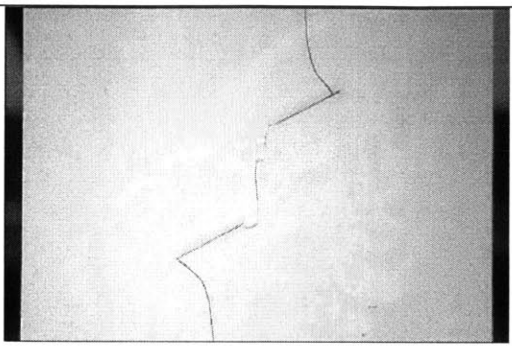 Type II coalescence occurs. (at 25.08 MPa)	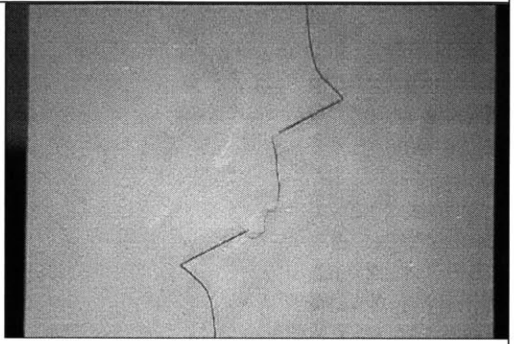 Type II coalescence occurs. (at 2 cycles (σ_{max} : 22.28 MPa)
45-2a-2a	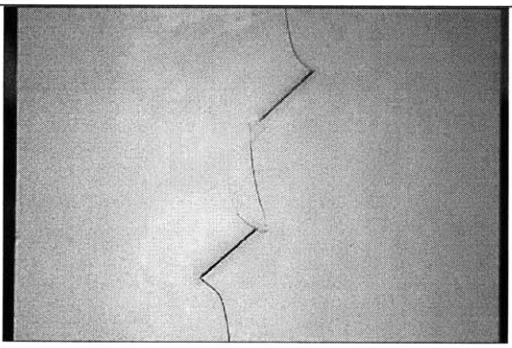 Type II coalescence occurs. (at 29.41 MPa)	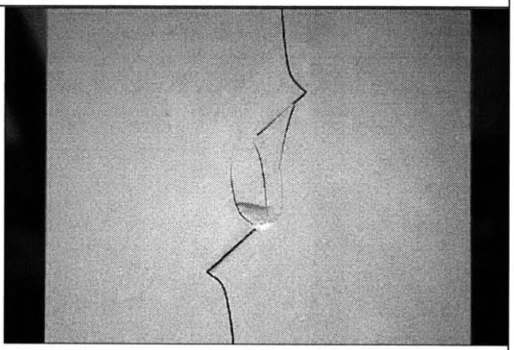 Type II coalescence occurs. (at 1300 cycles, σ_{max} :22.86 MPa)
60-2a-2a	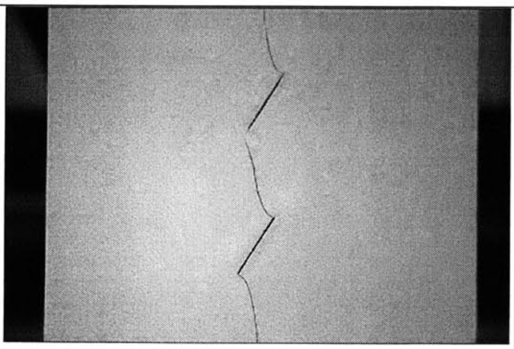 Type III-A coalescence occurs. (at 35.77 MPa)	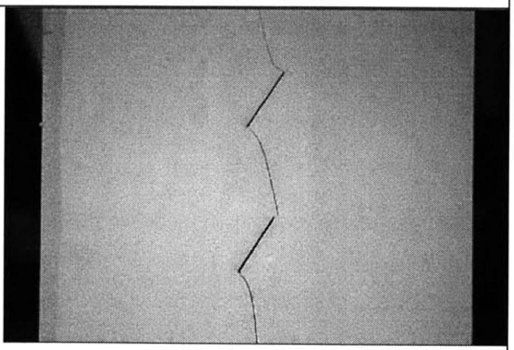 Type III-A coalescence occurs. (at 3 cycles, σ_{max} : 27.94 MPa)

Figure C.10 Comparisons of the coalescence type for 2a-2a geometry in monotonic and cyclic tests.

Geometry	Monotonic test	Cyclic test
30-2a-3a	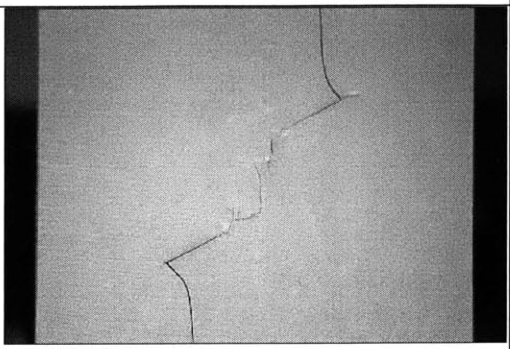 Type II coalescence occurs. (at 28.32 MPa)	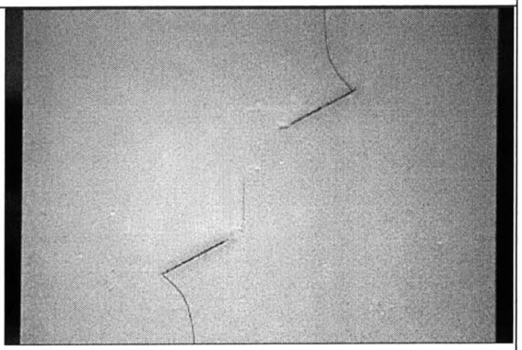 Type II coalescence occurs. (at 202 cycles, σ_{max} : 24.04 MPa)
45-2a-3a	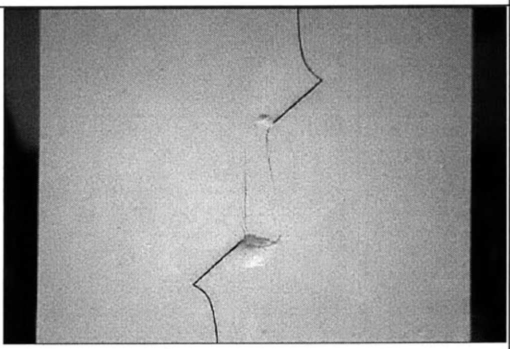 Type II coalescence occurs. (at 31.431 MPa)	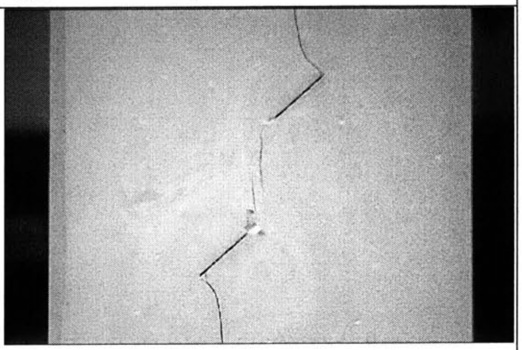 Type II coalescence occurs. (at 845 cycles, σ_{max} : 27.46 MPa)
60-2a-3a	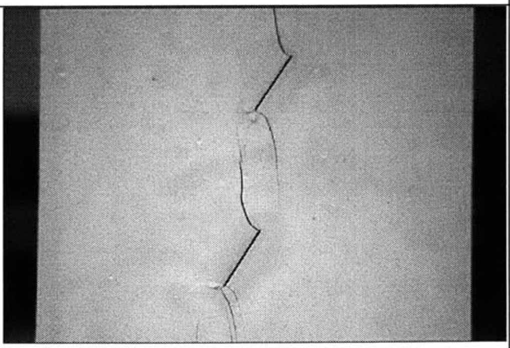 Type III-B coalescence occurs. (at 36.768 MPa)	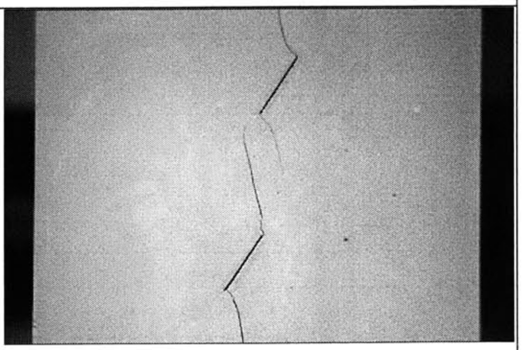 Type III-B coalescence occurs. (at 6 cycles, σ_{max} : 35.83 MPa)

Figure C.11 Comparisons of the coalescence type for 2a-3a geometry in monotonic and cyclic tests.

Appendix D:
Crack growth sequence

D.1 Crack growth sequence in monotonic tests

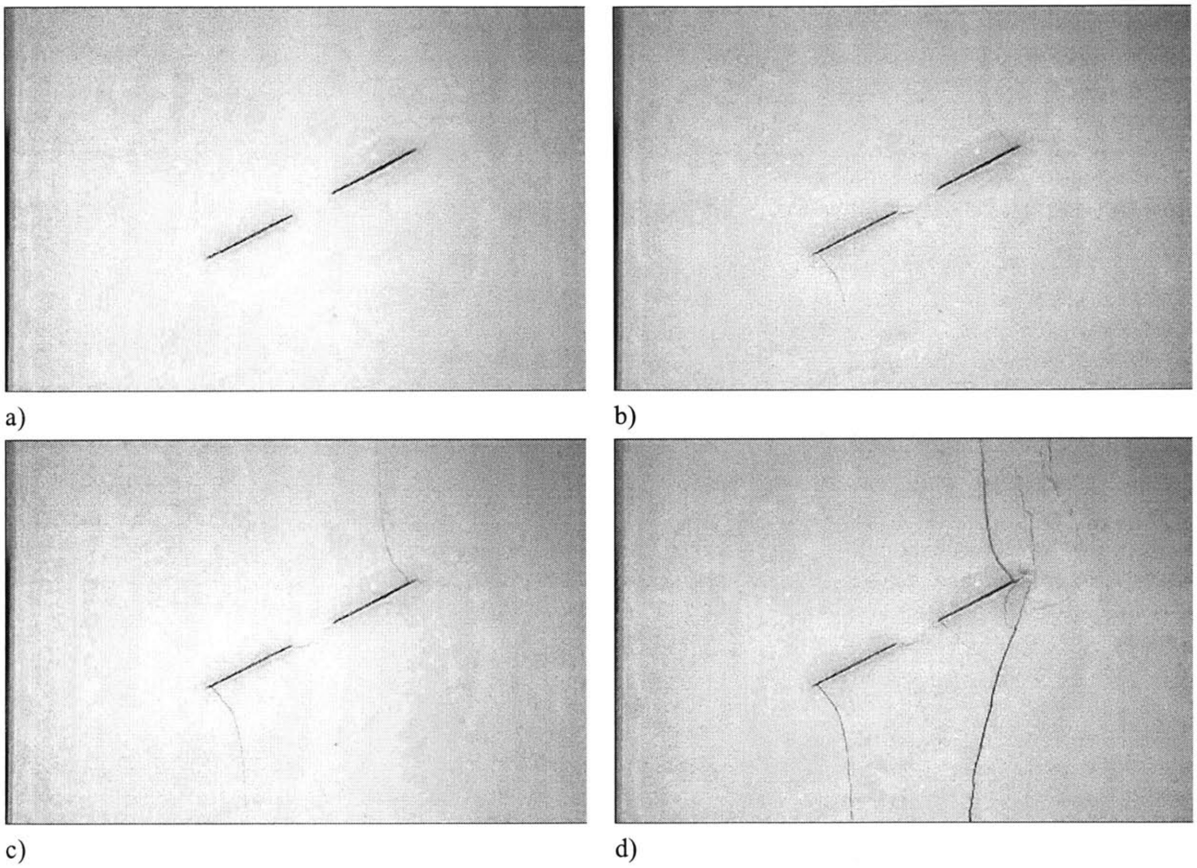

Figure D.1 Cracking sequence of 30-0-a geometry in monotonic test; a) Initial configuration b) External wing cracks initiate near the external tip of the flaws. Coalescence occurs due to the internal shear crack (at 19.84MPa). c) External shear cracks occur at the external tip of the upper flaw (at 21.18 MPa). c) Failure occurs (at 21.99 MPa).

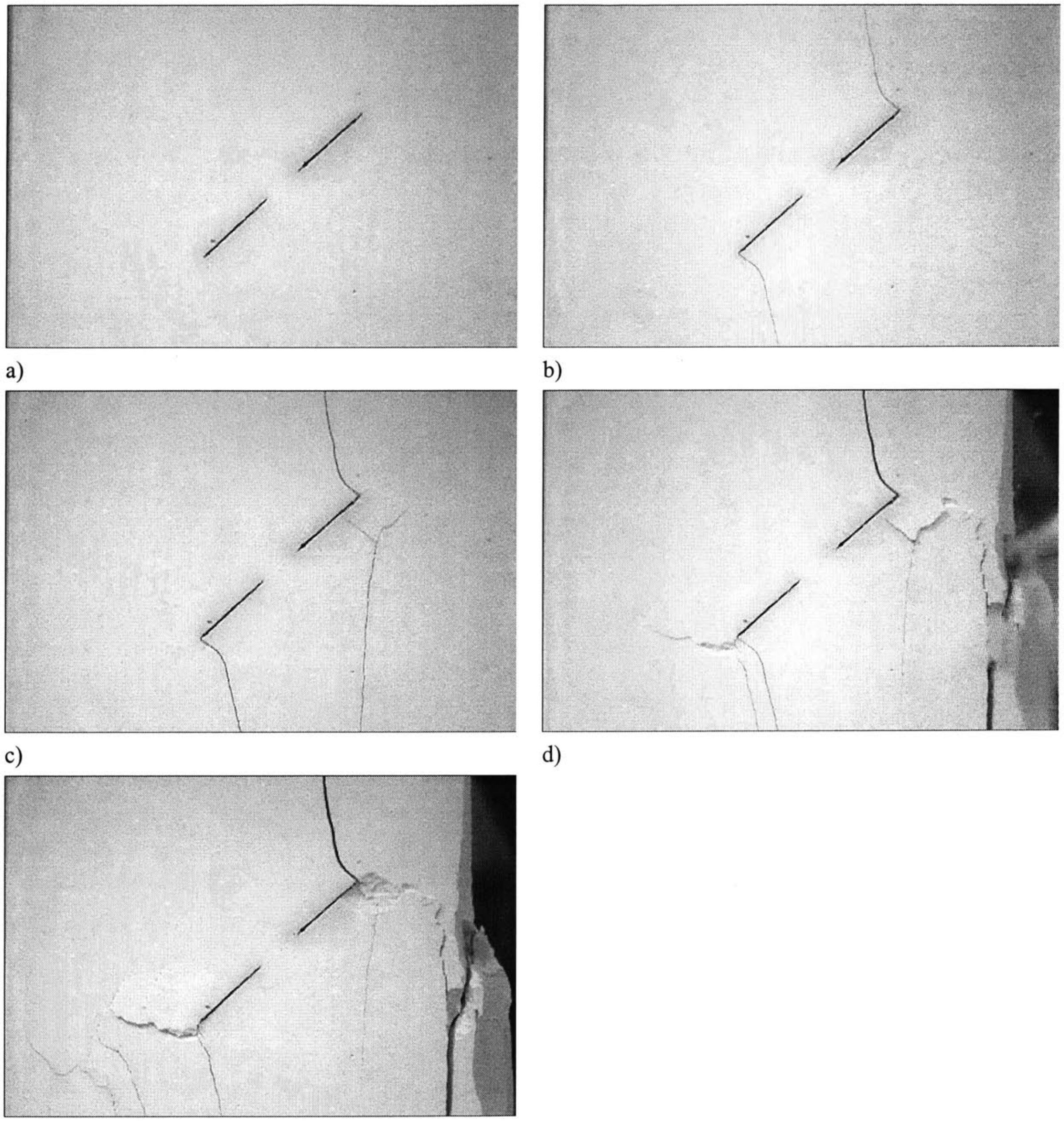

a)

b)

c)

d)

Figure D.2 Cracking sequence of 45-0-a geometry in monotonic test; a) Initial configuration b) External wing cracks initiate at the external tip of the flaws. Coalescence occurs due to the internal shear crack (at 17.47 MPa). c) Another tension crack accompanied by shear cracks occurs around the external tip of the upper flaw (at 22.12 MPa). d) Vertical splitting occurs. Another tension crack accompanied by shear cracks (or surface cracks) occurs around the external tip of the lower flaw (at 22.31 MPa). e) Failure occurs (at 22.46 MPa).

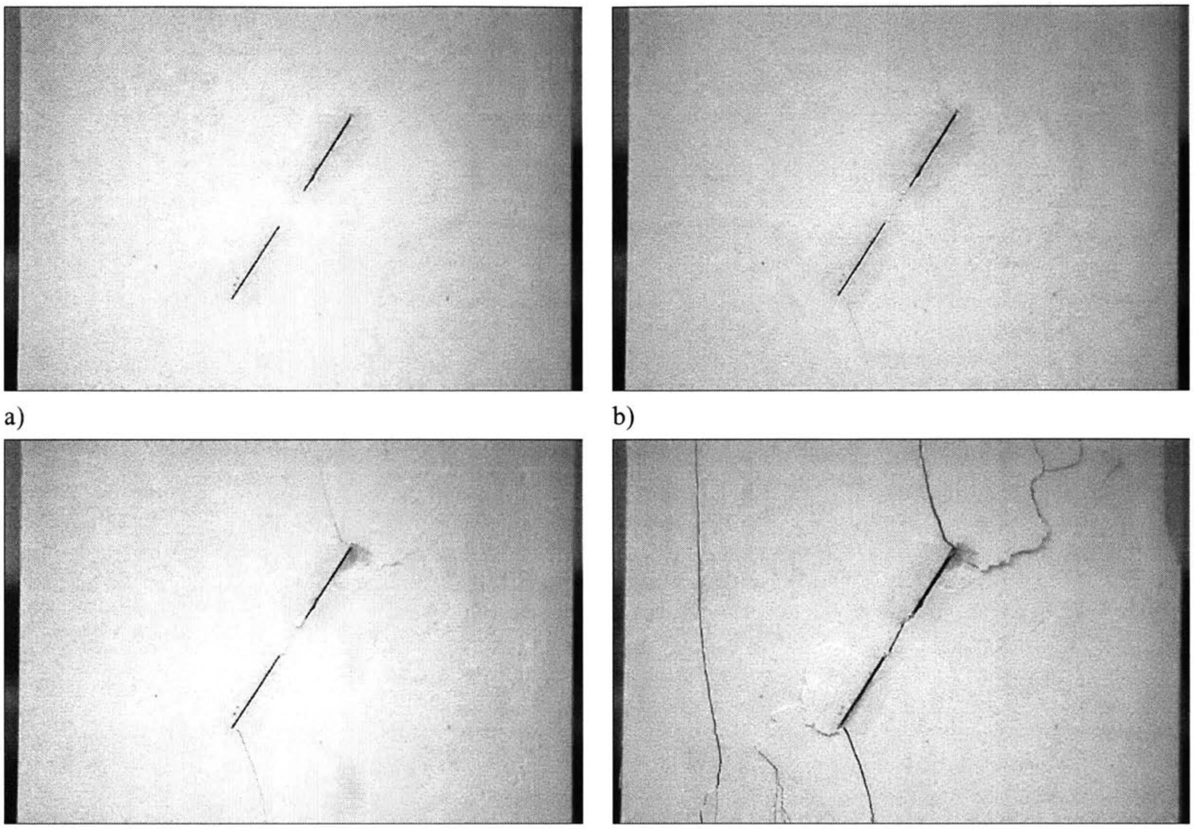

a)

b)

c)

d)

Figure D.3 Cracking sequence of 60-0-a geometry in monotonic test; a) Initial configuration b) External wing cracks initiate at the external tip of the flaws. Coalescence occurs due to the internal shear crack (at 23.15 MPa). c) Shear cracks (or surface cracks) develop at the external tip of the upper flaw (at 25.15 MPa). d) Failure occurs (at 25.59 MPa).

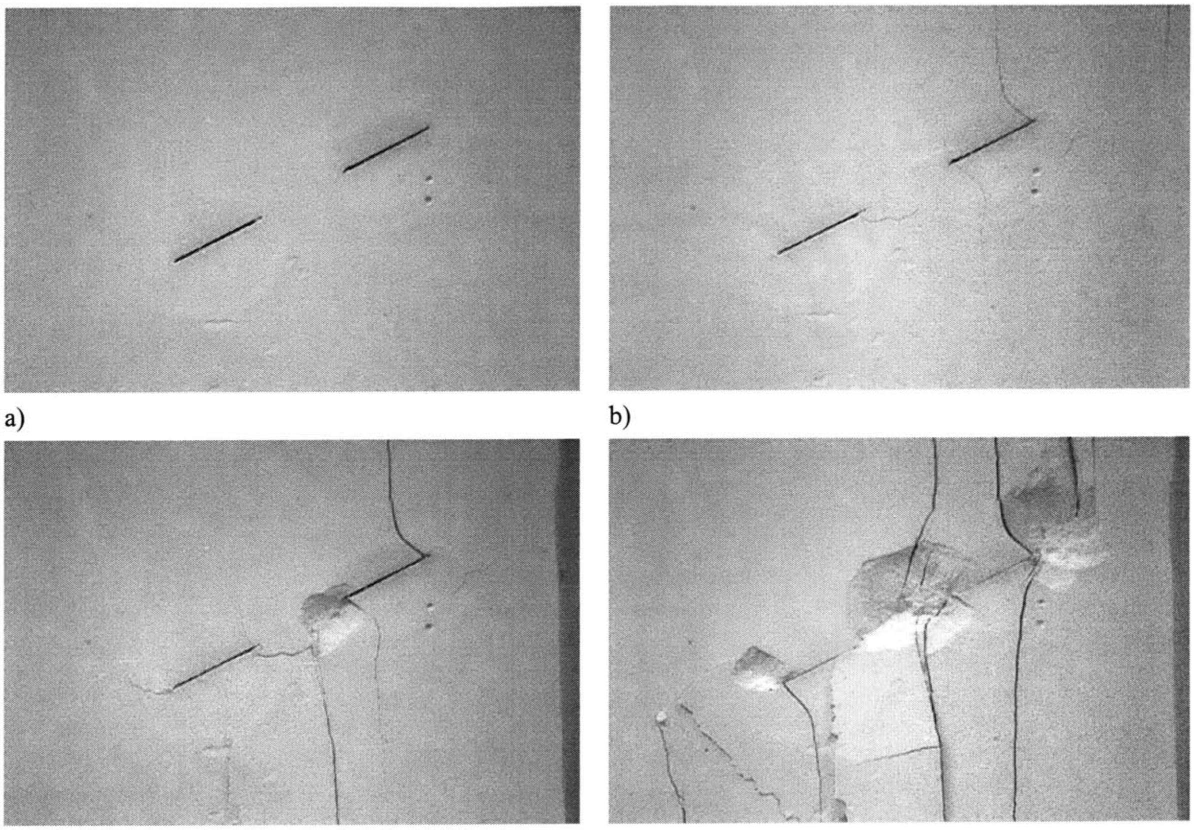

a) b) c) d)

Figure D.4 Cracking sequence of 30-0-2a geometry in monotonic test; a) Initial configuration b) External wing cracks initiate near the external tip of the flaws (at 22.26 MPa). Coalescence initiate near the internal tip of the flaws. External shear cracks occur at the external tip of the upper flaw (at 24.12 MPa). Internal wing cracks initiate near the internal tip of the flaws (at 27.33 MPa). c) Coalescence completed (at 28.75 MPa). d) Failure occurs (at 28.76 MPa)

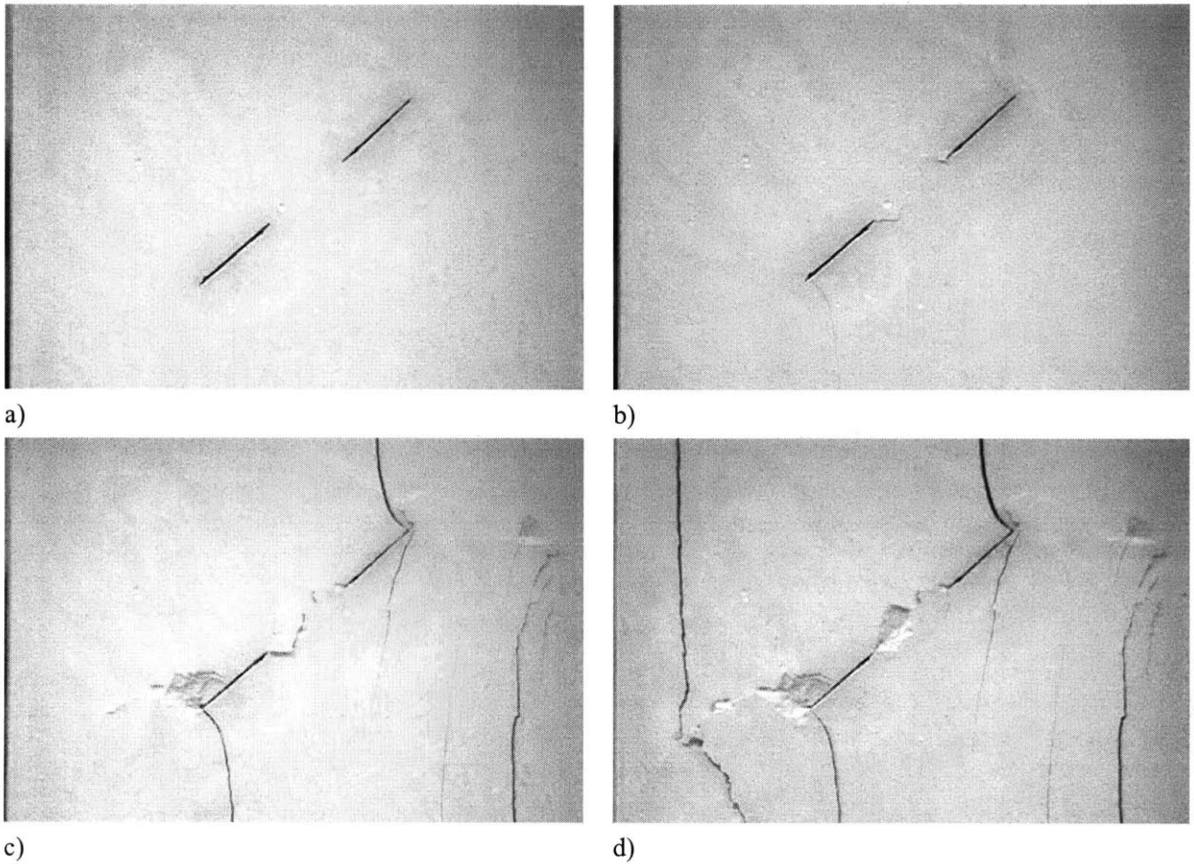

Figure D.5 Cracking sequence of 45-0-2a geometry in monotonic test; a) Initial configuration b) External wing cracks initiate. Coalescence occurs due to the internal shear crack (at 27. 34 MPa). c) External shear cracks occur at the external tips of the flaw (at 27.62 MPa). d) Failure occurs (29.51 MPa).

.

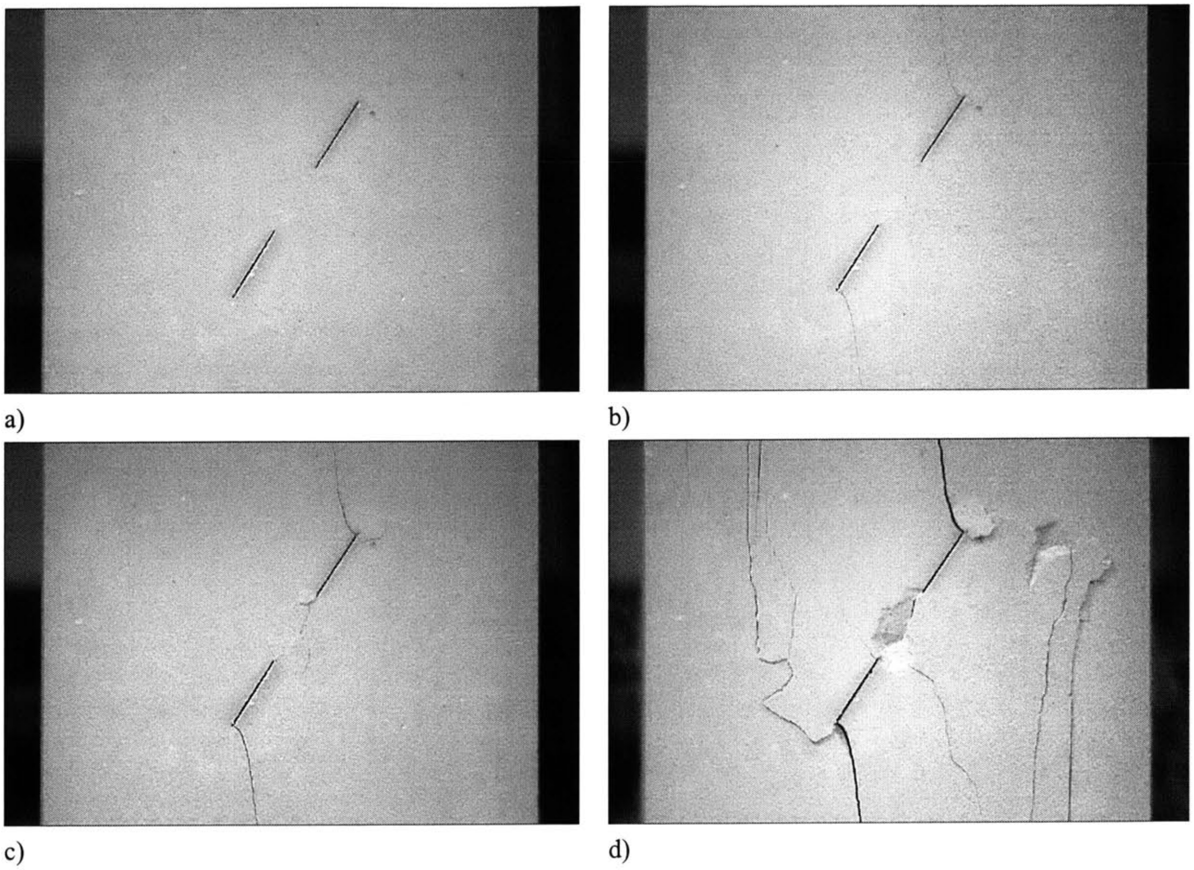

Figure D.6 Cracking sequence of 60-0-2a geometry in monotonic test; a) Initial configuration b) External wing cracks initiate at the external tip of the flaws. Coalescence occurs at the internal tips of the flaws (at 27.19 MPa). c) Shear cracks occur at the external tip of the flaws (at 27.03 MPa). d) Failure occurs (at 29.34 MPa).

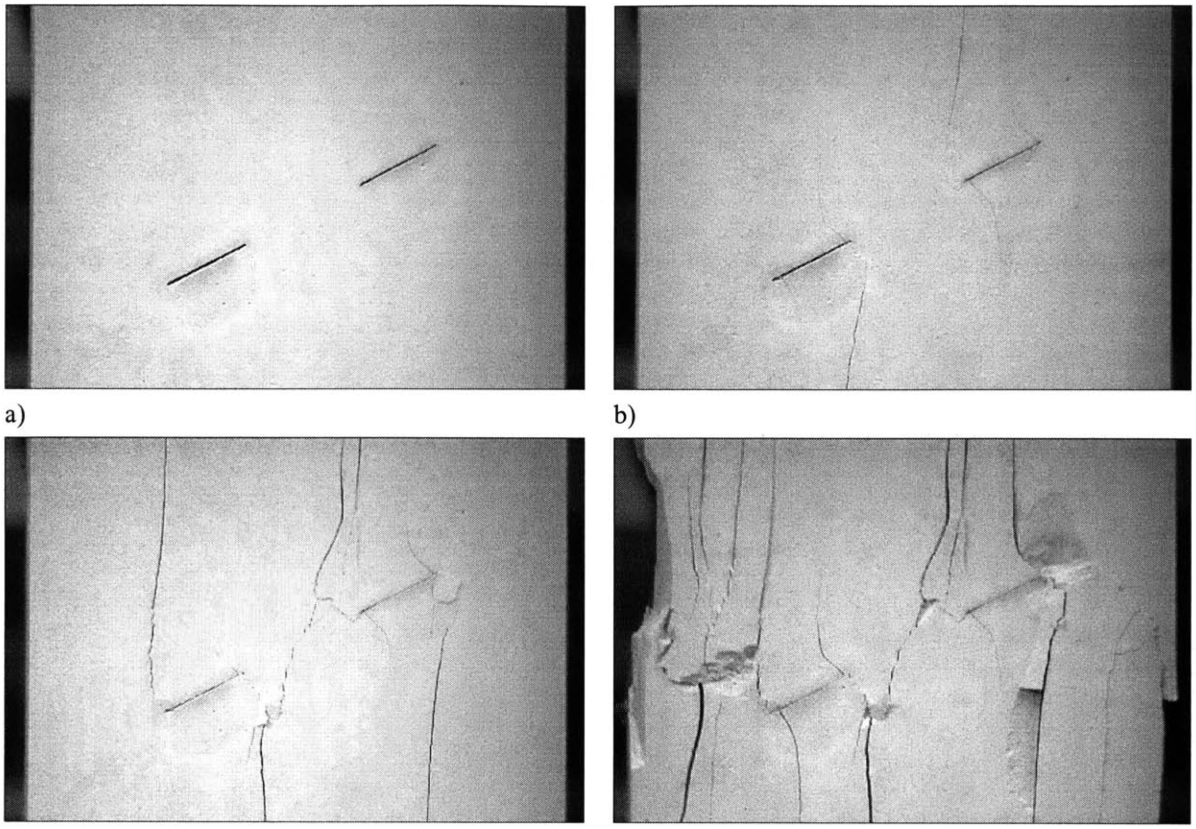

a)

b)

c)

d)

Figure D.7 Cracking sequence of 30-0-3a geometry in monotonic test; a) Initial configuration b) External wing cracks initiate at the external tips of the flaws (at 25.91 MPa). Internal wing cracks initiate near the internal tips of the flaws (at 27.25 MPa). Internal shear cracks occur around the internal tip of the upper flaw (at 27.38 MPa). c) Another tension cracks occur between internal tips of the flaws (at 27.42 MPa). d) Failure occurs. Coalescence doesn't occur (at 27.81 MPa).

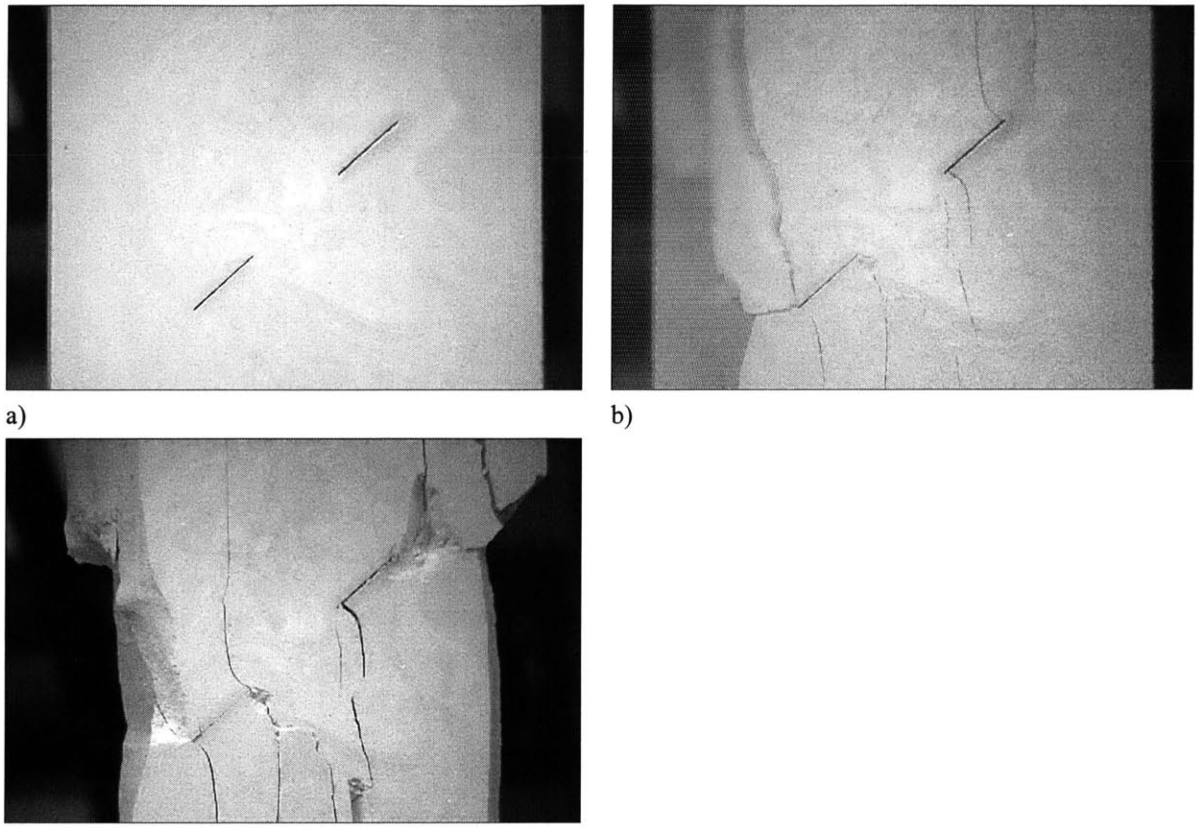

a) b)

c)

Figure D.8 Cracking sequence of 45-0-3a geometry in monotonic test; a) Initial configuration b) External wing cracks initiate at the external tips of the flaws (at 26.55 MPa). Internal wing cracks initiate at the internal tips of the flaws (at 28.64 MPa). c) Failure occurs (at 28.69 MPa). Coalescence doesn't occur.

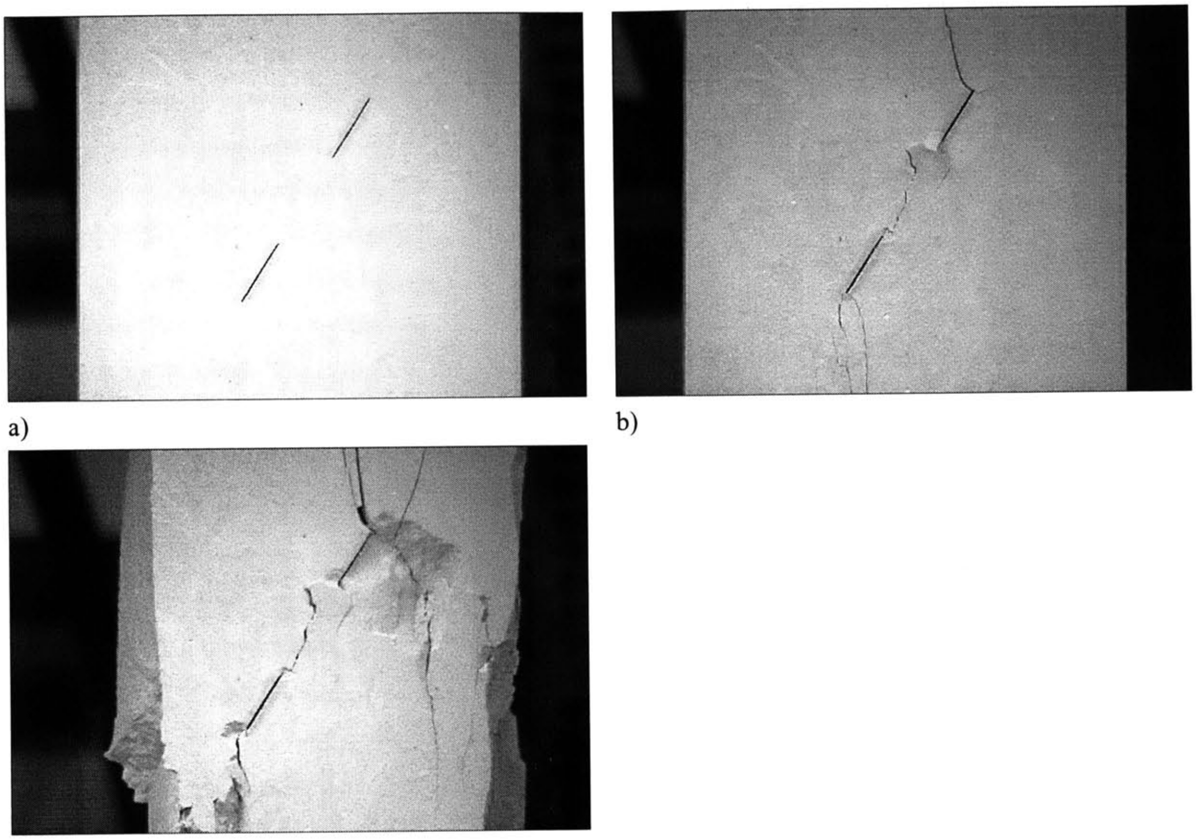

a)

b)

c)

Figure D.9 Cracking sequence of 60-0-3a geometry in monotonic test; a) Initial configuration b) External wing cracks initiate at the external tips of the flaws (at 31.99 MPa). Coalescence occurs (at 32.10 MPa). c) Failure occurs (32.63 MPa).

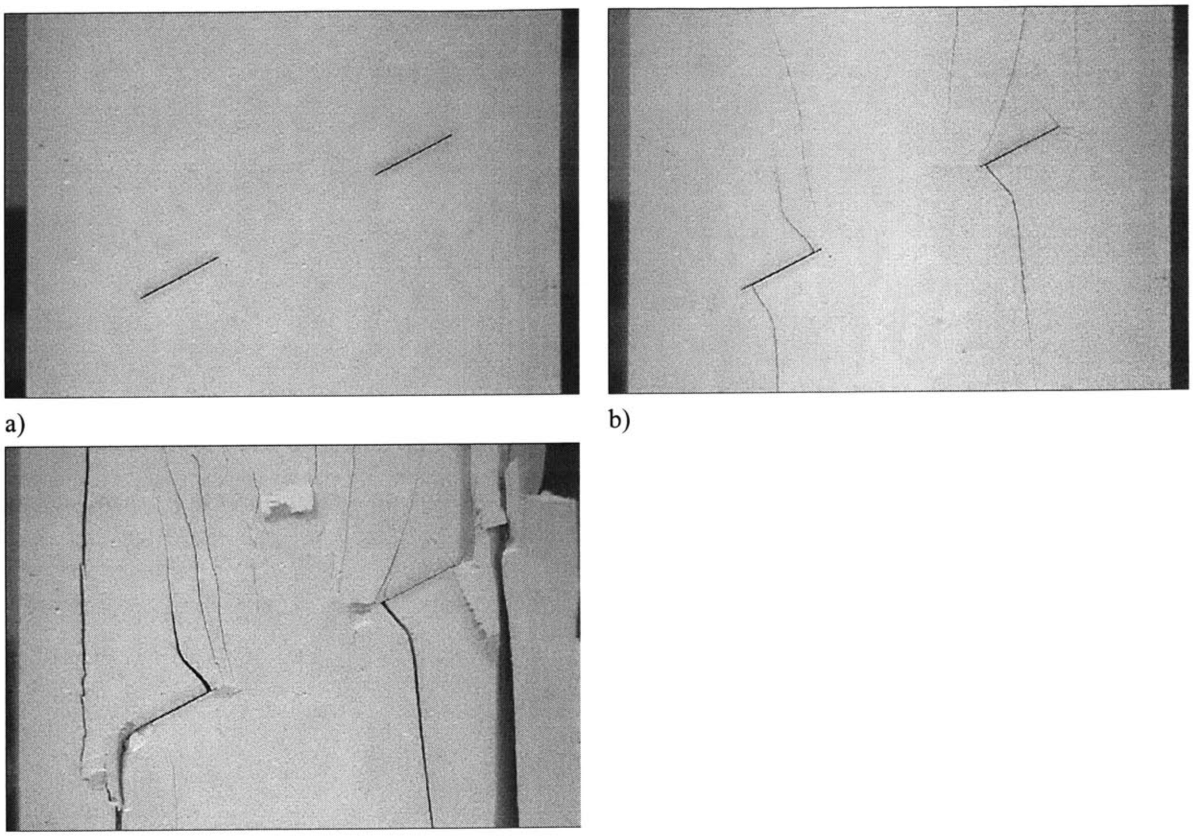

a)

b)

c)

Figure D.10 Cracking sequence of 30-0-4a geometry in monotonic test; a) Initial configuration b) External wing cracks initiate (at 27.30 MPa). Internal wing cracks initiate (at. 28.75 MPa). c) Failure occurs (at 29.87 MPa). Coalescence doesn’t occur.

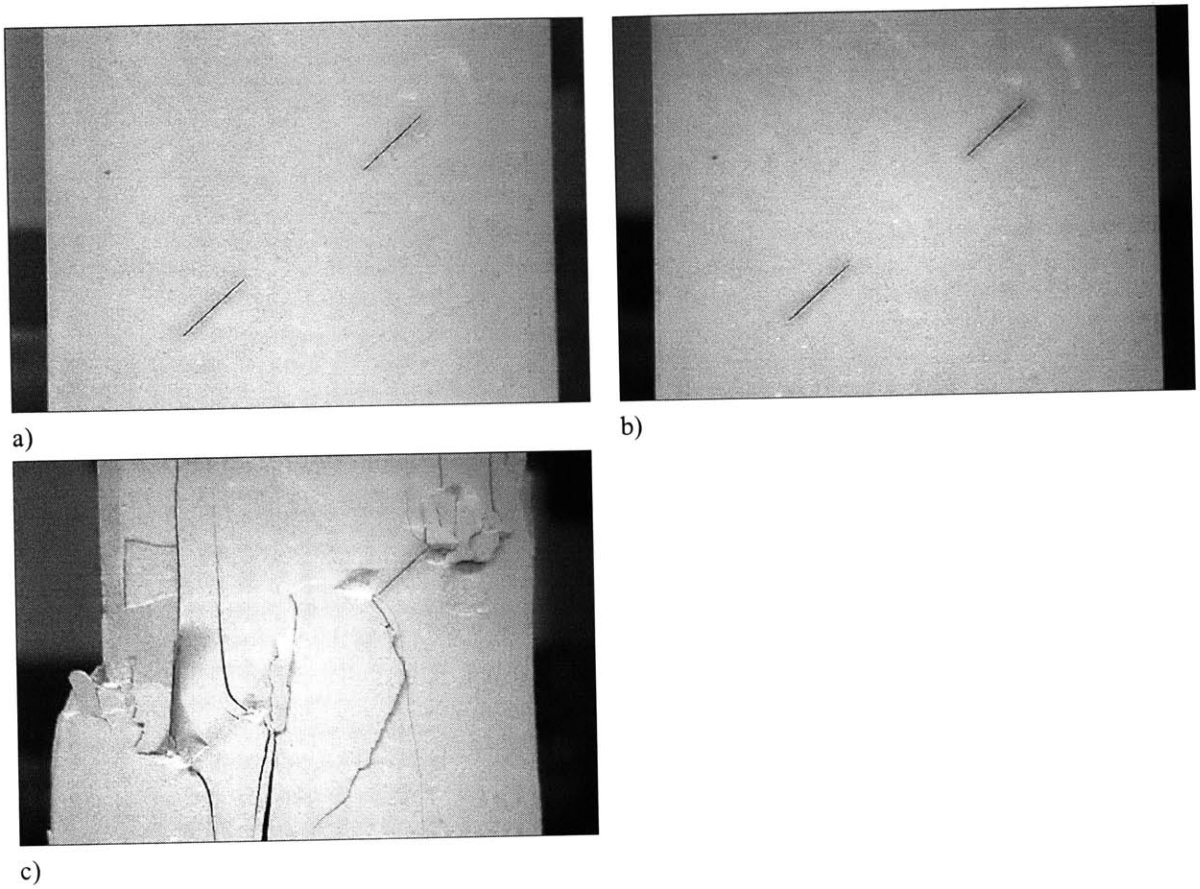

Figure D.11 Cracking sequence of 45-0-4a geometry in monotonic test; a) Initial configuration b) External wing cracks initiate at the external tips of the flaws (at 28.70 MPa). Internal wing cracks initiates at the internal tips of the flaws (at 30.72 MPa). c) Failure occurs (at 33.69 MPa). Coalescence doesn't occur.

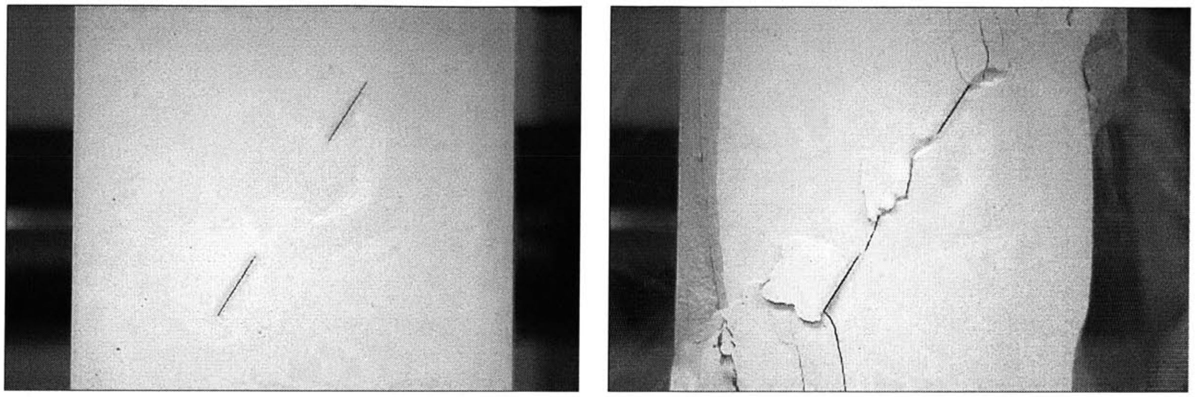

a) b)

Figure D.12 Cracking sequence of 60-0-4a geometry in monotonic test; a) Initial configuration b) External wing cracks initiates at the external tips of the flaws. Coalescence occurs. Failure occurs (at 33.58MPa).

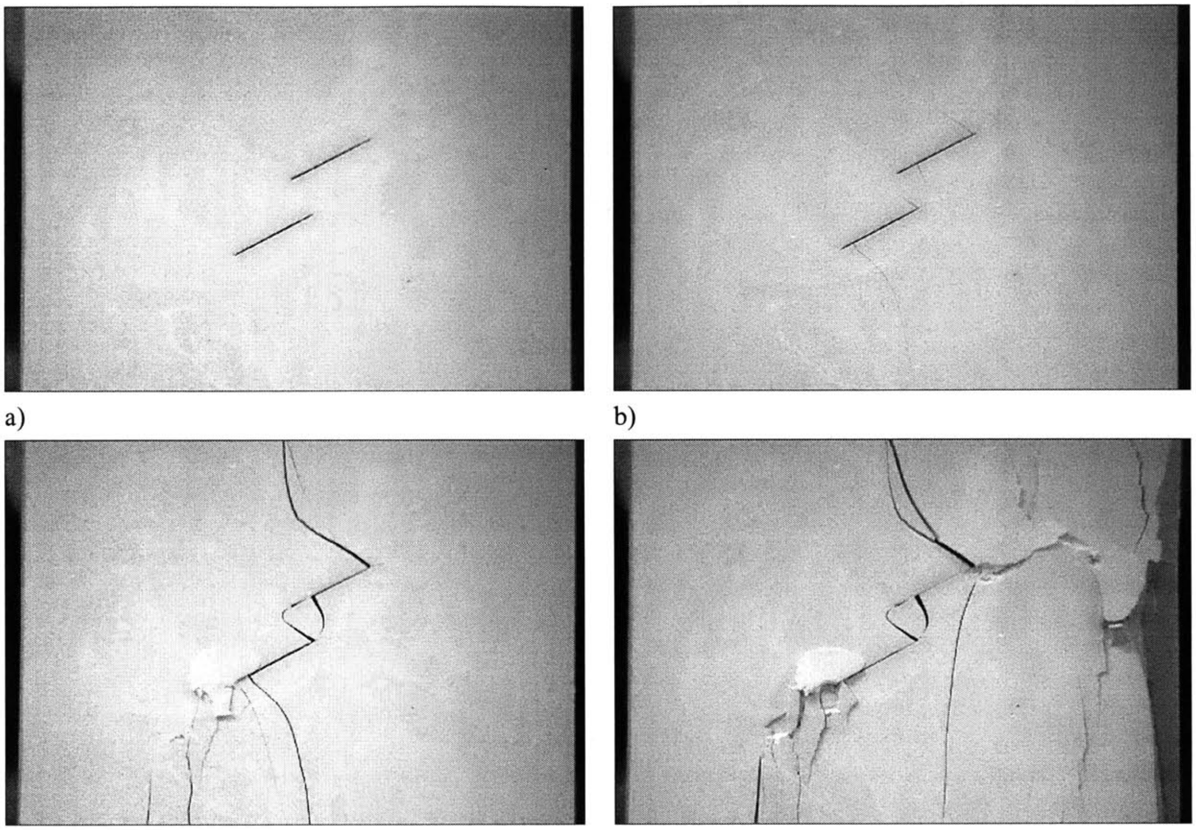

a) b) c) d)

Figure D.13 Cracking sequence of 30-a-0 geometry in monotonic test; a) Initial configuration b) External wing cracks initiates at the external tips of the flaws (at 13.07 MPa). Internal wing cracks initiate near the tips of the flaws (at 15.90 MPa.) Coalescence developed due to the internal wing cracks (at 22.74 MPa). c) External shear cracks initiate at the external tip of the lower flaw (at 22.89 MPa). External shear cracks initiate at the external tip of the upper flaw (at 24.45 MPa). d) Failure occurs (at 20.57 MPa).

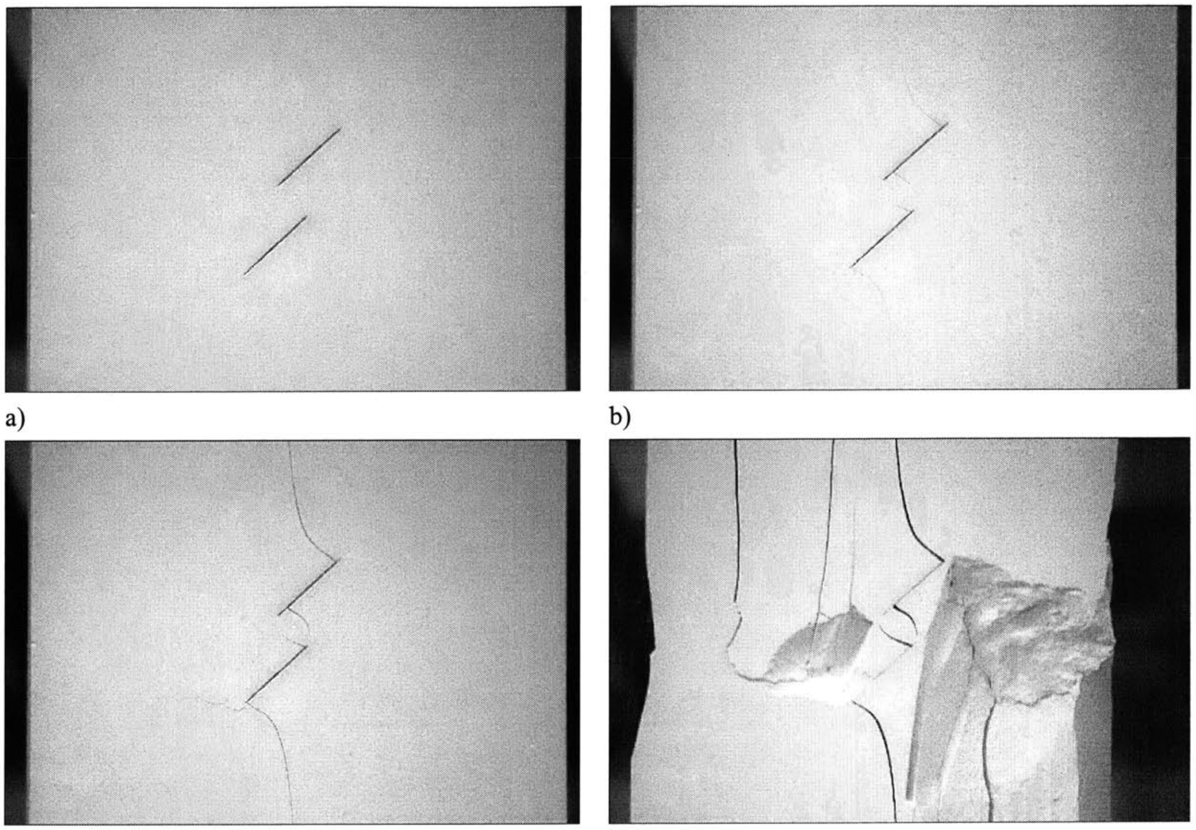

a)

b)

c)

d)

Figure D.14 Cracking sequence of 45-a-0 geometry in monotonic test; a) Initial configuration b) External wing cracks initiate. Internal wing cracks initiate (at 23.15 MPa). Coalescence developed due to internal wing cracks (at 28.80MPa). c) External shear cracks initiate at the external tips of the flaws (at 30.05 MPa). d) Failure occurs (at 30.94 MPa).

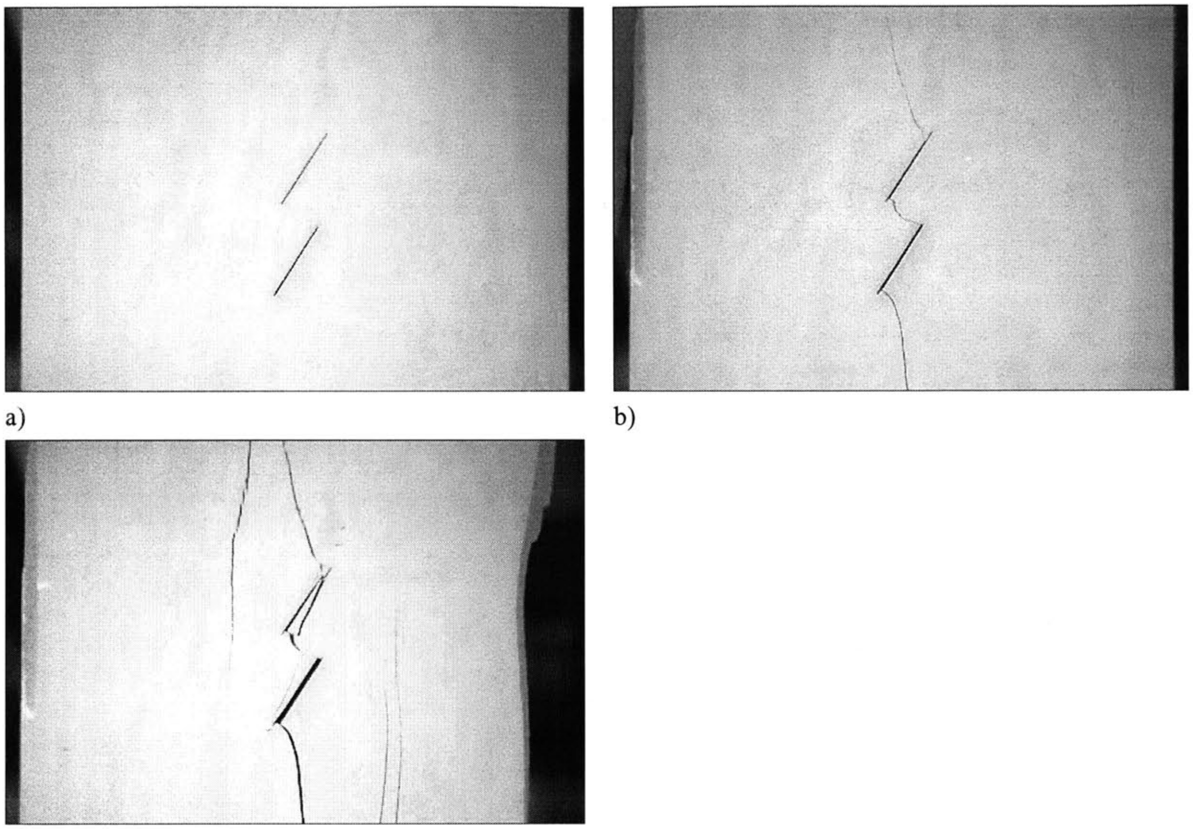

a)

b)

c)

Figure D.15 Cracking sequence of 60-a-0 geometry in monotonic test; a) Initial configuration b) External wing cracks initiate. Internal wing cracks initiate. Coalescence developed due to the internal wing crack (at 32.22 MPa). c) Failure occurs (at 31.63 MPa).

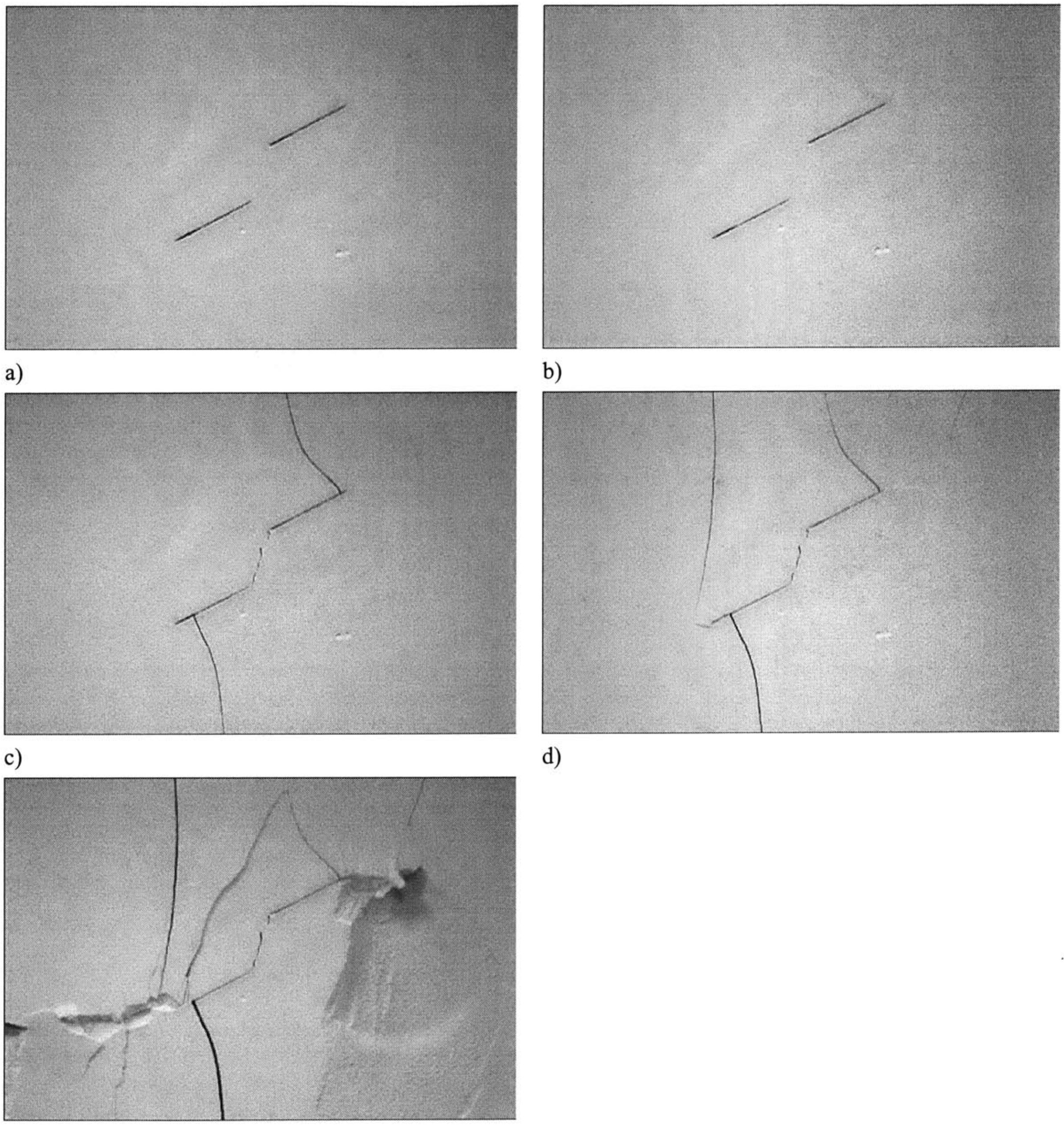

a)

b)

c)

d)

e)

Figure D.16 Cracking sequence of 30-a-a geometry in monotonic test; a) Initial configuration b) External wing cracks initiate in the middle of external tip of the flaws (at 12.81 MPa). c) Coalescence occurs due to an internal shear crack (at 22.46 MPa). d) External shear crack occurs around the external tip of the lower flaw (at 22.16 MPa). External shear crack occurs around the external tip of the upper flaw (at 22.20 MPa). e) Failure occurs (at 22.34 MPa).

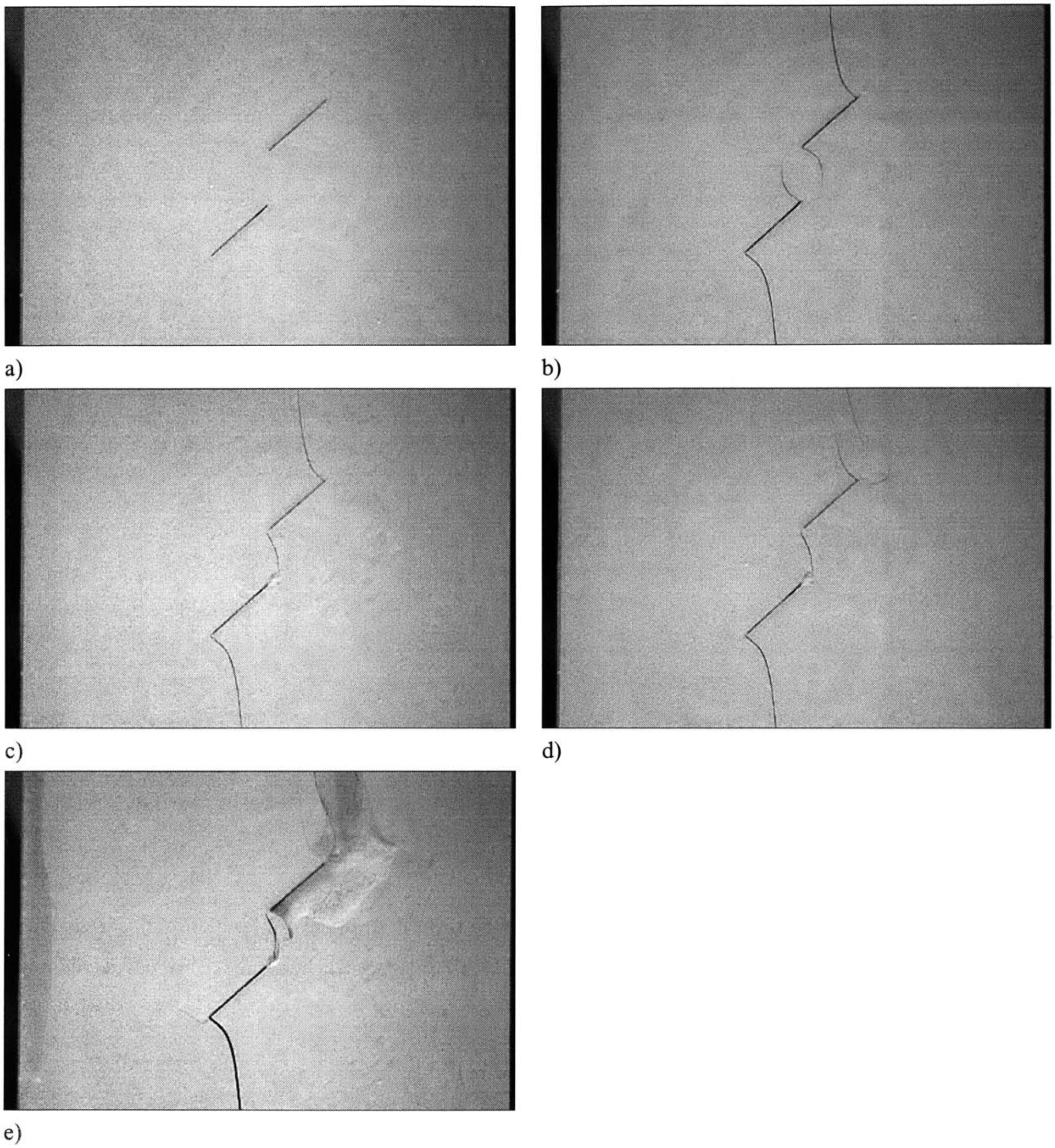

a) b) c) d) e)

Figure D.17 Cracking sequence of 45-a-a geometry in monotonic test; a) Initial configuration b) External and internal wing cracks initiate (at 10.54 MPa). c) Coalescence occurs (at 23.65 MPa). d) External shear crack occurs at the external tip of the upper flaw (at 24.50 MPa). External shear crack occurs at the external tip of the lower flaw (at 26.28 MPa). e) Failure occurs (at 28.64 MPa).

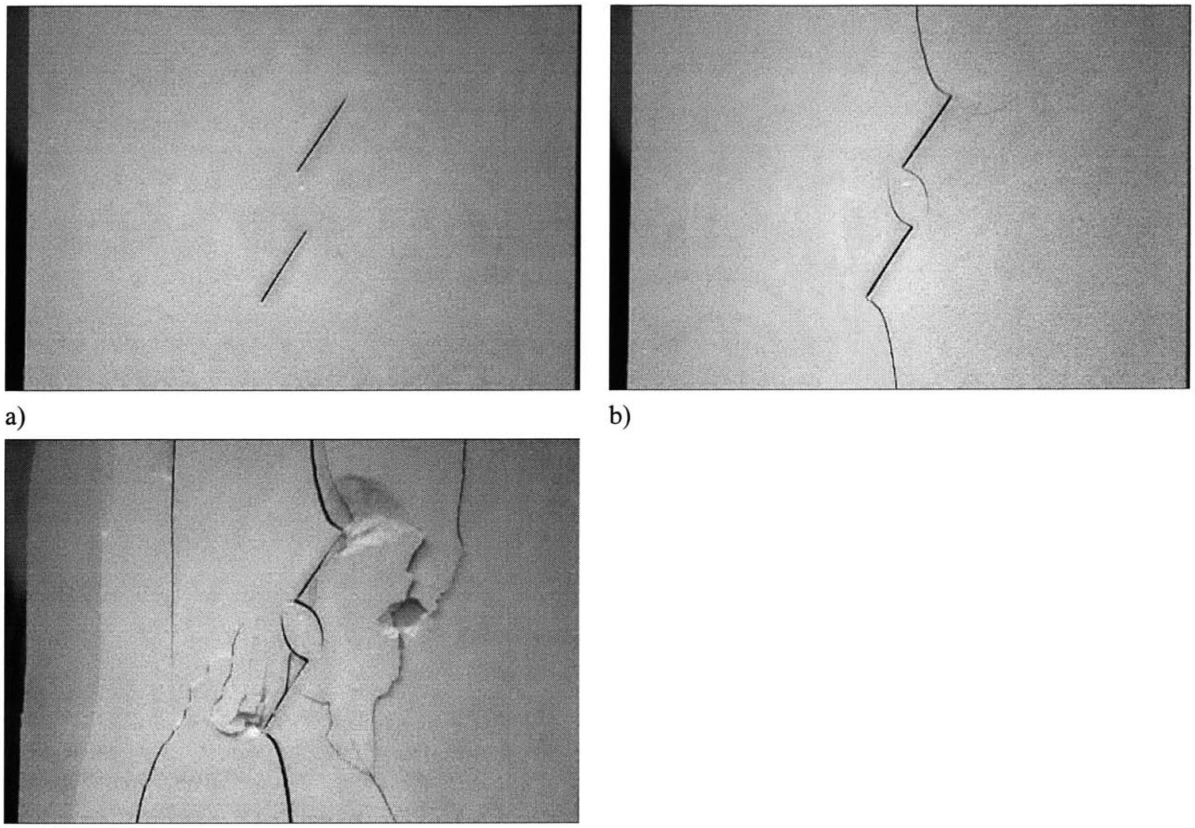

a)

b)

c)

Figure D.18 Cracking sequence of 60-a-a geometry in monotonic test; a) Initial configuration b) External and internal wing cracks initiate at the tip of the flaws (at 20.34 MPa). External shear cracks are developed near the external tip of the upper flaw (at 32.85 MPa). c) Failure occurs (at 31.66 MPa).

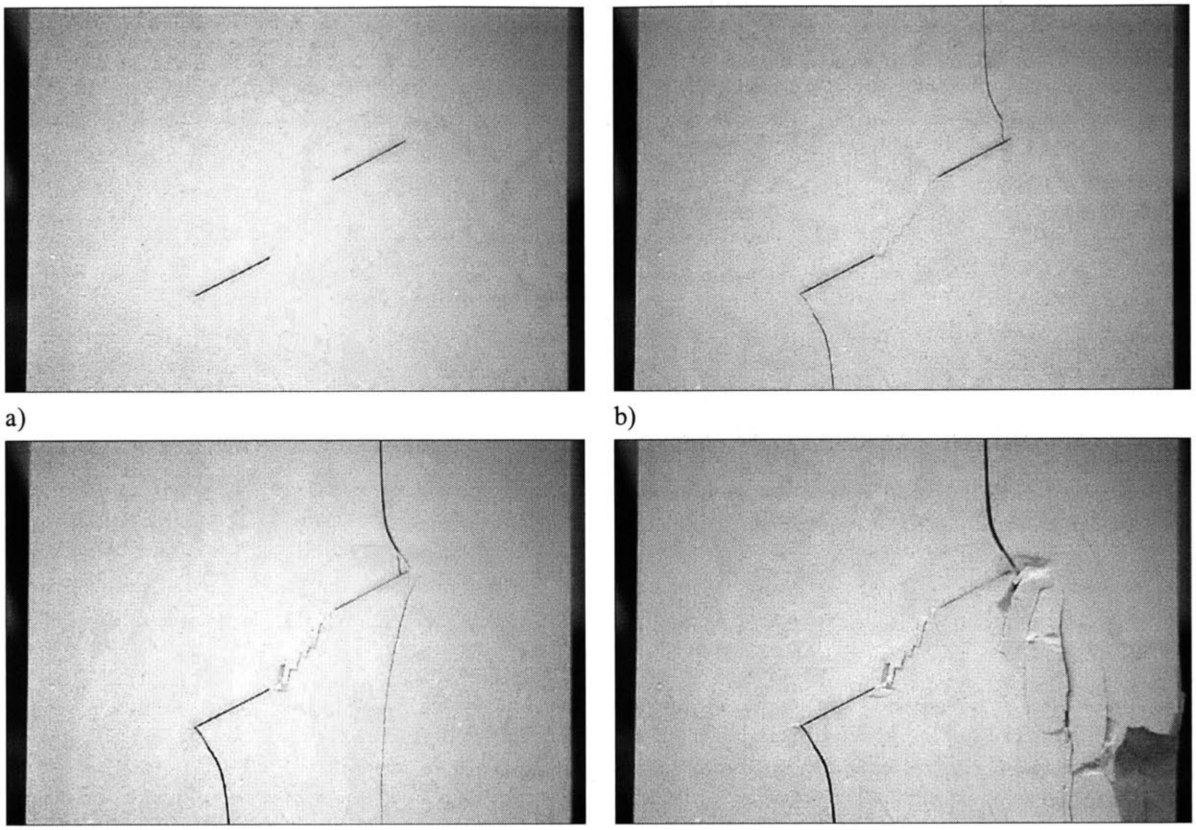

a)

b)

c)

d)

Figure D.19 Cracking sequence of 30-a-2a geometry in monotonic test; a) Initial configuration b) External wing cracks initiate at the external tips of the flaws (at 16.44 MPa). Coalescence occurs due to the shear crack (at 22.14 MPa). c) External shear cracks occurs at the external tips of the flaws (at 22.78 MPa). d) Failure occurs (at 21.28 MPa).

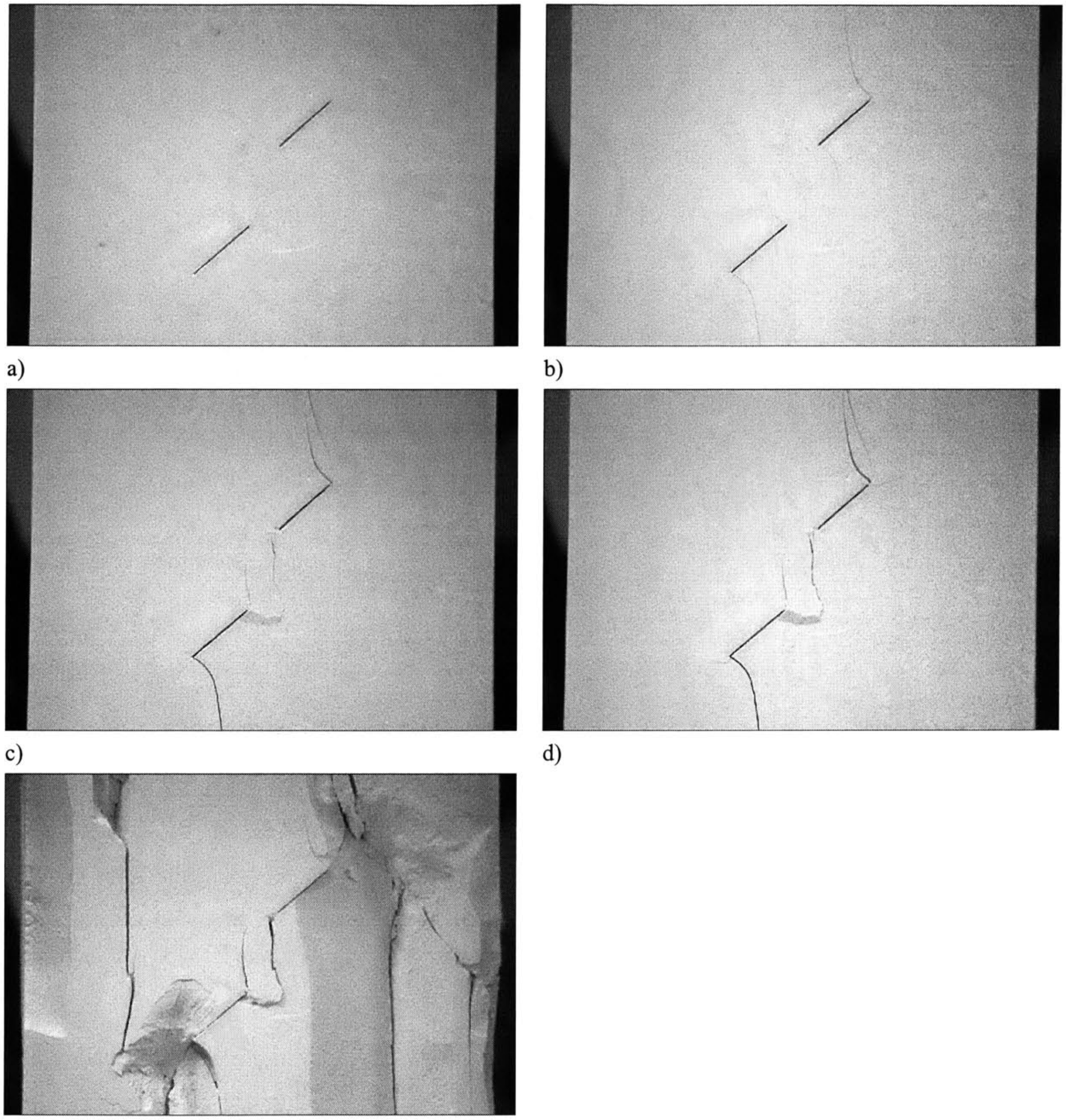

a)

b)

c)

d)

Figure D.20 Cracking sequence of 45-a-2a geometry in monotonic test; a) Initial configuration b) External wing cracks initiate at the crack tips (at 11.34 MPa). Internal wing cracks initiate at the crack tips (at 21.19 MPa). c) Coalescence occurs (at 21.67MPa). d) External shear cracks occur near the external tips of the flaws (28.89MPa). e) Failure occurs (at 28.95 MPa).

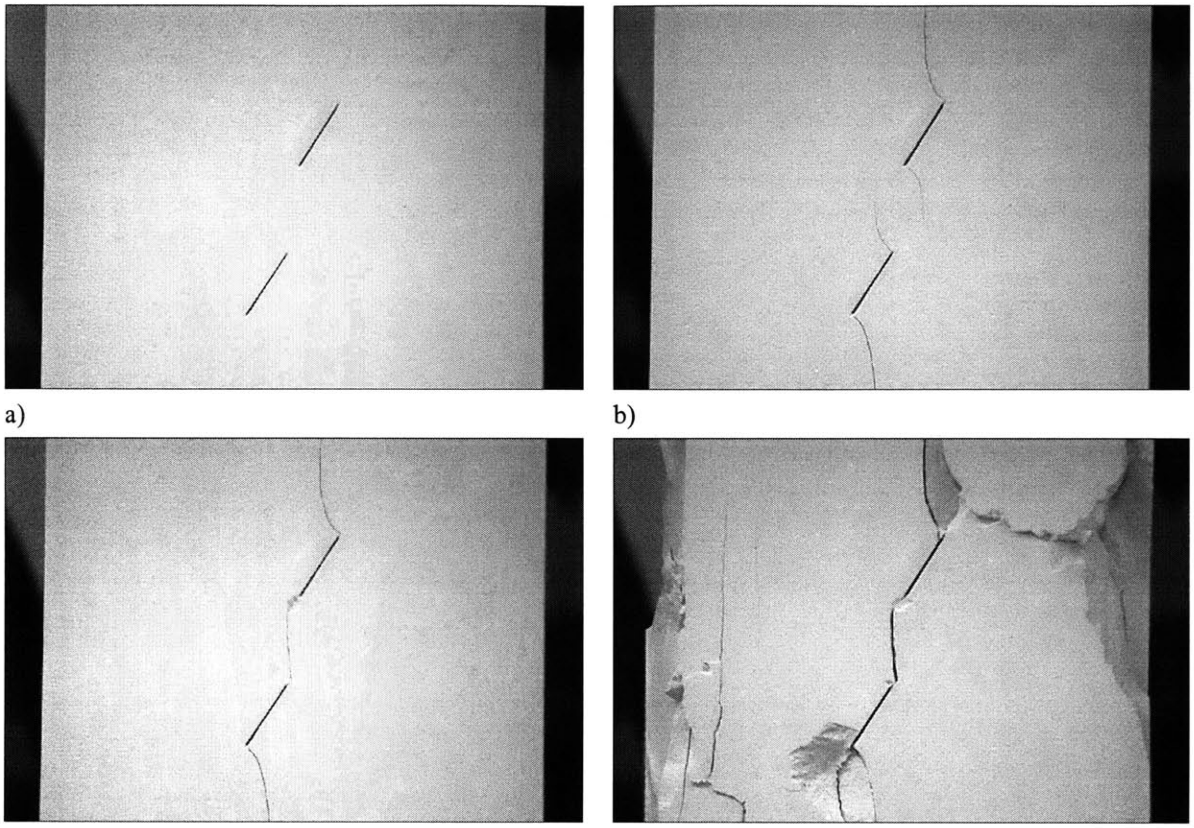

a) b) c) d)

Figure D.21 Cracking sequence of 60-a-2a geometry in monotonic test; a) Initial configuration b) External and Internal wing cracks initiate at the crack tips (at 28.66 MPa). c) Coalescence occurs (29.88 MPa). d) Failure occurs (29.88 MPa).

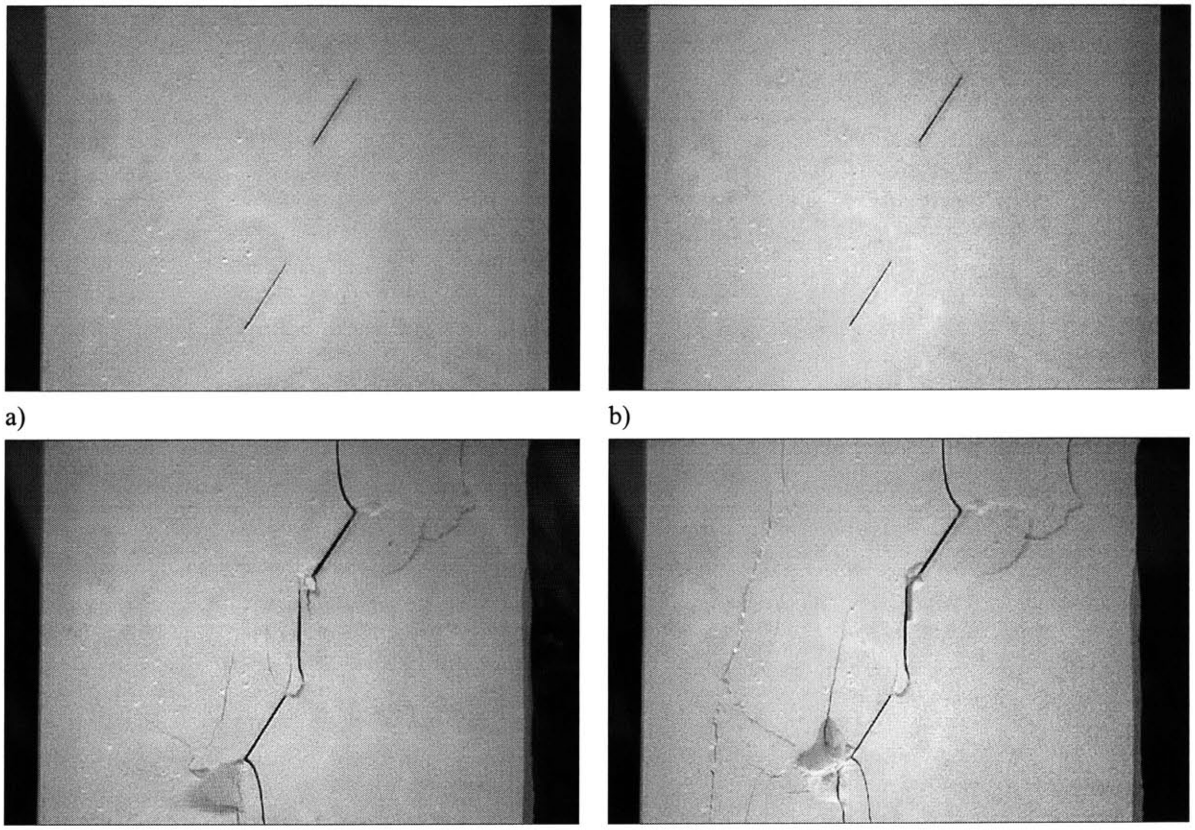

a) b)

c) d)

Figure D.22 Cracking sequence of 60-a-3a geometry in monotonic test; a) Initial configuration b) External and internal wing cracks initiate (at 24.04 MPa). c) Coalescence occurs (at 28.23 MPa). d) Failure occurs (at 28.50 MPa).

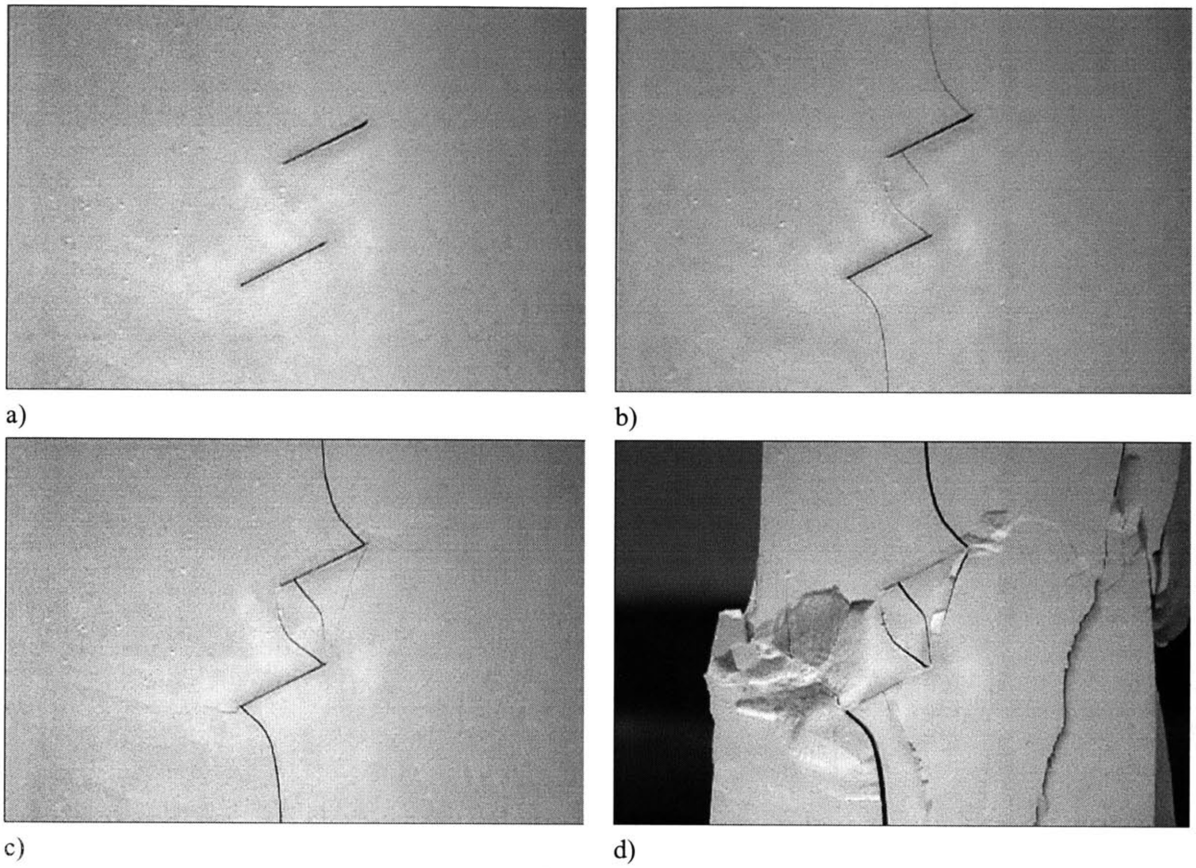

Figure D.23 Cracking sequence of 30-2a-0 geometry in monotonic test; a) Initial configuration b) External and internal wing cracks initiate at the tips of the flaws (at 11.03 MPa). Coalescence occurs due to the internal wing crack (at 20.16 MPa). c) External shear cracks occur at the external tips of the flaws (at 29.27 MPa). d) Failure occurs (at 28.62 MPa).

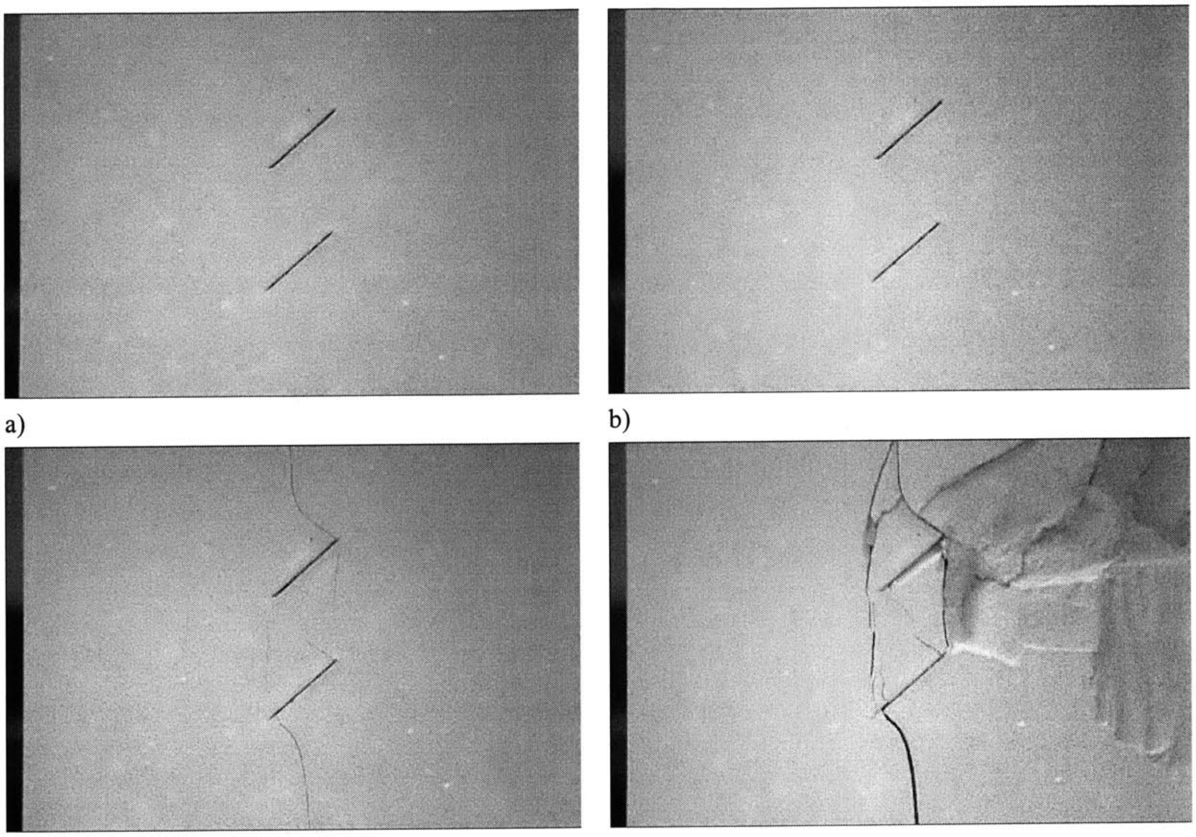

a)

b)

c)

d)

Figure D.24 Cracking sequence of 45-2a-0 geometry in monotonic test; a) Initial configuration b) External and internal wing cracks initiate at the tips of the flaws (at 26.95 MPa). c) Another tension crack occurs between external tip of the upper flaw and internal tip of the lower flaw (at 29.81 MPa). Another tension cracks occur between external tip of the lower flaw and internal tip of the upper flaw (at 32.74 MPa). d) Failure occurs (at 33.43 MPa).

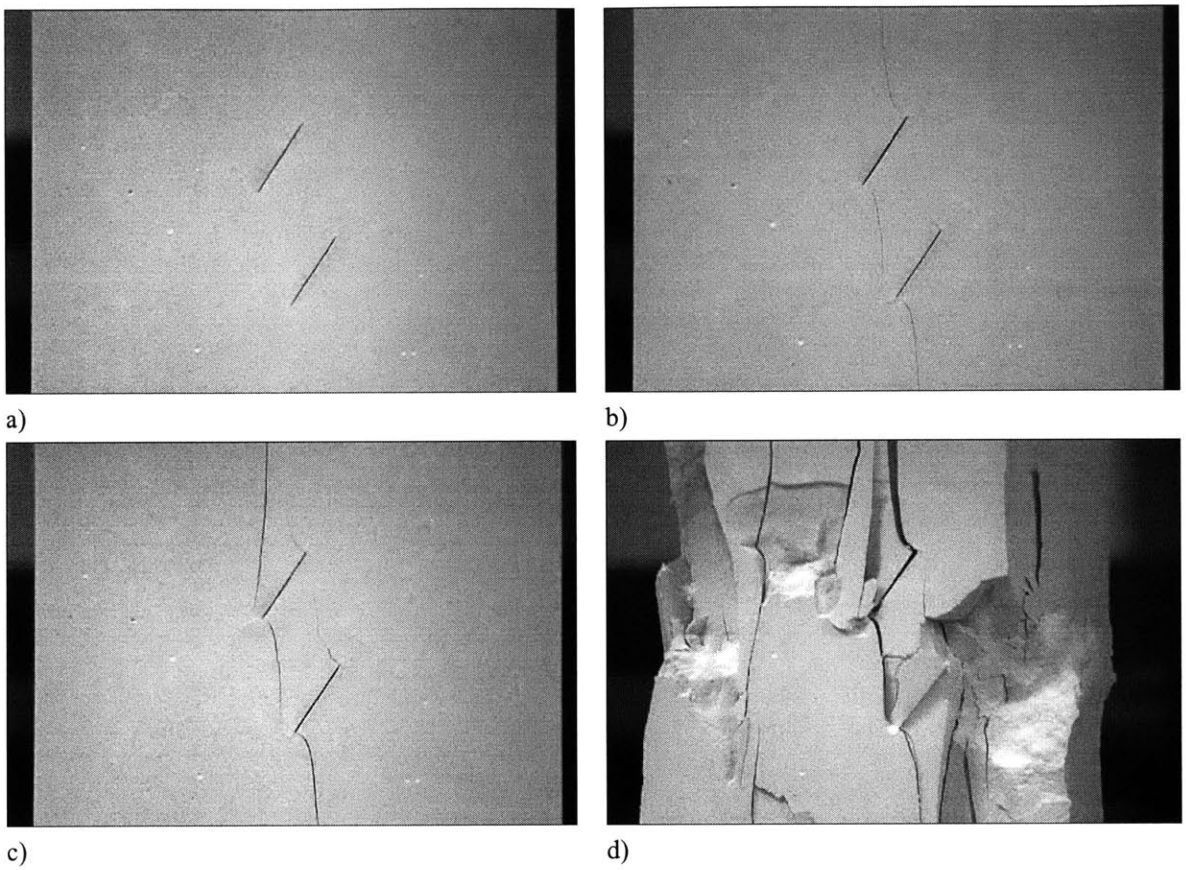

Figure D.25 Cracking sequence of 60-2a-0 geometry in monotonic test; a) Initial configuration b) External wing cracks initiate at the external tips of the flaws. Internal wing crack initiates at the internal tip of the upper flaw(at 36.39 MP). Internal wing crack initiates at the internal tip of the lower flaw (at 40.77 MPa). c) Coalescence occurs due to the internal wing crack and shear crack. Shear crack occurs around the internal tip of the upper flaw (at 40.93 MPa). Another tension crack occurs around the internal tip of the upper flaw (at 40.93 MPa). d) Failure occurs (at 41.21 MPa).

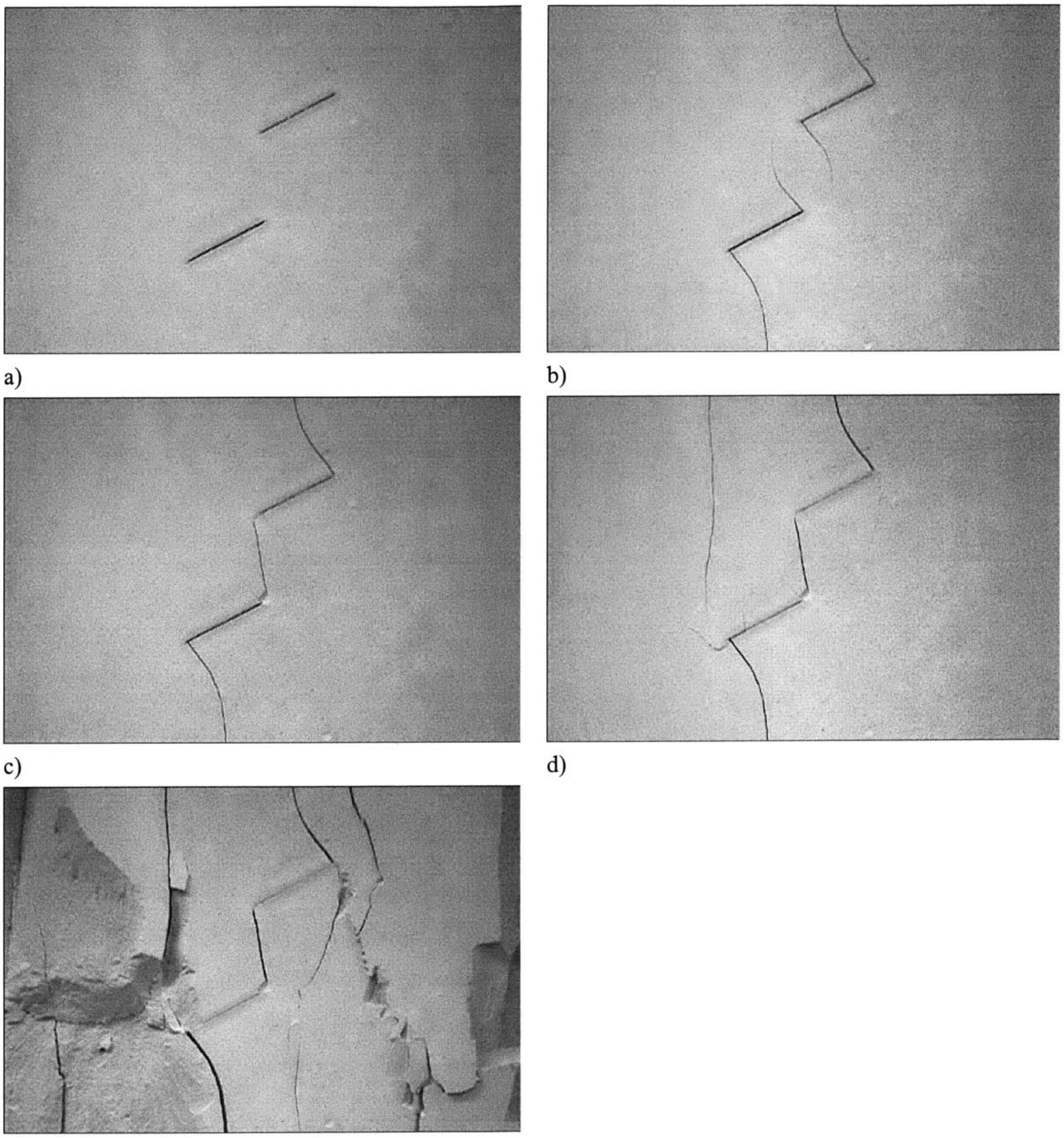

a) b) c) d) e)

Figure D.26 Cracking sequence of 30-2a-a geometry in monotonic test; a) Initial configuration b) External and internal wing cracks initiate (at 11.74 MPa). c) Coalescence occurs due to the linkage of the tension crack and internal shear cracks (at 22.05 MPa). d) Shear cracks occur around the external tip of the lower flaw (at 24.43 MPa). A vertical tension crack occurs around the external tips of the lower flaw (at 26.82MPa). e) Failure occurs (at 27.18 MPa).

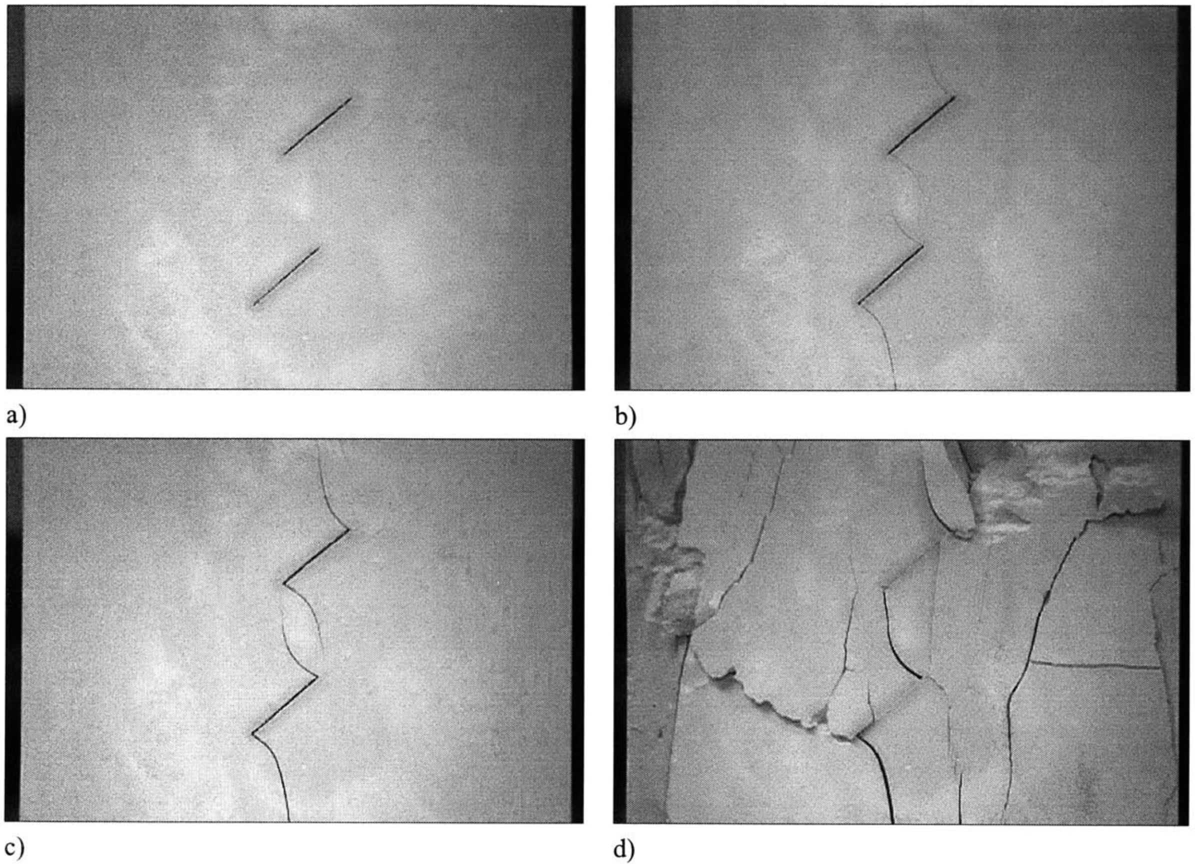

Figure D.27 Cracking sequence of 45-2a-a geometry in monotonic test; a) Initial configuration b) External and internal wing cracks initiate at the tips of the flaws (At 15.02 MPa). c) External shear cracks occur around the external tips of the flaws (at 32.69 MPa). d) Failure occurs (at 34.99 MPa).

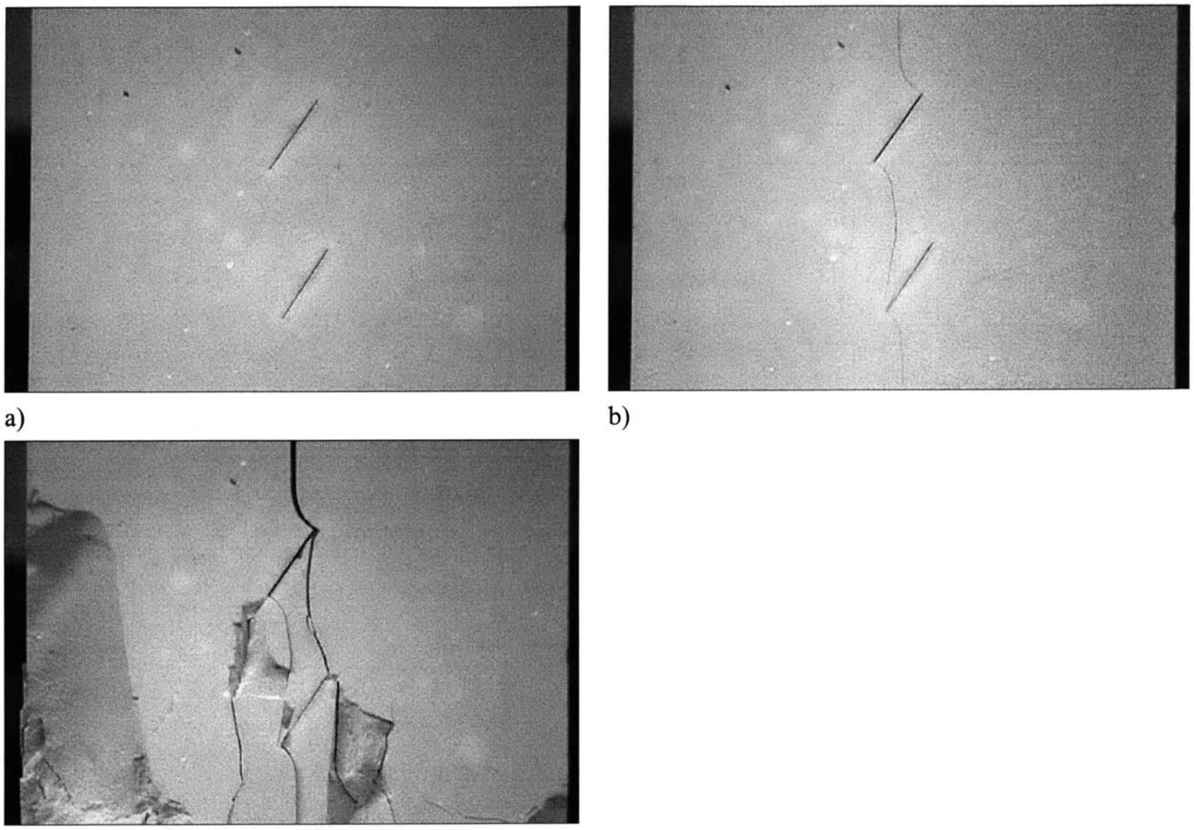

a)

b)

c)

Figure D.28 Cracking sequence of 60-2a-a geometry in monotonic test; a) Initial configuration b) External and internal wing cracks initiate (at 33.33 MPa). c) Internal wing crack occurs at the internal tip of the lower flaw. Failure occurs (at 37.98 MPa).

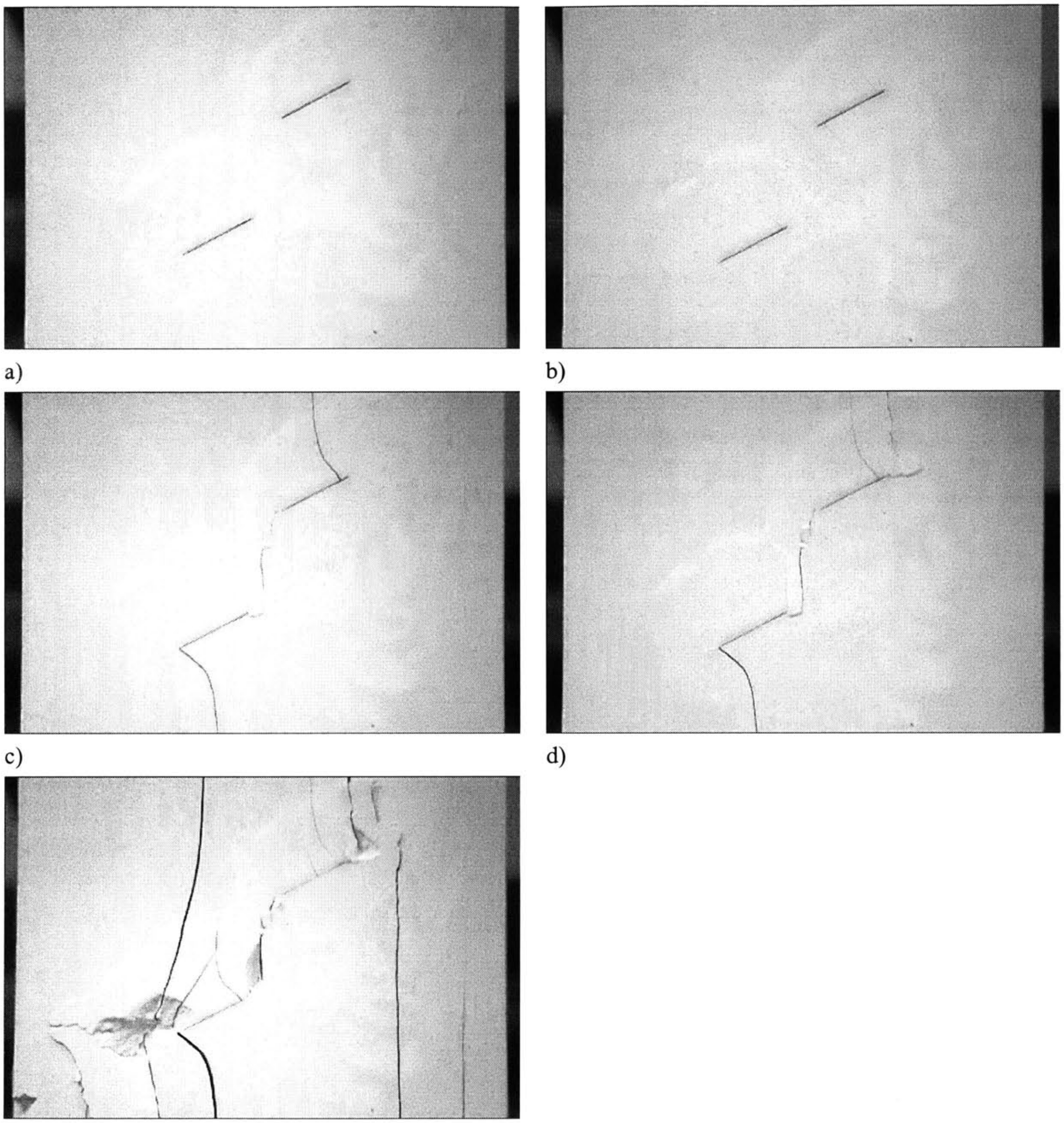

a) b) c) d) e)

Figure D.29 Cracking sequence of 30-2a-2a geometry in monotonic test; a) Initial configuration b) External and internal wing cracks initiate near the tips of the flaws (at 19.20 MPa). c) Coalescence occurs due to the internal shear crack and vertical tension crack (at 25.08 MPa). d) External shear cracks occur at the external tips of the flaws (at 25.70 MPa). f) Failure occurs (at 26.21 MPa).

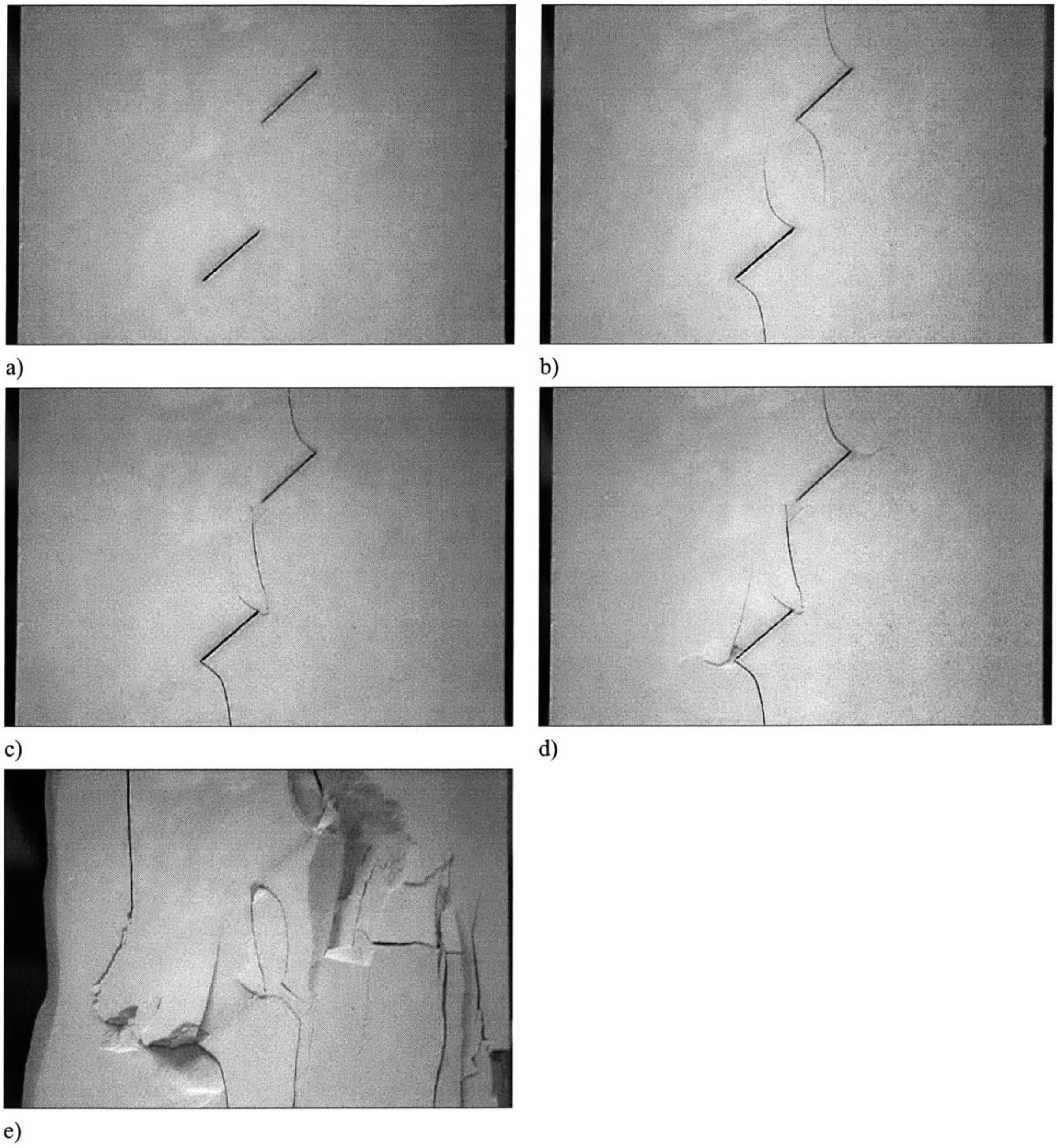

Figure D.30 Cracking sequence of 45-2a-2a geometry in monotonic test; a) Initial configuration b) External and internal wing cracks initiate near the tips of the flaws (at 15.78 MPa). c) Coalescence occurs due to the internal shear crack and vertical tension crack (at 29.41 MPa). d) External shear cracks occur at the external tips of the flaws (at 28.43 MPa). Another tension crack occurs around the external tip of the lower flaw (at29.29 MPa). f) Failure occurs (at 27.69 MPa).

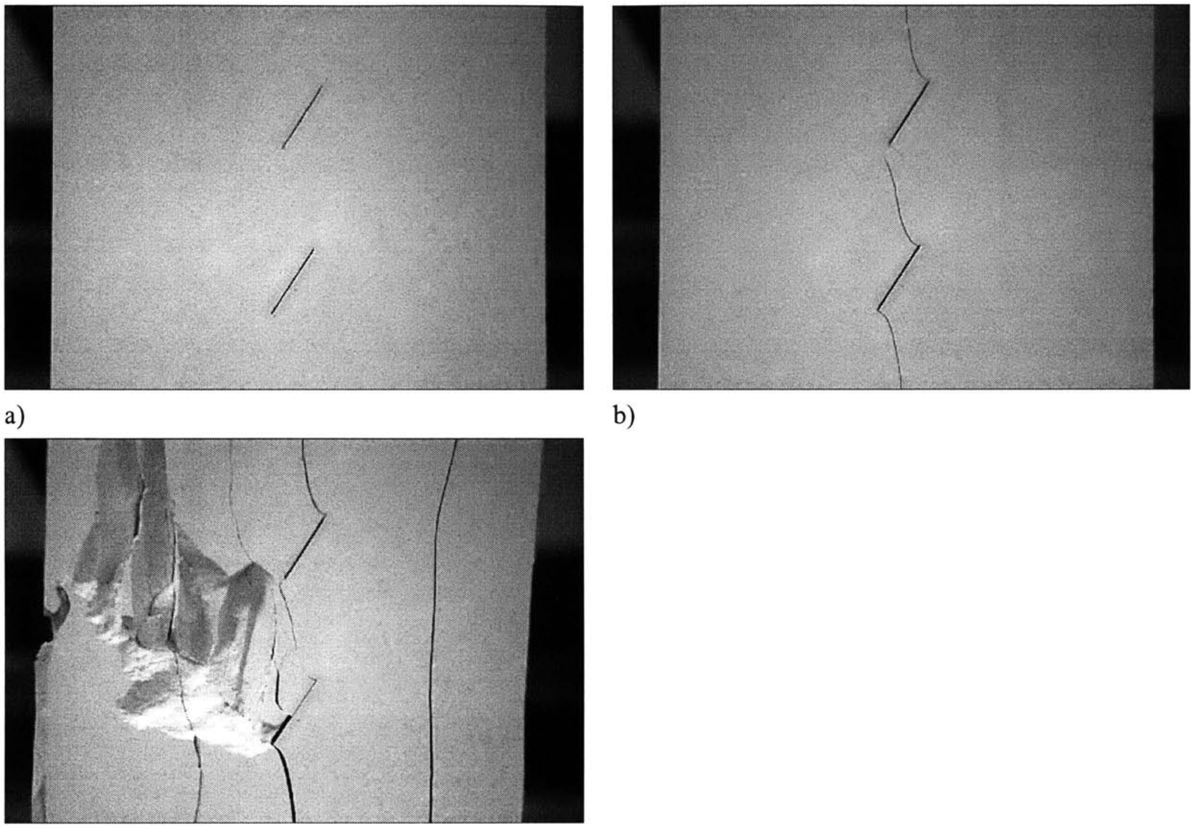

a)

b)

c)

Figure D.31 Cracking sequence of 60-2a-2a geometry in monotonic test; a) Initial configuration b) External wing cracks initiate. Coalescence occurs due to the internal wing crack (at 31.17 MPa). c) Failure occurs (at 35.45 MPa).

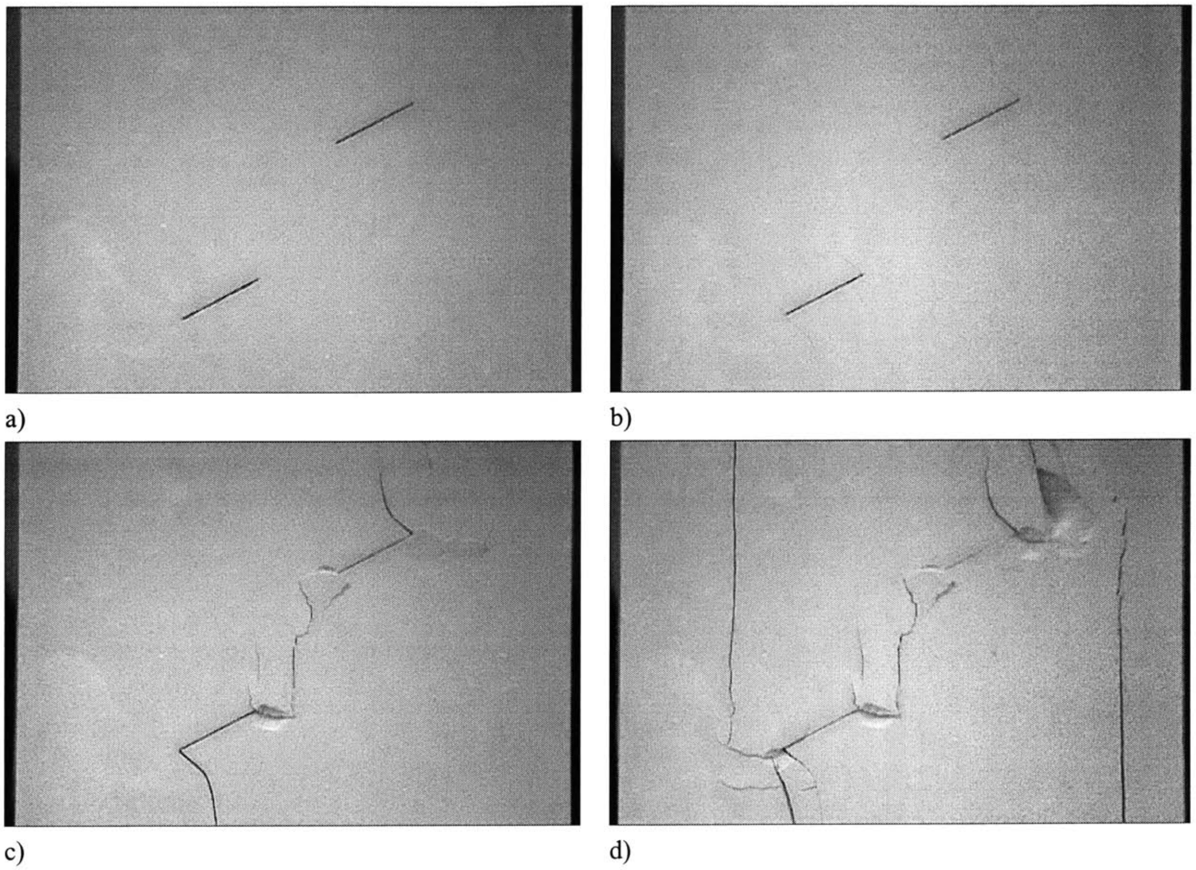

Figure D.32 Cracking sequence of 30-2a-3a geometry in monotonic test; a) Initial configuration b) External and internal wing cracks initiate (at 18.33 MPa). c) Coalescence occurs due to internal shear cracks and a vertical tension crack. External shear cracks occur around the external tip of the flaws (at 25.06 MPa). d) Failure occurs (at 21.76 MPa).

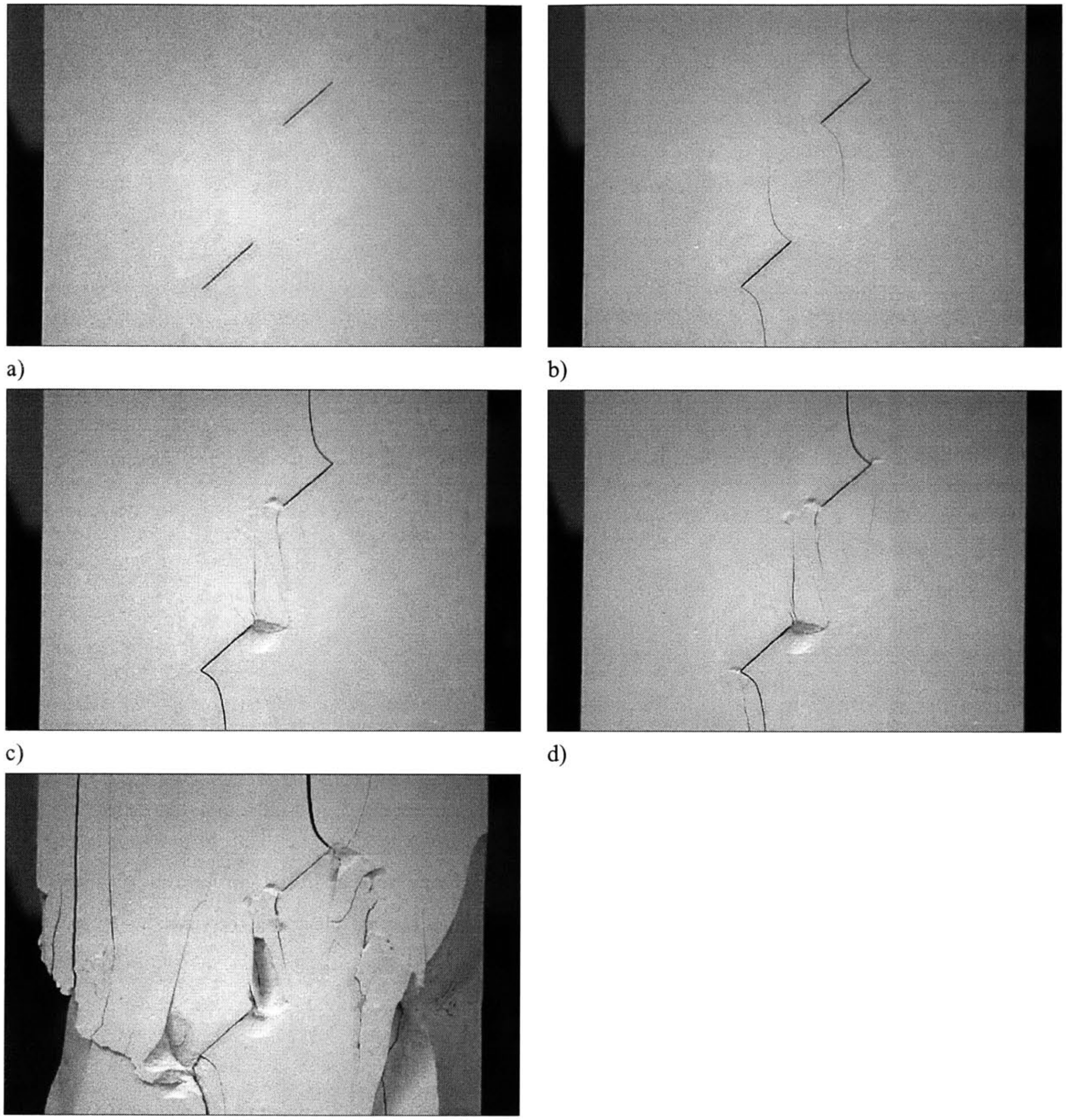

a) b) c) d) e)

Figure D.33 Cracking sequence of 45-2a-3a geometry in monotonic test; a) Initial configuration b) External and internal wing cracks initiate (at 19.68 MPa). c) Coalescence occurs due to internal shear cracks and a vertical tension crack (at 31.43 MPa). d) External shear cracks occur around the external tip of the flaws (at 29.00 MPa).e) Failure occurs (at 26.77 MPa).

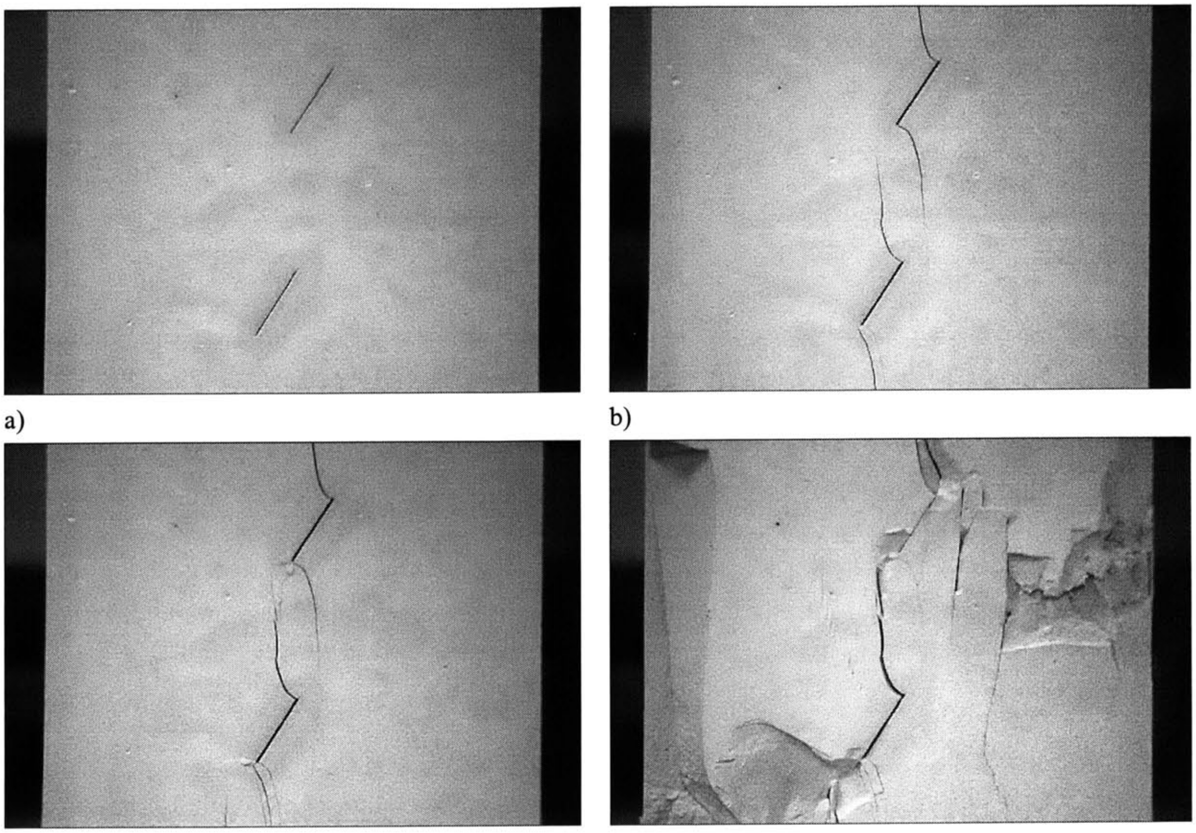

a)

b)

c)

d)

Figure D.34 Cracking sequence of 60-2a-3a geometry in monotonic test; a) Initial configuration b) External and internal wing cracks initiate (at 36.44 MPa). c) Coalescence occurs due to an internal shear crack and internal wing crack. External shear cracks occur around the external tip of the lower flaw (at 36.76 MPa). d) Failure occurs (at 33.15 MPa).

D.2 Crack growth sequence in cyclic tests

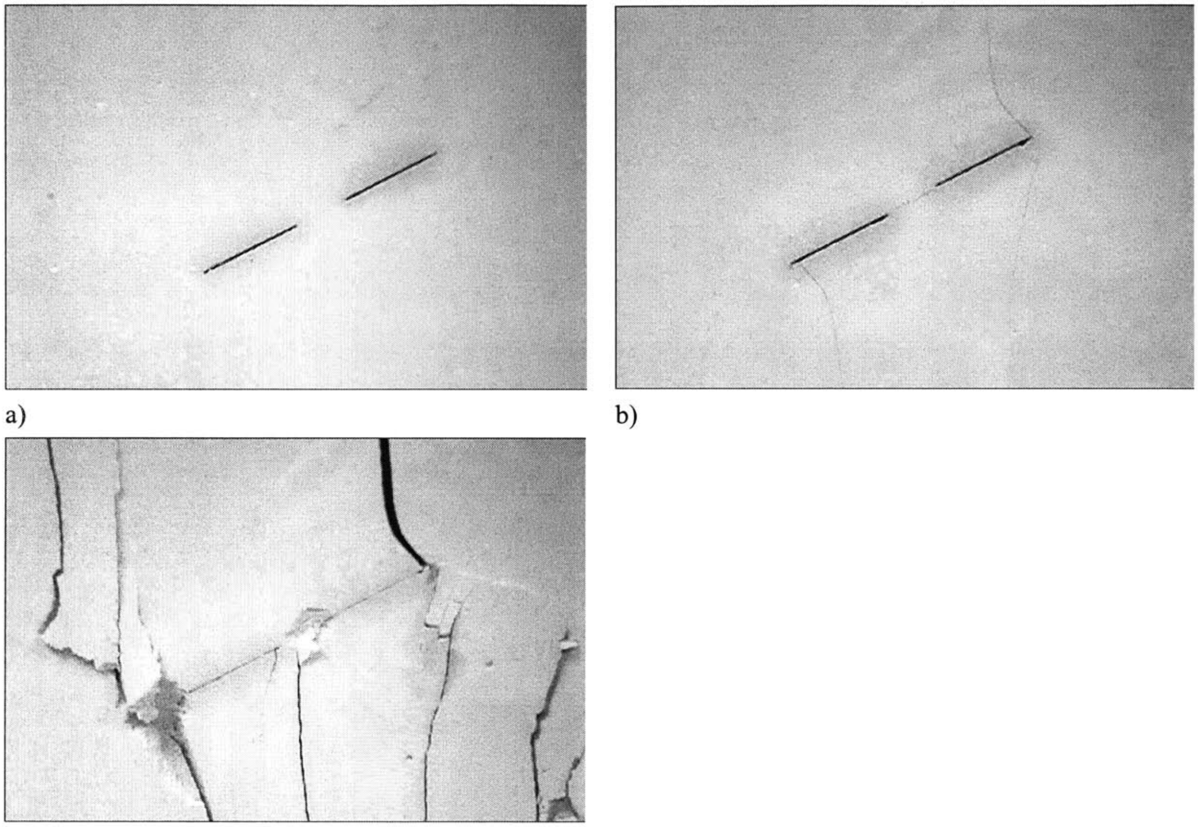

a)

b)

c)

Figure D.35 Cracking sequence of 30-0-a geometry in cyclic tests. $\sigma_{max}/\sigma_c = 0.9$, $\sigma_{max=}$ 23.7MPa; a) Initial configuration b) External wing cracks initiate. Coalescence occurs (1 cycle). c) Failure occurs (12 cycles).

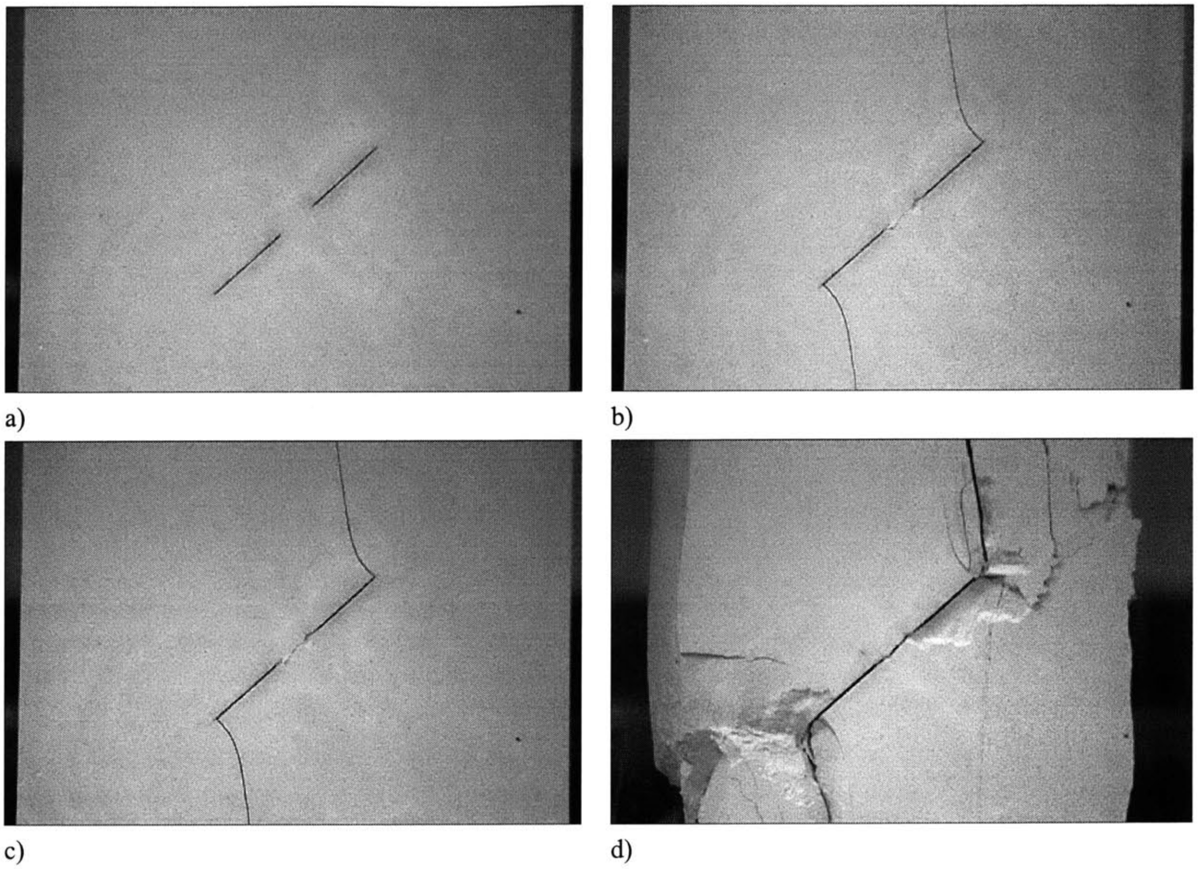
a)
b)
c)
d)

FigureD.36 Cracking sequence of 45-0-a geometry in cyclic test. $\sigma_{max}/\sigma_c = 0.85$, σ_{max}=22.28 MPa ; a) Initial configuration b) External wing cracks initiate. Coalescence occurs (1 cycle). c) External shear cracks develop at the external tip of the flaws (1602 cycles). d) Failure occurs (2735 cycles).

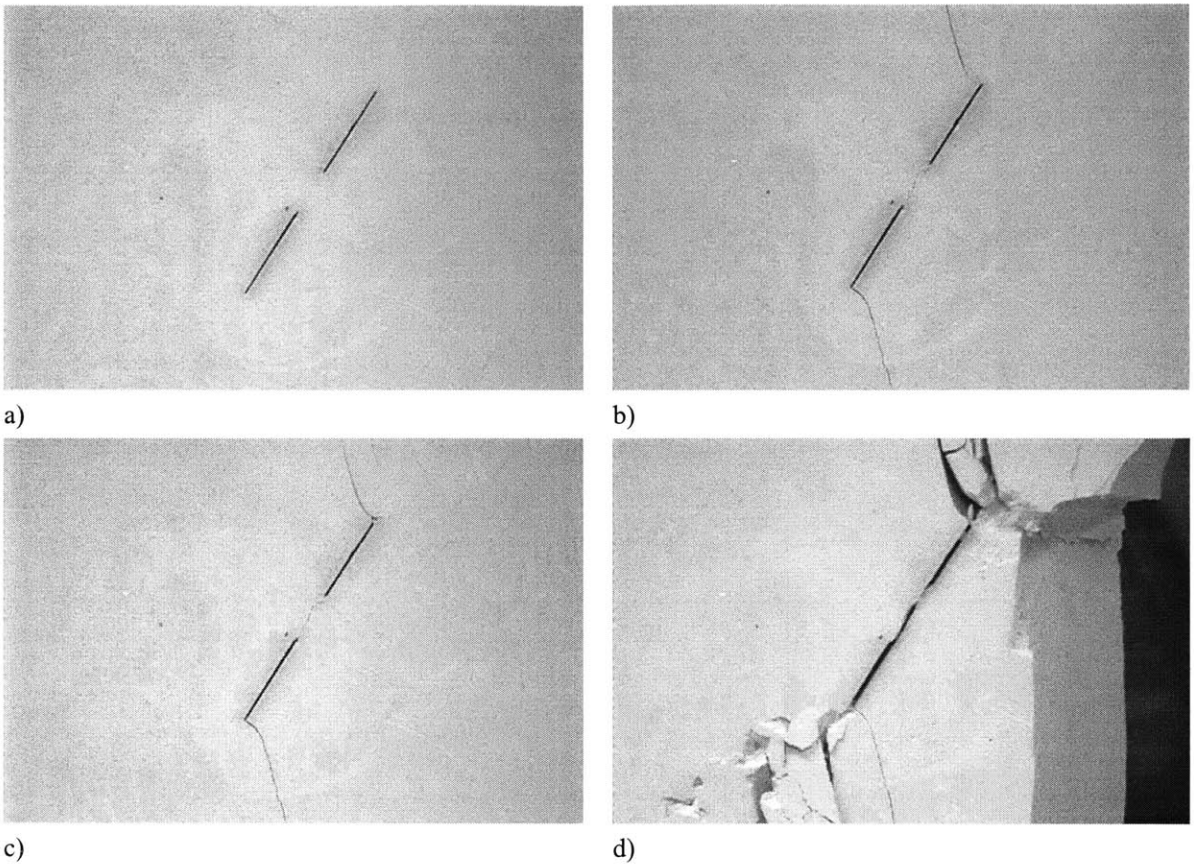

a)
b)
c)
d)

Figure D.37 Cracking sequence of 60-0-a geometry in cyclic test. $\sigma_{max}/\sigma_c = 0.85$, $\sigma_{max} = 23.66$ MPa; a) Initial configuration b) External wing cracks initiate. Coalescence occurs (1 cycle). c) External shear cracks develop at the external tip of the flaws (83 cycles). d) Failure occurs (578 cycles).

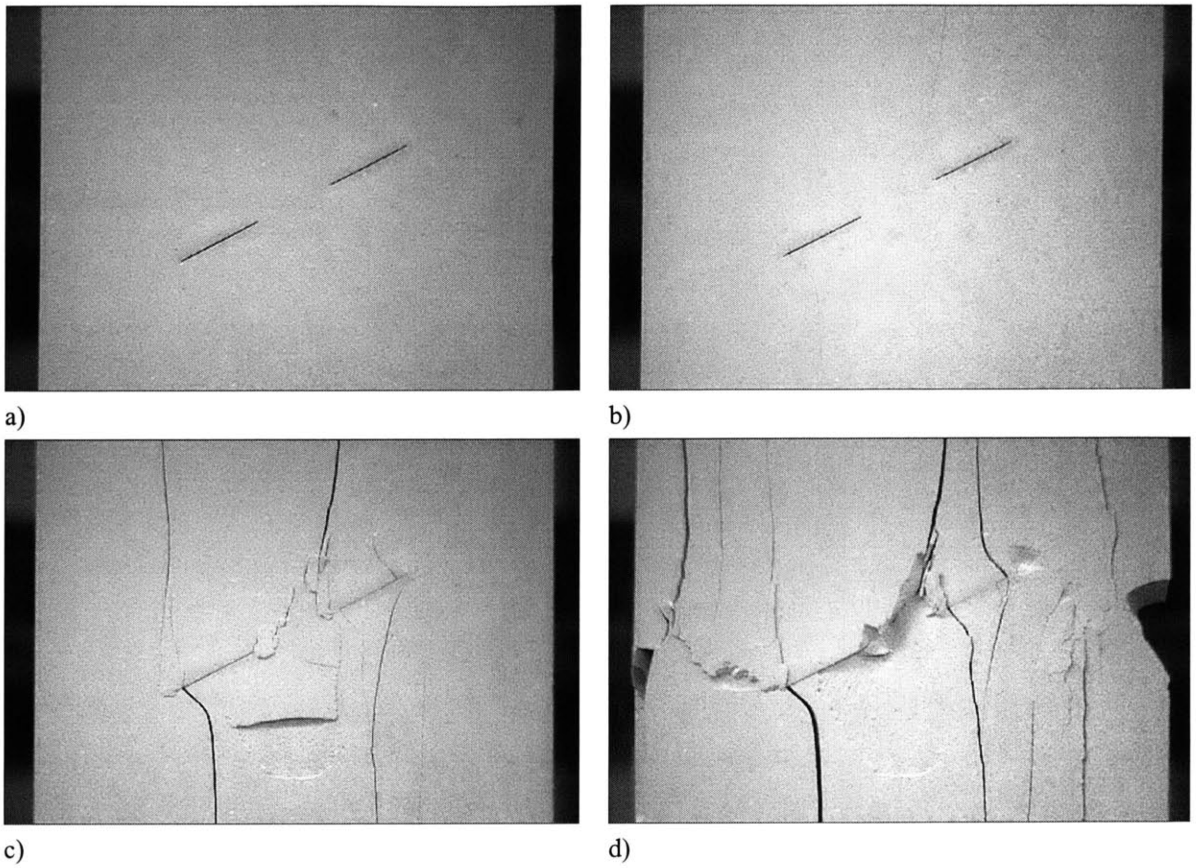

Figure D.38 Cracking sequence of 30-0-2a geometry in cyclic test. $\sigma_{max}/\sigma_c = 0.85$, $\sigma_{max} = 22.23$ MPa; a) Initial configuration b) External and internal wing cracks initiate near the tips of the flaws (12 cycles). Another tension crack occurs around the internal tip of the upper flaw (346 cycles). c) Another tension crack accompanied by shear cracks occurs around the external tip of the lower flaw (348 cycles). Another tension crack occurs at the external tip of the upper flaw (349 cycles). d) Failure occurs (352 cycles). Coalescence does not occur.

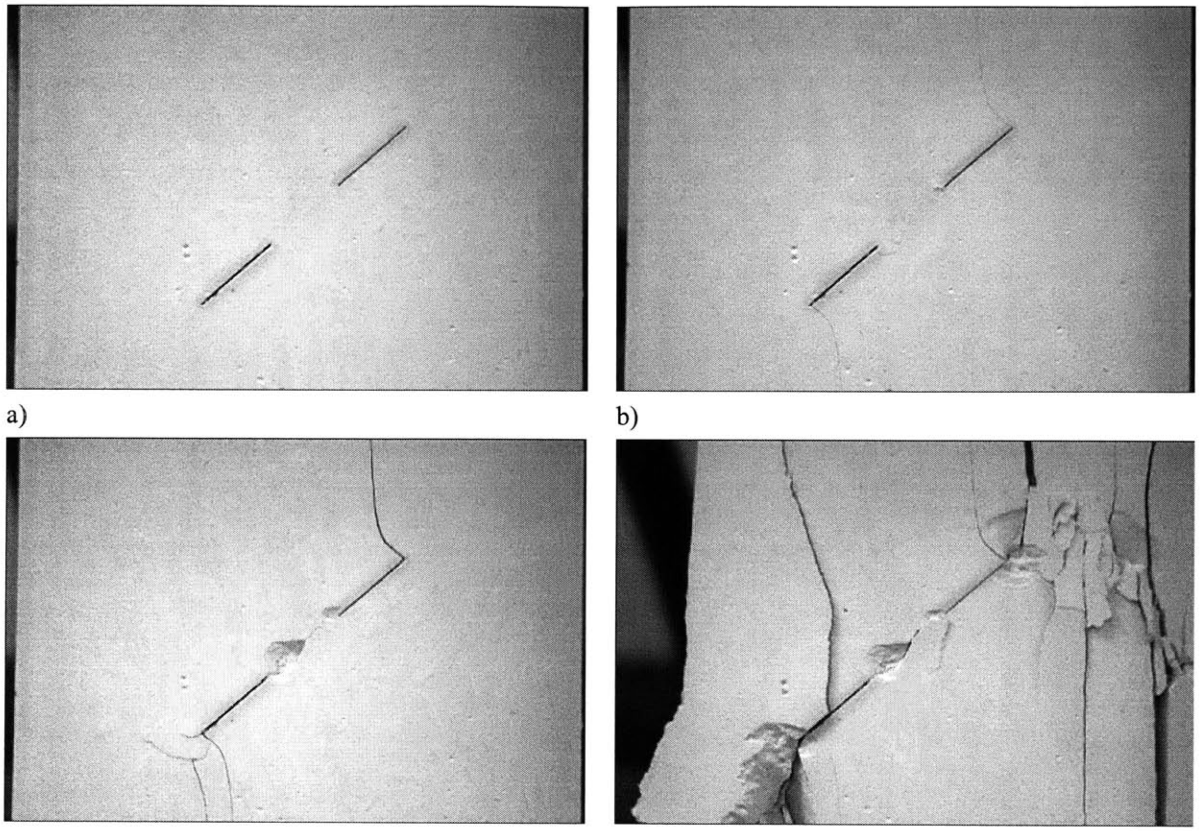

a)

b)

c)

d)

Figure D.39 Cracking sequence of 45-0-2a geometry in cyclic test. $\sigma_{max}/\sigma_c = 0.8$, $\sigma_{max} = 22.70$ MPa; a) Initial configuration b) External wing cracks initiate at the external tips of the flaws (2 cycles). Coalescence occurs (19 cycles). c) Surface spalling is visible at the internal tips of the flaws (207 cycles). Another tension crack accompanied by shear cracks occurs around the external tip of lower flaw (208 cycles). d) Failure occurs (216 cycles).

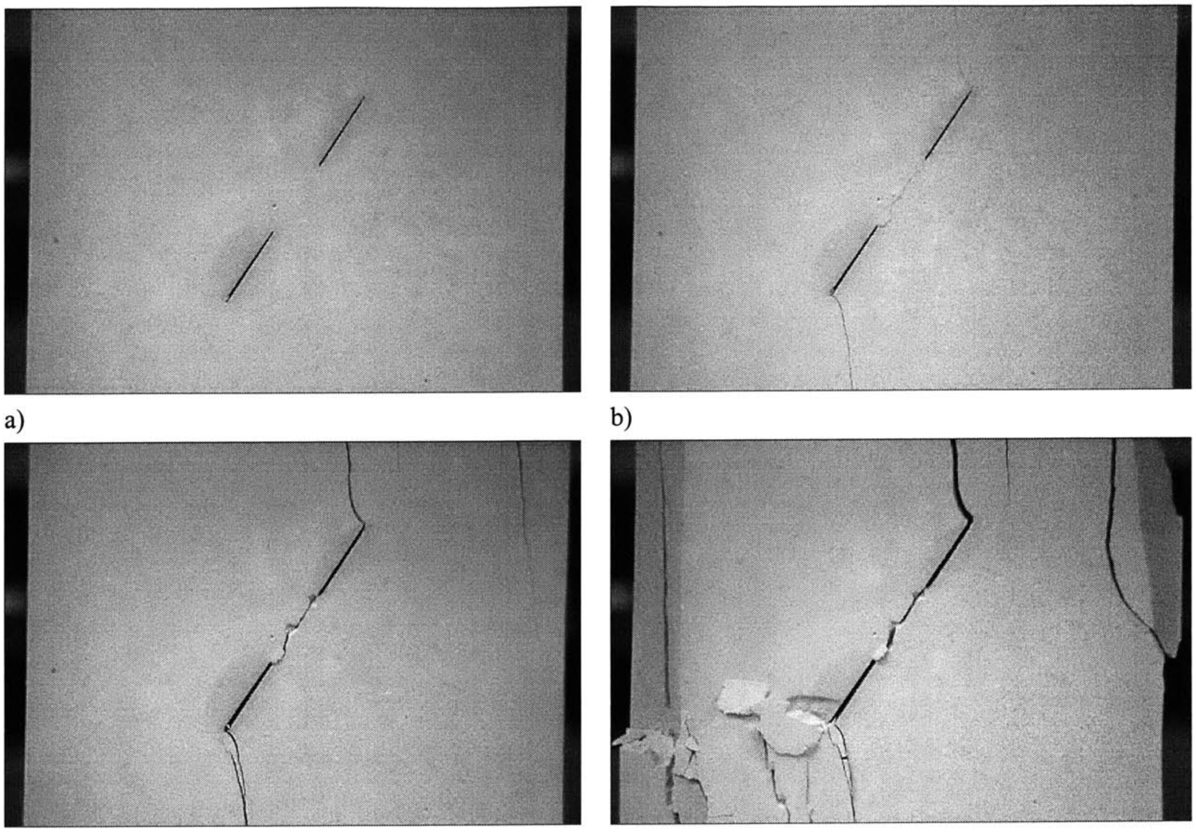

a) b) c) d)

Figure D.40 Cracking sequence of 60-0-2a geometry in cyclic test. $\sigma_{max}/\sigma_c = 0.8$, $\sigma_{max} = 25.25$ MPa; a) Initial configuration b) External wing cracks initiate at the external tips of the flaws (80 cycles). Coalescence occurs (80 cycles). c) Shear cracks occur around the external tip of the flaws (240 cycles). Vertical splitting occurs (255 cycles). d) Failure occurs (257 cycles).

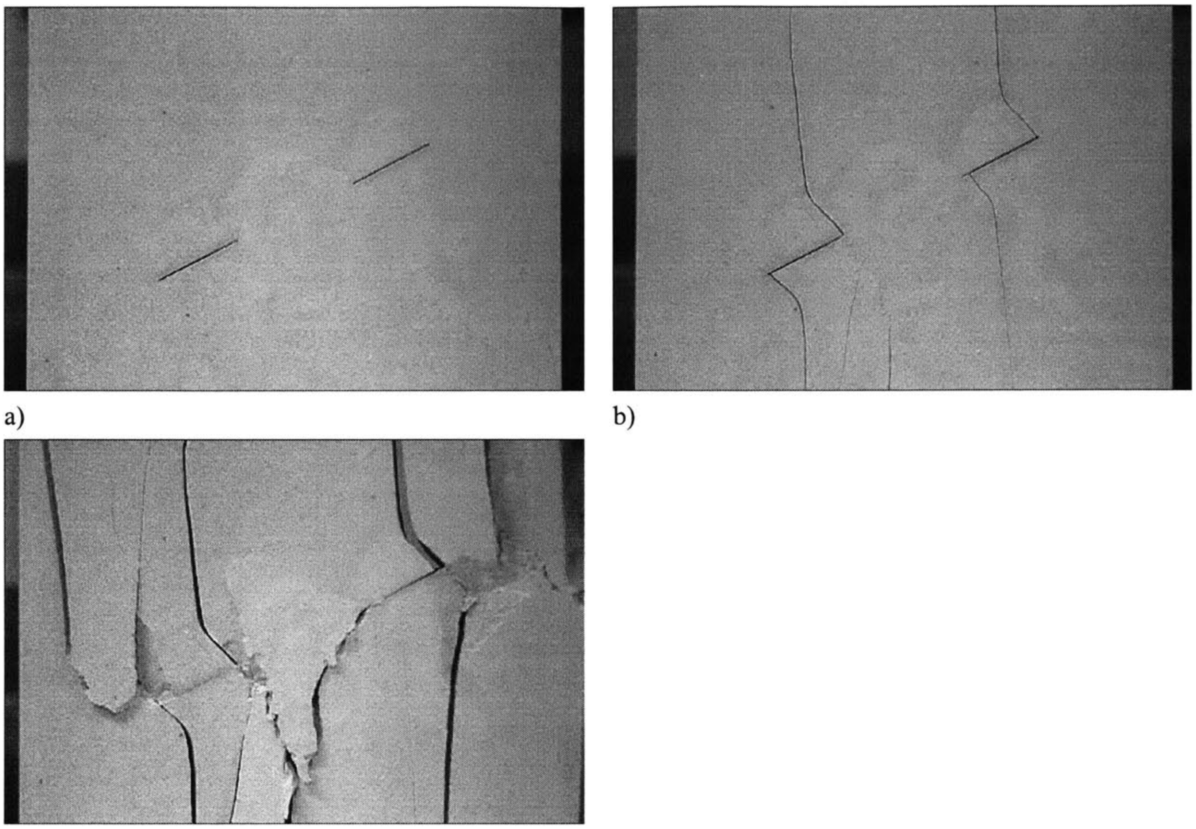

a)

b)

c)

Figure D.41 Cracking sequence of 30-0-3a geometry in cyclic test. $\sigma_{max}/\sigma_c = 0.8$, $\sigma_{max} = 23.49$ MPa; a) Initial configuration b) External and internal wing cracks initiate at the tips of the flaws (2 cycles). Another tension crack occurs around the internal tip of the lower flaw (686 cycles). c) Failure occurs (689 cycles). Coalescence does not occur.

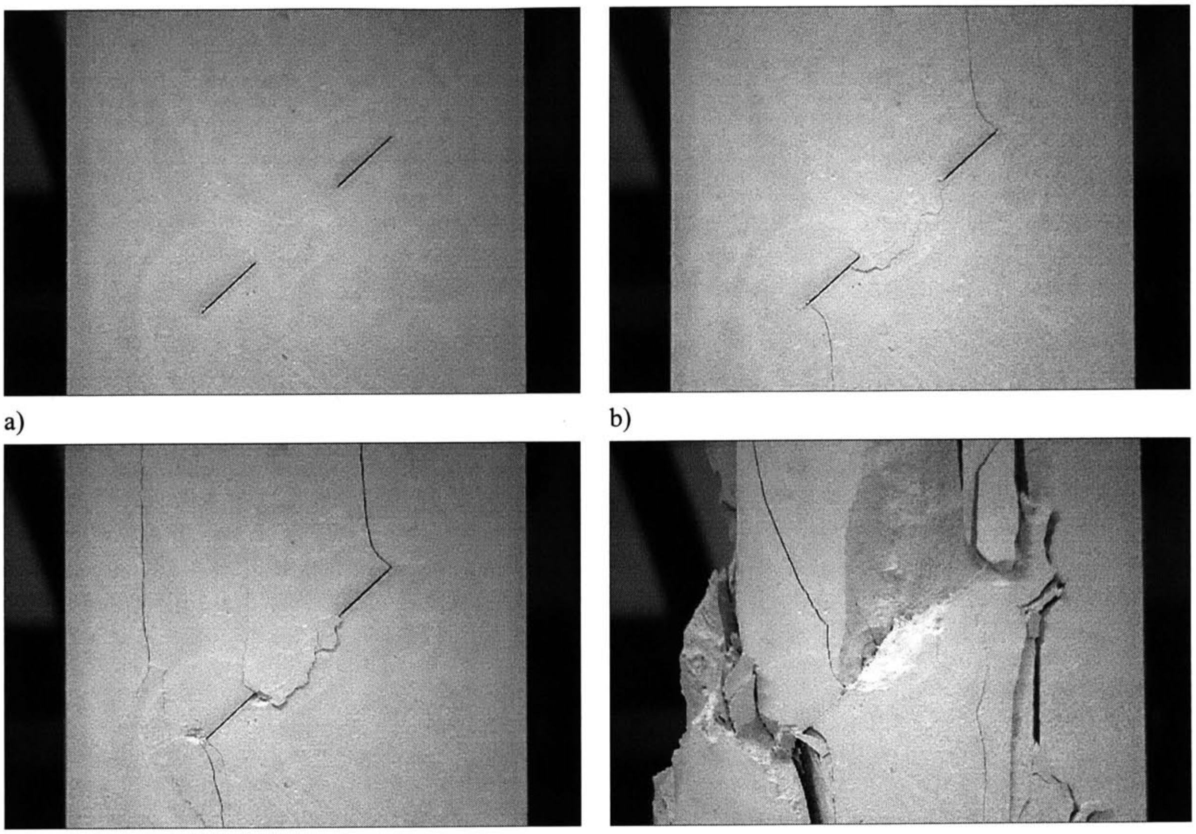

a)

b)

c)

d)

Figure D.42 Cracking sequence of 45-0-3a geometry in cyclic test. $\sigma_{max}/\sigma_c = 0.9$, $\sigma_{max} = 25.16$ MPa; a) Initial configuration b) External wing cracks initiate at the external tips of the flaws (5 cycles). Coalescence occurs (101 cycles). c) Another tension crack accompanied by shear cracks occurs around the external tip of the lower flaw (102 cycles). d) Failure occurs (105 cycles).

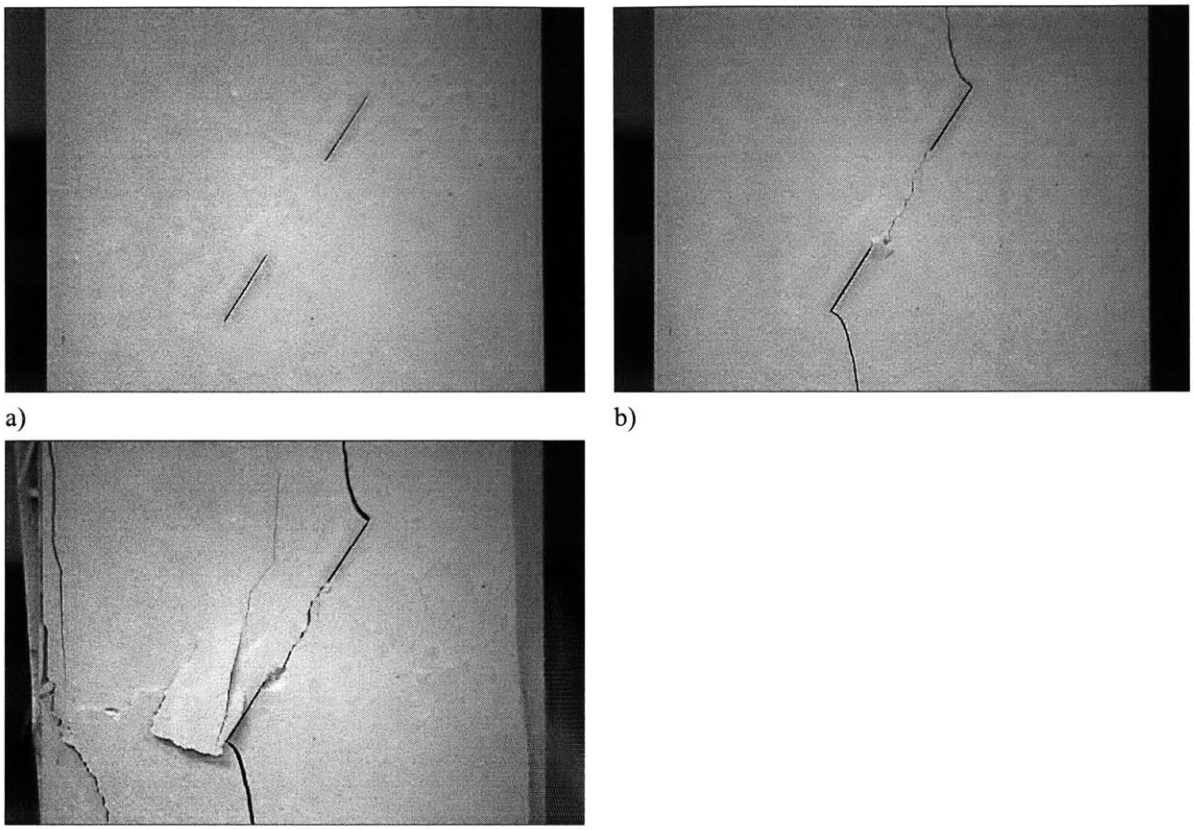

a)

b)

c)

Figure D.43 Cracking sequence of 60-0-3a geometry in cyclic test. $\sigma_{max}/\sigma_c = 0.8$, $\sigma_{max} = 24.62$ MPa; a) Initial configuration b) External wing cracks initiate at the external tips of the flaws (830 cycles). Coalescence occurs (831 cycles). c) Failure occurs (832 cycles).

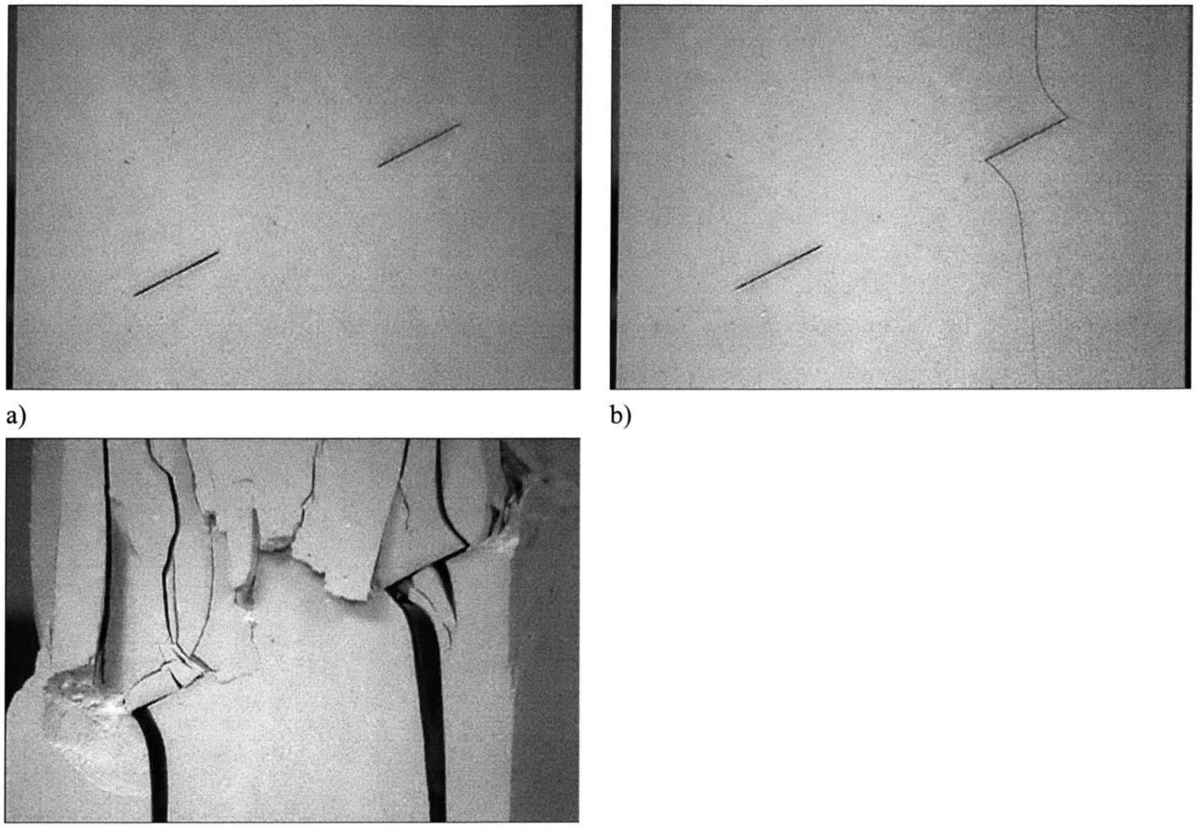

a)

b)

c)

Figure D.44 Cracking sequence of 30-0-4a geometry in cyclic test. $\sigma_{max}/\sigma_c = 0.8$, $\sigma_{max} = 25.13$ MPa; a) Initial configuration b) External and internal wing cracks initiate at the tips of the flaws (1 cycle). c) Failure occurs (567 cycles). Coalescence does not occur.

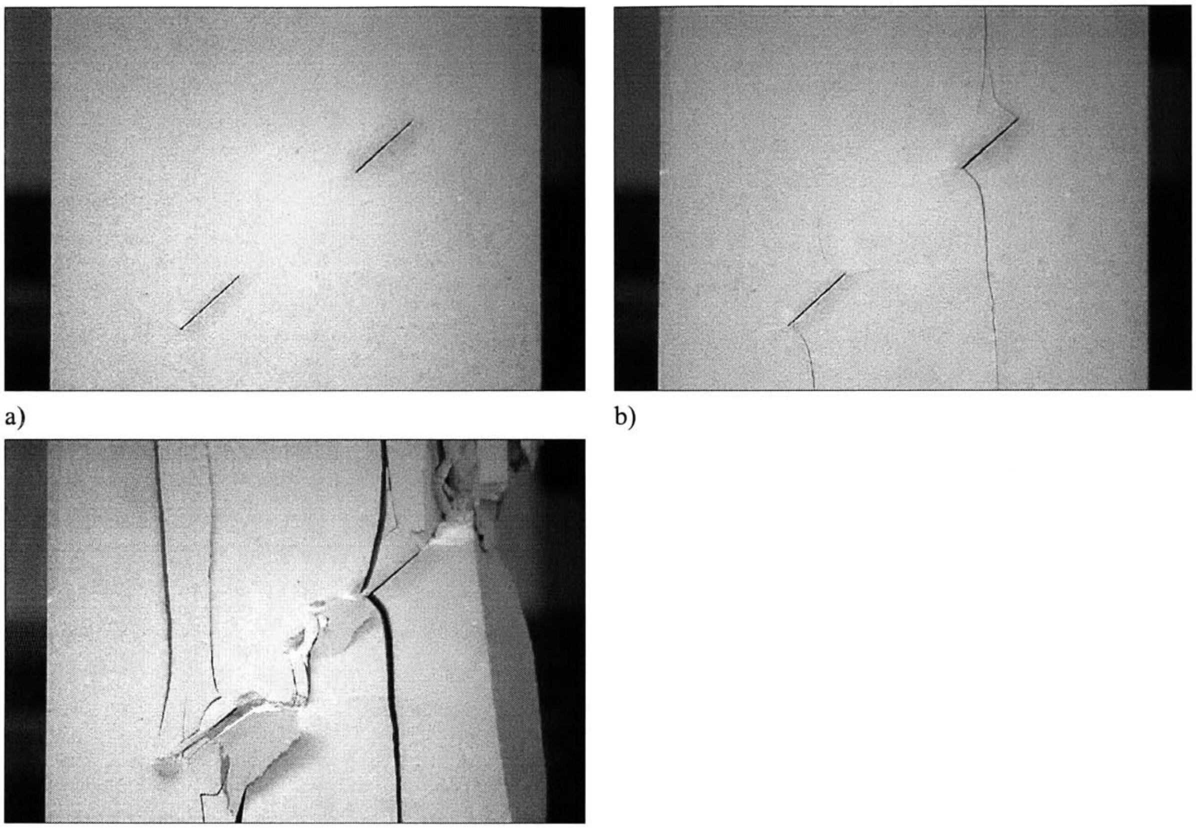

a)

b)

c)

Figure D.45 Cracking sequence of 45-0-4a geometry in cyclic test. $\sigma_{max}/\sigma_c = 0.85$, $\sigma_{max} = 28.62$ MPa; a) Initial configuration b) External and internal wing cracks initiate at the tips of the flaws (1 cycle). Another tension crack occurs around the internal tip of the upper flaw (14 cycles). Shear cracks occur at the tips of the flaws (14 cycles). c) Failure occurs (15 cycles). Coalescence does not occur.

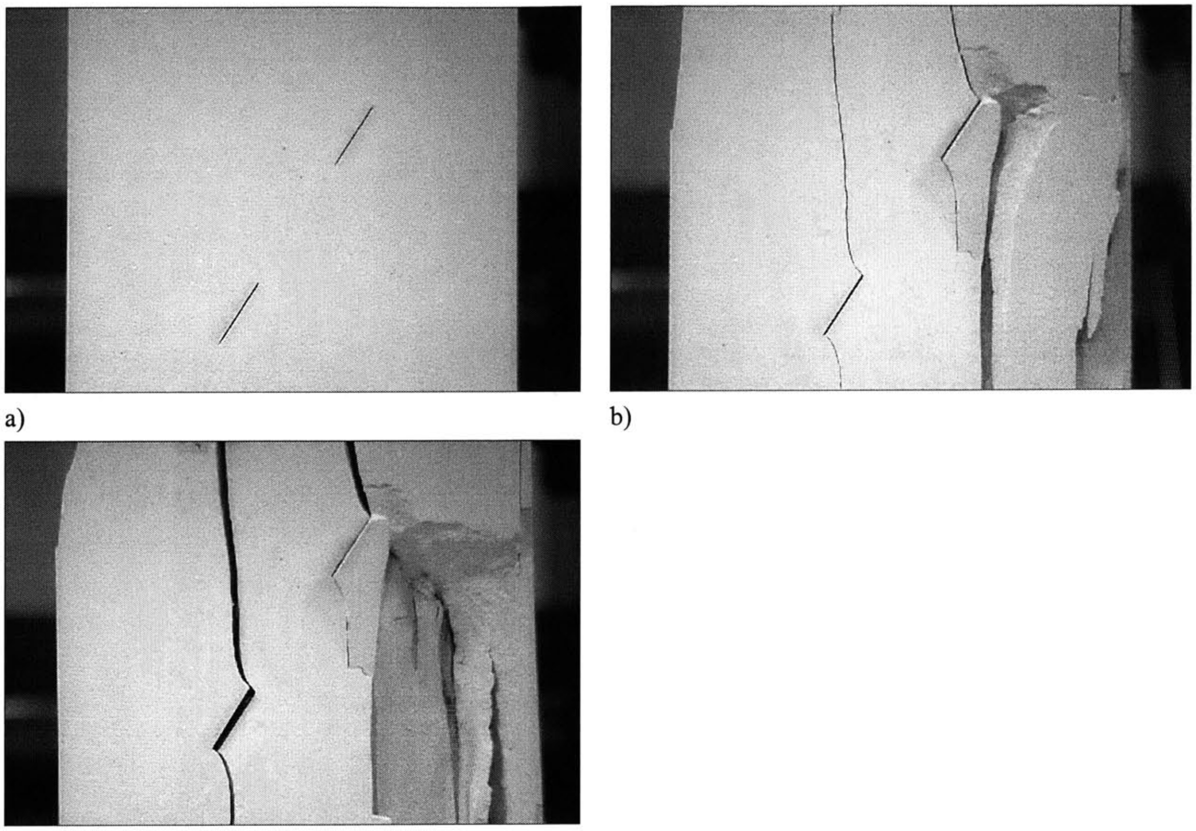

a)

b)

c)

Figure D.46 Cracking sequence of 60-0-4a geometry in cyclic test. $\sigma_{max}/\sigma_c = 0.8$, $\sigma_{max} = 28.84$ MPa; a) Initial configuration b) External and internal wing cracks initiate at the tips of the flaws (291 cycles). c) Failure occurs (292 cycles). Coalescence does not occur.

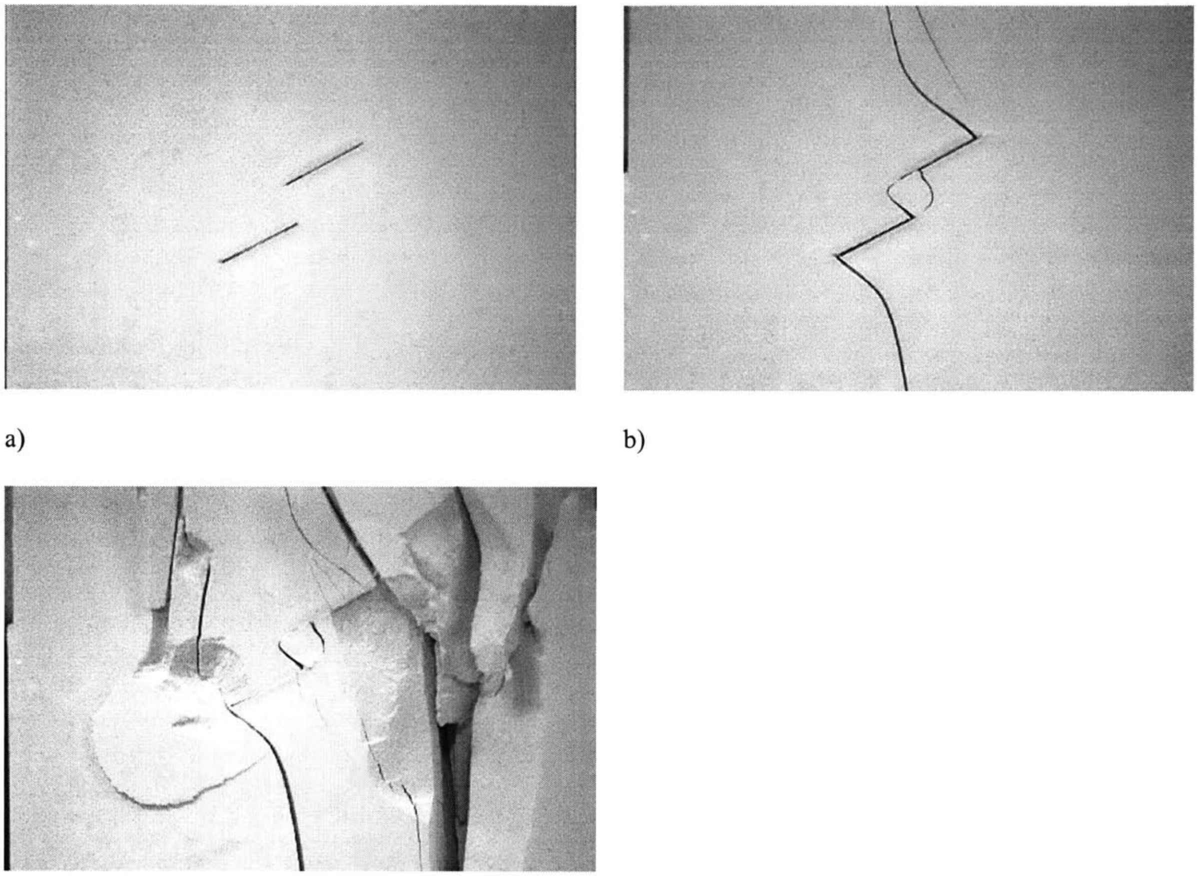

a)

b)

c)

Figure D.47 Cracking sequence of 30-a-0 geometry in cyclic test. $\sigma_{max}/\sigma_c = 0.85$, $\sigma_{max} = 20.87$ MPa; a) Initial configuration b) External and internal wing cracks initiate at the tips of the flaws (1 cycle). Coalescence occurs (1 cycle). Another tension crack occurs at the external tip of the upper flaw (25 cycles). c) Failure occurs (29 cycles).

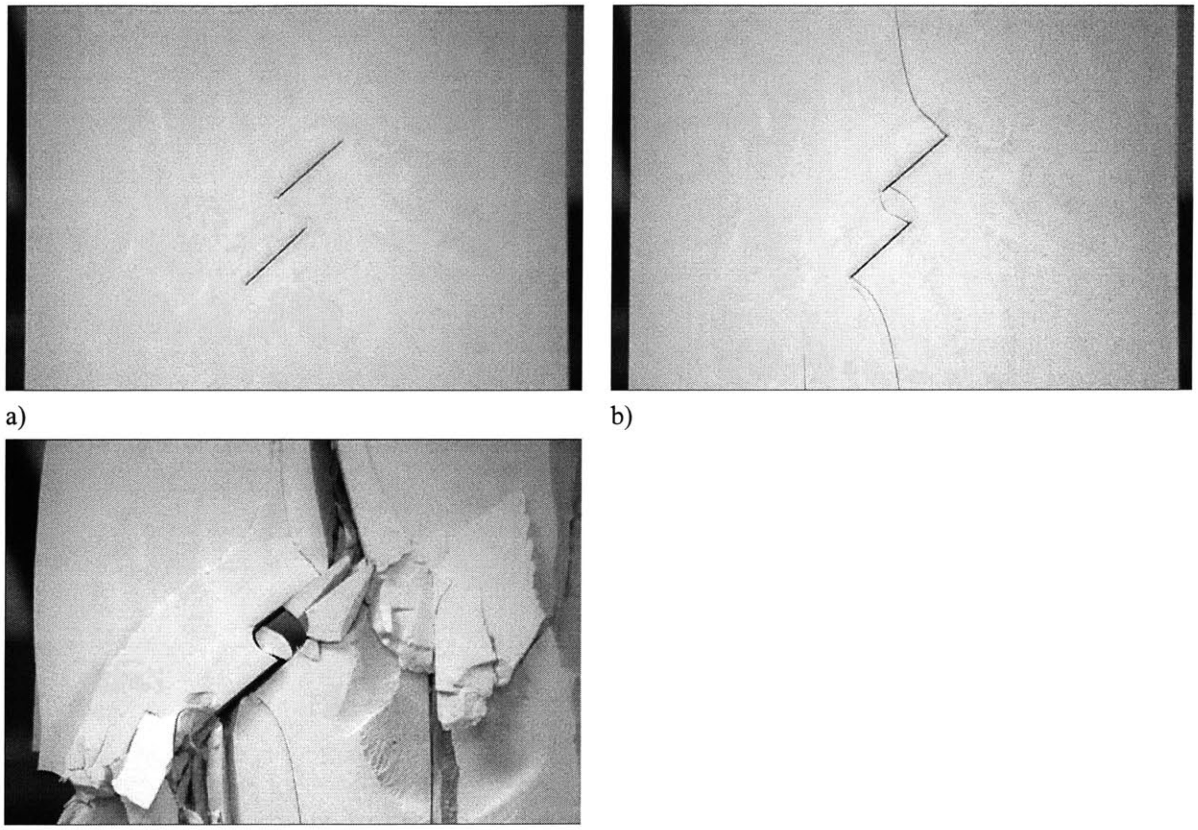

a)

b)

c)

Figure D.48 Cracking sequence of 45-a-0 geometry in cyclic test. $\sigma_{max}/\sigma_c = 0.9$, $\sigma_{max} = 26.17$ MPa; a) Initial configuration b) External and internal wing cracks initiate at the tips of the flaws (1 cycle). Coalescence occurs (1 cycle). Another tension crack occurs from the lower left crack tip (5 cycles). c) Failure occurs (63 cycles).

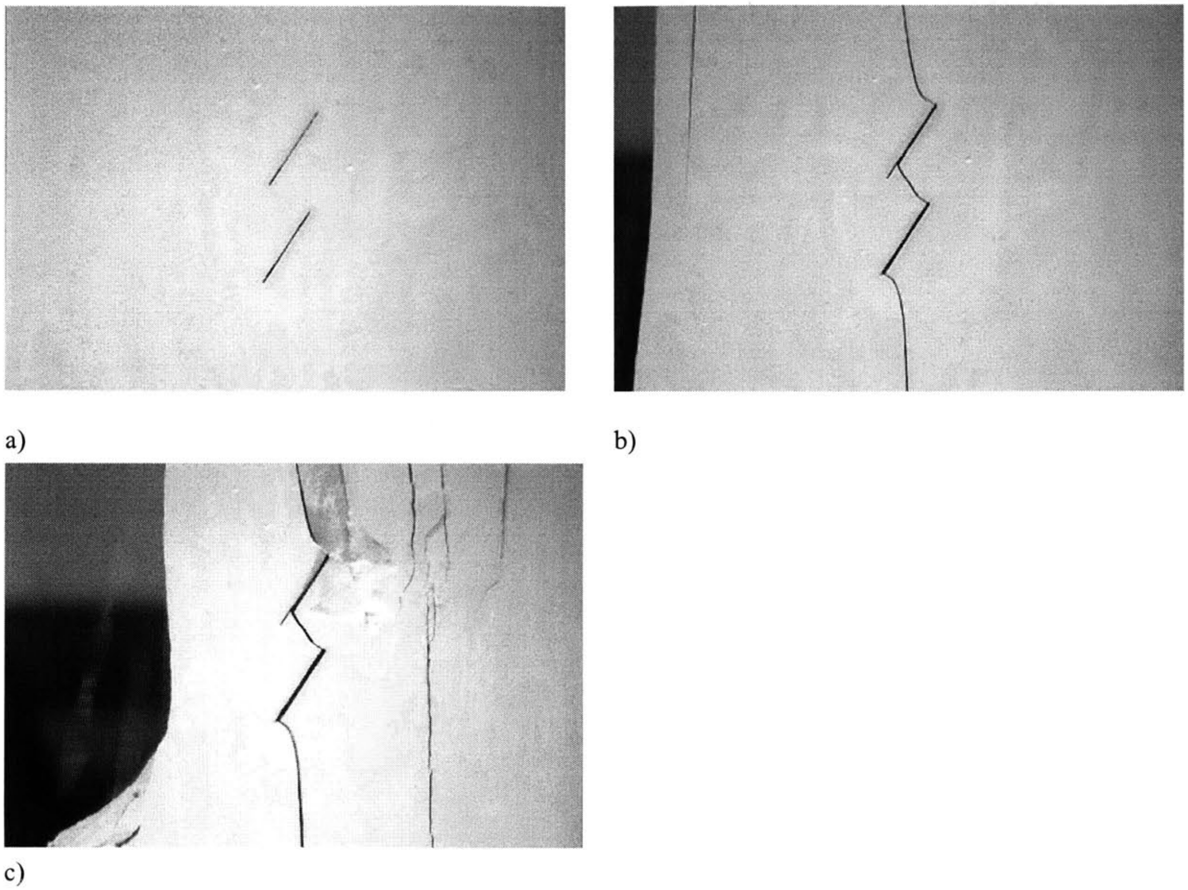
a)
b)
c)

Figure D.49 Cracking sequence of 60-a-0 geometry in cyclic test. $\sigma_{max}/\sigma_c = 0.85$, $\sigma_{max} = 27.73$ MPa; a) Initial configuration b) External wing cracks initiate at the external tips of the flaws (12 cycles). Coalescence occurs (12 cycles). Another tension crack occurs (20 cycles). c) Failure occurs (22 cycles).

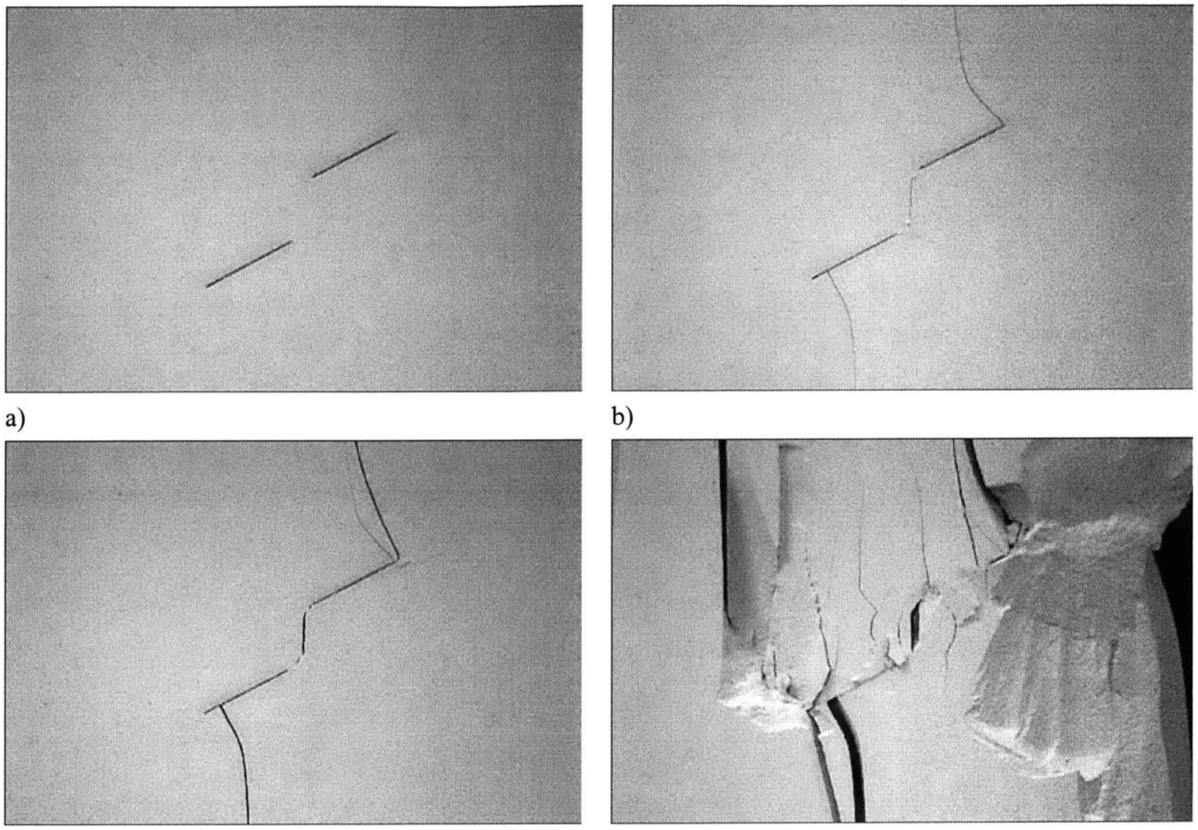

a)

b)

c)

d)

Figure D.50 Cracking sequence of 30-a-a geometry in cyclic test. $\sigma_{max}/\sigma_c = 0.85$, $\sigma_{max} = 19.85$ MPa; a) Initial configuration b) External wing cracks initiate at the external tips of the flaws (1 cycle). Coalescence occurs (1 cycle). c) Another tension crack occurs around the external tip of the upper flaw (4 cycles). An external shear crack occurs around the external tip of the upper flaw (7 cycles). d) Failure occurs (10 cycles).

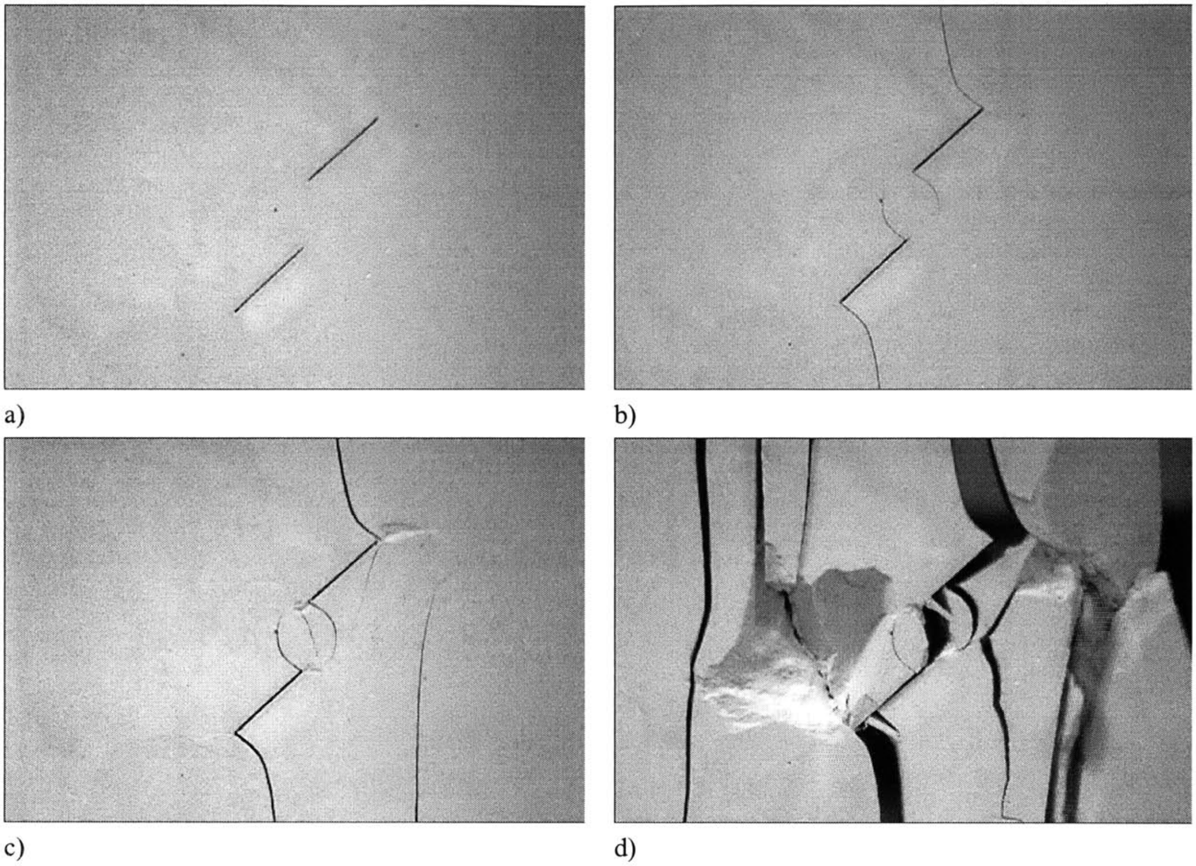

Figure D.51 Cracking sequence of 45-a-a geometry in cyclic test. $\sigma_{max}/\sigma_c = 0.8$, $\sigma_{max} = 22.97$ MPa; a) Initial configuration b) External and internal wing cracks initiate at the tips of the flaws (1 cycle). c) Another tension crack accompanied by shear cracks occurs around the external tip of the upper flaw (1189 cycles). Coalescence occurs (1196 cycles). d) Failure occurs (1202 cycles).

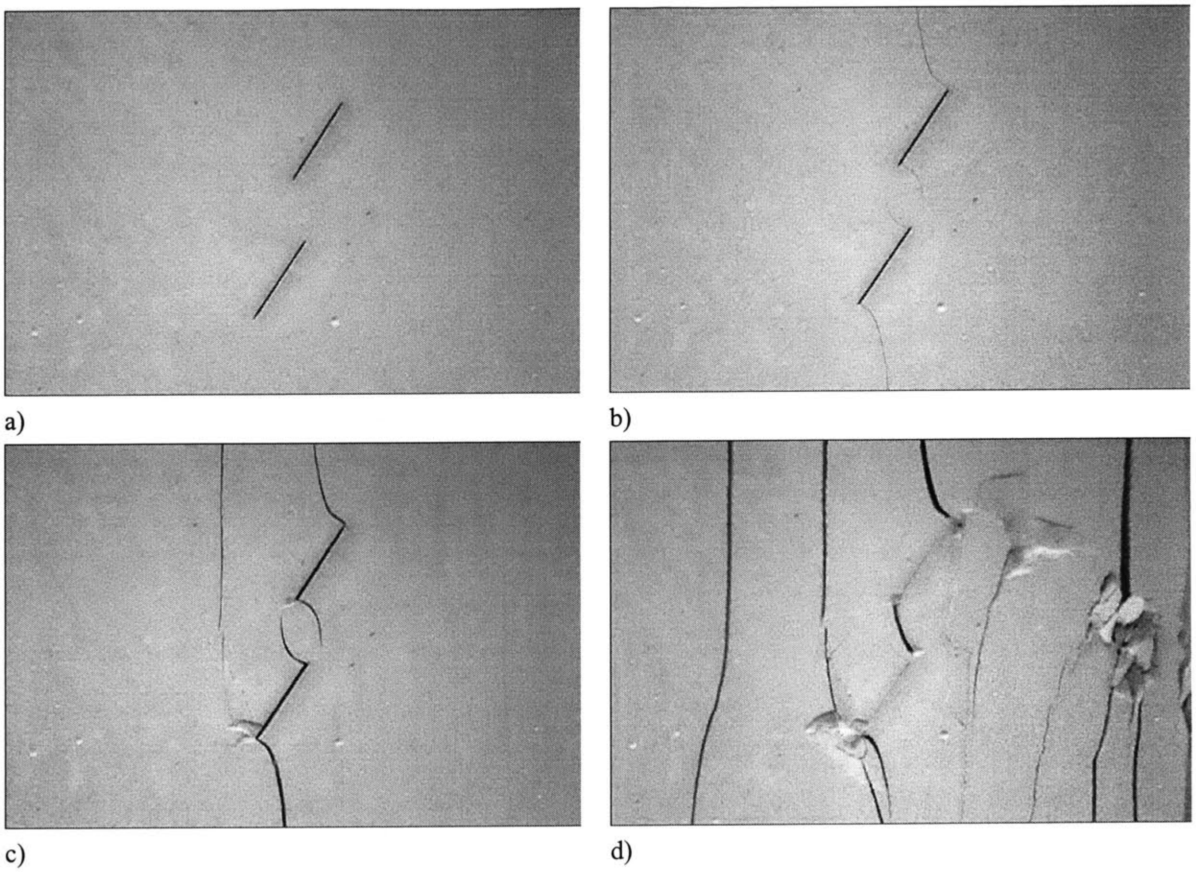

Figure D.52 Cracking sequence of 60-a-a geometry in cyclic test. $\sigma_{max}/\sigma_c = 0.8$, $\sigma_{max} = 28.08$ MPa; a) Initial configuration b) External and internal wing cracks initiate at the tips of the flaws (2 cycles). c) Another tension crack accompanied by shear cracks occurs around the external tip of the lower flaw (613 cycles). d) Coalescence occurs (615 cycles). Failure occurs (615 cycles).

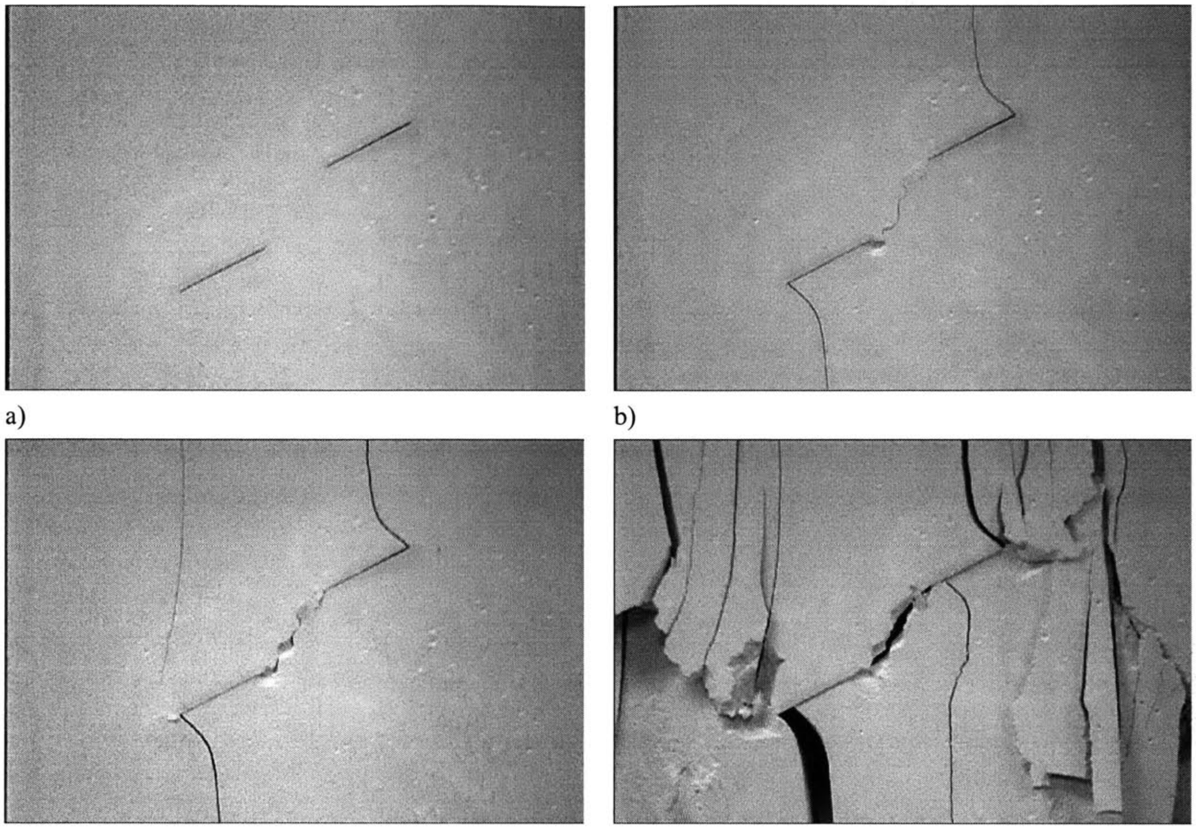

a) b) c) d)

Figure D.53 Cracking sequence of 30-a-2a geometry in cyclic test. $\sigma_{max}/\sigma_c = 0.9$, $\sigma_{max} = 22.02$ MPa; a) Initial configuration b) External wing cracks initiate at the external tips of the flaws (2 cycles). Coalescence occurs (3 cycles). c) Another tension crack accompanied by shear cracks occurs around the external tip of the lower flaw (5 cycles). d) Failure occurs (8 cycles).

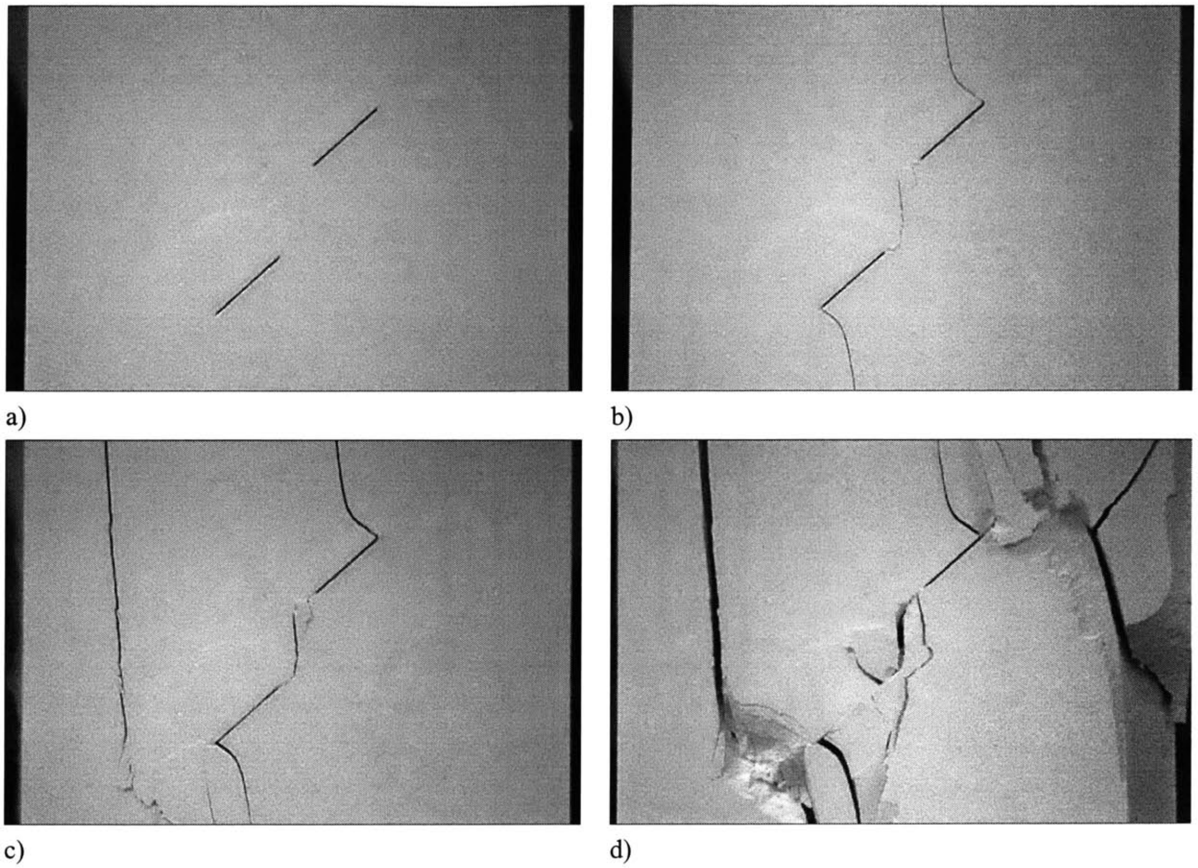

Figure D.54 Cracking sequence of 45-a-2a geometry in cyclic test. $\sigma_{max}/\sigma_c = 0.9$, $\sigma_{max} = 24.36$ MPa; a) Initial configuration b) External wing cracks initiate at the external tips of the flaws (2 cycles). Coalescence occurs (2 cycles). c) Another tension crack accompanied by shear cracks occurs around the external tip of the lower flaw (10 cycles). A vertical tension crack occurs at the left side (11 cycles). d) Failure occurs (12 cycles).

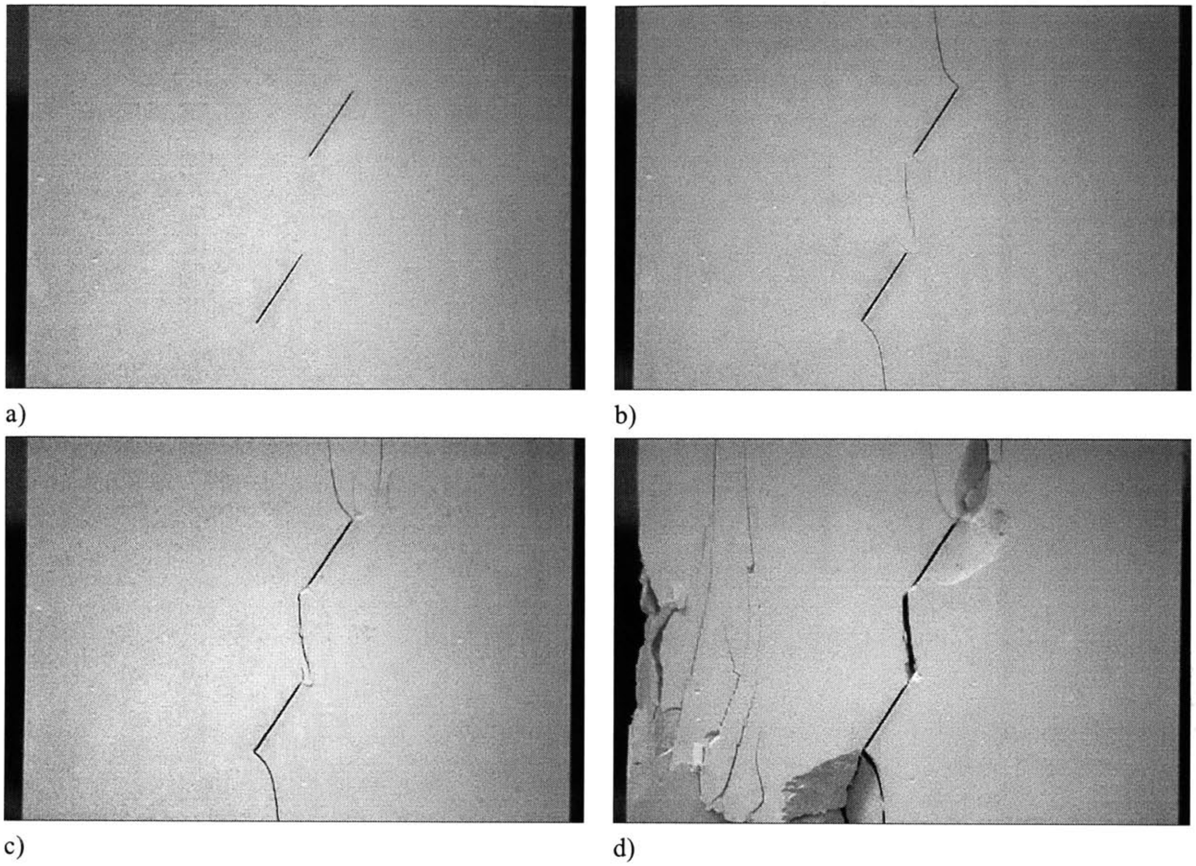

Figure D.55 Cracking sequence of 60-a-2a geometry in cyclic test. $\sigma_{max}/\sigma_c = 0.85$, $\sigma_{max} = 28.96$ MPa; a) Initial configuration b) External and internal wing cracks initiate at the tips of the flaws (5 cycles). Coalescence occurs (29 cycles). c) Another tension crack accompanied by shear cracks occurs around the external tip of the upper flaw (36 cycles). d) Failure occurs (37 cycles).

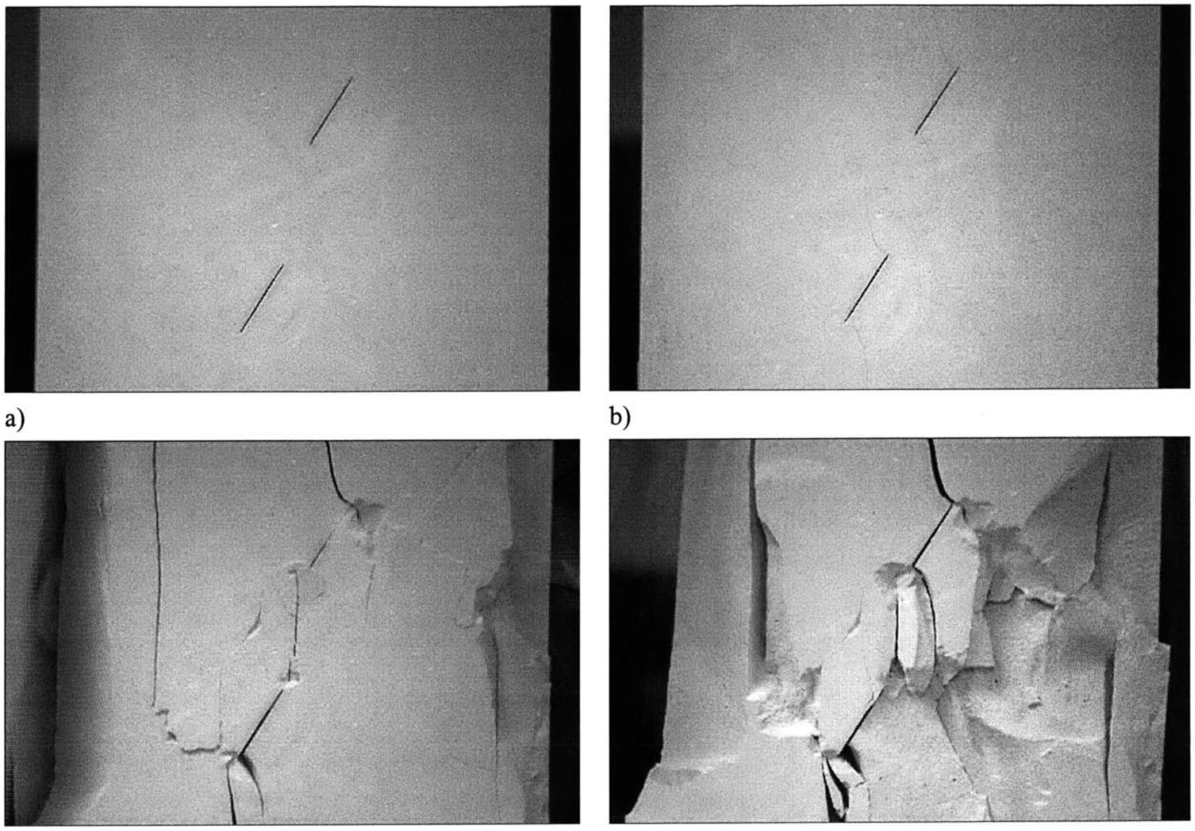

a)

b)

c)

d)

Figure D.56 Cracking sequence of 60-a-3a geometry in cyclic test. $\sigma_{max}/\sigma_c = 0.85$, $\sigma_{max} = 28.69$ MPa; a) Initial configuration b) External and internal wing cracks initiate at the tips of the flaws (154 cycles). c) Another tension crack occurs in the left side (156 cycles). Coalescence occurs (157 cycles). d) Failure occurs (158 cycles).

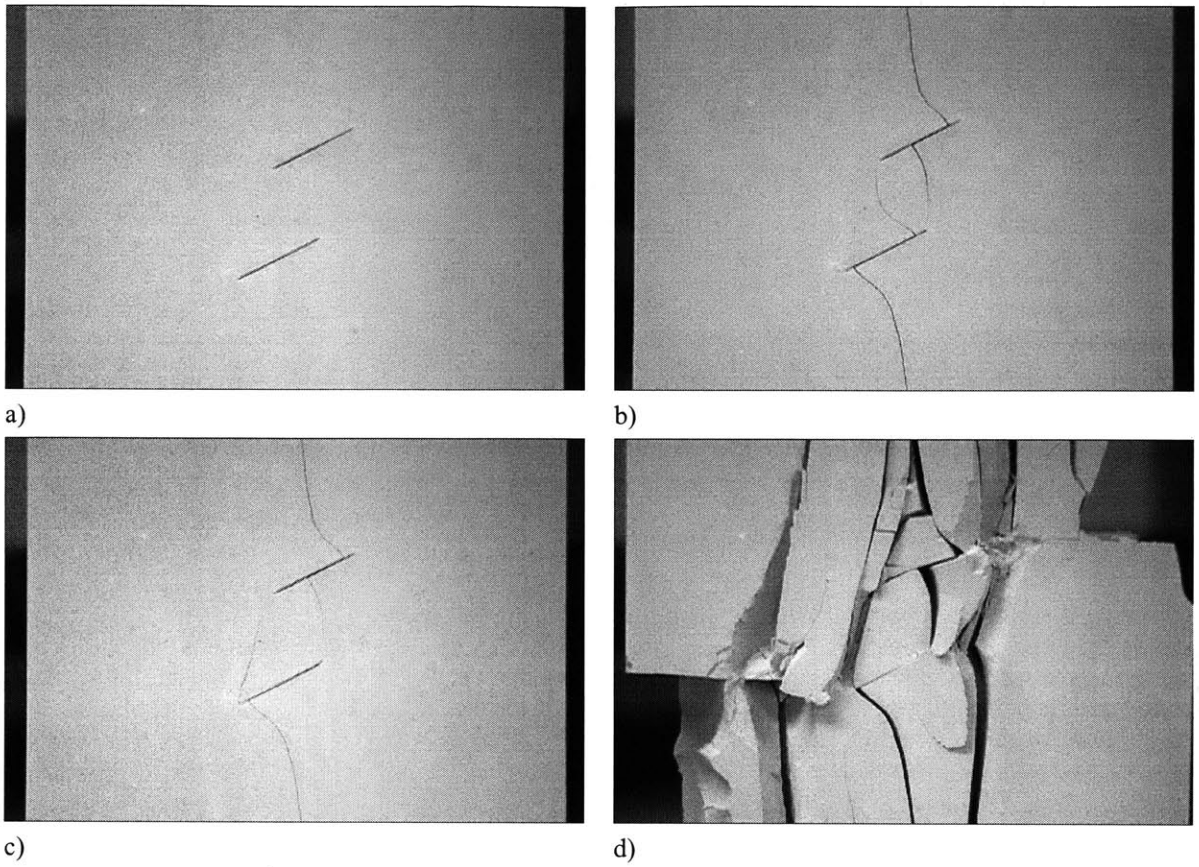

Figure D.57 Cracking sequence of 30-2a-0 geometry in cyclic test. $\sigma_{max}/\sigma_c = 0.85$, $\sigma_{max}= 26.18$ MPa; a) Initial configuration b) External and internal wing cracks initiate at the tips of the flaws (1 cycle). Coalescence occurs (19 cycles). c) Another tension cracks occur around the external tip of the lower flaw (640 cycles). d) Failure occurs (728 cycles).

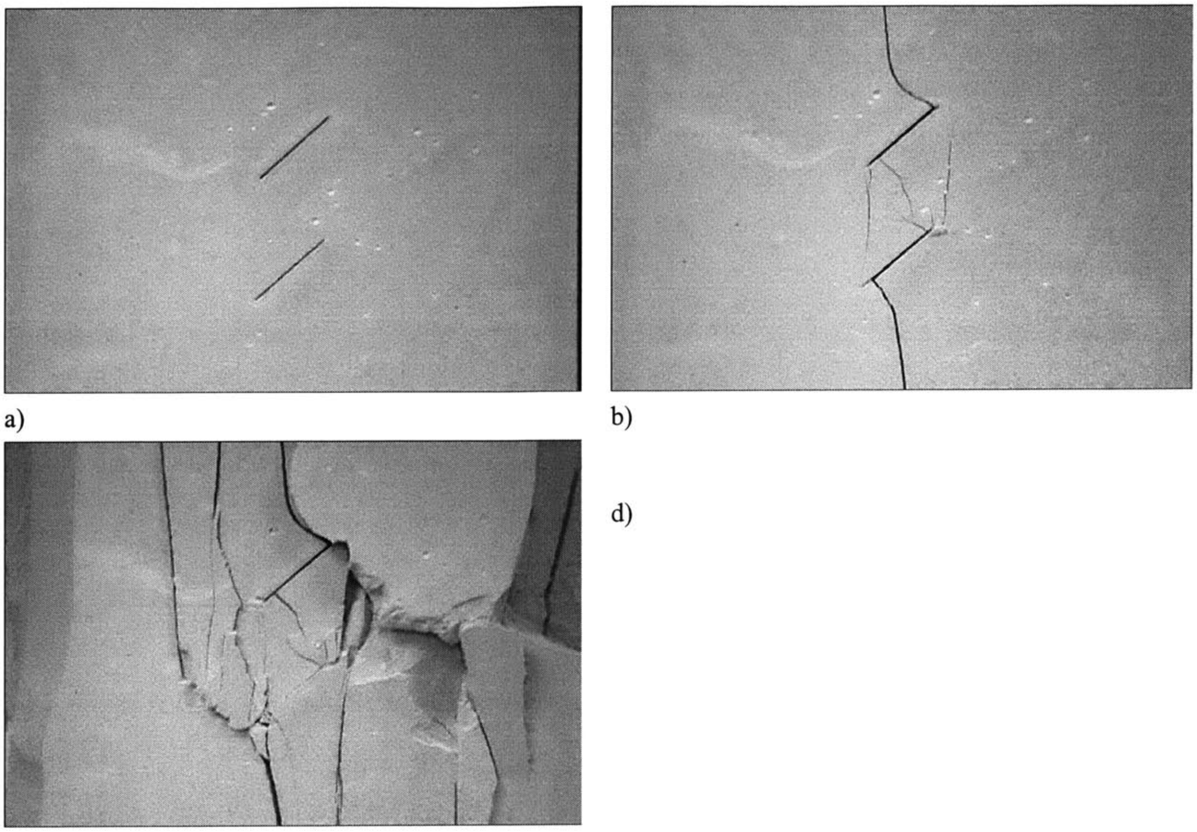

a)

b)

d)

c)

Figure D.58 Cracking sequence of 45-2a-0 geometry in cyclic test. $\sigma_{max}/\sigma_c = 0.9$, $\sigma_{max} = 33.73$ MPa; a) Initial configuration b) External and internal wing cracks initiate at the tips of the flaws (1 cycle). Another tension crack accompanied by shear cracks occurs around the internal tip of the lower flaw (45 cycles). Another tension crack accompanied by shear cracks occurs at the internal tip of the upper flaw (271 cycles). Coalescence occurs (271 cycles). c) Failure occurs (288 cycles).

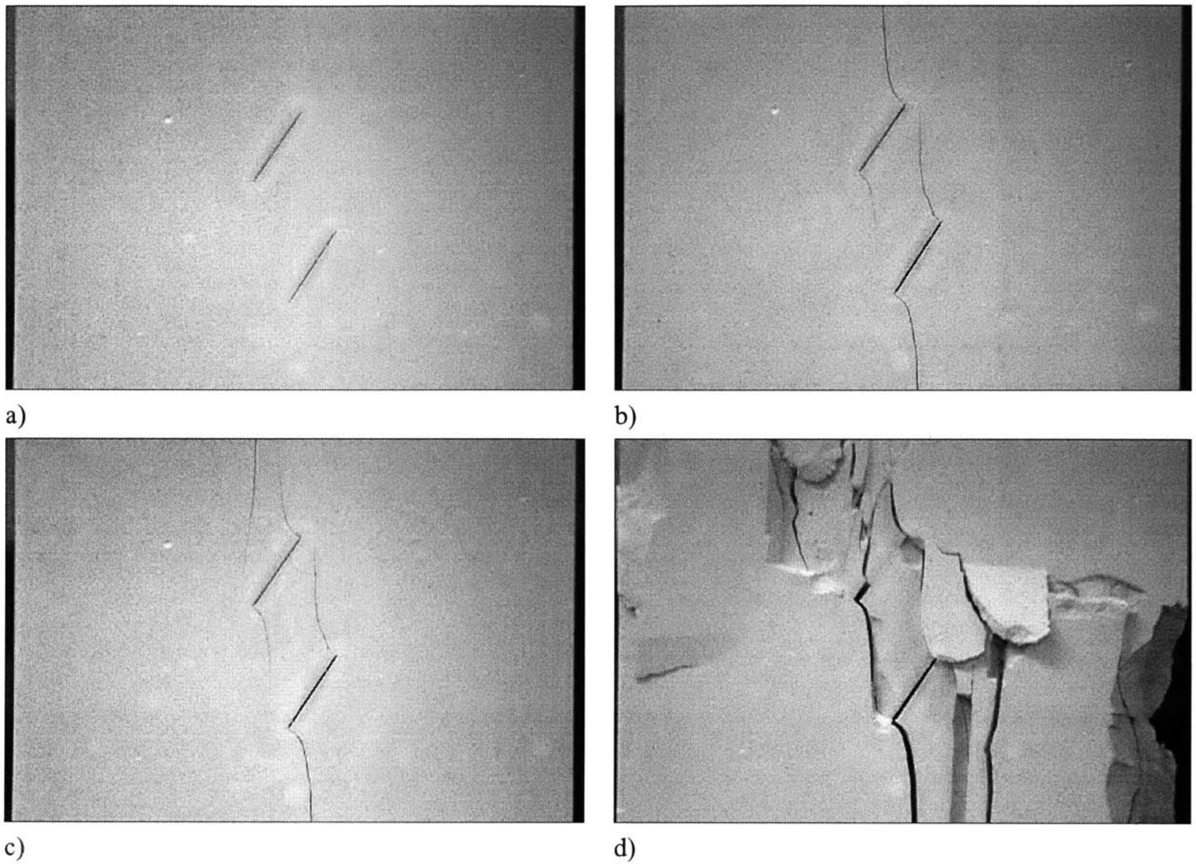

a) b) c) d)

Figure D.59 Cracking sequence of 60-2a-0 geometry in cyclic test. $\sigma_{max}/\sigma_c = 0.9$, $\sigma_{max} = 35.58$ MPa; a) Initial configuration b) External and internal wing cracks initiate at the tips of the flaws (1 cycle). c) Another tension crack occurs around the internal tip of the upper flaw (25 cycles). Coalescence occurs (25 cycles). d) Failure occurs (29 cycles).

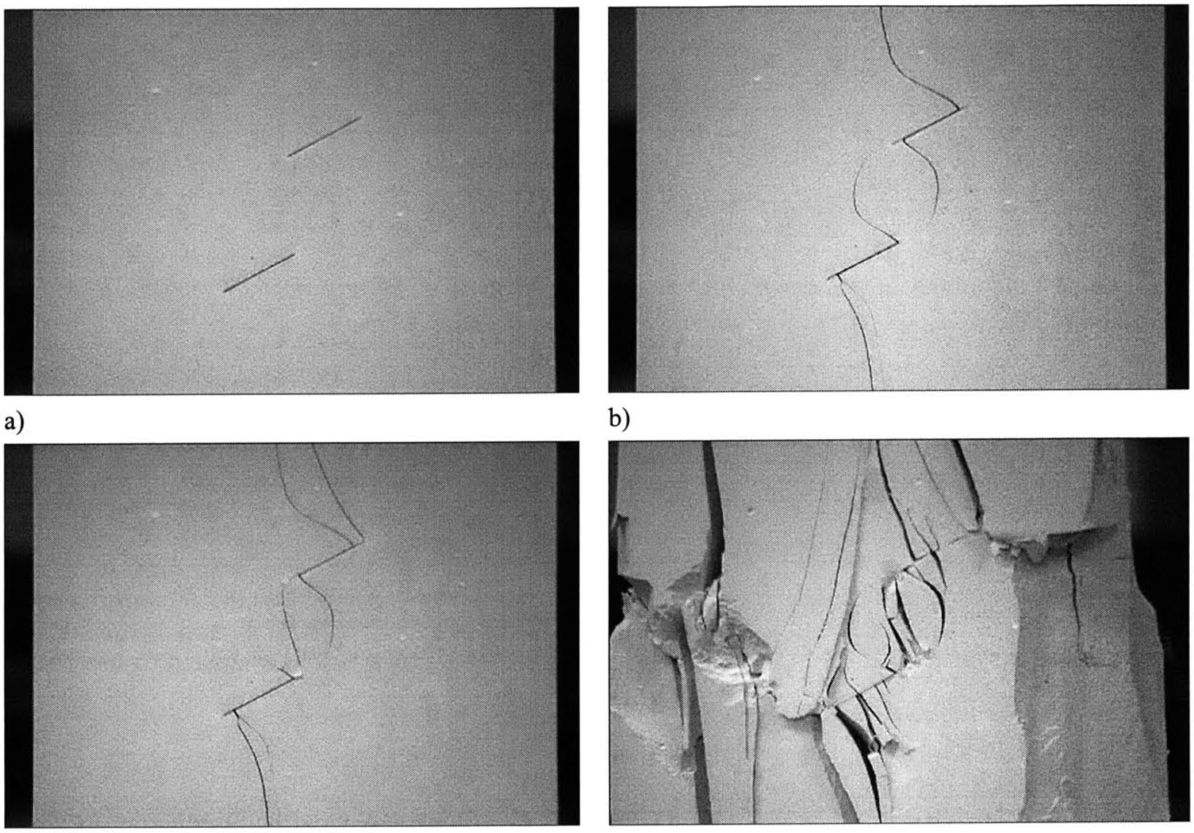

a)

b)

c)

d)

Figure D.60 Cracking sequence of 30-2a-a geometry in cyclic test. $\sigma_{max}/\sigma_c = 0.9$, $\sigma_{max} = 31.02$ MPa; a) Initial configuration b) External and internal wing cracks initiate at the tips of the flaws (1 cycle). c) Coalescence occurs (2 cycles). Another tension crack occurs at the external tip of the upper flaw (2 cycles). d) Failure occurs (6 cycles).

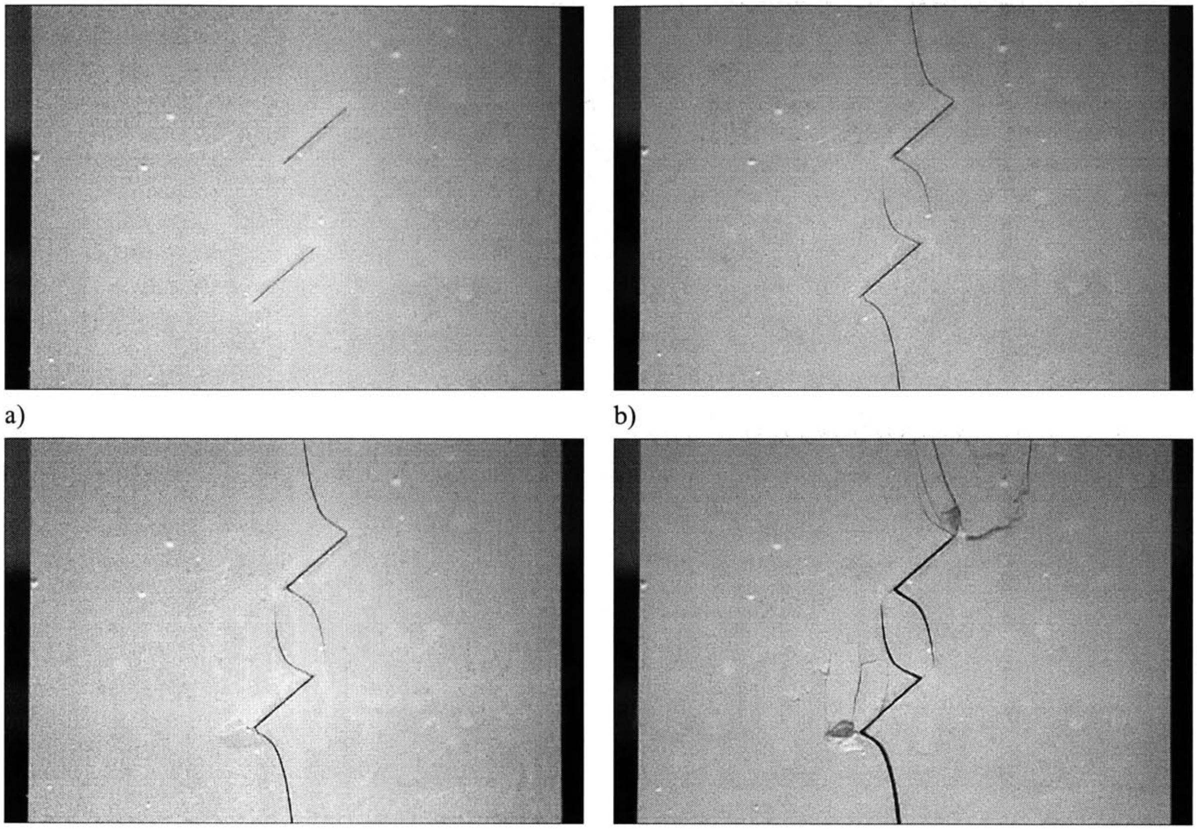

a) b) c) d)

Figure D.61 Cracking sequence of 45-2a-a geometry in cyclic test. $\sigma_{max}/\sigma_c = 0.85$, $\sigma_{max} = 33.00$ MPa; a) Initial configuration b) External and internal wing cracks initiate at the tips of the flaws (1 cycle). c) Coalescence occurs (30 cycles). External shear cracks occur at the external tips of the flaws (30 cycles). d) Failure occurs (88 cycles).

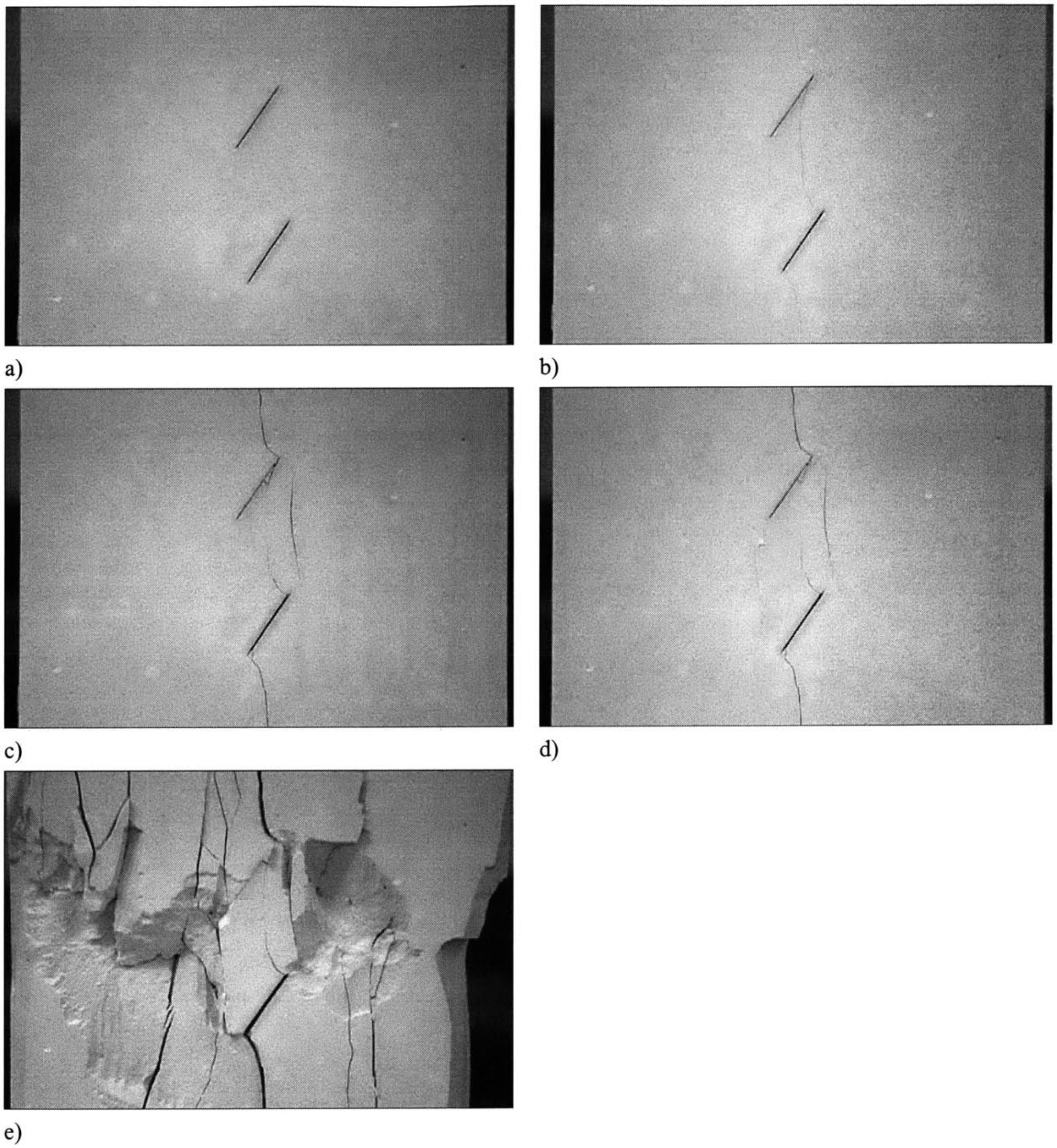

Figure D.62 Cracking sequence of 60-2a-a geometry in cyclic test. $\sigma_{max}/\sigma_c = 0.85$, $\sigma_{max} = 35.82$ MPa; a) Initial configuration b) External wing cracks initiate at the external tips of the flaws (1 cycle). Internal wing cracks initiate at the external tip of the upper flaw and the internal tip of the lower flaw (1 cycle). c) Another tension crack occurs between the external tip of the upper flaw and the internal tip of the lower flaw (1682 cycles). d) Another tension crack occurs between the external tip of the lower flaw and the internal tip of the upper flaw (1722 cycles). e) Failure occurs (1995 cycles). Coalescence occurs (1995 cycles).

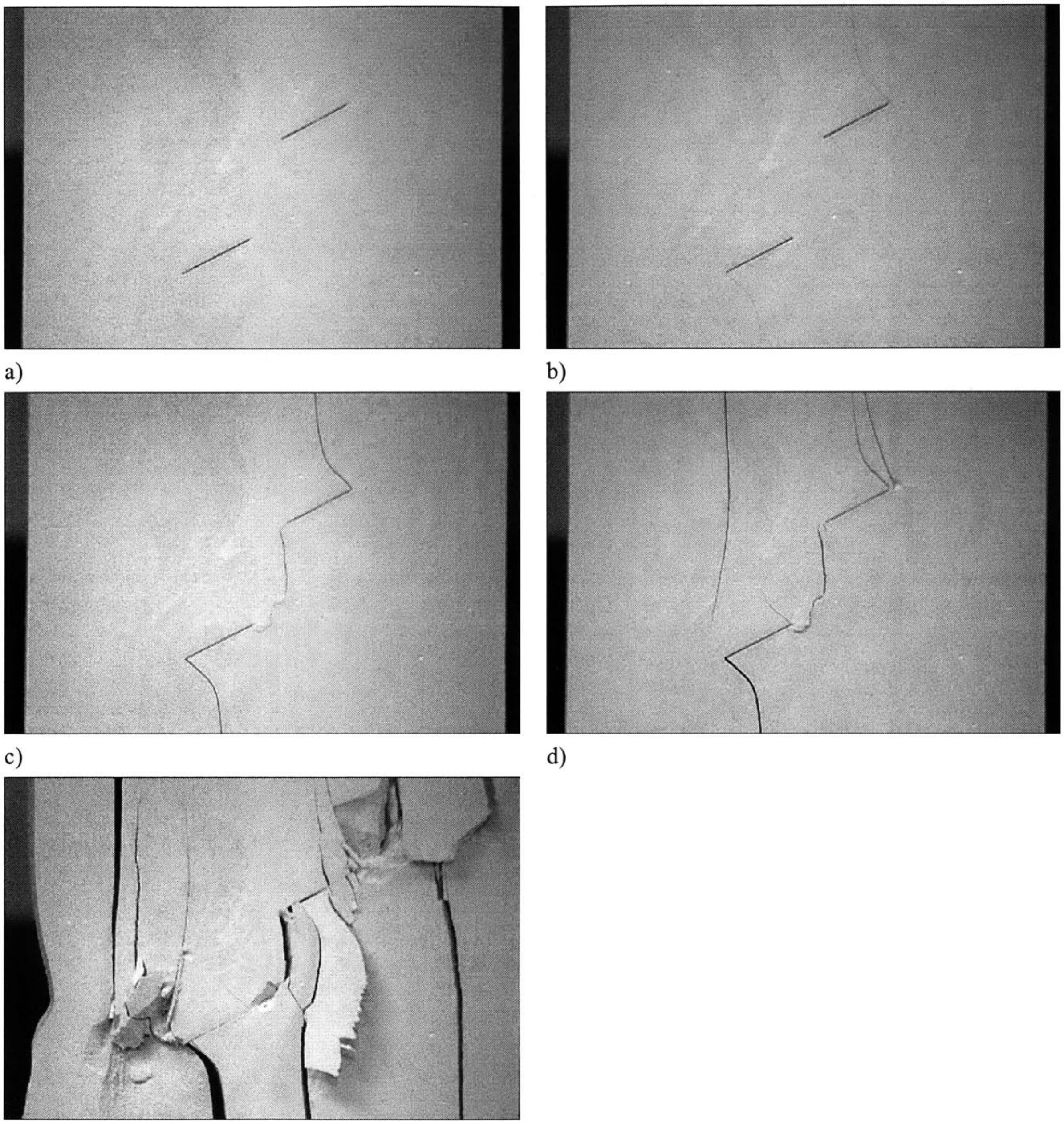

a) b) c) d) e)

Figure D.63 Cracking sequence of 30-2a-2a geometry in cyclic test. $\sigma_{max}/\sigma_c = 0.9$, $\sigma_{max} = 22.28$ MPa; a) Initial configuration b) External and internal wing cracks initiate (1 cycle). c) Coalescence occurs (2 cycles). d) Another tension crack occurs around the external tip of the upper flaw (3 cycles). Another tension crack occurs around the external tip of the lower flaw (11 cycles). Shear cracks are developed at the external tip of the flaws (11 cycles). e) Failure occurs (16 cycles).

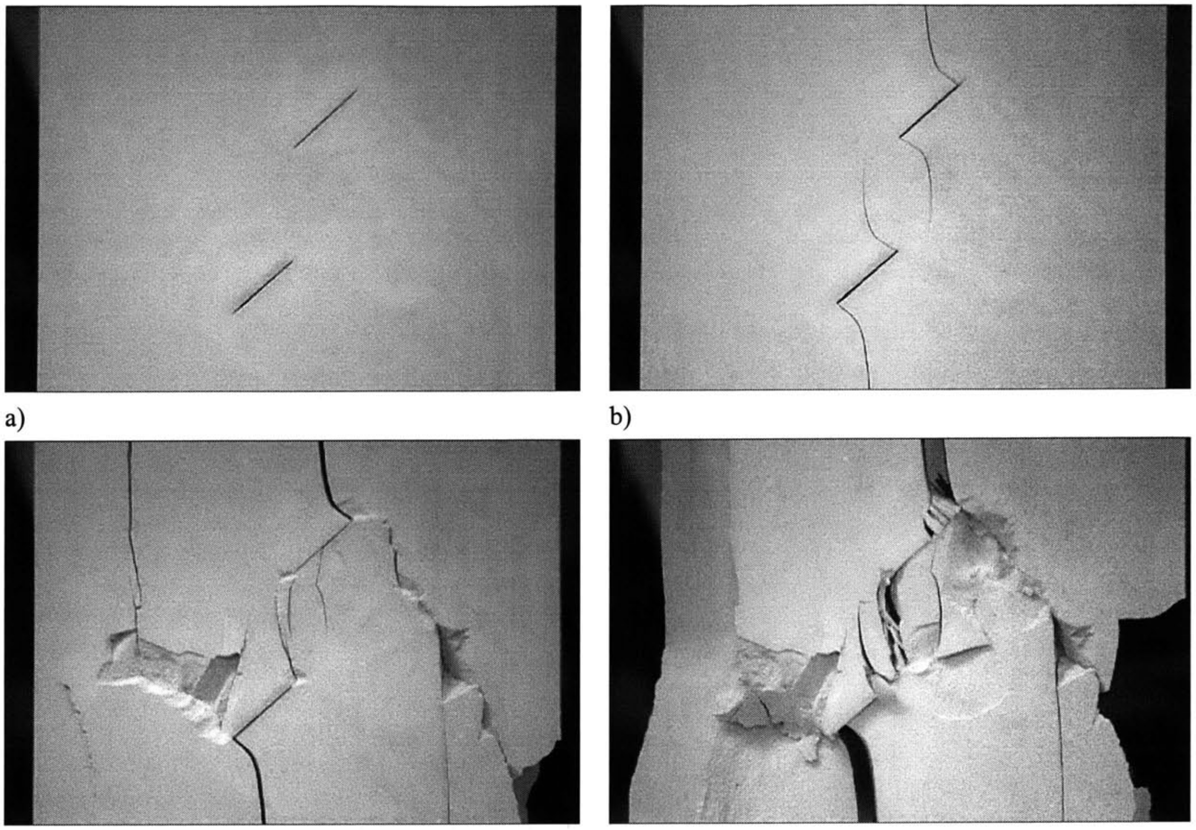

a)

b)

c)

d)

Figure D.64 Cracking sequence of 45-2a-2a geometry in cyclic test. $\sigma_{max}/\sigma_c = 0.85$, $\sigma_{max} = 24.42$ MPa; a) Initial configuration b) External and internal wing cracks initiate (1 cycle). c) Coalescence occurs (259 cycles). d) Failure occurs (260 cycles).

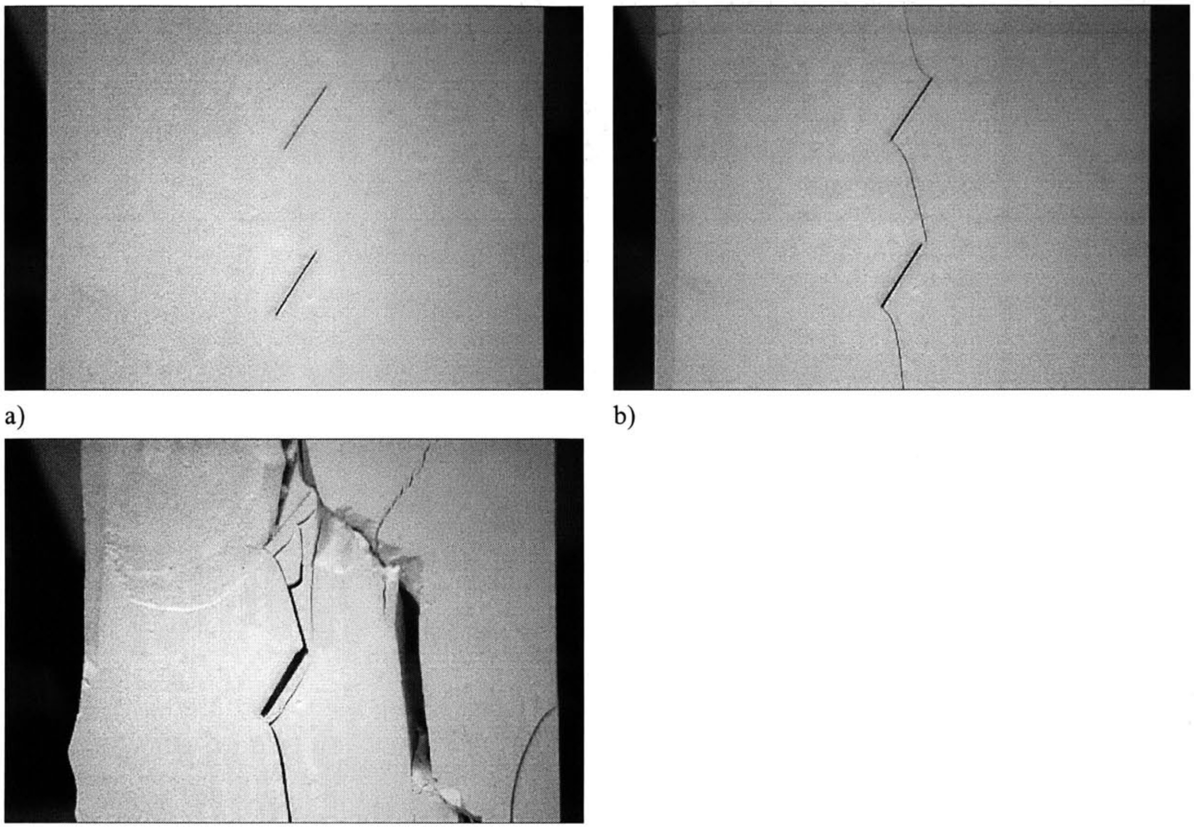

a)

b)

c)

Figure D.65 Cracking sequence of 60-2a-2a geometry in cyclic test. $\sigma_{max}/\sigma_c = 0.9$, $\sigma_{max} = 27.94$ MPa; a) Initial configuration b) External wing cracks initiate at the external tips of the flaws (3 cycles). Coalescence occurs (3 cycles).c) Failure occurs (5 cycles).

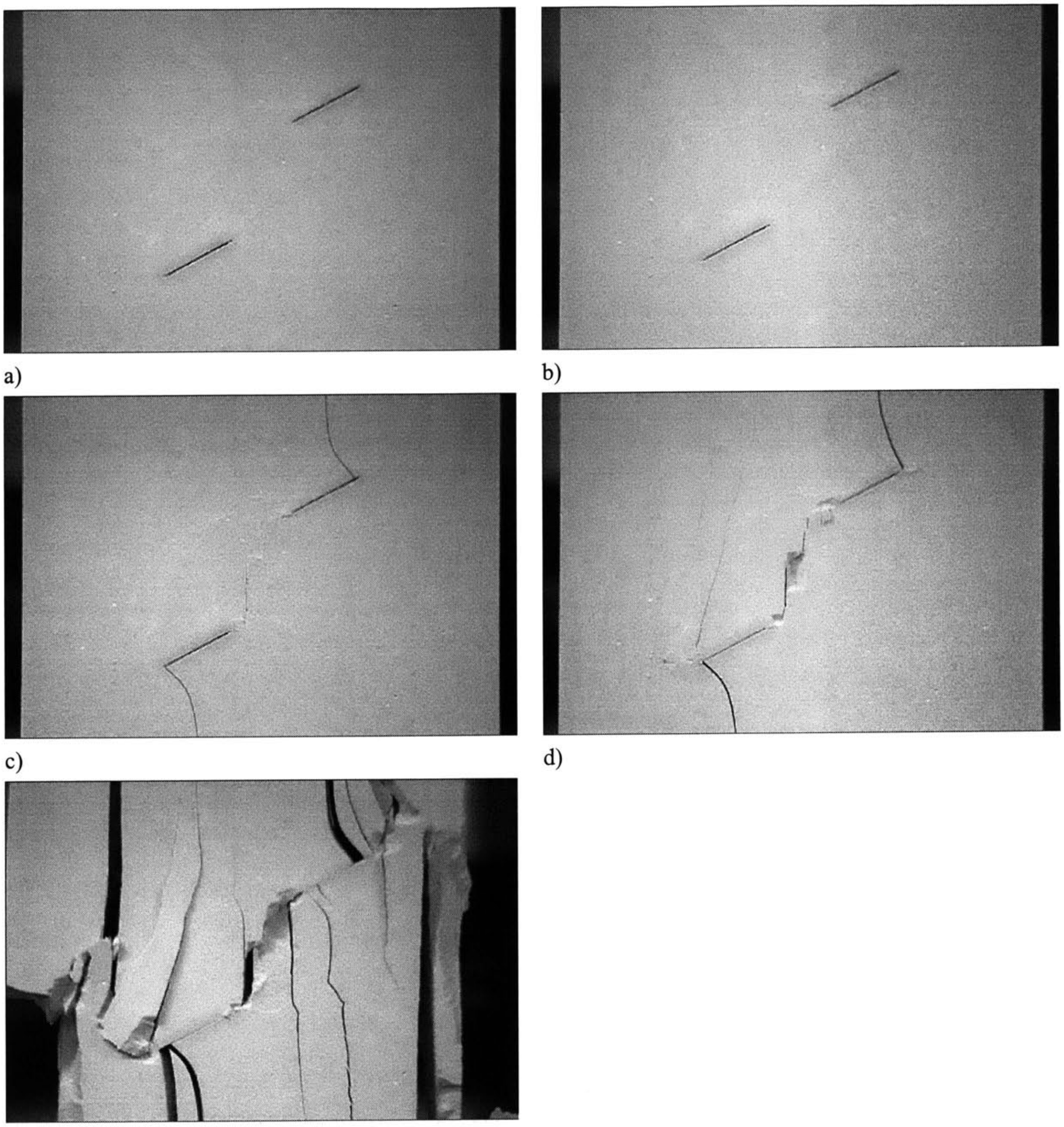

a) b) c) d) e)

Figure D.66 Cracking sequence of 30-2a-3a geometry in cyclic test. $\sigma_{max}/\sigma_c = 0.85$, $\sigma_{max} = 24.04$ MPa; a) Initial configuration b) External and internal wing cracks initiate (2 cycles). c) Coalescence occurs (202 cycles). d) Shear cracks occurs at the external tip of the upper flaw (606 cycles). Another tension crack accompanied by shear cracks occurs around the external tip of the lower flaw (606 cycles). e) Failure occurs (639 cycles).

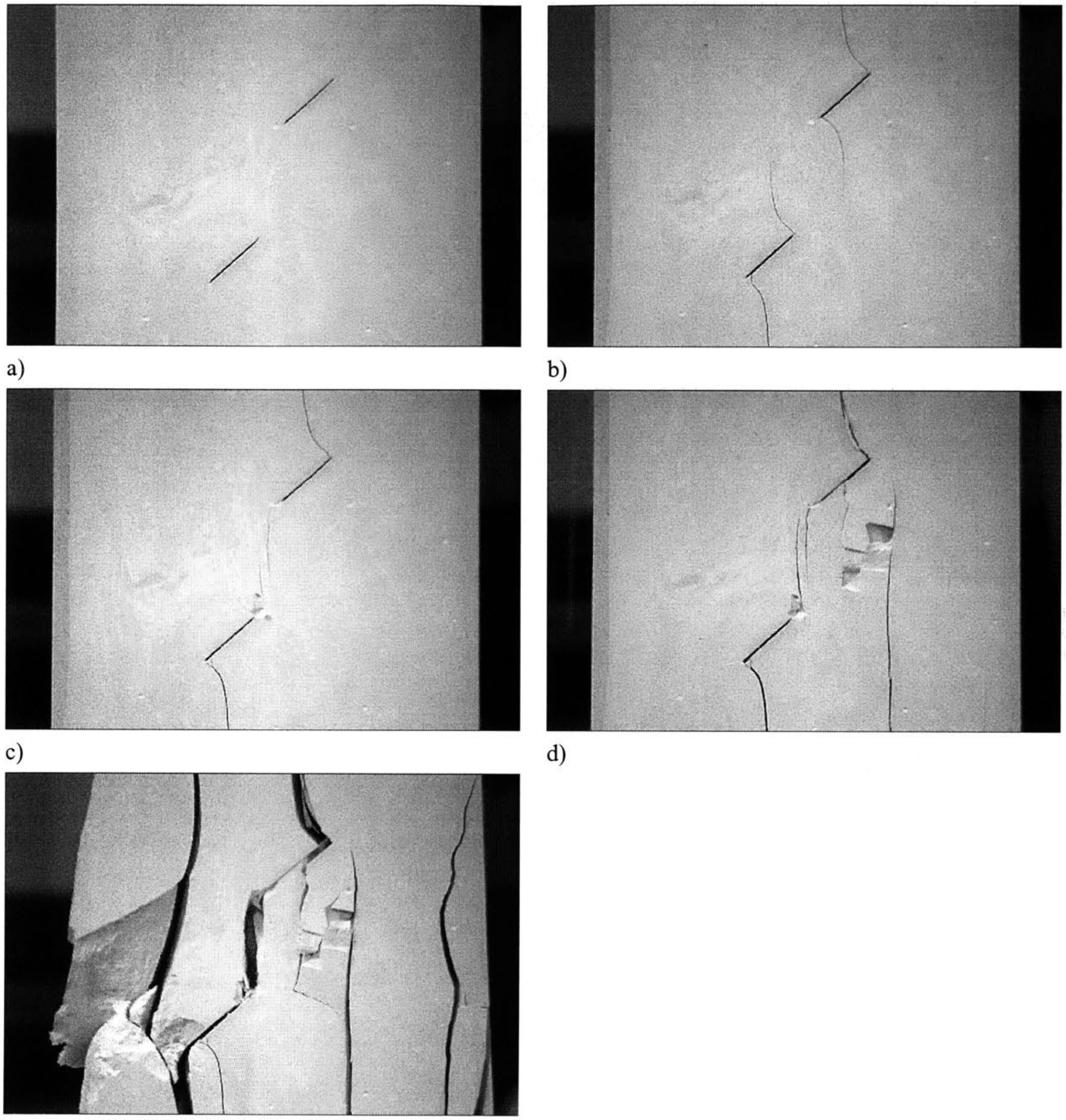

a) b) c) d) e)

Figure D.67 Cracking sequence of 45-2a-3a geometry in cyclic test. $\sigma_{max}/\sigma_c = 0.85$, $\sigma_{max}= 27.46$ MPa; a) Initial configuration b) External and internal wing cracks initiate (1 cycles). c) Coalescence occurs (845 cycles). d) Vertical splitting occurs (850 cycles). Shear cracks occur at the external tip of lower flaw (850 cycles). e) Failure occurs (851 cycles).

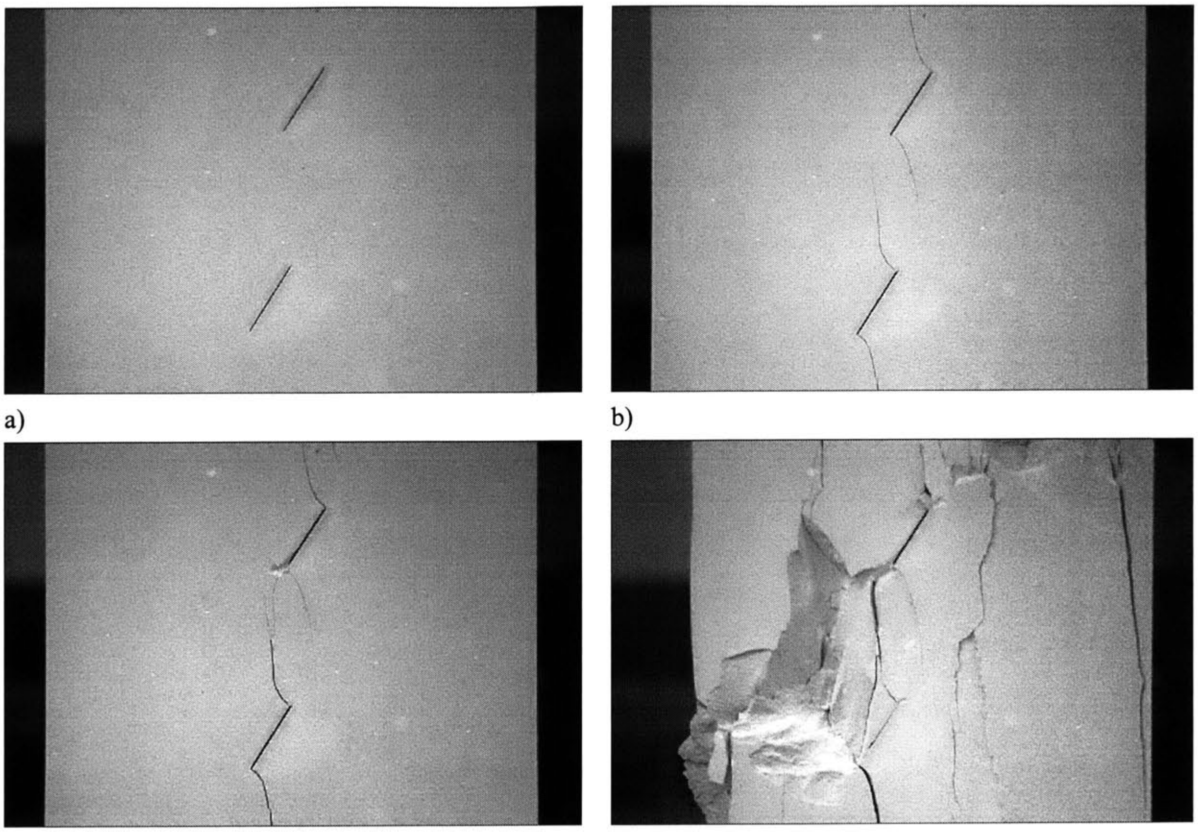

a)

b)

c)

d)

Figure D.68 Cracking sequence of 60-2a-3a geometry in cyclic test. $\sigma_{max}/\sigma_c = 0.8$, $\sigma_{max} = 31.96$ MPa; a) Initial configuration b) External and internal wing cracks initiate (121 cycles). c) Coalescence occurs (502 cycles). d) Failure occurs (735 cycles).

REFERENCES

Ashby, M. F. and S. D. Hallam, The Failure of Brittle Solids Containing Small Cracks Under Compressive Stress States. Acta metal. Vol. 34(3), pp. 497-510, 1986.

Attewell, P.B. and Farmer, I. W., Fatigue Behaviour of Rock. Int J Rock Mech Min Sci, Vol. 10, pp. 1–9. 1973.

Barquins, M. and J. -P. Petit. Kinetic instabilities during the propagation of a branch crack: effects of loading conditions and internal pressure. Journal of Structural Geology Vol. 14(8/9), pp. 893-903, 1992.

Bobet, A. Fracture Coalescence in Rock Materials: Experimental Observations and Numerical Predictions. Sc. D. Thesis, Massachusetts Institute of Technology, Cambridge, U.S.A., 1997.

Bobet, A. and Einstein, H.H. Fracture Coalescence in Rock-type Materials under Uniaxial and Biaxial Compression. International Journal of Rock mechanics and Mining Science. Vol. 35, No. 7, pp. 863-888, 1998

Brace, W. F. and E. G. Bombolakis., A note on brittle crack growth in compression. Journal of Geophysical Research Vol. 68 No. 2, pp. 3709-3480, 1963.

Brown E. T. and Hudson J. A., Fatigue Failure Characteristics of Some Models of Jointed Rock. Earthquake Eng Struct Dyn Vol(2), pp. 379-386, 1974.

Burdine N.T., Rock Failure under Dynamic Loading Conditions. Soc Petr Eng J Vol. 3, pp.1-8, 1963.

Chen, G. et al., Fracture Propagation and Coalescence in Marble Plates with Pre-cut Notches under Compression. Symposium on Fractured and Jointed Rock Mass pp, 443-448, 1995.

Costin, L.S. and Holcomb, D. J., Time-dependent Failure of Rock under Cyclic Loading. Tectonophysics Vol .79, pp.279-296, 1981.

Einstein, H. H. and Hirschfeld, R.C. Model Studies on Mechanics of Jointed-Rocks. ASCE Journal of the Geotechnical Division Vol. 99, SM3, pp 229-248, 1973.

Erdogan, F. and Sih, G. C., On the Crack Extension in Plates under Loading and Transverse Shear, J. Basic Eng., Vol. 85, 1963.

Griffith, A. A., The Phenomenon of Rupture and Flow in Solids. Phil. Trans. R. Soc. London, Series A, Vol.221 pp. 163-198, 1921.

Griffith, A. A., The Theory of Rupture. Proc. 1st Int. Congr. Appl. Mech., pp.56-63, 1924.

Haimson, B. C. and Kim, C. M., Mechanical Behaviour of Rock under Cyclic Fatigue. In: Cording EJ, editor. Stability of rock slopes, Proceedings of the 13th Synposium on Rock Mechanics, New York:ASCE, pp. 845-863, 1971.

Haimson, B. C., Mechanical Behavior of Rock under Cyclic Loading, in Advances in Rock Mechanics (Proc. 3rd Congress of the Intl. Soc. for Rock Mechanics), II, 373-378, 1974.

Hardy, H. R. and Chugh, Y. P., Failure of Geologic Materials under Low Cycle Fatigue. In: Proceedings of the Sixth Canadian Symposium on Rock Mechanics, Montreal, pp.33-47, 1970.

Hawkes, I. and Mellor M. Uniaxial Testing in Rock Mechanics Laboratories. Engineering Geology (Special issue), Vol. 4, No. 3, pp. 177-285, 1970.

Hoek, E and Bieniawski, Z. T., Brittle Fracture Propagation in Rock under Compression. Int. J. Frac. Mech., Vol. 1, pp.137-155, 1965.

Horii, H., and S. Nemat-Nasser. Compression-Induced Microcrack Growth in Brittle Solids: Axial Splitting and Shear Failure. Journal of Geophysical Research Vol. 90(B4), pp. 3105-3125, 1985.

Huang et al. An Experimental Study of the Strain Field Development Prior to Failure of a Marble Plate under Compression. Tectonophysics, Vol. 175: 269-284, 1990.

Hussain, M. A., Pu, S. L. and Underwood, J., Strain Energy Release Rate for a Crack under combined mode I and mode II, Fracture Analysis, ASTM STP 560, pp.2-28, 1974.

Ingraffea, A.R. & Heuze, F.E. Finite Element Models for Rock Fracture Mechanics. International Journal for Numerical and Analytical Methods in Geomechanics Vol. 4 pp, 25-43, 1980.

Irwin, G. R., Analysis of Stresses and Strains near the Ends of a Crack Traversing a Plate. *J. Appl. Mech.* Vol. 24, pp.361-364, 1957.

Jafari et al. Evaluation of Shear Strength of Rock Joints Subjected to Cyclic Loading, Soil Dynamics and Earthquake Engineering Vol. 23 pp. 619-630, 2003.

Kemeny, J. M. and N. G. W. Cook, Crack Models for the Failure of Rock under Compression. In Proc. 2nd Int. Conference Constitutive Laws for Engineering Materials, Theory and Applications, Tucson, Arizona, C. S. Desai, E. Krempl, P. D. Kiousis, and T. Kundu, eds., vol. 1, 879.887. Elsevier Science Publishing Co., 1987.

Lajtai, E.Z. Brittle Fracture in Compression. International Journal of Fracture, Vol. 10, No. 4, pp, 525-536, 1974.

Li, N., Chen, W., Zhang, P., and Swoboda, G.. The Mechanical Properties and a Fatigue-damage Model for Jointed Rock Masses Subjected to Dynamic Cyclical Loading, Int. J. Rock Mech. Min. Sci., Vol. 38 No.7, pp. 1071-1079, 2001.

Li, N., Zhang, P., and Chen, Y.and Swoboda, G. Technical note: Fatigue Properties of a Cracked, Saturated and Frozen Sandstone Samples under Cyclic Loading. Int J Rock Mech Min Sci. Vol.

40, pp.145-50, 2003.

Martinez, A., Fracture coalescence in natural rocks, S. M. Thesis, MIT, Cambridge, U.S.A., 1999.

McClinock, F. A. and Walsh, J. B., Friction on Griffith Cracks in Rock under Pressure. Proc. 4th us Natl. Congr. Appl. Mech., Berkely, pp.1011-1021, 1962.

Nelson, R., Modeling a Jointed Rock Mass, S. M. Thesis, MIT, Cambridge, U.S.A., 1968.

Palinaswamy, K. and Knauss, W. G., Propagation of a Crack under General, In-plane tension, Int. J. Frac. Mech., Vol. 8, pp.114-117, 1972.

Petit, Jean-Pierre, and Michel Barquins. Can Natural Faults Propagate under Mode II Conditions? Tectonics Vol. 7(6), pp. 1243-1256, 1988.

Prost C. L., Jointing at Rock Contacts in Cyclic Loading. Int J Rock Mech Min Sci Geomech Abstr Vol.25 No. 5, pp. 263-272, 1988.

Pruitt, L. and Suresh, S., Cyclic Stress Fields for Fatigue Cracks in Amorphous Solids-Experimental Measurements and Their Implications. Philosophical Magazine, A 67, pp. 1219-1245, 1993.

Reyes, O. & Einstein, H.H. "Failure Mechanism of Fractured Rock – A Fracture Coalescence Model." *Proceedings 7th International Congress of Rock Mechanics*, Vol. 1, pp. 333-340, 1990.

Reyes, O., Experimental Study and Analytical Modelling of Compressive Fracture in Brittle Materials, Ph. D. Thesis, MIT, Cambridge, U.S.A., 1991.

Royer-Carfagni, G., and Salvatore, W., The characterization of marble by cyclic compression loading: experimental results, Mech. Cohes.-Frict. Mater., 5, pp.535-563, 2000.

Sagong, M. and Bobet, A. , Coalescence of Multiple Flaws in a Rock-model Material in Uniaxial Compression , Int. J. Rock Mech. Min. Sci. Vol. 39, pp. 229.241, 2002.

Sagong, M., The Study on the Fracture of Multiple Flaw Specimenms, Ph. D. Thesus, Purdue University, U.S.A., 2001.

Shen, B., Stephansson, O., Einstein, H. H., and Ghahreman, B., Coalescence of fracture under shear stresses in experiments, J. Geophys. Res., 100, B4, pp. 5975-5990, 1995.

Sih, G., C., Methods of Analysis and Solutions of Crack Problems, Mechanics of Fracture, 1, Noordhoff International Publishing, Leyden, 1973.

Surresh, S., Fatigue of Materials - 2nd ed., Cambridge university press, 1998.

Takeuchi, K., Mixed-mode Fracture Initiation in Granular Brittle Materials, S. M. Thesis, MIT, Cambridge, U.S.A., 1991.

Wong, R. H. C., and Chau, K. T., Crack Coalescence in a Rock-like Material Containing Two

Cracks, Int. J. Rock Mech. Min. Sci., Vol. 35 No. 2, pp.147-164, 1998.

Zhenyu, T. and Haihong, M. Technical note: An Experimental Study and Analysis of the Behaviour of Rock under Cyclic Loading. Int J Rock Mech Min Sci Geomech Abstr Vol. 27No. 1, pp.51-56, 1990.